Comportement des mortiers haute performance sous sollicitations de fatigue en compression

Erisa Myrtja

université PARIS-SACLAY

Behavior of high-strength grouts under compressive fatigue loading

Thèse de doctorat de l'Université Paris-Saclay

École doctorale n° 579 : Sciences Mécaniques et Énergétiques, Matériaux et Géosciences (SMEMAG)
Spécialité de doctorat: génie civil
Unité de recherche : Université Paris-Saclay, ENS Paris-Saclay, CNRS, LMT - Laboratoire de Mécanique et Technologie, 91190, Gif-sur-Yvette, France.
Référent : ENS Paris-Saclay

Thèse présentée et soutenue à Gif-sur-Yvette, le 05/10/2020 par

Erisa MYRTJA

Composition du Jury

Jean-François GEORGIN Professeur, INSA Lyon	Rapporteur
Ahmed LOUKILI Professeur, École Centrale de Nantes	Rapporteur
Farid BENBOUDJEMA Professeur, ENS Paris-Saclay	Examinateur & Président
Luz GRANIZO Ingénieur DR, Sika Technology AG	Examinateur
Mohend CHAOUCHE Directeur de Recherche CNRS, ENS Paris-Saclay	Directeur de thèse
Evelyne PRAT Directrice R&D, Parex France / Sika Technology	Co-Encadrante
Jérôme SOUDIER Ingénieur R&D, Parex France / Sika Technology	Co-Encadrant

Thèse de doctorat

NNT : 2020UPASTO17

Remerciements

Je tiens tout d'abord à remercier les membres du jury pour avoir participé à ma soutenance de thèse. Un grand merci aux rapporteurs Jean-François Georgin et Ahmed Loukili d'avoir apporté les corrections, remarques et suggestions liées à mon travail de thèse. Mes remerciements vont particulièrement au président du jury, FariD Benboudjema pour la richesse des questions et nos échanges lors de ces années au LMT.

Bien évidemment, je remercie mon équipe d'encadrement commençant par mon directeur de thèse Mohend Chaouche, qui m'a donné l'opportunité de réaliser ce travail et m'a soutenu devant chaque difficulté. Je tiens également à remercier mes encadrants industriels Evelyne Prat et Jérôme Soudier qui m'ont accompagné, guidé et m'ont transmis leur connaissances.

Cette thèse m'a permis de me développer non seulement sur un plan scientifique, mais aussi sur un plan humain par de très belles rencontres dans les deux laboratoires. Ainsi, depuis mon bureau stagiaires/doctorants au CIP, j'ai fait connaissance avec des personnes très professionnelles travaillant dans un environnement convivial. Je ne peux pas oublier l'aide qu'Olivier et Guillaume m'ont donnée durant la dernière année sur les nombreuses gâchées qui se sont enchainées.

Ce travail n'aurait pas pu se réaliser sans l'aide des membres du LMT et DGC, en particulier Bubu, Remi et Olivier. Leur aide, disponibilité et soutien dans la réalisation des essais (mais pas que) a été d'une grande valeur. Et enfin merci à tous les doctorants, postdocs et les meilleurs collègues de bureau qui ont rendu cette expérience inoubliable.

Falenderoj mbi të gjitha prindërit e mi që më kanë mbështetur gjithmonë dhe në çdo hap, gjatë doktoraturës dhe gjatë studimeve të mia relativisht të gjata. Pa ndihmën e tyre, sot nuk do t'ia kisha dalur të kem këto arritje akademike. Do ju jem falenderuese gjithmonë.

Enfin, merci à toi Martin ! Pour ton aide, relecture du manuscrit, conseils, soutien, présence et amour pendant cette thèse et depuis tant d'années.

Table of content

List of figures

List of tables

Nomenclature - Abbreviations

σ_c or f_{cm}	Quasi-static compressive strength [MPa]
ε_u	Strain at peak load during quasi-static loading [‰]
ε_f	Strain at failure [‰]
E_O	Young's Modulus [GPa]
E_s	Secant Modulus [GPa]
ΔE	Total decrease of stiffness compared to the first cycle in fatigue [%]
E_{dyn}	Dynamic Stiffness[GPa]
ϑ	Poisson's Ratio [-]
c_p	Ultrasonic velocity [m/s]
$\alpha_{c,el}$	Limit of elastic zone in quasi-static compressive tests [-]
ϕ	Porosity [%]
$\varepsilon_{c,u}$	Strain evolution during compressive fatigue loading [‰]
$\varepsilon_{c,max}$	Maximum strain evolution during compressive fatigue loading [‰]
$\varepsilon_{c,min}$	Minimum strain evolution during compressive fatigue loading [‰]
$\dot{\varepsilon}_{max,II}$	Gradient of the secondary strain development [–]
$\Delta\varepsilon_{c,max}$	Relative strain evolution
$S_{c,max}$	Maximum stress level applied during compressive fatigue loading [–]
$S_{c,min}$	Minimum stress level applied during compressive fatigue loading [–]
R	Stress ratio between minimum and maximum stress level [–]
N_f	Number of cycles to failure "Fatigue Life"
f	Loading frequency [Hz]
$\bar{\theta}$	Mean temperature increase [K]
$\Delta\theta$	Temperature increase during loading [K]
T_{th1}; T_{th2}	Temperature measured by thermocouples on the specimen [°C]
T_{up}; T_{lp}	Temperature measured on the machine plates [°C]
$\bar{\theta}_{sf}$	Mean temperature increase in self-heating tests [K]
$t_{0,sf}$	Time of a loading step [s]
$\dot{\varepsilon}$	Strain rate of loading during a quasi-static compressive test [s^{-1}]
$\dot{\sigma}$	Stress rate of loading during a quasi-static compressive test [$MPa.s^{-1}$]
f_d	Dynamic strength due to stress rates [MPa]

d_{max}	Maximum aggregate size [mm]
D	Diameter of the specimen [mm]
H	Specimen height [mm]
T_{amb}	Room temperature [°C]
HR	Relative humidity [%]
W/B	Water – binder ratio

NSC	Normal-strength Concrete
HSC	High-strength Concrete
UHSC	Ultra-High strength Concrete
HSG	High-strength Grout
UHSG	Ultra-High strength Grout

CSH	Calcium Silicate Hydrate
$Ca(OH)_2$ or CH	Calcium Hydroxide
ITZ	Interface Transition Zone

DIC	Digital Image Correlation
ROI	Region of Interest
fps	Frames per second
MIP	Mercury Intrusion Porosimetry

R-Bau	Reference mix with bauxite aggregates
Qua	Mix with quartz aggregates
Tab	Mix with tabular alumina aggregates
Bau-G	Mix with bauxite as coarse aggregates and quartz as fine aggregates
Qua-G	Mix with quartz as coarse aggregates and bauxite as fine aggregates
A-Bau	Reference mix with increased air content
W-Bau	Reference mix with increased w/b ratio

Introduction

Background

Cementitious materials used in structures such as wind turbines, bridges, railway slab tracks, offshore platforms and concrete pavements are not exposed only to static loads. Depending on the environment and external nature of loading, cyclical stresses are applied over time. If these cyclical loads occur repeatedly over the lifetime of the structure, they lead to internal changes, durability issues and a decrease in load bearing capacity. This process is called fatigue and involves the main purpose of this research work. Cementitious materials have typically been employed in structures with large cross-sections, where the variable loads are not significant compared to the permanent loads and therefore they are not affected by fatigue. However, recent modern structures characterized by a slender shape, such as wind turbines are composed of concrete (foundations) and grout parts (transition piece), which make them prone to fatigue loading.

The fatigue behavior of concrete has been part of research for a long time, however there are large gaps in knowledge regarding this phenomenon. Indeed, the early work was mainly focused on fatigue behavior of normal-strength concrete with a target on estimating the number of cycles to failure which the material can endure before failure. Only in the recent years, the fatigue behavior of high-strength and ultra-high strength concrete is examined. Even fewer studies are reported on high-strength grouts. Numerous wind farms constructed with plain grouted connections in monopile structures resulted to have settled and presented cracking due to fatigue. Therefore, during the 10 recent years, fatigue behavior of high-strength grouts is of increasing relevance and additional exhaustive research is essential for further applications.

Furthermore, many documented investigations in the literature aim to estimate the fatigue strength and endurance limit or describe the fatigue failure regarding the static behavior. However, the evolution of deformations and stiffness should also be evaluated in order to provide a better comprehension of damage mechanisms. This would also allow conducting more accurate dimensioning for structures submitted to fatigue loading. Finally, cementitious materials with high-strength properties tend to become more brittle. Hence, previous knowledge gained from normal strength concrete is not necessarily applicable to high-strength concrete or grout. Against this background, providing more information on the fatigue behavior of high-strength grouts is of great importance. The main objectives will be presented in the next section.

Research objectives

The main research objectives in this thesis are defined based on the previous addressed issues and the outcomes of the literature research, which will be presented in chapter 1. Against this background, two main directions were followed. *Firstly*, the aim is not only to provide the fatigue life or strength of the investigated grout, but also to describe and analyze the material response during fatigue loading. Therefore, a large number of experimental tests were carried out on one mix called "reference" throughout this manuscript. These tests are intended to gain insight into the behavior of high-strength grouts in fatigue. Based on previous methods used into evaluating the damage process, the test programs were developed in order to include different examination approaches, in addition to investigating different parameters. An important part of this work consisted in identifying the parameters which have an influence on fatigue life and the related strain or stiffness development during fatigue loading, such as loading frequency and maximum stress level.

Secondly, the test programs were designed to provide reliable comparisons between different grout types and evaluate relevant parameters which could lead to a better understanding of the fatigue behavior. Therefore seven grout mixes will be discussed, based on the influence of microstructure and different mix components on fatigue behavior.

Due to the knowledge gaps related to fatigue behavior of high-strength grouts, the thesis has followed a predominant experimental direction. Analytical predictive methods for estimating the endurance limit and a model describing the strain development during fatigue is also given in the following chapters. However, the informations acquired with the large amount of experiments provide valuable information for the calibration and development of numerical models.

It should be noted, that the two aforementioned objectives are both related to fatigue in compression. One essential application for the studied grout is in joints of wind turbines, where the current guidelines suggest the evaluation of fatigue in compression for this application. The same loading type is recommended for high-strength concrete used in foundations. Hence, the material behavior in *compressive fatigue* is the main focus in this thesis. Nevertheless, the flexural fatigue will also be examined in the last part of the manuscript, but to a lower extent.

Outline

This manuscript is structured in five chapters, where each chapter incorporates a different direction followed in the comprehension of fatigue related to grouts. In addition, an introductory paragraph brings forward a description of the associated work and the main outcomes are summarized in the conclusions section of each chapter. An overview is given below.

Chapter 1 firstly presents the field of application of high-strength grouts and evokes possible microstructure dissimilarities with high-strength concrete. Subsequently, a state of the art of the current outcomes in the fatigue behavior of grout and concrete are presented. The damage mechanisms and possible influencing factors on the fatigue life are reviewed, based on documented results. Furthermore, a description of creep in concrete is given, where possible analogies with fatigue loading are discussed. This chapter is finalized by the main questionings that the thesis will attempt to answer.

Chapter 2 describes the followed methodology for establishment of grout mixes, tested and analyzed further in the manuscript. Additionally, the steps from specimen casting to testing are detailed. The measurement technology used during fatigue tests and the testing protocols are outlined. Finally, a description is given on the different techniques used for characterizing the material microstructure.

Chapter 3 contains the main part of the thesis related to the comprehension of damage mechanisms in compressive fatigue, for a reference high-strength grout. The experimental results derived from the described methods in the previous chapter are presented. The fatigue behavior is analyzed at two loading frequencies and different parameters are evaluated to provide a better understanding of the damage process. A comparison with the material behavior in quasi-static tests is also examined. Moreover, analytical methods are employed to predict the fatigue life of the grout. Finally, the microcracking during loading is examined and post-mortem analyses are carried out.

Chapter 4 addresses the influence of mix components on the fatigue life and deterioration mechanisms. This chapter is subdivided in three main parts, where initially the influence of aggregate type on the compressive fatigue life and damage mechanisms are evaluated. A relation with differences in microstructure is also established. In the second part, tests on the effect of two aggregate types at different fractions are carried out. Lastly, the porosity increased in the form of added water content and induced air is measured and its possible effect on fatigue life is analyzed. Based on the gained knowledge

from the tests, a description of the damage process involved in high-strength grout with possible influencing factors is given.

Chapter 5 aims to evaluate the fatigue life in flexural tests, in contrast to previous chapters focused mainly on fatigue in compression. Indeed, grouting materials can also be implemented in applications submitted to flexural loadings. Thus, the purpose is to estimate whether any difference takes place in number of cycles to failure between the two different testing methods and if the fatigue life is independent on the type of test.

The conclusions and essential results of the present research work are summarized at the end of this manuscript. Subsequently, the main findings are followed by an outlook on further research on fatigue of concrete and grout.

Chapter 1
State-of-the-art

1.1 Introduction

The thesis is focused on the fatigue behavior of high-strength grouts and therefore this first chapter contextualizes why this type of loading is relevant for this material. The high-strength concrete and grout have excellent characteristics in static, but very few knowledge is available in terms of fatigue life and damage development, compared to normal strength concrete. Within this framework, the chapter begins with a reminder of the main application fields of high-strength grouts. The microstructural properties and possible differences with normal and high-strength concrete are presented. Further in the manuscript, reference is made to the grout microstructure for the understanding of the damage process and its possible influence on fatigue behavior. Subsequently, the mechanical behavior of the grout is overviewed, starting with the compressive quasi-static strength and followed by the strain rate effects, which enables to establish the link between quasi-static and fatigue. The fatigue phenomenon is then defined by discussing basic principles, approaches and current standards. Additionally, different factors which can influence the fatigue life and deterioration process are reviewed, while simultaneously providing current inconsistencies and knowledge gaps. The strain and stiffness development and energy dissipation during loading are discussed as indicators in the damage evolution. This analysis provides the basis for evaluating the test results in further chapters. A particular attention is given to the internal temperature generation during compressive fatigue loading, with possible effects in terms of fatigue life. From this phenomenon, the self-heating method commonly applied in steel materials, is derived and described as possible alternative method in evaluating the endurance limit in high-strength grouts. Finally, the creep mechanisms are described and analogies with fatigue are presented. A description in modelling the fatigue loading, based on creep behavior is presented and it will be applied further in chapter 3.

1.2 Field of application of high-strength grouts

Grouted connections are structural connections, which consist of two centric tubular or conical sections where the annulus between the outer and the inner tubular or conical section is filled with grout [1], see figure 1.2-1. They are very well known in oil and petroleum industry for offshore platforms. More recently, these connections have found larger applications in different industries, road joints or wind energy, such as in wind turbines. These connections differ from conventional applications, by being part of more slender structures with smaller cross-section areas. Therefore, this makes them more prone to fatigue loading, in conditions where complex nonlinear loads are applied.

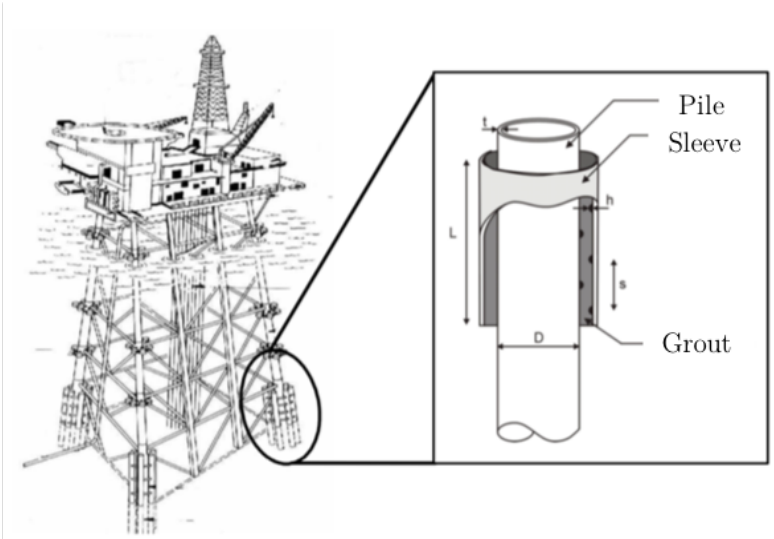

Figure 1.2-1 *Grouted joints in offshore platforms : location and general construction [2]*

The grouted joints are used in almost all wind turbine structures, such as onshore, monopiles, tripods and jacket foundations. The choice of the type of structure in offshore wind turbines depends on the water depth on site. Monopile wind turbines have been the most common used due to their effectiveness in structural simplicity and easier installation process in sea depths up to 30 m (with or without shear keys) see figure 1.2-2. Recent demands of more effective wind conditions have pushed the wind industry towards higher sea depths [3], where gravity based foundations, tripod or jacket foundations are used. Floating wind turbines seem to be applicable in even deeper seas, nevertheless they do not use grouting. It should be mentioned that the floating raises additional dynamic loads in the structure.

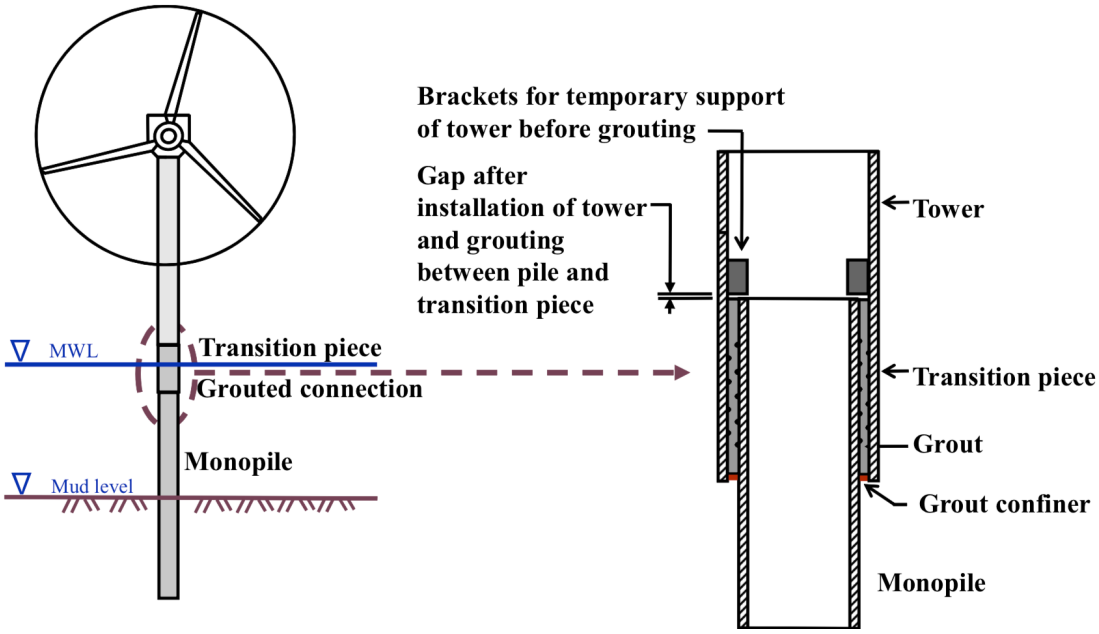

Figure 1.2-2 *Principle of grouted connection in monopile structure [1]*

Monopile wind turbines are designed for a service life of 20 - 25 years and withstand load cycles up to 10^9 [4]. The cyclic loads are mainly due to wind, wave or ice loadings inducing high bending moments in the structure. According to Lotsberg [5] "The stresses in the monopile due to the bending moment from wind loading can be more than one order of magnitude larger than those due to the axial load alone. Owing to the large diameter to thickness ratio, the grouted connections become rather flexible with respect to bending moment and a radial cracking of the grout may be expected."

Therefore as presented in this section, grouts can be exposed to fatigue loading, but these mechanical cyclic stresses can also be applied to concrete structures. Firstly, concrete tower wind turbines with UHPC and a steel top section (hybrid towers) have been proposed [6], and they would be exposed to the same issues. Moreover, fatigue loading is also present in concrete highway and bridge structures under random vehicle loadings. Hence, fatigue loading in these materials is not to be neglected and will be the main focus in this thesis.

1.3 Microstructural properties of high-strength grout and concrete

1.3.1 Distinction between concrete and grout

Concrete is a complex heterogenous material composed of coarse and fine aggregates and binder. The binder is generally composed of cement and water, but also of additives (also

called supplementary cementitious materials) in order to develop a more sustainable concrete or a lower cost concrete. Finally admixtures are used to improve concrete properties depending on the final application and on-site requirements.

Grouts and mortars have a similar composition to concrete, but no coarse aggregates are present (see figure 1.3-1) and they have a high flowable consistency. However, this statement is true when compared to conventional concrete. During the last decades, research has conducted in developments of Ultra-High Performance Concrete (UHPC), with a compressive strength of 140 MPa or higher, by eliminating coarse aggregates and improving homogeneity, among other methods, such as Reactive Powder Concrete RPC [7].

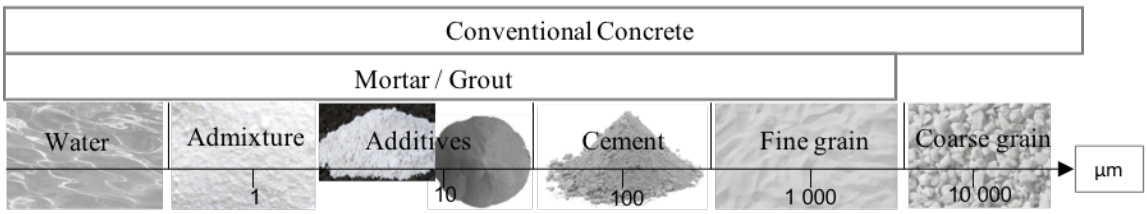

Figure 1.3-1 *Schematic representation of mixture components in conventional concrete and grout*

Thus, it can be accepted that the main distinction between Ultra-High Strength Grout and Ultra-High Strength Concrete is the purpose of application. Concrete is used as a structural component to bear loadings, whereas grout is used as a joint to transfer loads.

Due to comparable microstructural properties and the limited research on fatigue behavior of the grout, the analysis of the data further in the thesis will be often compared to concrete results. Moreover, Lohaus et al. [8] carried out fatigue tests for a high strength concrete and grout and found a similar behavior and number of cycles to failure for different stress levels at $f = 10\text{Hz}$.

It can be unclear the distinction between ultra-high strength (UHSC) and high-strength concrete (HSC) and grout (HSG), in terms of terminology. Often, ultra-high strength is considered, when the compressive strength is higher than 140 or 150 MPa. In other reports, a temperature treatment is used to produce ultra-high strength concrete. It will be shown later that the grouts tested in this research a have higher compressive strength than 140 MPa. We will be referring to these grouts as *high-strength* grout.

1.3.2 Interactions aggregate – cement matrix

Different high-strength concrete mixes have been developed in the last 50 years, starting from Brunauer [9] in the 70s with a target of a cement paste with low porosity and followed by Bache, who developed the DSP (Densified with Small Particles) concrete [10]. Moreover, the macro-defect free concrete MDF was developed by Birchall [11], where special polymers were included, but they may have a high sensitivity to water [12]. In the 90s, the Reactive Powder Concrete RPC [7] was introduced and improved further by optimizing the particle packing. Various laboratory techniques can ensure higher mechanical strengths such as autoclaving, compaction under pressure, temperature treatment etc., however they are not implemented in this work as they are difficult to be executed for on-site applications.

Recent modern high-strength grouts, have been inspired by these developments, where a lower **aggregate size** is used. Indeed, a higher aggregate size, might induce more microcracking in the interfacial transition zone (ITZ) as shown in [7], where it is assumed that the microcrack size is directly related to the aggregate size. When compressive forces are applied, shear and tensile stresses appear at the interface generating cracks, schematically represented by Petkovic [13] in figure 1.2-2.

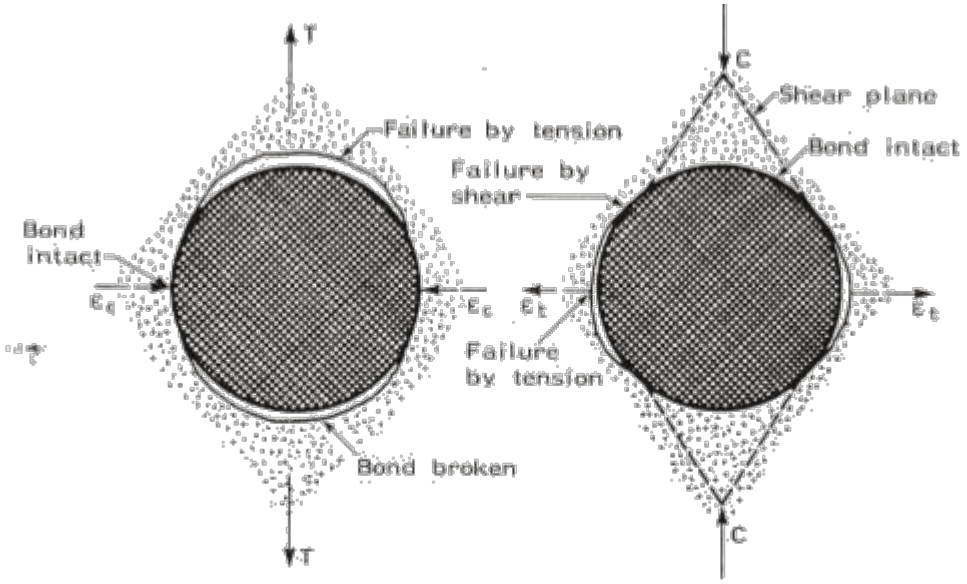

Figure 1.3-2 *Local stresses around aggregate particle under tensile and compressive [13]*

The interfacial transition zone can be the weakest part of the microstructural system in a conventional concrete. It is often described as an area created by the packing of cement grains against large aggregate particles [14]. Therefore, a better **bond between the aggregate and the matrix** can lead to a smaller ITZ and improve the mechanical strength. In high-strength concrete and grout this bond is improved by creating a

densification of the interface zone with the use of silica fume or other small particle silica additives (further detailed in chapter 2.2.2).

Three main mechanisms are identified when considering the interaction between the aggregate and the matrix described by Zhang [15] :

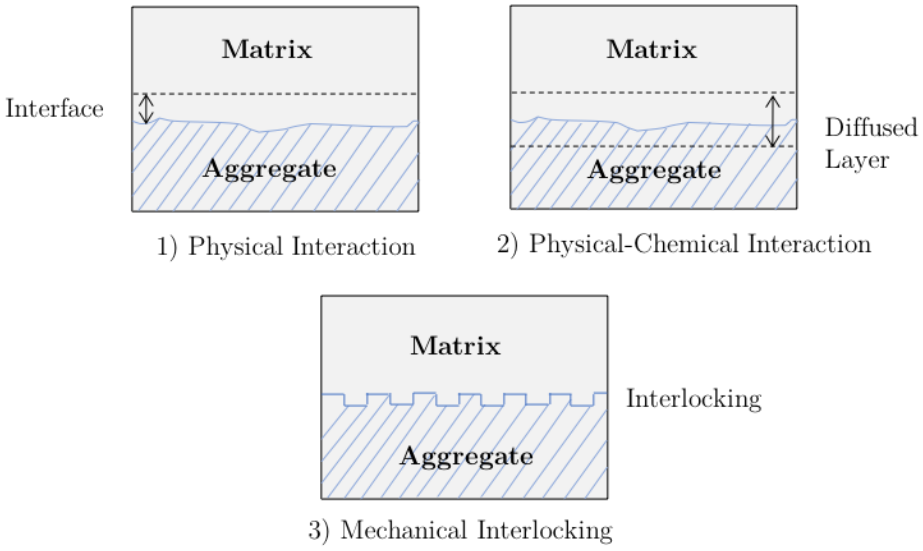

Figure 1.3-3 *Schematic presentation of the interfacial zone between cement paste matrix and aggregate adapted from Zhang [15]*

⇒ Physical Interaction, which is the case of well-polished mineral surfaces such as quartz sand, where the bond strength can be negligible. However, only small interaction can be observed due to the water absorption of the aggregates from the matrix, which locally decreases the water/binder ratio.

⇒ Physical-Chemical Interaction, which is the case of a chemical interaction between aggregates and the matrix such as carbonate rocks with high-purity alite cement as shown in [16], or fly ash aggregates [17].

⇒ Mechanical Interlocking, which is the case for porous aggregates with a rough surface. The cement hydration products, may penetrate in the large pores of the aggregate surface.

In conventional concrete, there is generally a lack of **compatibility** between the aggregate and the cement paste. The matrix has a lower Young's modulus than the aggregate, and the cracking due to loading generally goes through the matrix or the interface, which is the weakest area. However in high-strength concrete, by improving the properties of the matrix and having a comparable Young's modulus to the aggregate,

the cracks will tend to manifest a “branching” type, by propagating through the aggregate, matrix and the ITZ as described in CEB-FIP [18]. When the Young’s modulus is comparable, a better bonding is created between the aggregate and the matrix and therefore local stresses due to a mismatch in elastic properties are decreased [19].

1.3.3 Fresh state properties

In offshore industry, grouted joints consist of two steel pipes filled with high-strength grout in a circumferential shape. The grout is generally pumped into the connection below the sea-level [20]. For this reason the grout system needs a highly flowable consistency with a high stability in the fluid phase. Moreover, it must have self-compacting properties and the maximum grain size should be generally between 1 mm and 6 mm. Due to large bearing loads and continuous cyclic loading applied, high strength properties are also required.

The offshore conditions require quite complex logistics, and the pumping process in filling the joint must not create segregation within the material. Common grouted joints can reach lengths up to 10 m and thickness in the range 50 - 120 mm, therefore the grout should be homogeneous and not show segregation or sedimentation.

Rapid hardening and high strength at early age should also be ensured. The grout can be submitted to wave loading even before hardening, within the first 24 hours and often exposed to low temperatures as recommended in DNVGL-ST-0126 [21].

Despite the compressive fatigue loads, important shear forces and local tension are present within the material. Therefore, some authors [2,22] suggested the use of steel fibers to improve the load bearing capacity and improve ductility, since the grout can demonstrate brittle behavior. Lee [23] showed that their use in concrete improves fatigue life in flexion, but not in compression. In addition, the use of fibers can also worsen the workability and pumpability [20]. Steel fiber grouts will not be studied in this research, because their application is not common. Moreover, the focus is led specifically on the fatigue behavior of the plain grout and not the total structure behavior. Nevertheless, some of the requirements in fresh state properties will be taken into account for the establishment of the mix composition.

This section was focused on a global description of the properties of high strength grouts. In chapter 2, more literature review will be given on each mix component separately, while justifying the choice of each element in the mixes used throughout the thesis.

1.4 Mechanical behavior of high-strength grout and concrete

1.4.1 Quasi-Static behavior – uniaxial compression

Uniaxial compressive tests are the most common test method, carried out on cylinders or cube shape. Overall, the tests are carried out on specimens with a ratio Height/Diameter of 2, based on French standard [24]. In order to avoid stress rate effects, the loading should be applied in stress controlled mode between 0,2 and 1 MPa/s, or in displacement controlled mode with a strain rate between 10^{-6} s^{-1} and 1,6 x 10^{-5} s^{-1}.

In general, the normalized test is controlled at an imposed stress rate, but in order to obtain the post-peak regime, an imposed displacement can be applied [25]. At a meso-scale level, the grout is characterized by a heterogeneous composition, and even after mix optimization, microcracking is present even before loading, due to shrinkage and drying. When compressive stress is applied, these microcracks are stable up to 30% [26] or 40% and the stress-strain relation is elastic linear with no evolution of the elasticity modulus and Poisson coefficient [27]. Beyond 30% up to 70-80%, the existing microcracks propagate very slowly and a few other microcracks are created in the interface, due to stress concentrations around the aggregates (see figure 1.4-1).

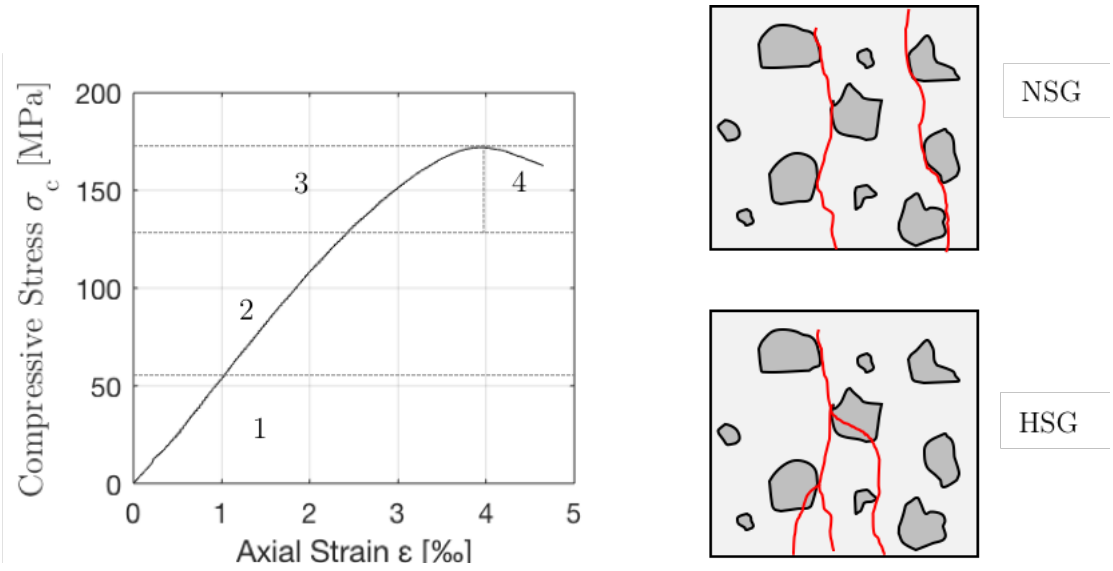

Figure 1.4-1 *Stress - strain relation during uniaxial compressive test and the four evolution phases – variable boundaries according to strength (a) Schematic crack paths in normal and high - strength grouts (b)*

This upper level generally defines the boundary of the elasticity zone and it varies between a normal or high-strength concrete. Thus, in high-strength and ultra-high strength concrete it can be higher, up to 95% of the compressive strength. A third phase characterized by an unstable crack growth vertically and irreversible strain up to the maximum stress f_c described as compressive strength. Finally the microcracks merge and the lateral displacements increase very rapidly up to failure of the specimen. In the post-peak area, the crack propagates through the aggregates in addition to interface and matrix for a high-strength grout or concrete. Whereas in a normal strength concrete the crack propagation is mainly through the ITZ (figure1.4-1 (b)).

Compared to a normal concrete, the ultra-high strength concrete and grout have a higher elastic linear branch, a higher stiffness and a steeper slope of the descending part. However, this last element can be highly dependent on the interaction with the testing system as shown by Shah [28]. The difference in stiffness describes different crack growth between normal and high-strength concrete.

1.4.2 Strain rate dependency

High-strength grouts can have various applications, where not only quasi-static behavior should be considered. Cyclic loading due to earthquakes or fatigue loading due to traffic, wind and waves can take place. Therefore, the grout shows a dependency on the strain-rate, as shown by Bischoff and Perry [29] for concrete (see figure 1.4-2). The compressive strength increases with an increasing rate, which is a phenomenon widely considered in impact and dynamics. A variation between $\dot{\varepsilon} = 10^{-6}$ /s and $\dot{\varepsilon} = 10$ /s can induce an increase in compressive strength of 1,5 times for normal concrete.

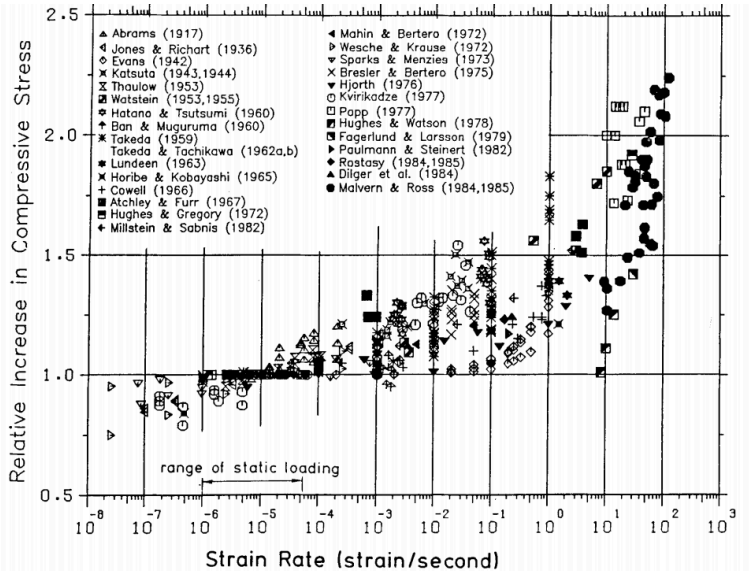

Figure 1.4-2 *Logarithmic strain-rate influence on the relative compressive strength [29]*

This increase is related to the viscosity of the cement matrix, where the free water in the micropores exhibits the Stefan effect according to Rossi [30]. High-strength concrete and grout have an optimized water/binder ratio, however small quantities of free water are still present in the matrix and in C-S-H hydrates, therefore the mechanical strength is still increased [31,32] with an increasing rate. The level of increase in this case, is expected to be lower than for a lower strength concrete [33,34].

This hypothesis has also been encouraged by a few studies, where dry concrete shows no dynamic strength increase [30] or a very small one [35]. Another mode responsible for the strength increase is the inertia effect, which creates important radial constraints acting like a confining pressure. Nevertheless, this is valid when strain rates higher than 10 /s are applied, which is the case of impact loading, and is not the focus of this thesis.

1.4.3 Fatigue behavior of plain concrete and grout in compression

It was presented earlier, that high strength grouts and concrete have an increased application in structures subjected to fatigue loading such as bridges, wind turbines, pavements, airport runways etc. Hsu [36] classified the load cycles likely to be supported by different structures (Table 1-1). It should be noted that from research in literature review, there seems to be a confusion between cyclic loading and fatigue. We will consider further that fatigue is a long term phenomenon due to cyclic loading and the number of cycles to failure are 10^3 or higher. Structures submitted to lower cycles, such as earthquakes, manifest a different behavior and is not analyzed here.

Table 1-1 *Classes of fatigue loads according to Hsu [36]*

Low-cycle fatigue			**High-cycle fatigue**		**Super-high-cycle fatigue**				
1	10^1	10^2	10^3	10^4	10^5	10^6	10^7	10^8	10^9
Structures subjected to earthquakes			Airport pavement and bridges		Highway; railway bridges and highway pavements		Mass rapid transit structures		Sea structures

The improvement of concrete and grout technology and their development with higher strengths, means that structures are built with lower cross-sections making them more disposed to fatigue loading. Existing bridge structures are exposed to more traffic and higher loads, not taken into account in design and leading to crack and durability issues. The stresses applied in these structures differ from structures in quasi-static in terms of rates and cycles. Indeed, the material properties can be affected by the repeated loading as Hordijk showed in [37], among others. At the same time, it was presented that

cementitious materials manifest different behavior depending on the strain rate applied. Thus, it is necessary that the fatigue behavior is "completely" understood in these applications.

1.4.3.1 Definition and history

In a recent book on bridge design, Pipinato and Brühwiler [38] define fatigue as follows: "Fatigue consists of the localized alternating repetitions of concentrated stress cycles in a structure induced by the external application of loads such as vehicles, winds, waves, and temperature. These elements, when below of the structural capacity of the structure, could induce fracture, and over a long period, eventually cause total collapse". In a material scale, fatigue fracture occurs at significantly lower stress levels than the static strength of the material.

Schütz reported in a paper on the history of fatigue [39] that Wilhelm Albert is the first to describe the fatigue phenomenon in 1837. The most known work on fatigue is by the German railway engineer August Wöhler in 1860, who noticed structures failing under the static limit. His work resulted during the years in the definition of endurance limit, the relation between amplitude and number of cycles to failure. Later in 1936, his data were expressed by his successor Spangenberg, as curves and were called "Wöhler curves", still used these days.

Fatigue in concrete appeared later in the 1970s after structural problems in offshore structures, such as Holmen [40], Aas-Jakobsen [41] and Hsu [42]. Many research on the fatigue of concrete was found until the 1990s. Only in the recent 10 years, due to change in concrete technology and structures becoming more slender, a lot of research is dedicated to fatigue of concrete, mortars and grouts by studying different aspects and different loading types.

1.4.3.2 Classic approaches in fatigue

Approach in crack propagation

This approach is based on the Linear Elastic Fracture Mechanics on Griffith work in 1920 and energy-balance. It is supposed that the presence of a micro-crack in brittle materials introduce high stress concentrations near the tip. Thus, there is a critical stress level at which the crack becomes unstable and will propagate. According to Neville [26] an event taking place in an element is identified with the same event taking place in the body as a whole. Later Paris and Erdogan [43] modified the law which made it applicable to cyclic and fatigue loading. The Paris law stated that the crack length increment per

cycle da/dN is a power function of the stress intensity factor amplitude ΔK defined by the following equation

$$\frac{\Delta a}{\Delta N} = C\ (\Delta K)^m \tag{1.1}$$

Where, C and m are coefficient materials obtained experimentally.

This law is not directly applicable to concrete because it requires a large Fracture Process Zone (FPZ), but it was later modified by Bažant [44] by incorporating a size adjusted stress intensity factor.

However, this approach is valid in tensile and flexural testing methods, where generally one ideal crack is initiated (notched specimen) [11]. For applications interested in this thesis, the concrete and grout are submitted to compressive and shear forces, which induce several micro-cracks, creating damage within the specimen. Thus, this approach will not be used in further analysis.

Approach in crack initiation (Deterministic approach)

This approach implies that the initial structure has no flaws and the failure occurs firstly by crack initiation, which propagate up to a macroscopic crack. This approach consists in defining a threshold in the evolution of a macroscopic parameter (ex: strain, Young's modulus) beyond which failure is inevitable. Then, the analysis is made with an endurance curve. The endurance limit corresponds to the maximum stress which the material can sustain for an infinite number of load cycles, according to CEB-FIP [45]. However, the endurance limit is a controversial matter, since it has not been proven to exist in concrete and it does not necessarily give a relation between stress level and number of cycles to failure. Thus, the approach is generally expressed by the Wöhler curve. It should be noted that the endurance limit in concrete materials is often considered at 2×10^6 cycles.

The Wöhler curves are presented in a semi-logarithmic scale, as in figure 1.4-3 and stress levels are calculated based on the quasi-static compressive strength σ_c. $S_{c,max}$ is the maximum stress applied in fatigue loading $\sigma_{max,applied}/\sigma_c$, N (or N_f) is the number of cycles to failure and $S_{c,min}$ is the minimum stress level applied. The stress is applied as a sinusoidal wave function, which is the most common "pattern" (other methods will be briefly described later).

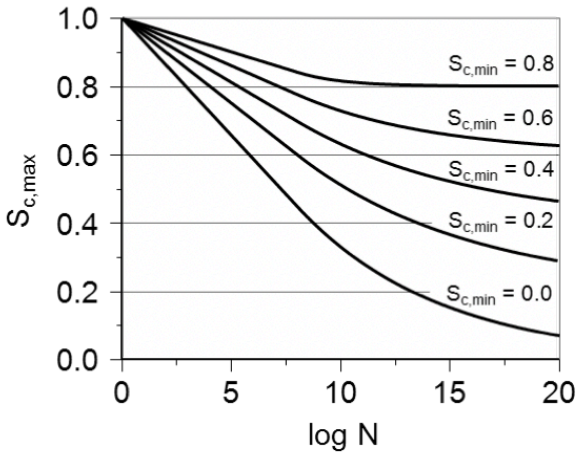

Figure 1.4-3 *S-N relations in concrete according to [46]*

Many authors have attempted to find an empirical relation to predict the fatigue life. Aas-Jakobsen [41] proposed the following expression based on S-N curves:

$$\frac{f_{max}}{f_c} = 1 - \beta\,(1 - R) log_{10} N \qquad (1.2)$$

Where R = f_{min} / f_{max} is the fatigue stress ratio in the range [0, 1] and coefficient β = 0,064. Tepfers verified this equation for a coefficient β = 0,0685.
These approaches do not take into account other parameters which may influence the fatigue life. Recent research on concrete or grout fatigue is based on these approaches, however they attempt to take into account other parameters.

The main drawback of this approach is that fatigue stress is calculated based on the mean compressive strength. Therefore, due to the heterogeneous nature of concrete and grout, the compressive strength from quasi-static tests can show variability, which is reflected in a more pronounced dispersion in fatigue results and can influence the validity of fatigue-test. This is a major problem in fatigue analysis, where it is crucial to alleviate other parameters that can influence the data scatter, such as : a strict protocol for the batch mix, avoid eccentricity while placing the specimen as mentioned in Cerib report [47], carry out tests on at least 5 specimen [48]. These factors were taken into account during the experimental set-up and are explained further in chapter 2.4.

Probabilistic approach

Due to dispersive nature of the data in fatigue, a probabilistic approach and statistical analysis is often used. Some authors [49] give the S-N relation by including the failure probability, and establish the S-N-P curves. The two-parameter Weibull distribution function is the most common used in fatigue analysis of concrete as firstly described by

Oh [50] and later in [51,52]. Oh [50], demonstrated that the probabilistic distribution of fatigue life of concrete depends on the stress level applied. Other authors successfully used the McCall model to predict the fatigue life of normal and high-strength concrete [40,53]. In order to establish the best fitting distribution to the experimental data, a goodness-of-fit test could be used.

The two parameter Weibull Probability Distribution Function is given by equation 1.3 where α is the scale parameter or characteristic life and β the shape parameter or slope.

$$f(x) = \frac{\beta}{\alpha}\left(\frac{x}{\alpha}\right)^{\beta-1} \exp\left\{-\left(\frac{x}{\alpha}\right)^{\beta}\right\} \tag{1.3}$$

In compressive fatigue in concrete x is expressed as N_f and the scale parameter is approximately related to the average of the distribution, so it can be assigned a physical meaning, according to Ortega [54]. Thus, a smaller scale parameter describes a shorter fatigue life. The shape parameter controls the slope of the distribution and it is related to the scatter. Therefore, it can vary depending on the stress level applied.

The maximum likelihood also called the Cumulative Distribution Function is given by :

$$F(x) = 1 - \exp\left\{-\left(\frac{x}{\alpha}\right)^{\beta}\right\} \tag{1.4}$$

Recently, different authors have proposed new probabilistic models, to take into consideration the statistical distribution of concrete strength [55] for fatigue tests, based on a normal distribution. Saucedo et al. [56] developed a fatigue model for concrete by taking into account the statistical distribution of the determined strength and the influence of loading frequency and stress ratio. Other authors proved the validity of this model with the experimental data [57,58].

1.4.3.3 Standards in fatigue life design

Standards that describe the fatigue behaviour of concrete and grout, imply carrying out fatigue tests in a sinusoidal signal between $S_{c,max}$ and $S_{c,min}$ at different frequencies, stress ratios and loading frequencies. CEB-FIP Model Code 10 [18] describe the fatigue behavior of concrete as shown previously in figure 1.4-3, and it is noted that the equations are also valid for high-strength and ultra-high strength concrete, up to C200 in pure compression. According to [8] the fatigue behavior described in this standard can be used to estimate the fatigue life in high-strength grout. A low $S_{c,min}$ value, which gives a higher loading amplitude can be considered as the worst case scenario during fatigue tests. Therefore, authors generally define this value at 0,05 or 0,1, since it can be difficult to

experimentally execute tests at $S_{c,min} = 0$. The case scenarios in compression-tension and pure tension will not be studied in this thesis. For log N > 8 the curves asymptotically approach the minimum stress level, which could be considered as the endurance limit. Moreover, these curves are valid for frequencies higher than 0,1 Hz and do not take into account the frequency effect on fatigue life. Another standard that take into fatigue verification is Eurocode 2 (NF EN 1992-2)– Part 2 : Concrete bridges [59], which does not have limits of application as seen in Model Code.

DNV-OS-J101 [1] describes the design of offshore wind turbines and has a specific section for the grouted connections in jacket and monopile structures. It recommends calculating the characteristic number of cycles to failure of the grout N from :

$$log_{10}N = C_1\left(1 - \frac{\sigma_{max}}{f_{rd}}\right) / \left(1 - \frac{\sigma_{min}}{f_{rd}}\right) \tag{1.5}$$

where f_{rd} is the design reference strength, σ_{max} is the largest value of the maximum principal compressive stress during a stress cycles within the stress block, σ_{min} is the smallest compressive stress in the same direction during this stress cycle and C_1 is a constant factor which varies depending on air or water condition and pure compression or compression-tension range. This equation is valid up to a defined level depending on C_1, and afterwards another equation is given.

We compared in the following figure the three standards for $S_{c,min} = 0{,}2$ (for the DNV curve C_1 is taken for air condition in conical grouted connection). While the figure gives a comparison up to log N = 8, the area of analysis generally ends at log N = 6 or 7 in the tests carried out in this work.

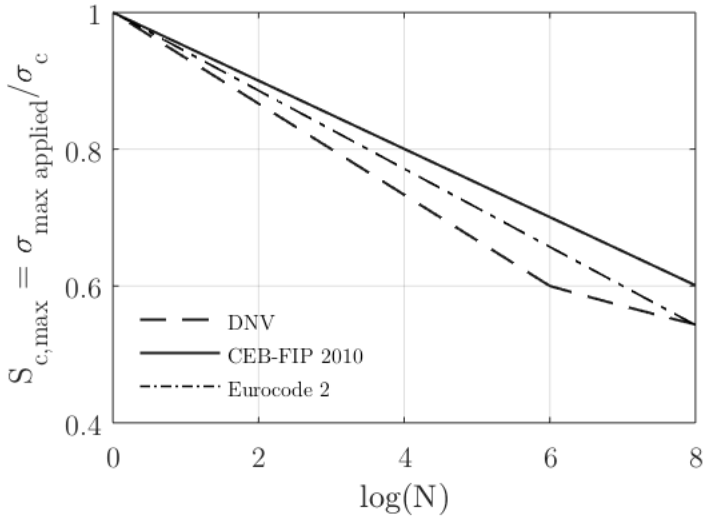

Figure 1.4-4 *Comparison of three standards for $S_{c,min} = 0{,}2$*

1.4.3.4 Parameters influencing fatigue life

Many parameters have an influence on fatigue life, both internal and external. Internal parameters signify elements related to the mix composition of the grout or concrete and external parameters can be due to loading or curing conditions, which can bring alterations to the microstructure. The most significant parameters will be mentioned hereafter.

Loading Frequency

Several studies have tried to investigate the influence of the frequency of testing on the number of cycles to failure and conflicting results are obtained. This can be due to different loading conditions between authors, and also different microstructural properties of studied mixes. In general, authors test concrete specimen under the frequency of 10 Hz, in order to accelerate the duration of the tests, while in practice loading frequencies at 1 Hz or lower are expected.

Firstly, it was commonly accepted that the frequency of loading does not influence fatigue life based on the work of [60] and equations used to predict the fatigue life did not take into account this parameter. Moreover, Sørensen [61] conducted compressive fatigue tests on high strength grout and showed that when tested in air environment, the frequency level does not influence fatigue life. However, later work showed that the change of frequency might have an influence on the fatigue life. Medeiros in [62] shows that for high strength concrete tested on 100x100x100mm cubes and under the stress level $S_{c,max}$ = 0,85, the fatigue life decreases, while decreasing the frequency of loading. This article studies 4 frequencies : 4 Hz, 1 Hz, 0,25 Hz and 0,0625 Hz and it is the most common result obtained from literature review. Flexural tests in fatigue of concrete by Zhang [63] indicate the same tendency and they were also tested at a high stress level $S_{c,max} = 0{,}80$. Similar results were found in [64] in compressive tests where for lower loading rates, lower number of cycles to failure were reached for normal strength concrete as prism specimens of 102x102x203mm at three different stress levels. However, it was noticed that at lower stress levels the effect of loading frequency becomes smaller and the difference in fatigue life at the lower stress levels is smaller than for higher stress levels. This phenomenon has often been explained by the dynamic effect induced by higher rates as explained in 1.4.2.

Elsmeier [65] tested fatigue behaviour of two high-strength grouts and also found that a lower fatigue life is obtained at 1Hz instead of 10Hz, at $S_{c,max} = 0{,}85$. However, at lower stress levels $S_{c,max} = 0{,}75$ and 0,65 the tendency changes, and a higher fatigue life is obtained at 1Hz (see figure 1.4-5). This phenomenon of tendency change depending on the stress level, is also observed recently from other authors. Oneschkow [66], found that

lower loading frequencies lead to lower number of cycles to failure for high stress levels ($S_{c,max}$ = 0,80, 0,90 0,95) and frequencies between 10Hz, 5Hz, 1Hz and 0,1Hz. But for lower stress levels such as $S_{c,max}$ = 0,70, higher number of cycles to failure are reached at a lower frequency at 5Hz compared to 10Hz. Similarly, Von der Haar [67] obtains higher number of cycles to failure for lower frequencies at $S_{c,max}$ = 0,70 and 0,65, but similar fatigue life for $S_{c,max}$ = 0,80.

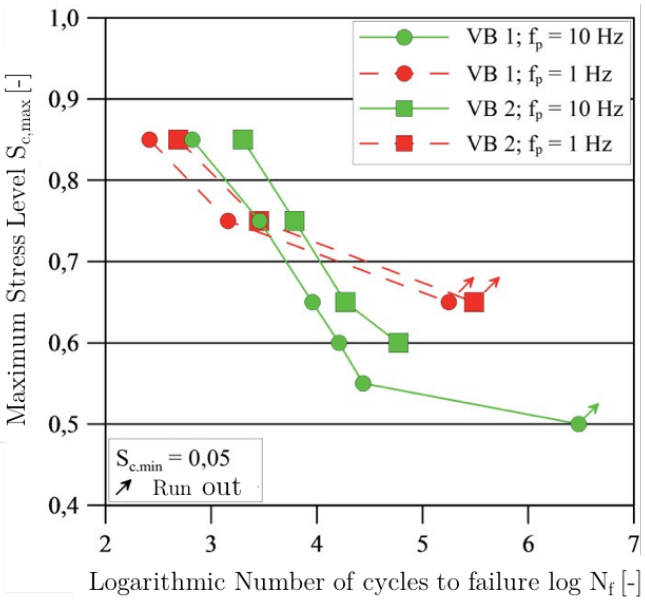

Figure 1.4-5 *Influence of the testing frequency on the ultimate number of cycles to failure according to Elsmeier [65]*

These recent results, show the relevance in testing different stress levels when the influence of frequency is studied. Many authors tend to study this effect by taking into account different frequency values, but at only one stress level. Nevertheless, there might be a different behavior depending on the stress level applied. This behavior could be due to temperature increase within the specimen, which will be explained chapter 3.3.3.

According to the model code [46], there is little information regarding the effect of high stress or strain rates on the shape of the stress-strain diagrams. This relation will be analysed in chapter 3.

Moisture content

Sørensen [61] conducted compressive fatigue tests on a high-strength grout with quasi-static strength 170 MPa under three frequency levels and two environments, air and water. The saturated specimen tested under water showed a remarkably lower fatigue life as shown in figure 1.4-6. He suggested that during cyclic loading water is trapped and exerts a high pressure to cause progressive crack formation.

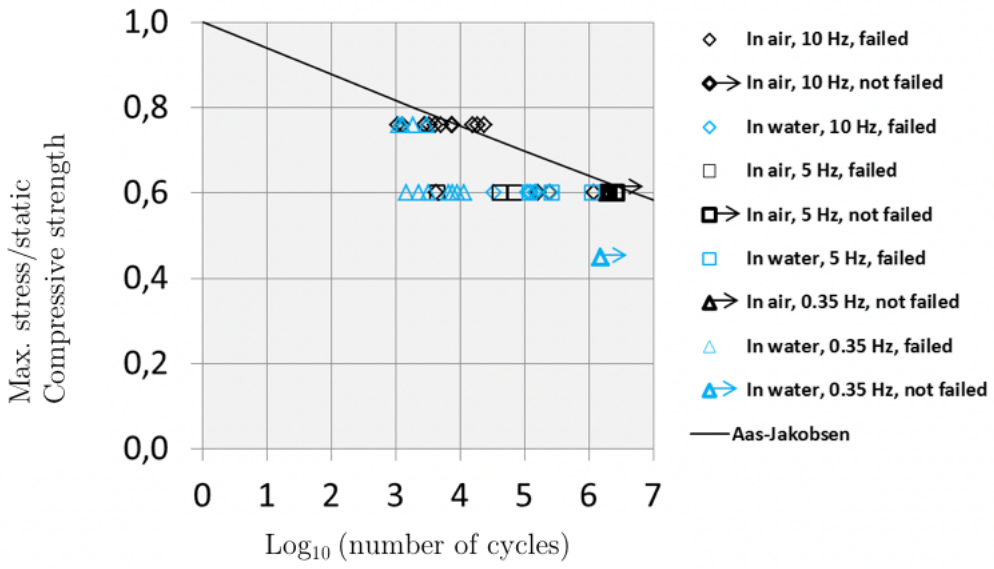

Figure 1.4-6 *Ratio of maximum stress to static compressive strength versus the number of load cycles to failure (or until discontinuation of the test) Sørensen [61]*

Tomann [68] recently conducted fatigue tests in a high-strength concrete under five different conditions at f = 1Hz (i.e. dry, climate chamber, intrinsic moisture, water storage and under water testing). He demonstrated that it is not the wet environment responsible for the reduction of the fatigue life, but the moisture content in the microstructure. He shows that the number of cycles to failure decreases with increasing moisture. Both studies agree that the magnitude of impact of the water content is higher when applying low loading frequencies. An explanation on the mechanisms, however is not given.

These results seem inconsistent with the explanation in 1.4.2 about strain rate effects, where higher strength is expected with increasing loading rates, due to free water exerting the Stefan effect. It was shown in this part that for dry concrete, an increasing rate has almost no impact in the strength of concrete. Sørensen tests in air seems to validate this point in fatigue, because less water is present in the specimen.

Indeed, when water is present in the mix, lower fatigue life is obtained in the presence of water, in Sørensen and Tomann tests (f = 1Hz). At lower frequencies Sørensen obtained a higher influence of water content on fatigue life. Therefore, there might be a contradictory mechanism in the presence of water in fatigue, especially when tested at higher frequencies. We can conclude from the results observed in literature that the strain rate effect at 1Hz is lower, and the presence of water has a more damaging influence due to water pressure conducting to earlier failure. In higher frequencies the damaging effect of the local water pressure can be compensated by the Stefan effect. However, in chapter 3 this is analyzed more thoroughly.

The observation of the results at low frequencies for dry or saturated specimen seem consistent with some of the results observed in quasi-static conditions. While a few authors obtain lower compressive strengths in dry concrete, it is more commonly accepted that dry specimens have a higher compressive strength than saturated specimens according to the literature review in Benboudjema [69]. The strength increase is due to capillary pressure and an increase of surface tension due to less adsorbed water quantity. This is valid for specimens in air (or dry) and water conditions tested at a "late-age" state. At early-age the specimens preserved in water curing condition present a higher compressive strength.

Matsushita [70] confirmed that not only the pore water pressure, but the surface tension of the liquid where the specimen is immersed has a high influence on the fatigue life. He conducted compressive static and fatigue tests in liquids with different surface tensions, and found that fatigue decreases significantly when the specimen is immersed in liquid with a higher surface tension. Moreover, he points out that seawater has a larger surface tension than water used in tests, therefore in marine structures shorter fatigue life should be expected.

Finally, some authors [71] explain this phenomenon by the leaching of $Ca(OH)_2$ from the interface between aggregates and matrix and thus creating more porosity. Although different mechanisms are mentioned, it is recognized that the presence of water in fatigue in compression has a negative effect.

Size Effect

The size effect might have a strong influence on the compressive strength of specimens. Overall, larger specimens are expected to have a lower strength. However, some authors suggest no influence or a very slight one of the specimen size on the strength of concrete for cylindrical specimens, especially for high-strength concrete [26]. In [72] the size effect was examined in cylindrical specimens with D/H = 1/2 between two different diameters, 75mm and 100mm in quasi-static tests for high-strength concrete. The size effect resulted to be almost negligible in terms of strength and the post-peak softening branch.

Not many research is available on possible influence on fatigue life. A recent study [73] also showed no strength variations for different cylindrical specimen size in quasi-static tests. However, in compressive fatigue, lower number of cycles were reached for a larger specimen size. Another study [74] also considered the influence of specimen size in the fatigue life, and in addition the possible influence on the damage process is also analyzed. The slenderness considered is D/H=1/3 with diameter 100mm and 400mm. A decrease in quasi-static strength of 8 % is demonstrated, which is reflected in a decrease of fatigue life. The damage process is reported overall to be similar, but with much larger levels of strain evolution and stiffness degradation. Nevertheless, it is reported that investigations

are carried out only on 2 specimens and somewhat at different loading conditions, i.e. different loading frequencies. Therefore, the validity of these results can be questionable. No other research has been documented to the authors knowledge, of the size effect on the fatigue life in compressive fatigue for concrete or grout. Hence, this will be a parameter of interest analyzed in chapter 3.

Concrete strength

Fatigue strength is influenced by the same parameters that influence static strength, as for example parameters in mix composition : water-cement ratio, curing conditions, age of loading. For some authors the representation of fatigue results as a Wöhler curve, eliminates the influence of static strength to fatigue strength [25,49]. However other researchers have reported a different fatigue life, for fatigue tests in concrete of different strengths, different aggregate types, moisture content etc., thus different microstructures. Therefore, indirectly the microstructure can affect the fatigue life. Lenschow in [75] reported that in order to examine concrete fatigue in compression, factors such as aggregates and proportions, humidity and stress gradients as internal parameters should be considered in analysis. Additionally, the strain development and stiffness damage evolution can show different behaviours, depending on the microstructure.

Currently, the influence of concrete strength and microstructure on fatigue life in compression is still controversial. Furthermore, not many results exist on high-strength concrete. Kono [76] compared three high strength concretes at 100 MPa, 120MPa and 170MPa and found a longer fatigue life for a higher strength concrete, in low cycle fatigue. Adversely, Kim [77] studied four different strength concrete between 26 MPa and 103 MPa and found a lower fatigue life for a higher strength concrete, which is noted that can be due to the more brittle nature of the high-strength concrete. Bažant and Schell [78] also confirmed that high-strength concrete is more brittle than normal-concrete under fatigue loading. Finally, Petkovic [79] and Do [53] found no significant influence of concrete strength on fatigue life. However, their tests were conducted on concrete with compressive strength lower than 100MPa. More recently, Lohaus [80] tested two ultra-high strength concretes with quasi-static strength of 160MPa and 180MPa and found no significant difference on the fatigue behaviour. All these comparisons are given for compressive fatigue.

The research studies mentioned here, compare concrete of different strengths, but the nature of the microstructure is not always mentioned. Between researchers different formulation parameters might be used to lower the concrete strength (i.e. higher w/c, different aggregates). Therefore, the comparison can take place between mixtures of two different nature, where different parameters where changed at the same time, which can modify interface properties, nature of hydrates and porosity. Thus, it can be more

relevant to analyse the influence of elements in the mix composition instead of the material strength.

Mix components

The **aggregate nature** is a component which can highly affect the quasi-static compressive strength of concrete and grout. Very few studies have been carried out to study its influence on fatigue life and even fewer are conducted in compressive conditions. Former research that focused on observing its influence on fatigue, are mostly carried out on limestone and gravel aggregates. Hordijk [81] obtained no significant influence in fatigue life in compression between a 73 MPa concrete with limestone aggregates and 78 MPa concrete with river gravel aggregate. Sparks [64] also tested the same aggregates in addition to a lightweight aggregate and his results show a slight increase in fatigue life for limestone concrete, which was the aggregate with the highest stiffness. In both studies only two or three specimens were tested for each load level. Therefore, due to scatter in fatigue tests these results can be considered inconclusive.

Another more recent study in [82] compared basalt and granite aggregates in HSC, where basalt has a higher stiffness. Only three specimens were also tested at two stress levels and showed that the differences in terms of number of cycles to failure are small, but the damage mechanisms demonstrated by acoustic emission measurements, are different. Korte [83] referred to Hanjari who studied concrete with aggregates of normal density, lightweight and high-strength properties in compression. The results show a lower fatigue strength for the normal density aggregates, compared to high strength and lightweight. Most of these studies do not analyze interface properties which can be a weak link in concrete, or the shape of the aggregate. Very few information is given on the damage mechanisms which take place depending on the aggregate type. Moreover, not enough specimens are used in order to give a general conclusion.

Recent research has been carried out in more “modern” aggregates. Sohel [84] examined by means of flexural tests two lightweight aggregates : expanded clay and a higher resistant and thermally stable aggregate, cenosphere. He obtained a higher fatigue life for the concrete with cenosphere aggregate, where also PVA fibers were used. Onoue [85] found a better compressive fatigue life when using polished hot metal pre-treatment slag as aggregates for applications in marine and harbor structures. Due to the polished surface of these aggregates, he reported cracking mainly occurring in the interface area. Finally, Farooq [86] tested Blast-Furnace-Slag (BFS) and crushed sand aggregates and found a higher fatigue life in the BFS mixture, (which also had a higher compressive strength) and he claims it can be due to less plastic strain development and at a lower rate.

Some researchers have been more focused on the influence of **cement matrix components** on the fatigue behavior. A few studies such as Lee [87] and Klaiber [88] both carried out on flexural tests showed a decrease of the fatigue life with increasing air content and increased water quantity.

Seitl [89] conducted flexural tests and showed that the use of microsilica does not necessarily improve the fatigue of concrete. However, it helps increase the modulus of elasticity and obtain different fracture mechanisms in fatigue. Concrete with this additive shows that cracking also occurs through the aggregates, as opposed to concrete without microsilica. Zhang [90] found that the use of GGBS creates a densification of the cement matrix and ITZ and was beneficial of the fatigue flexural life of concrete. Moreover, Guo [91] demonstrated that a different crack propagation takes place between a concrete with fly ash and GGBS admixtures under different stress levels. The study showed a higher "crack-resistance", due to the high specific surface area and a more densified cement paste.

A few studies incorporated fibers as in Lee & Barr [23], where fibers improved the fatigue life in flexural tests because of a bridging effect, but had no effect in compression. Whereas Poveda [92] tested different fiber contents in low-cycle fatigue and found that there is an optimum quantity which improves the compressive fatigue life.

As it was shown here, very few research is available on the influence of mixture components on fatigue life, and some of these elements seem to be of a significant influence. Because of the limited literature data in compressive fatigue, comparisons were shown in some cases for flexural tests. However, the impact might be different depending on the type of loading.

Loading Conditions

Apart from the frequency level mentioned earlier, other loading conditions might influence the fatigue behaviour of concrete and grout such as : the loading ratio, waveform signal, confining pressure, rest periods. However, from literature review, authors seem to agree on the effect of these parameters, thus they were not studied further. In this thesis the most common values for these parameters were chosen, such as : a low loading ratio, sinusoidal waveform, no confining pressure and no rest periods. Nevertheless, the choices for these parameters will be justified further in chapter 2.

1.4.3.5 Strain Development during fatigue loading

Literature review in previous sections showed that it is difficult to estimate a reliable relation between stress level and number of cycles to failure. The quasi-static strength can have a large scatter, which will influence the fatigue life. Although, this macroscopic relation can be important to describe fatigue behaviour, an interest should be given to other criteria related to the mechanical behaviour of the material [93]. Therefore, the progressive damage of the material can be quantified by the strain development, evolution of dynamic modulus and hysteresis area.

Strain at failure

The propagation of microcracks results in a significant increase of irrecoverable strain for different stress ratios (see figure 1.4-7). Hence, in addition to fatigue strength, the deformation properties should be investigated [77]. The cyclic compressive stress can be represented in the $\sigma - \varepsilon$ diagram, where it is presented in a hysteretic form. Some authors consider the quasi-static curve as an envelope curve and have developed fatigue prediction models, which incorporate the nonlinear characteristics of concrete and stiffness degradation.

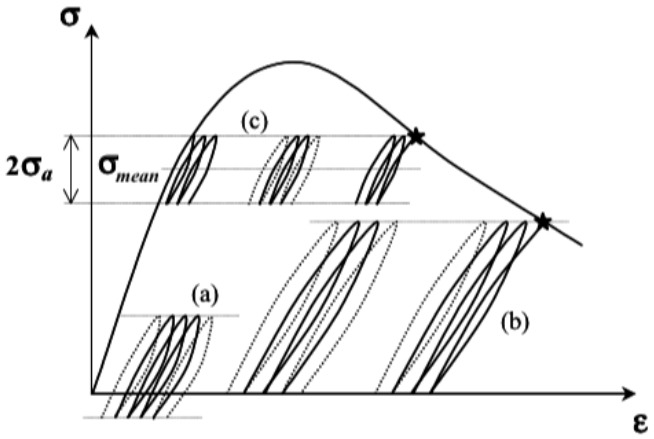

Figure 1.4-7 *Behavior of concrete under cyclic loading a) alternate loading b) repeated loading c) undulated loading [25]*

As shown in figure 1.4-7, some of these models, such as Park [94], assume that fatigue failure occurs when the hysteresis loops reach the negative branch of the envelope curve. Similar results were proposed by Plizzari [95] in bending tests, but the model is based on fracture mechanics and crack growth. Other authors [53] also found similar strains at failure on static and fatigue tests. However, the reliability of these models can be questionable, due to the sequence of loading which can influence the fatigue failure. Moreover, the strain at failure in fatigue does not always necessarily correspond to the strain of the envelope curve. Neville [26] and Thiele [74] suggests that the strain at failure in fatigue is much larger than in static failure. Concurrently, Von der Haar [67] showed

that 78% of the ultimate fatigue strain values are lower than the failure strain in static compression test. He also showed a difference of ultimate strain depending on the loading frequency applied. A low frequency could lead to higher strains at failure due to creep effects. Similar results were obtained in [86,96].

It is important to note that the experimental tests listed here are carried out on different concrete compositions and different compressive strengths. Thus, due to a more brittle nature of high-strength concrete or grout, lower strains at failure could be expected, compared to a normal strength concrete.

Authors, generally agree that a higher strain at failure is obtained for lower stress levels and higher fatigue life.

Strain Evolution

Strain evolution in fatigue is generally characterized by a sinusoidal shape (other signal types could also be used) within one cycle due to loading and unloading. When plotted over the number of cycles to failure or test duration, it is characterized by an "*S*-shape", involving three characteristic phases giving the failure mechanism in fatigue (see figure 1.4-8).

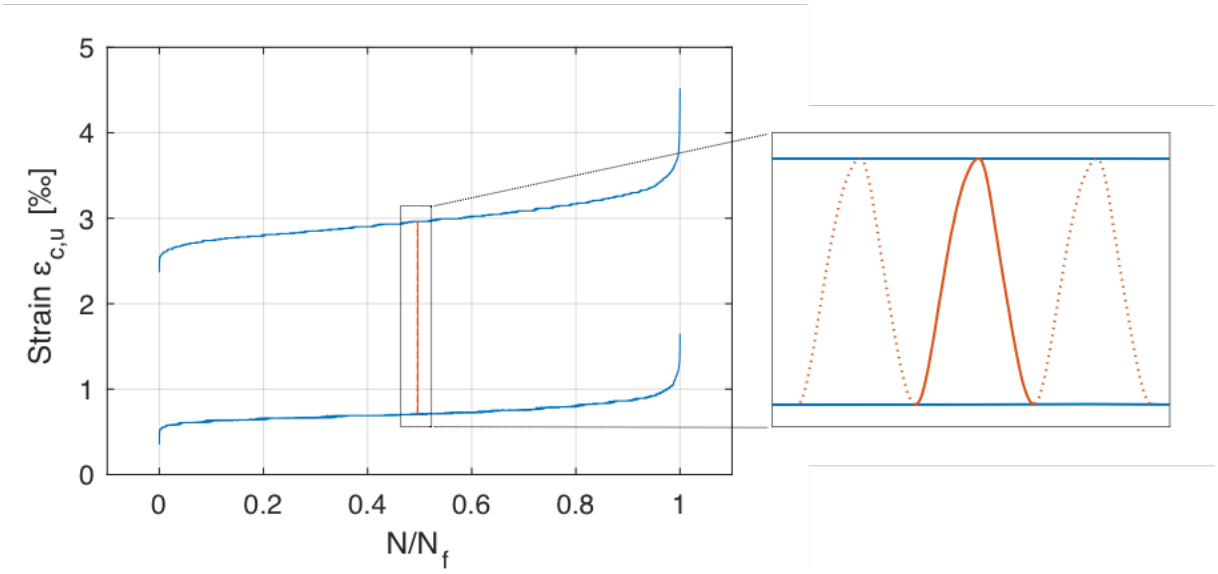

Figure 1.4-8 *Strain development with respect to the ratio of the number of cycles to failure and schematic representation of the sinusoidal signal*

Commonly accepted in the literature, the first phase is characterized by a rapid increase of strain due to the creation of microcracks. The second phase has a linear shape and it corresponds to a stable crack growth. Finally, the microcracks coalescent to create a macrocrack and the failure of the specimen. This phase is characterized by a short

duration and the strain increases quickly. If a specimen does not fail under fatigue loading, the second phase will continue to grow linearly and the third phase will not be observed. Thus, the plastic strains remain small and the evolution is very slow or there is a quasi-absence of evolution.

Although this damage mechanism seems to be in agreement with all compressive or flexural fatigue tests in concrete and grout, the transition phases I – II and II – III can vary depending on the concrete strength tested. A comparison we made between different authors, shows that the first and last phase are shorter for a higher strength concrete (see table 1-2).

Table 1-2 *Comparison of transition phases in strain development depending on the concrete strength*

	Transition phase (I-II) N/Nf [%]	**Transition phase (II-III) N/Nf [%]**	**Compressive Strength [MPa]**	**Concrete Type**
Wefer	5	95	160	UHSC
Oneschkow [96]	11	93	95	HSC
Medeiros [62]	10 to 15	85	75	HSC
Hümme [97]	9	92	70	HSC
Do [53]	10	80	70-95	HSC
Holmen [40]	10	80	40	NC
Huang [2018]	5 à 10	80-90	43-48	UHTCC
Kim [77]	10	80	26 -103	NC & HSC

As explained earlier, the first phase consists in creating microcracks and for a higher strength concrete an optimization of the cement matrix and particle packing is previously made. Therefore, there are less initial flaws and the cycling loading creates less cracking during the first phase. The failure of the specimen in this case is mainly due to the propagation of the microcracks. However, the estimation of these transitions has often been neglected or considered the same, in spite of the concrete strength. Oneschkow [98] mentioned that shorter phases (I and III) are expected for a higher strength concrete. However, no explanation on the mechanisms was given.

Secondary strain development

The second phase which previously was defined as crack growth and as a linear phase is characterized by constant increase of deformation per load cycle. The slope of this secondary branch is called secondary strain rate and noted here as $\dot{\varepsilon}_{max,II}$ or $\frac{\partial \varepsilon}{\partial n}$. Previous

research for concrete [53,56,81] has shown a linear relation between the increase of strain in this secondary branch and the number of cycles to failure when plotted in a double-logarithmic scale. In [81] Hordijk estimated a similar secondary strain for two concrete mixes of different aggregate type as shown in figure 1.4-9. However no research was found on this behaviour for mortars or grout. Experimental tests conducted in this thesis will show if this linear relation is valid for high-strength grouts.

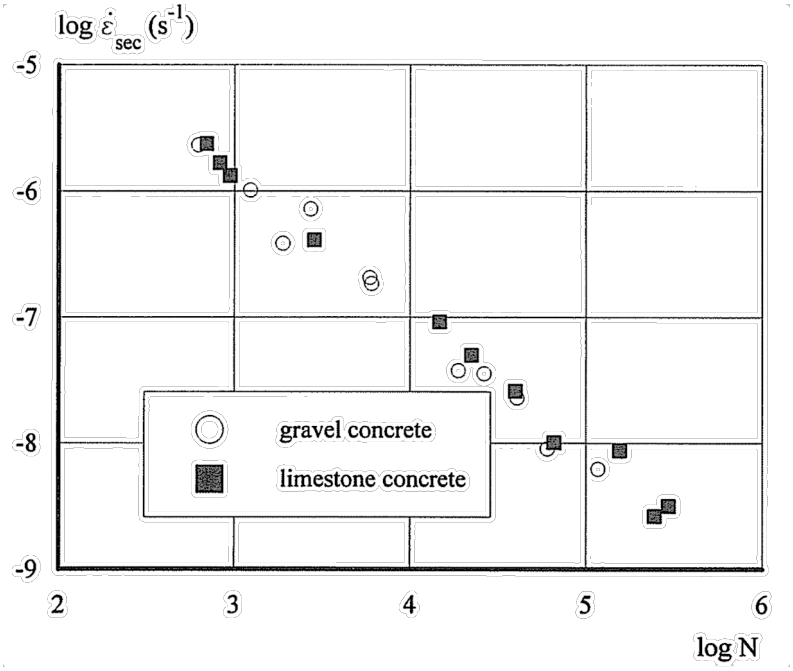

Figure 1.4-9 *Relation between secondary strain rate and number of cycles to failure in compression fatigue tests according to Hordijk [81]*

1.4.4 Energy dissipation

The interest in the hysteresis loop arises from the fact that its area represents the irreversible energy of deformation, and is manifested by a rise in temperature of the specimen [26]. Thus, the total dissipated energy is composed of the energy released in the form of heating (E_H) and energy due to damage (E_D):

$$E = E_D + E_H \tag{1.6}$$

For a better accuracy energy measurements in fatigue tests should be performed under adiabatic conditions [99]. The irreversible strain involved is probably in the form of microcracking. Therefore, the analysis of energy dissipation during fatigue can be an indication of the damage process within the specimen. According to these definitions the energy dissipation is represented by area of the hysteresis curve [100] as follows :

$$w_d = \oint \sigma d\varepsilon \tag{1.7}$$

where w_d is the dissipation due to damage. Lei [100] assumes that the heat energy dissipation in fatigue loading is constant. Thus, the total dissipated energy is assumed to be the energy due to damage. The accumulated dissipated energy is defined as the sum of all the single-cycle energy dissipation :

$$W_d = \sum_{i=1}^{N} w_d^i \tag{1.8}$$

Tepfers [99] analysed the absorption of energy in fatigue compressive tests for normal strength concrete and concluded that the energy absorbed by concrete at failure is the same for static and fatigue tests with different intensities. Moreover, low frequencies give increased hysteresis loops. In addition, many authors [53,100] showed that hysteresis areas decrease after the first cycles and later become large when the specimen is close to failure (see figure 1.4-10). This phenomenon of decrease in the first stage is explained by the decrease of the energy associated with thermal capacity ($E_{tc} = \rho c \frac{\partial T}{\partial t}$) at the beginning of the test, albeit the increase of energy dissipation due to damage. Therefore, Lei [100] assumes that when the load applied is low, the energy due to damage is small comparing with the heat energy dissipation, and the total energy will decrease in the first stage. While when the load increases, the energy dissipation due to damage increases and the total energy dissipation shows no decrease in the first stage.

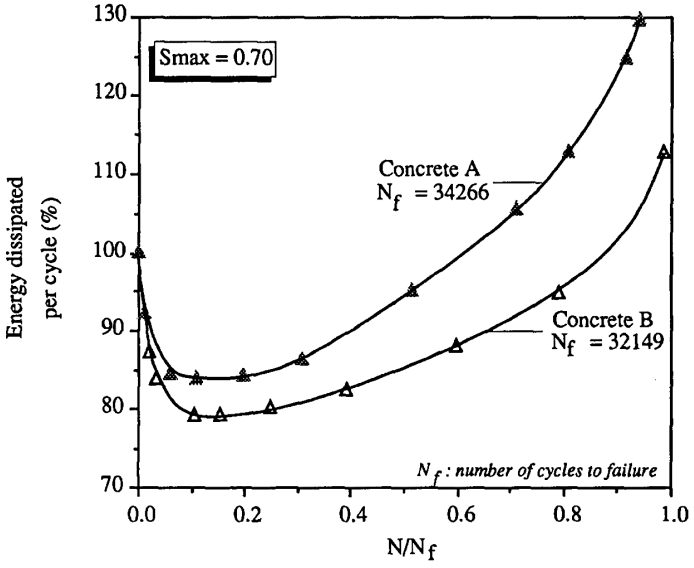

Figure 1.4-10 *Variation of Energy Dissipated with respect to life ratio of two types of concrete [53]*

The energy near failure can be 1,2 to 1,5 times the initial value. Parant [93] found an increase in energy dissipation 10 times higher between the first and last cycle for a fibre

reinforced concrete. Therefore, the total increase might depend on the mix composition. The single cycles energy dissipation is also dependent on the stress level applied, and it increases with an increasing stress level. However, the total accumulated dissipated energy W_d for some authors seems to be independent on the stress level applied [99] for a constant maximum stress level. Inconsistent results are reported from [101], where it seems to vary depending on the loading scenario applied. The accumulative dissipated energy increases linearly up to failure and it increases more rapidly for larger loads according to [100]. On the other hand, Song [101] found an "S-shaped" evolution of the accumulated energy, where the fatigue life of the two specimen tested was very low (up to 35 cycles).

1.4.5 Temperature effect

Compressive fatigue tests can induce a temperature increase within the specimen [2,65,67]. This phenomenon seems to be a property of fatigue in compression, since it has never been observed in flexural or tensile tests, to our knowledge. Moreover, in concrete and grout this increase has very rarely been discussed and even sometimes neglected. However, recent studies in high performance concrete show significant temperature increase depending on the frequency level, which might influence the fatigue life and is a phenomenon that has to be taken into account. This temperature increase is independent of the ambient temperature or heating exchange from the testing machine.

1.4.5.1 Influence of temperature on fatigue loading

The temperature increase due to fatigue loading is induced at almost all frequencies applied, however not at the same level. Higher test frequencies, lead to higher temperature increase. In [67] fatigue tests at 10Hz for concrete with a compressive strength of 70MPa, the surface temperature before failure reached 69°C for $S_{c,max} = 0{,}60$. This was also confirmed for high strength grouts and concrete. Elsmeier [65] studied three high strength grouts at $f = 10$ Hz and observed surface temperature ΔT higher than 40K increasing linearly. At $f = 1$ Hz temperature increase between 4 K and 11 K were observed. This study also shows that more heating is generated within a specimen, when the maximum aggregate size in is smaller. Thus, grouts commonly having smaller aggregate size than concrete, might experience higher warming. This is also confirmed in a very recent study on UHPC [102], where the maximum increase in temperature is approximately 18 K, 40 K and 68 K at $f = 3$ Hz, 10 Hz and 20 Hz , respectively. The most "extreme" temperature increase found in the literature is Anders' work [2] for a polymer reinforced concrete at $f = 63$ Hz and surface temperature reached 180°C.

Thus it is obvious that temperature increase is dependent on the frequency applied. In addition, it can influence fatigue life. Part 1.4.3.4 showed that many authors agree that

higher fatigue life is obtained at higher frequency levels due to viscous effects. However, in compressive fatigue tests these levels of temperature increase, induce more damage within the specimen and reduce the fatigue life. In [65] was shown that this is valid at $S_{c,max} = 0{,}75$ and 0,85, where less heating is observed. But the results are reversed at $S_{c,max} < 0{,}75$, where lower number of cycles to failure are reached for $f = 10$ Hz instead of $f = 1$ Hz. Thus, this temperature increase results in significant temperature gradients and high pore water pressure which can lead to residual stresses and lower number of cycles to failure.

The origin of this temperature increase is supposed to be an internal friction [103]. However, it has not been previously demonstrated experimentally whether this hypothesis is true or whether there might be other heating sources. Later in the thesis, attempts to verify this statement will be made.

1.4.5.2 Self-Heating Method

Fatigue tests as conducted earlier, are very consuming in time and specimen quantity. The characterization of fatigue properties requires at least 25 specimens at one frequency level. The duration of these tests can be extended further, if high-cycle fatigue tests are required in order to determine the endurance limit (level of stress under which the specimen does not fail under fatigue failure) or if lower loading frequencies are applied. Thus, alternative methods have been developed, in order to characterize fatigue properties and the most widely used in non-cementitious materials, is the "self-heating" method. This method is based on measurements of the specimen temperature under fatigue loading in order to determine the endurance limit. The advantage of this method is the short time needed to perform the tests compared to the traditional high cycle fatigue tests [104]. It is widely applied in materials such as steel, aluminium, composite materials or rubber-like materials. However, it is worth noting that an endurance limit for concrete has not been proven to exist and is a controversial matter. Thus, this method might be an indication of the endurance limit, but its applicability in concrete or grout has not been attempted in other research, to our knowledge.

The temperature elevation can be measured by thermocouples, such as [105] where the temperature is measured punctually or by infrared thermography, such as [106], where the temperature field is obtained. When a certain stress level is applied, the temperature firstly increases rapidly as a result of a dissipated heating provoked by the loading, then stabilizes when a balance between dissipation and heat loss in the environment (air or platens) is established and finally it belatedly increases until failure during the propagation of the preponderant crack [106].

The self-heating test consists in the application of a successive series of cyclic loadings, with increasing stress amplitude [107] and the stress ratio is kept the same. Every step is followed by an increase of temperature within the specimen until reaching a steady-state, where the temperature reaches a stabilized value (see figure 1.4-11 (a)). The last step is defined when the temperature does not reach a stabilized value.

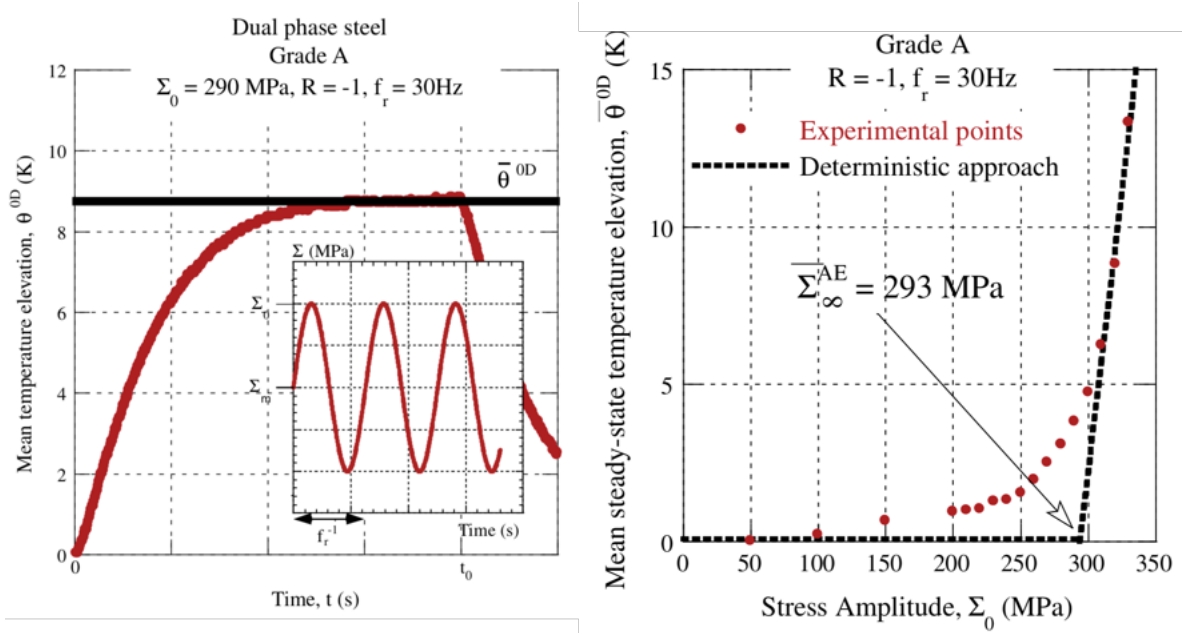

Figure 1.4-11 *Self-heating measurements under cyclic loadings (a) temperature evolution during one series of cyclic loadings (b) change of the mean steady-state temperature with the load amplitude and identification of the mean endurance limit with a deterministic approach [107]*

The self-heating curve is obtained when the stabilized temperature is given with respect to the amplitude of stress applied as can be seen in figure 1.4-11 (b). The endurance limit is estimated empirically from the intersection of two straight lines, one being the linear regression of the first three points and the second being the linear regression of the last 3 points. Since the first part of the curve does not have significant change, some authors estimate the endurance limit as the intersection between the linear regression of the last 3 points and the abscissa axis.

This curve is characterized by two clearly distinguished self-heating regimes, one of a small slope and a secondary slope associated with a progressive appearance of microplasticity areas [107]. The temperature increase comes from an intense microplastic activity, which at long term brings to the creation of multiple microcracks [106]. This is the concept on which is based the application of this method.

This method seems to be a very “attractive” alternative in order to estimate the endurance limit and fatigue life of concrete and grout. However, many challenges and

some limitations are presented, when wanting to apply this method to cementitious materials, which will be explained further in chapter 3.

1.4.6 Basic creep of concrete and grout in compression

Creep is the long-term strain evolution under a constant external mechanical load. It is defined as a delayed effect, as it includes an increasing non-linear strain with time. Therefore, due to its long-term effect, an analogy can be made with the strain evolution due to fatigue. Both behaviors, include an increased strain with time and the main difference is that creep is due to a constant loading, while fatigue is due to long-term cyclic loading between two (or more) stress levels. Moreover, many authors [62,108] consider the strain development under fatigue loading as "cyclic-creep curve". Bažant [109] recently stated that "The cyclic creep of concrete, also called the fatigue creep or vibro-creep, is the long-time deformation produced by cyclic load in excess of the static creep." It is also assumed that the cause of cyclic creep is the fatigue growth of pre-existing micro-cracks in hydrated cement. Whereas, Hsu [36] stated that high-cycle fatigue is associated with bond cracking. Due to similar time-dependent properties, fatigue and creep, mainly cyclic creep are occasionally confounded. The main difference seem to derive from the frequency level applied. Finally, Whaley and Neville [110] point out that the effect of cyclic stress is to accelerate the process of creep under a static stress. Therefore, it can be assumed that the fatigue loading consists in an accelerated "version" of creep.

Thus, despite the similarity of these two phenomena, a confusion based on terminology should be avoided. Further in the manuscript, the increase of strain in fatigue loading will be called as "strain development" or "strain evolution". While, the increase of strain under a constant stress, will be called as "creep" curve.

1.4.6.1 Micro - mechanisms of basic creep

According to Acker [111] the deformation due to creep is very sensitive to water and water/cement ratio and can be separated in two components related to two different physical mechanisms : basic creep which considers the deformation of a specimen without hydric exchange and drying creep incorporates a higher increase of strain due to lateral drying of a specimen in case of a compressive test. Only the basic creep will be considered for later analysis without taking into account the drying creep.

Basic creep is composed of two regimes with different kinetics :

⇒ Short-term creep (see figure 1.4-12 (a)) where in a microscopic scale, the external loads are transmitted to the hydrates surrounding the capillary pores. A loss of

the thermodynamic equilibrium of adsorbed water is created and in order to restore the equilibrium, the water from adsorbed layers diffuse to the capillary pores. This water diffusion creates deformation of the solid skeleton.

⇒ Long-term creep (see figure 1.4-12 (b)) has a mechanical origin due to Bažant [112]. The bonding forces between solid adjacent surfaces within the adsorption zones, balance the disjunction pressure. Local unstable bonds are likely to break and due to C-S-H sliding, they reform in zones with less pressure.

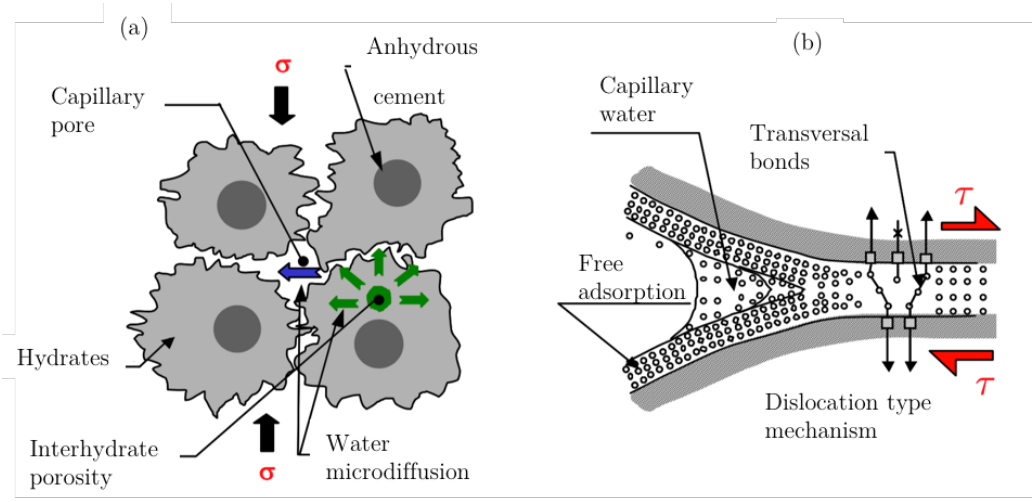

Figure 1.4-12 *Mechanisms of creep (a) Short-term mechanism (Benboudjema [69] adapted from [113]) (b)Sliding of C-S-H sheets long term creep mechanism*

1.4.6.2 Creep model coupled with cracking in compression

Basic Creep

Several models are proposed in the literature in order to describe the non-linear creep strain, due to different mechanisms introduced to explain this behaviour. Most common models are based on rheological elements, springs and dashpots, which will be used to predict the fatigue life of the grout.

A Kelvin-Voigt chain is used to model the short-term creep based on k_{kv} (stiffness) and η_{kv} (viscosity) parameters. This chain is combined in series with an aging dashpot $\eta_{am}(t)$, in order to take into account the long-term creep as described in [114] (see figure 1.4-13). The basic creep strain is then given by the sum of the two elements:

$$\dot{\varepsilon}_{bc} = \dot{\varepsilon}_{kv} + \dot{\varepsilon}_{am} \tag{1.9}$$

The evolution of the hydration degree ξ described by Briffaut in [115], will be neglected due to the fact that the experiments were conducted at 8 weeks. The stress σ is given by : $\sigma = \sigma_k + \sigma_\eta$ and the creep strain for each elements is given as follows:

$$\dot{\varepsilon}_{kv} = \frac{\dot{\sigma} - \dot{\sigma}_\eta}{k_{kv}} \tag{1.10}$$

$$\dot{\varepsilon}_{kv} = \frac{\sigma_\eta}{\eta_{kv}} \tag{1.11}$$

$$\dot{\varepsilon}_{am} = \frac{\sigma}{\eta_{am}(t, t_0)} \tag{1.12}$$

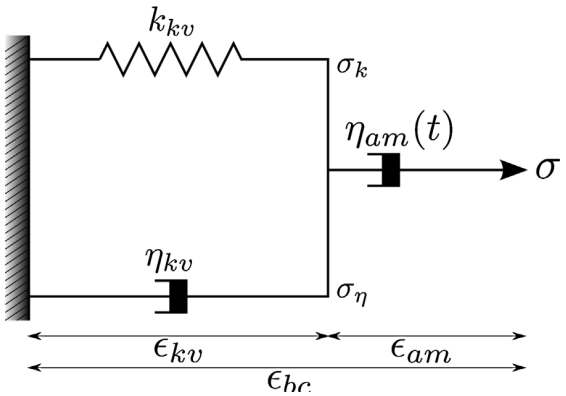

Figure 1.4-13 *Rheological model of basic creep [114]*

According to Brooks [116], the basic creep continues to develop linearly and does not show an asymptotic behaviour (for stress levels lower than 50%). Thus, the viscosity of the dashpot depends on time and the age of loading t_0 : $\eta_{am}(t, t_0) = \eta_{am}^0 \cdot \frac{t}{t_0}$.

If a constant stress level σ_0 is applied at the age loading t_0, the resulting basic creep is given in figure 1.4-14.

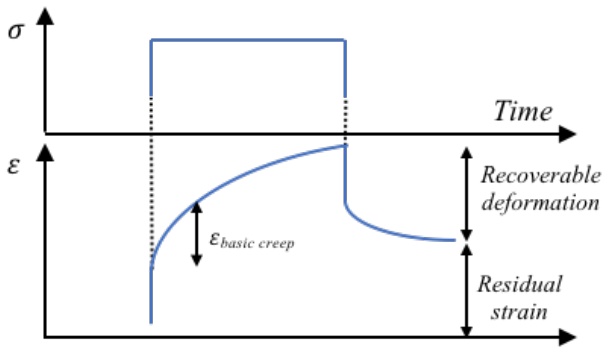

Figure 1.4-14 *Strain evolution under constant stress*

Moreover, according to [69] in the Kelvin-Voigt chain (a spring in parallel with a dashpot), the compliance is expressed as an exponential function. Therefore, the strain is expressed as follows:

$$\varepsilon_{kv} = \frac{\sigma_0}{k_{kv}} \cdot \left(1 - e^{-\frac{k_{kv} \cdot t_0}{\eta_{kv}}}\right) \tag{1.13}$$

$$\varepsilon_{am} = \frac{\sigma_0 \cdot t}{\eta_{am}^0} \cdot \ln\left(\frac{t}{t_0}\right) \tag{1.14}$$

Coupling basic creep and damage

In section 1.4.3.5 it was shown that the strain development during fatigue loading is composed of three phases. After the second phase with an almost linear behavior, the third phase takes place with a rapid increase of strain up to failure. Similar evolution is observed for concrete creep under high stress levels ($\geq 70\%$) according to Carpinteri [117] and the third phase is commonly called tertiary creep. Al-Kubaisy [118] also described for high stress levels the development of micro-cracking in the aggregate-matrix interface, which conducts to macro-crack in the cement matrix and fracture. In addition, Shah et Chandra [119] did not observe specimen failure after 4 hours in compression with stress levels lower than 70%. The non-linearity in the third phase [120] of strain development due to creep leading to failure mainly occurs for stress levels higher than the elastic limit.

A similar behavior was found by Mazzotti and Savoia [121] in uniaxial compression, where a creep-damage model was proposed to describe the nonlinear creep behavior. Likewise, Reviron [122] retrieved the non-linear basic creep evolution for high stress levels based on Mazzotti and Savoia by introducing a constant reduction factor β identified from experimental tests. The proposed model was able to reproduce the non-linear creep in compression and bending. This model will be used to simulate the strain evolution under fatigue loading from our tests and predict the time of failure.

Damage model

The damage concept was firstly introduced by Kachanov [123] and later developed by Lemaitre [124] in metals. Mazars [27] adapted this concept for quasi-fragile materials. It consists using a scalar variable D associated to the degradation process induced by mechanical loading and defined as the ratio between the micro-crack state and the representative elementary volume (see figure 1.4-15). The damage D values are between 0 and 1.

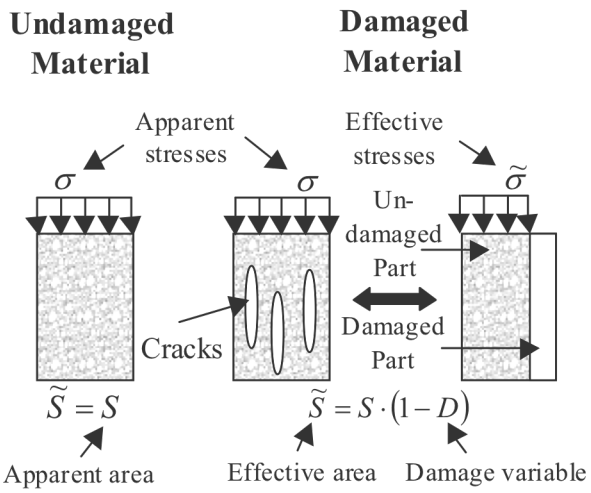

Figure 1.4-15 *Definition of the damage variable according to* [122]

In isotropic damage, the effective stress transmitted by the non-damaged area is given as :

$$\tilde{\sigma} = \frac{\sigma}{(1-D)} \tag{1.15}$$

The damage variable is then introduced as a loss of the material elastic stiffness E_0:

$$\sigma = (1-D)E_0 \cdot \varepsilon_e \tag{1.16}$$

The damage threshold is defined by $f = \varepsilon_{eq} - \kappa_0$ where ε_{eq} is the equivalent strain notion introduced by Mazars [27] defined as the norm of the positive eigenvalues of the strain tensor as follows, where the positive part $\langle\cdot\rangle_+ = 0$ if $\varepsilon_i < 0$ and $\langle\cdot\rangle_+ = \varepsilon_i$ if $\varepsilon_i \geq 0$:

$$\varepsilon_{eq} = \sqrt{\sum_{i=1}^{3} \langle\varepsilon_i\rangle_+^2} \tag{1.17}$$

According to Mazzotti and Savoia [121] and Reviron [122], the basic creep ε_{bc} can be introduced to this equation with the material parameter β in order to take into account the non-linear basic creep.

$$\varepsilon_{eq} = \sqrt{\langle\varepsilon_e\rangle_+ : \langle\varepsilon_e\rangle_+ + \beta\langle\varepsilon_{bc}\rangle_+ : \langle\varepsilon_{bc}\rangle_+} \tag{1.18}$$

The evolution of the damage variable in compression is given in exponential form and includes constant material parameters A_c and B_c identified from quasi-static tests:

$$D_c = 1 - \frac{\kappa_0 (1 - A_c)}{\varepsilon_{eq}} - \frac{A_c}{\exp\left(B_c\left(\varepsilon_{eq} - \kappa_0\right)\right)} \tag{1.19}$$

Mazars damage model is widely used to model the behavior of concrete in traction or compression due to its simplicity. As described in this chapter, this model will be used further in order to retrieve the strain development of a high-strength grout under fatigue compressive loading and estimate the time to failure under different stress levels.

1.5 Conclusions

The literature research on fatigue behavior of concrete and grout demonstrates the relatively low current knowledge in the comprehension of fatigue damage mechanisms. Despite some research available, the physical processes leading to changes in the material microstructure are barely explained. Additionally, limited number of specimens are often used for a particular stress level and frequently comparisons between different mixes are carried out at only one stress level or one frequency level. However, for an accurate description of the fatigue process and estimation of fatigue life, different mechanisms can be induced from these effects and thereby different stress levels should be applied at more than one loading frequency.

Despite an increasingly recent research on the fatigue of concrete and grout, the current work in comprehension mechanisms is rather limited with considerable inconsistent results. Even fewer results are reported on high-strength grouts. Therefore, there is not enough basis for developing models that can represent these processes in a realistic way. In this context, the main focus of this thesis is firstly to provide a better understanding of the fatigue behavior in cementitious materials by carrying out experimental tests on a “reference” high-strength grout on different stress levels and two loading frequencies. Another essential direction followed during this work consists in studying the influence of grout microstructure on the fatigue life and deterioration process, where a considerable lack of results intervenes. Thus, different high-strength grout mixes are developed and the experimental results are regularly confronted to the reference mix.

Based on the research presented in this chapter, the aim of this thesis is to answer a few questions barely addressed :

⇒ The compressive fatigue loading results in stiffness deterioration, strain evolution and in increased level of energy dissipated, which are considered as damage indicators. However, is the level of alteration independent on the stress level applied? Additionally a few models have been proposed in the literature based on : similar strains to failure in quasi-static and fatigue and the same secant modulus evolution. Can this be applicable to high-strength concrete and high-strength grout? How does the stress-strain relation change ?

⇒ Compressive fatigue in concrete is characterized by a three-step stage, where the transition phases occur at similar ratios of fatigue life. Is this the case for high-strength grouts ? Do the transition phases have the same extent regardless the stress level applied or the material strength ?

⇒ Overall, the loading frequency seems to have an influence on the fatigue life of concrete and grout and the damage evolution. Consequently, how the strain development, the stiffness and energy dissipation are affected ?

⇒ A temperature increase is reported in the recent years for compressive fatigue at high loading frequencies for concrete and grout. What is the level of temperature increase and what are the induced alterations and physical changes at a microscale level?

⇒ What indicators from experimental measurements can be used for fatigue life prediction?

⇒ What influence has the specimen size on the fatigue behavior of high-strength grouts?

⇒ What correlations can be made between creep and fatigue ? Is it possible to predict the strain development and fatigue life based on a constant upper stress level?

⇒ The scatter in number of cycles to failure is one of the major challenges encountered in fatigue of concrete and often is explained by the heterogenous microstructure. Can the scatter be reduced by using more homogenous aggregates in the grout mix?

⇒ How different mix components affect the fatigue life and the associated damage evolution?

⇒ Is fatigue life independent on the testing type i.e. bending and compression?

Against this background, the thesis has followed a predominant experimental direction. Analytical predictive methods for estimating the endurance limit and a model describing the strain development during fatigue is also given in the following chapters. The questions derived in this section combined with other addressed issues will be answered and analyzed gradually in the following chapters. The main outcomes in each chapter will be resumed in a conclusion section.

Chapter 2
Mixture Design and experimental methods

2.1 Introduction

This chapter presents the approach followed for mix design and experimental tests carried out at *Centre d'Innovation Parex* (CIP) of Parex France, Sika Technology AG and at *Laboratoire de Mécanique et Technologies* (LMT) at ENS Paris-Saclay.

The chapter can be divided into two main constitutive parts. The first part, sections 2.2 to 2.3, resume the methods followed for the mix design, while justifying the choice of different mix components used. It is also related to the first steps followed during the work in this thesis. The second part, sections 2.4 to 2.6, gives a description of the specimen geometries and preparation steps. Furthermore, the experimental set-up with the measuring methods are presented and this part constitutes the main core for the results and discussions carried out in chapter 3, 4 and 5. It is followed by a description of the test procedures defined for quasi-static and fatigue tests. A few additional techniques used for microstructure characterizations are described with the corresponding objectives.

2.2 Mix Design of the reference high-strength grout

2.2.1 Strategies for optimization

A reference high-strength grout (HSG) mix is established, in order to have a good flowability consistency (self-compacting) and a high mechanical strength. This mix is characterized further in the thesis, and used as a "model" grout for the comprehension of the fatigue behavior.

In order to develop the HSG mix, different parameters were taken into account such as:

⇒ Reduction of the intragranular porosity
⇒ Reduction of matrix porosity
⇒ Use of high-quality aggregates
⇒ Optimizing mixing and casting procedures

The selection of almost all mixture components was based on the knowledge gained from preliminary tests before this thesis. A few of the optimization methods will be described here. The aggregate chosen for the reference mixture is bauxite, for its high compressive strength and the maximum grain size is 6 mm. As shown from literature review, a higher aggregate size, might induce more microcracking in interfacial transition zone (ITZ) [7], since the microcrack size is directly related to the aggregate size. Moreover, the bauxite aggregates used here, are characterized by a porous microstructure and rough surface, which can improve the mechanical interlocking. In addition, the reduction of the intragranular porosity begins with a good particle packing, which is a crucial factor in order to obtain a high mechanical strength as described in chapter 2.2.3.

The cement paste also needs to be optimized, in order to avoid its incompatibility in hardness with the high-strength aggregate. If the matrix has a low Young's modulus as is the case in normal strength concrete, the cracks will tend to develop through the matrix or the ITZ. When the Young's modulus is comparable, a better bonding is created between the aggregate and the matrix and therefore local stresses due to a mismatch in elastic properties are decreased [19]. This is achieved by different factors as the use of alternative binders, a low water/binder ratio and the introduction of superplasticizers. A more detailed optimization of the cement paste is given in section 2.2.2.

As mentioned, the target properties were a good consistency as self-compacting grout and a high mechanical strength. In order to establish the optimal mix, firstly the aggregates and the binder were optimized separately and afterwards slump tests were

conducted on the fresh mix. When the optimal slump is achieved, the mix is validated by flexural and compressive tests at 3, 7 and 28 days.

2.2.2 Optimization of the cement matrix

Parallel work was made while establishing the optimal cement matrix, the optimal particle distribution and the optimal ratio between them. Indeed, the aggregates can induce micro-flaws in the ITZ, however good quality aggregates with an improved packing, in an optimized matrix help increase the mechanical strength. A good rheology is required for the self-compacting grout and it is measured by the slump test.

The cement used is a Portland cement type (OPC) with a strength class of 52,5. Firstly, a "starter" mix is used with a good particle packing (detailed in section 2.2.3) and with high strength properties. The first purpose was to define the quantity of cement necessary in order to obtain a good rheology. Three different cement quantities were used, and a better slump was obtained for a lower cement quantity. The slump was defined as the time spread necessary to reach a certain fixed value of diameter. As shown on the figure below (2.2-1 right), less time is required to reach diameter d1, d2 and d3, for a lower amount of cement (where d1 < d2 < d3) . However, mechanical tests at three days showed lower flexural and compressive strength for a lower quantity of cement. This is due to a higher water/binder ratio obtained when decreasing the dosage of cement.

Nevertheless, at the lower cement amount, good flow properties were obtained, while still having a high mechanical strength. Thus, 15% cement by mass is chosen for the reference grout.

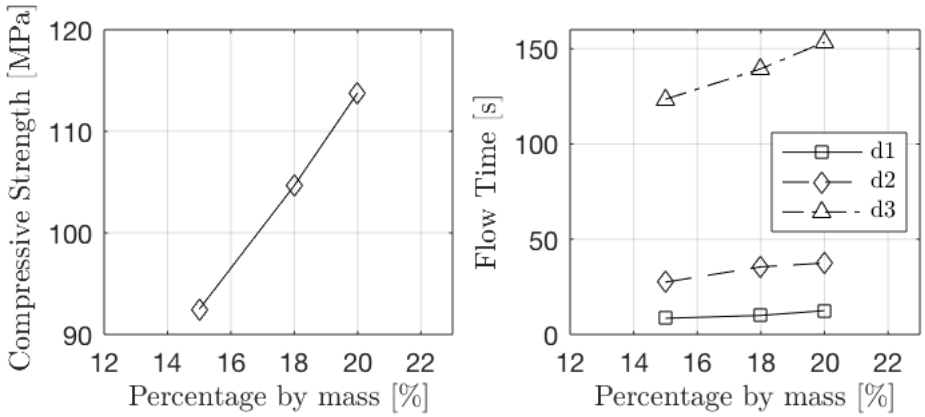

Figure 2.2-1 *Influence of cement dosage on the compressive strength and grout spread*

Other supplementary cementitious materials included are limestone fillers and silica fume. These fillers have a particle size smaller than cement thus they help improve the

particle packing. On one side, the advantage of using silica fume is the improvement of particle packing, because of the very small particles which pack tightly against the surface of the aggregate and also reduce the ITZ, as shown by Bache and Neville in [10,125]. A better rheology is obtained at the fresh state. Moreover, its pozzolanic properties with a high content of SiO_2, help reduce the Calcium Hydroxide crystals CH, by forming Calcium Silicate Hydrate (C-S-H) and thus improving the mechanical strength [7,26,126,127].

After defining the three main components of the binder: Portland cement, limestone filler and silica fume, a superplasticizer with good deflocculating properties was necessary. A polycarboxylic ether-based superplasticizer is used, due to its good water reducing capacity. The dispersing mechanism is related to the acrylate groups in the backbone and also the side chains (polyethylene oxide) that protrude from the cement surface into the pore solution to produce steric hindrance effect [128–130].

The preliminary tests with a dosage of superplasticizer of 0,35 % showed relatively good properties at fresh state. However, it was difficult to demold the specimen after 24 hours, because the hardening of concrete was not completely achieved. For practical reasons, in laboratory or field application, this is a non-negligible effect. Indeed, the superplasticizer has a retarding effect and a high amount was initially used, which can lead to a more viscous matrix and difficulties to demold the specimen after 24 hours.

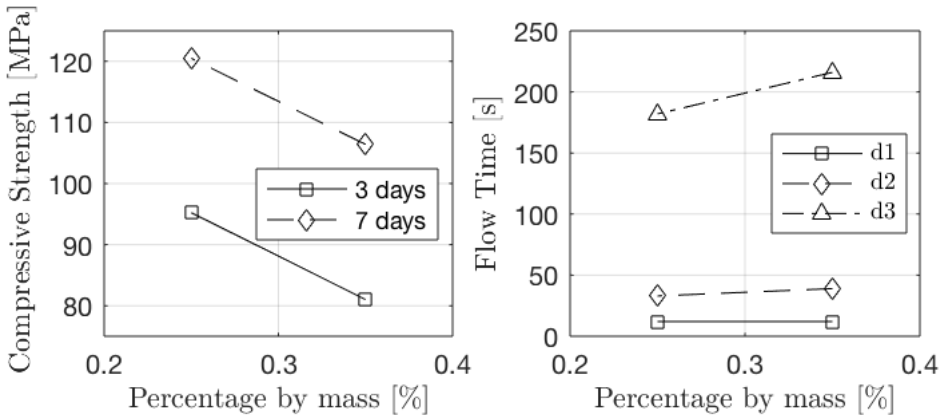

Figure 2.2-2 *Influence of superplasticizer amount on compressive strength and spread time*

A decrease of the amount of the superplasticizer, improved significantly the compressive strength (see figure 2.2-2). Thus, the retarding effect is less present and the hardening of the grout takes place faster. Additionally, the flow time was slightly improved.

The use of superplasticizers can induce air bubbles within the matrix, decreasing the surface tension during liquid phase. In order to avoid this effect defoamer admixtures can be used. According to Łaźniewska [131], the active components of the agent are distributed around air bubbles, displacing surfactant molecules. Consequently, the

thickness of the lamella wall built of surfactant destabilizes the air bubbles creating their fracture. In conjunction with the reduce of air-entrainment, defoamers also help improve the workability. Small quantities are used within the mixture.

The water/binder ratio is fixed at 0,26 which enables a good rheology for a good mechanical strength.

2.2.3 Particle Packing

The aggregates used for the reference mix are bauxite type as mentioned in section 2.2.1. The chemical composition, which will be necessary for further investigations (mainly in chapter 4), is given as follows :

Table 2-1 *Composition of bauxite aggregates*

	Al_2O_3	Fe_2O_3	SiO_2	TiO_2	CaO+MgO	K_2O+Na_2O
Composition [%]	78,3	2,3	14,7	3,7	0,5	0,4

The particle packing consists in selecting the proper sizes and proportions of small particles to fill larger voids. The small particles in turn contain smaller voids, that are filled with smaller particles and so on, according to Kumar [132] as described in the following figure. This concept is based on the well-known Apollonian gasket, by using discontinuous particle size distribution, where each “circle” is tangent to three other circles.

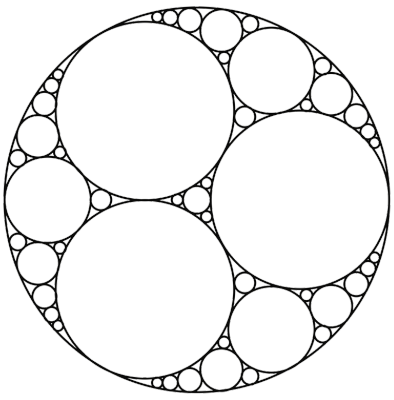

Figure 2.2-3 *Apollonian dense packing*

This method helps improve the strength of the concrete or grout, but also improves workability and reduces chloride permeability in hardened concrete [133]. Its beneficial effect, is observed when an optimum between different aggregate grades is achieved,

because on the other hand if the packing is too tight, the cement matrix will not separate the aggregates properly.

Multiple authors have worked on different particle packing models which can be categorized as discrete models and continuous models. The discrete models main assumption is that each class of particles will pack to its maximum density in the volume available [134]. De Larrard's work [135] was based on this approach by using a multimodal mixture model and he proposed the solid suspensions model SSM, where a distinction was made between the actual and virtual packing density. Further work took into account the compaction effort by introducing the compressible packing model (CPM). On the other side, continuous approach assumes that all possible sizes are present in the particle distribution system [134]. Adjacent size classes have ratios that approach 1:1 and no gaps exist between size classes. The most common method implementing this approach is the Andreasen model, which later was modified by Funk and Dinger [136] to take into account the minimum particle size. The modified model was previously proven to be efficient in aggregate particle packing for mortars and concrete [132,137] and it is used for the establishment of the reference mix grout.

The modified Andreasen model is given as follows :

$$CPFT = \frac{D^q - D_{min}^q}{D_{max}^q - D_{min}^q} \tag{2.1}$$

where

CPFT	is the "Cumulative Percent Finer Than"
D_{min} and D_{max}	the smallest and largest particle size
q	distribution coefficient, usually varying between 0,21 and 0,37, depending on the workability

The distribution coefficient determines the proportion between the fine and coarse aggregates and it is chosen at 0,3. This value is commonly used for non-spherical aggregates. Moreover, the use of an optimized curve (method not presented here) allows to achieve a target mix with more fine aggregates and an improved rheology. The proportions of the binder elements were preliminarily fixed and 5 grades of aggregates are chosen. This method takes into account the quantity of the fine elements of the binder in the calculation of optimizing the difference between "optimal mix" and the target model. However, it is very difficult to access to the right distribution of ultrafines and moreover the admixtures add complex chemical reactions, which cannot be taken into account in the program. Thus, after rheology adjustments were made, as described

in part 2.2.2, the particle size distribution obtained is presented in the following figure. The distribution for particle sizes < 0,05 mm is intentionally not displayed.

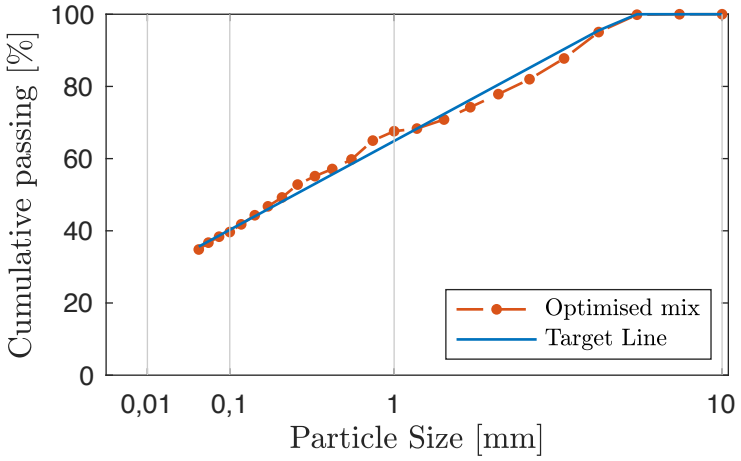

Figure 2.2-4 *Particle Size Distribution based on Andreasen Modified Model*

Final mix proportions for the reference grout are given in table 2.2-1. The water/binder ratio is settled at 0,26 and the maximum aggregate size is 6 mm. The mix has high a mechanical strength at early-age and long term. The results of quasi-static strength will be described in chapter 3.

Table 2-2 *Mix proportions of reference high-strength grout*

	Unit Content [kg/m3]
Bauxite aggregate (3/6 mm)	639
Bauxite aggregate (1/3mm)	388
Bauxite aggregate (0,5/1 mm)	361
Bauxite aggregate (0/0,5 mm)	357
Bauxite aggregate (0/0,2 mm)	638
Limestone Filler	230
CEM I 52,5	486
Silica Fume	77
Superplasticizer	6,7
Defoamer	1,3
W/B	0,26

Moreover, good flow properties are obtained and no sedimentation or segregation is observed. A cylindrical specimen with the mix content as described in table 2.2-1 was casted and demolded at 24 hours. Afterwards, the specimen was cut in two parts, along the height of the specimen, an example is given in figure 2.2-5. From visual observation, the specimen has a uniform distribution and no segregation is noticed.

Figure 2.2-5 *Vertical cross section of reference high-strength grout*

2.3 Establishment of other HSG

The previous reference mix of the high-strength grout is used throughout the thesis, in order to understand the failure mechanisms and damage process during fatigue. In addition, other mixes are developed in order to study the influence of different mix components in the process of fatigue and number of cycles to failure. A special focus is given to the deterioration mechanisms by different means of analysis. The two following sections describe the process followed to define the mixtures.

2.3.1 Grout mixes with different type of aggregates

2.3.1.1 Aggregate description

As mentioned, mixes with different nature of aggregates are developed in order to study their influence on the fatigue life. But, most importantly the center of attention is given on the damage mechanisms and the impact of the microstructure on fatigue damage.

The reference mix is composed of **bauxite aggregates**, where more than 70% of the composition is Al_2O_3 and secondly quantities of SiO_2 and Fe_2O_3 are also present. Two other mixes composed of other aggregates are also studied :

⇒ Tabular alumina is a pure sintered alpha-alumina, where sintering takes place at high temperatures (>1900°C). These aggregates are characterized by a high mechanical strength and a good chemical purity, which can be a beneficial factor when used in a material submitted to fatigue loading in laboratory conditions. Indeed, from fatigue loading large scatter of number of cycles to failure can be obtained, mostly due to the heterogenous microstructure of and also impurities

within the aggregates. Thus, aggregates with high chemical purity, might help reduce the data scatter. Moreover these aggregates largely used in industries such as steel and ceramics, have proven to be very efficient in thermal fatigue. The inconvenient of using tabular alumina in grouts for wind turbine industry is the high bulk density (~ 3,50 g/cm^3), where the matrix composition has to be adapted in order to avoid sedimentation.

⇒ Quartzite aggregate, widely used in concrete and grout technology is mainly composed of SiO_2, but traces of other elements are found such as Al, Fe, Mg, Ca (among others).

Therefore, the aggregates differ in chemical composition, but also in shape and surface roughness. In part 1.3.2 it was described that the aggregate texture can also influence interface properties. Hence, this is another parameter which will be analyzed further. Finally, the aggregates are characterized by different stiffnesses, and the compatibility with the cement matrix may lead to different damage mechanisms.

2.3.1.2 Strategies for mix design

The mix design of the next mixtures followed similar steps as those described in 2.2. However, in order for the mixes to be comparable and only take into account the influence of the nature of aggregates, a few conditions were initially imposed. Firstly, all mixes must have the same ratio of water to dry components in terms of volume. Moreover, the ratio between binder and aggregate content is also kept very similar in terms of volume. Only small adjustments in terms of rheology were allowed, in order to avoid sedimentation problems and achieve flow properties similar to the reference grout mix (see figure 2.3-1). Additionally, the grades of aggregates must be similar for the new mixtures.

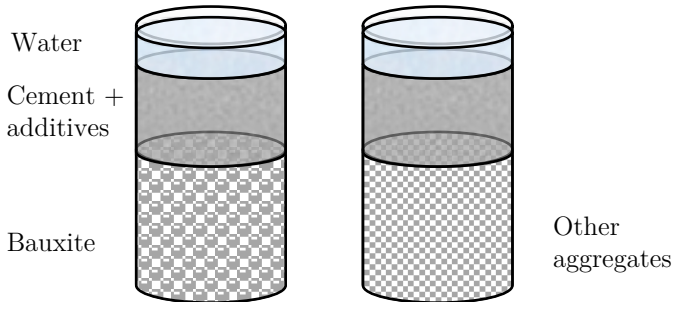

Figure 2.3-1 *Schematic representation of mix proportions in terms of volume for the reference grout and other mixes*

A step-by-step process of the methodology followed for the mix design of these grout mixes is given in in figure 2.3-2.

2.3.2 Grout mixes with different aggregate type in different fraction

In addition to the study of the influence of the nature of aggregates on fatigue damage, another analysis is carried out on mixes with different aggregate fraction of two natures. Therefore, two mixes are developed and both are composed of bauxite and quartz. Both mixes have the same volume of these aggregates, as "coarse" and fine, i.e. Mix 1 is composed of bauxite in the fraction of coarse aggregates ($d_{\max} \geq 1$mm) and quartz in the fraction of fine aggregates ($d_{\max} < 1$mm). Mix 2 has the inverse composition (quartz as coarse and bauxite as fine).

The method followed in the mix design is similar as the chart in 2.3-2., where in terms of volume : the fraction of water, the binder/aggregate and the flow properties are kept very similar. Figure 2.3-3 illustrates graphically the mix components (left) and shows a photo of the volume of aggregates between coarse and fine. Of course, the particle packing is different within the coarse and fine fraction, and consequently the fine fraction can appear slightly smaller. Nevertheless, the aim of this figure is to give a better graphical comprehension of the system used.

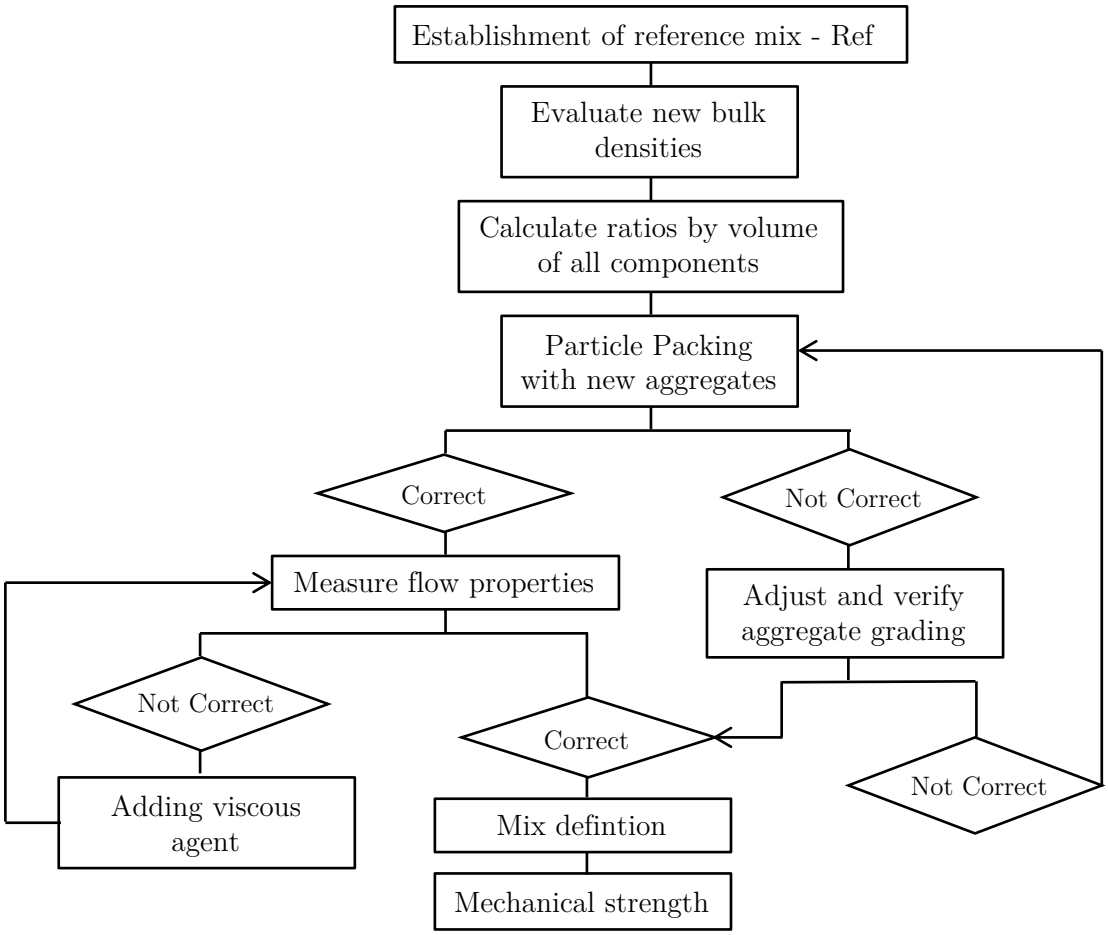

Figure 2.3-2 *Chart of mix design after the design of the reference mix*

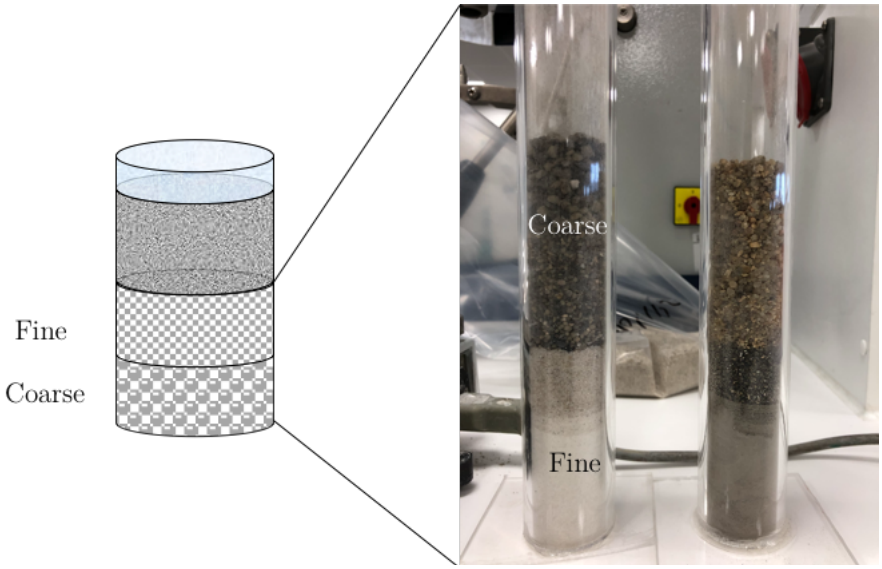

Figure 2.3-3 *Different aggregate types in different fractions of same volume*

2.3.3 Grout mixes with different porosity levels

Porosity in grout and concrete mixes is manifested in the form of entrapped air or water. However, mixes with high-strength properties have lower w/b ratio and thus less water is present in the microstructure. From literature review in chapter 2, it was shown that free water can have either a negative or positive effect on the fatigue life and the damage mechanisms. A conflictual mechanism can be found in a micro-scale level between the Stefan effect and pore water pressure. Moreover, the presence of air bubbles generally have a negative effect on mechanical strength, quasi-static and fatigue. Nevertheless, small quantities of entrained air might help in the process of damage in terms of energy absorption during fatigue.

The porous structure can differ in type of inclusion (air or water), shape (tortuosity, constrictivity) and pore size. The size can vary between a few to nanometers up to micrometer scale and can be divided as follows :

⇒ Macropores due to entrapped air which can influence the mechanical behavior
⇒ Capillary pores in a scale between 5 nm up to 5 µm influence the short-term creep
⇒ Hydrate pores between 0,5 to 10 nm and they can influence shrinkage and long term creep

The initial porosity of concrete can be around 8% of the total volume [25] and smaller values are expected in high-strength grouts. Two grouts mixes are also developed in order to analyze the influence of porosity on the damage process in fatigue following similar mixture method as presented in figure 2.3-2.

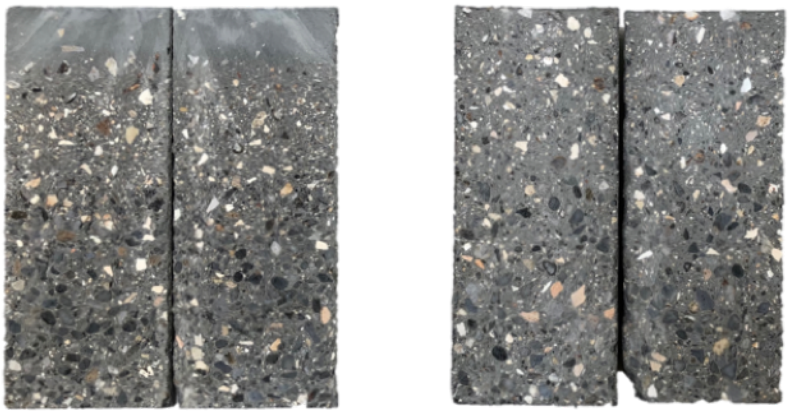

Figure 2.3-4 *Increased water quantity and segregation (left); use of viscous agent (right)*

In the first mix air is entrained by the means of an air-entraining agent. No other adjustments are carried out compared to the reference mis. Additionally, the second mix has an increased water content in a similar scale as the increase as the first mix. However,

the use of a viscous agent is necessary in order to avoid sedimentation as shown in figure 2.3-4, where cross sections of specimens with and without the use of a viscous agent are presented.

2.4 Specimen preparation

2.4.1 Specimen shape

Standards for concrete such as CEB-FIP [46] and guidelines for grout such as DNV [1], require uniaxial compressive tests conducted on cylindrical specimens with dimension D = 150mm and H = 300mm. A ratio D/H = 1/2 is necessary to obtain failure by cracking in the central part of the specimen as described schematically by Kim [138] (see figure 2.4-1. Moreover, the cylindrical shape allows for a better stress distribution in the cross-section.

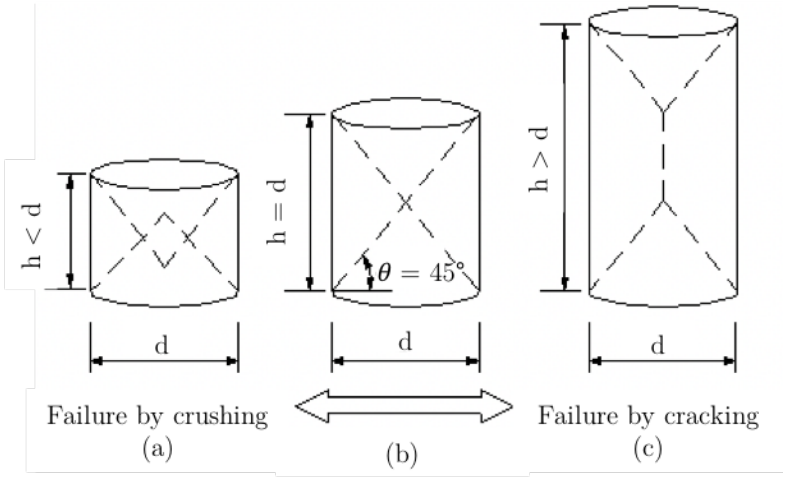

Figure 2.4-1 *Failure modes with specimen geometry according to Kim* [138]

The specimen is in contact with steel plates of the machine in compression loading, therefore friction is present between the two surfaces leading to the bracing of the edges of the specimen [25]. To avoid this phenomenon, Teflon plates could be used or other anti-bracing system such as grease, sand boxes, deformable supports etc. However, for practical reasons, and in order to obtain more easily the strain measurements in longitudinal axis, these anti-bracing systems could not be used, but a higher length compared to the diameter in the specimen is chosen. As a result, the friction effect near the edge fades while approaching the center of the specimen and the central part is under uniaxial stress state. The limitations by the machine used for the tests, imposed limits in the specimen sizes. Therefore dimensions of D = 60mm and H = 120mm are used, while keeping a ratio D/H = 1/2. Moreover, tests on D/H = 1/3 are also conducted later in order to assess the size effect and the influence of slenderness. This specimen size is

sufficient to give a representation of the heterogenous grout structure, where the maximum grain size is 6mm. The failure patterns of the specimens were consistently checked in order to verify if incorrect failure modes take place. Cerib [47], provides correct failure patterns to be expected in uniaxial compressive tests as presented in figure 2.4.2.

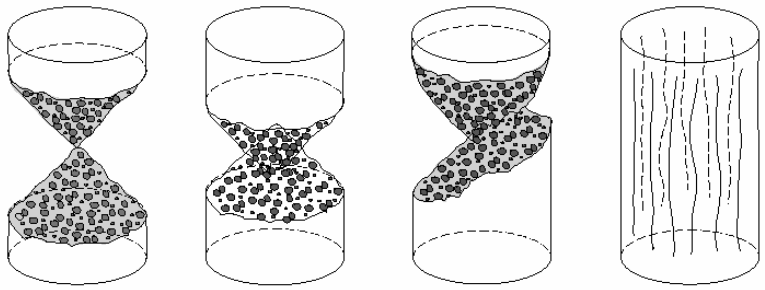

Figure 2.4-2 *Correct failure patterns of cylindrical specimen [47]*

2.4.2 Casting procedure and conservation

Water and dry components were mixed in two different speeds (low and high) for 7 minutes in total, in order to obtain a homogenous mixture. The mix was poured in PVC cylindrical molds with a diameter of 60mm and height 125mm. The mold is 5mm bigger than the specimen for the uniaxial tests, which was intentionally required in order to let sufficient margin for the grinding machine. Therefore the ratio D/H = 1/2 is strictly respected. No vibration is used after casting, as the properties are similar to a self-compacting concrete.

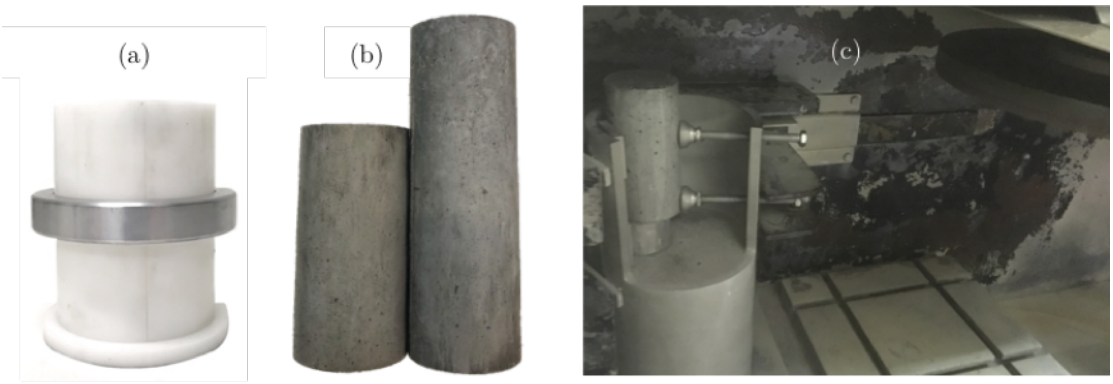

Figure 2.4-2 *Specimen mold (a) ; Two different specimen sizes (b) ; Grinding machine (c)*

After casting in a room controlled in hygrometry (HR = 65%) and temperature (T_{amb} = 23°C) the molds are stored for 24 hours for the hardening process. At 24 hours the specimens are demolded and immediately stored in sealed plastic bags. Therefore, the curing is made under intrinsic moisture and no special curing treatment is given to the specimens. This way of conservation is followed for 7 weeks in a temperature controlled

room, up to the grinding machine process. Planar parallel faces of the cylindrical specimen are required in order to obtain a uniform stress distribution from the machine. Therefore, both load application surfaces were rectified by a grinding machine. After this process the specimen are stored to the room of the testing machine until testing at 8 weeks or later. Some of the steps are shown in figure 2.4-2.

2.5 Experimental Set-up

The following part gives a thorough description of the set-up used for the experimental tests. Firstly, as the work in this thesis was mainly dedicated to the comprehension of the degradation mechanisms in compression, almost all the set-up presented here was started from scratch and was more meticulous than in flexural tests. As the strain development is adopted for most of the analysis, a particular attention was given to choose the right measuring system. The assessments had to be made with the least error and be repetitive. Therefore, classic measurements with strain gauges or LVDT sensors used in pre-tests at the beginning of the thesis, were disqualified. The strain gauges did not withstand well in fatigue loading and microcracks appearing in the surface damaged the gauges at times. Therefore, laser sensors were used (as will be described in 2.5.1.1) and a custom-made fixating system was processed. Other instrumentation, such as temperature and ultrasonic measurements will also be described. Furthermore, the test procedures are given for compressive and flexural tests. Although the thesis was mainly dedicated to understanding damage in compression tests, some flexural tests are also conducted and in this case the strain measurements are given with the Digital Image Correlation technique, as described in part 2.5.3. At last, microstructural observations are also carried out and all techniques will be briefly described.

2.5.1 Compressive tests

The compressive tests constitute the majority of the tests carried out in the thesis and most the analysis developed throughout the manuscript is based on the measurements and loading conditions described in this section. A few individual tests for the comprehension of certain phenomena have also been developed. These tests, will be not described in this section but will be detailed further in the text.

2.5.1.1 Equipment and measuring system

Quasi-static and fatigue tests in compression are conducted in MTS 50T servo-hydraulic testing machine (see figure 2.5-1 (a)) with a precision of ± 100 N. The machine is equipped with a load cell at the upper part, and it is possible to apply stresses in fatigue at different frequency levels. An acquisition system allows to record the imposed signal

of the force and the actual load applied on the specimen. Therefore the machine was continuously controlled on the precision of the applied force.

The displacements of the specimen are measured with laser distance sensors from Micro-epsilon, fixed at the lower plate of the machine. Three sensors are used to measure the longitudinal displacements and are placed at a 120° angle. Two other lasers are used to measure the lateral displacements and ensure at the beginning of each test that the specimen is well centered. Indeed, even a small eccentricity can have a big influence on the load application in compressive tests (see figure 2.5-1 (b)).

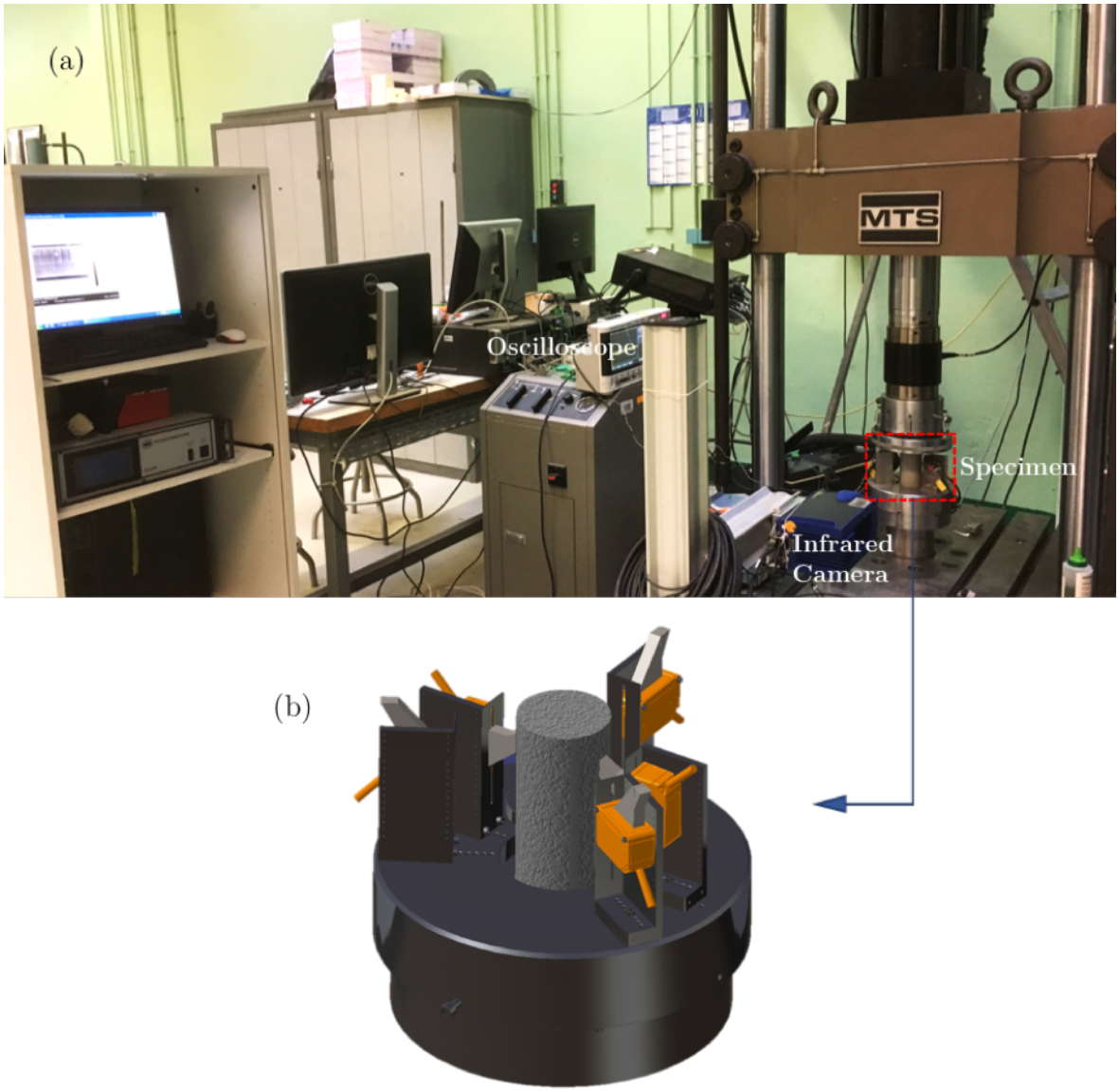

Figure 2.5-1 *50T MTS Testing machine in compression (a) ; 3D-view of the specimen and the laser distance sensors*

The laser sensors are connected to an amplifier and to the testing machine and have a measuring range of 10mm. The frequency of the data acquisition can be adjustable and

it was fixed at 600Hz for fatigue tests at f = 10Hz and 100Hz for tests conducted at f = 1Hz. Therefore, during one load cycle a minimum of 60 points are recorded, which is sufficient to obtain a good description of the cycle. They were used for both quasi-static and fatigue tests.

Some of the tests were also equipped with a system of ultrasonic measurements during the loading (see figure 2.5-2 (a)). A specimen with a decrease in stiffness or higher damage level is followed by a decrease of ultrasonic velocity. Therefore they can be used a damage level indicator. This method can be complementary to the strain development in fatigue testing or even used as a non-destructive method in structure monitoring. Usually, the measurements are conducted punctually before loading to differ specimen mixes and estimate the dynamic modulus. In very few recent research, such as from von der Haar [139] or Thiele [74], they were used during the test.

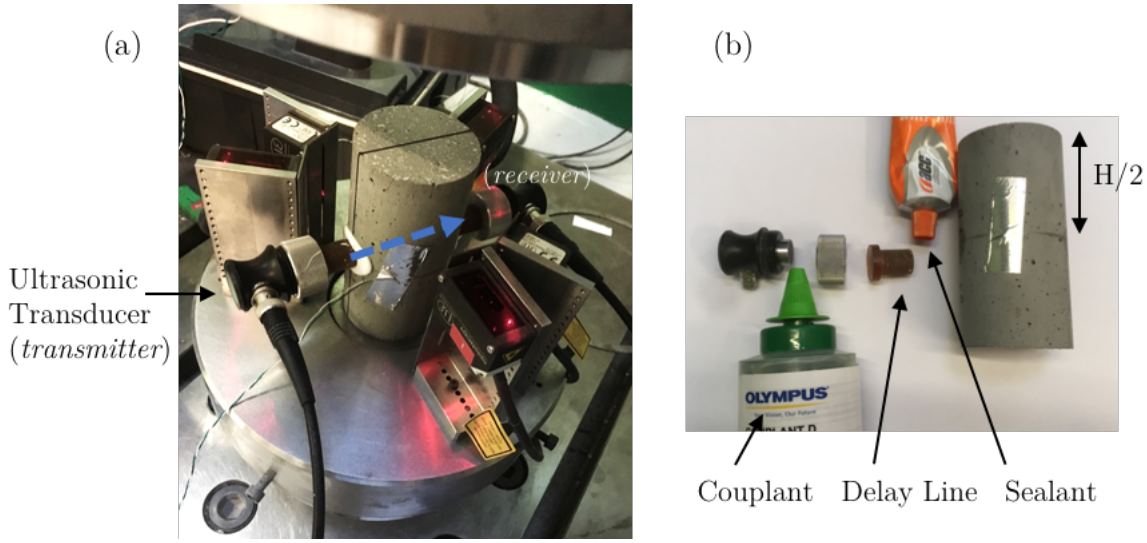

Figure 2.5-2 *Specimen equipped with thermocouples, ultrasonic transducers (a) ; Transducer with couplant, sealant and delay line used (b)*

In the compressive tests conducted here, the transmitter transducer (5MHz) sends an ultrasound signal, which goes through the sample and is received by another transducer. If cracking occurs in the specimen, the signal takes more time to cross the specimen and therefore the speed of propagation is reduced. During fatigue loading and the damage process, some noise can be present in the signal which might distort the propagation time. Therefore, a threshold level was defined in order to eliminate the noise during the test. In some cases this value was modified due to signal attenuation during loading.

Moreover, the signal from the transducer is connected to an oscilloscope which is connected in parallel to a computer for data acquisition. P-wave transducers are used, because p-waves propagate in all environments: solid, air and water, which are components of the samples used. The development of ultrasonic velocity was measured

during fatigue testing and the acquisition is made at a frequency of 10Hz. Thus, no rest-times are necessary for the measurements, as they could influence the fatigue life. The transducers are attached to the specimen with a temperature resistant acetoxy silicone sealant (see figure 2.5-2 (b)). A delay line is placed between the transducer and the specimen in order to create a protection against elevated temperature. It was noted that during fatigue compressive tests, surface temperature can increase up to 50°C or 60°C and the transducers used are sensitive when exposed to temperatures higher than 50°C. To ensure a good wave transmission, a couplant is used between the transducer and delay line.

The degradation of the dynamic stiffness could also be given by the means of this method as :

$$E_{dyn} = c^2 \frac{\rho\,(1+\vartheta)(1-2\vartheta)}{(1-\vartheta)} \tag{2.2}$$

Where, E_{dyn} is the dynamic stiffness [GPa], c the ultrasonic velocity [m/s], ρ the mortar density and ϑ the Poisson's ratio.

The development of Poisson's ratio in fatigue loading is non-linear and the equation above is given for an elastic material with a linear Poisson's ratio. Thus, firstly trials to estimate the evolution of Poisson's ratio will be made. Otherwise, instead of analyzing the development of the dynamic stiffness, only the development of the ultrasonic velocity can be analyzed.

2.5.1.2 Temperature measurements

It is expected that the fatigue loading will result in specimen heating. Thus, all specimens were equipped with 2 thermocouples disposed at mid-height. Two other thermocouples were placed at lower and upper compression plates next to the specimen. Due to the specimen heating, heat transfer to the plates takes place. The temperature of the loading plates is also influenced by the ambient temperature and by the hydraulic group, which warms up the oil and thus the plates. Therefore, the warming of the specimen is given as a difference between the mean value measured in the specimen and the plates. In addition, for some tests two other thermocouples were used in the upper and lower part of the specimen. The use of thermocouples gives information on averaged values of temperature in a very small millimeter square space and the time response can be limited. However, this was sufficient for the estimation of temperature increase during fatigue loading, where we were mostly interested on maximum temperature reached values.

In some of the tests, as is the case of self-heating method described in chapter 1, the temperature field over an area of interest is also measured with an infrared camera shown

in figure 2.5-1. The benefit of this method lies on the spatial information obtained and a higher frequency of acquisition, if necessary. It is a widely used measuring method for materials such as steel and some authors use it to describe the temperature evolution within one cycle, temperature gradients or obtain the heating source by inverse methods. The infrared camera used is Jade III Cedip with an image resolution of 320 × 240 pixels.

2.5.1.3 Fatigue Test Procedures

Firstly, quasi-static tests were conducted on 7 specimens in a displacement controlled mode, with a constant rate at 3 x 10^{-3} mm/s. The mean value of compressive strength obtained from the quasi-static tests serves as a value to determine the stress levels applied in fatigue tests. The maximum stress levels are expressed as a ratio to the mean compressive strength and for the tests carried out, they vary between 0,70 and 0,90. The stress ratio between $S_{c,min}$ and $S_{c,max}$ ($R = S_{c,min}/S_{c,max}$) is kept constant for all tests at 0,1. Based on literature research, there are numerous recommendations for fatigue testing to keep the ratio R as constant (as we proceeded). So, the $S_{c,min}$ value is calculated from the constant ratio R and the applied stress level $S_{c,max}$. However, in other studies $S_{c,min}$ is kept constant around 0,1 or 0,05 for all testing, which means that for any maximum stress level applied, the minimum stress level remains constant but the ratio R is variable. In these cases, $S_{c,min}$ is calculated from the reference compressive strength. The data analyzed from our fatigue testing will constantly be compared to values from the literature, which apply to both methods explained: R constant or $S_{c,min}$ constant. Nevertheless, the changes between the two methods are not very significant as the ratio $R = 0{,}1$ in our tests is equivalent to $S_{c,min}$: 0,07-0,09.

After determining the quasi-static strength, the stress levels and the loading frequency are determined according to the test required. The loading is consistently applied in a sinusoidal shape, which is the most similar loading type encountered in structures submitted to cyclical wind, traffic or streaming, as mentioned by Korte [140]. Some research is reported in the literature, where triangular and also rectangular signal is applied. It was found that the waveform can have a strong influence on fatigue life. Oneschkow [98] reported a longer fatigue life when a triangular waveform is applied in a high-strength concrete. Whereas, a rectangular loading can be more damaging, due to the fact that the loading remains longer in the peak load levels. Moreover, the strain rates are larger in a rectangular waveform [141]. A report by Rilem [142], based on Tepfers' work, confirmed the dependency on the waveform. Therefore time dependent effects, can be present depending on the loading type and create different damage mechanisms.

As the grout is submitted to wind and wave, a sinusoidal waveform is chosen for all tests at two different frequency levels $f = 10$ Hz and $f = 1$ Hz (see figure 2.5-3). Firstly, a

monotonic loading is applied in force controlled mode with $v = 1{,}5$ kN/s up to the mean value between $S_{c,min}$ and $S_{c,max}$. Subsequently, the fatigue loading is applied in force controlled mode, up to specimen failure.

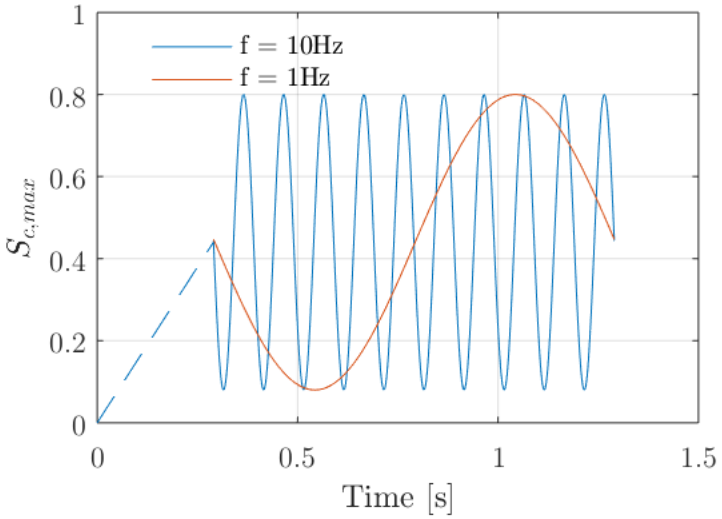

Figure 2.5-3 *Schematic representation of the fatigue loading procedure at two loading frequencies*

The loading was not interrupted by "rest-periods", for measurements. All test measurements were performed continously during loading up to failure. Indeed, depending on the acquisition system, some authors apply unloading up to a low stress level or sometimes to the mean value, in order to perform measurements. Hilsdorf and Kesler [143] were among the first to investigate the influence of rest-periods on fatigue life and found that these rest-periods would increase the number of cycles to failure, when applied for 5 minutes or lower. A longer rest-period would not have an influence on the fatigue life. This can be caused by the healing of cracks, which is due to transfer of material or Van der Waals forces pulling the cracks together and "shorten" them. Farhani [144] also investigated rest-periods of 500 seconds for two types of concrete and found a higher fatigue life. These rest-periods, add a creep-effect to the damage mechanism and thus can modify the behavior under fatigue. Hence, no rest-periods are applied in the tests presented in the thesis, unless specifically indicated.

Confining pressure in the lateral direction, when compressive fatigue loading is applied (i.e. biaxial loading), can have a beneficial effect on fatigue life. Petkovic reported results in concordance with this behavior and created a relation between the mean stress S_m , the stress range R and the fatigue life (see figure 2.5-4). Farhani [144] also found a higher fatigue life when applying confining pressure of 7 MPa in the lateral direction. Therefore, the loading during fatigue tests in this thesis is applied only uniaxially, in order to represent the unfavorable scenario.

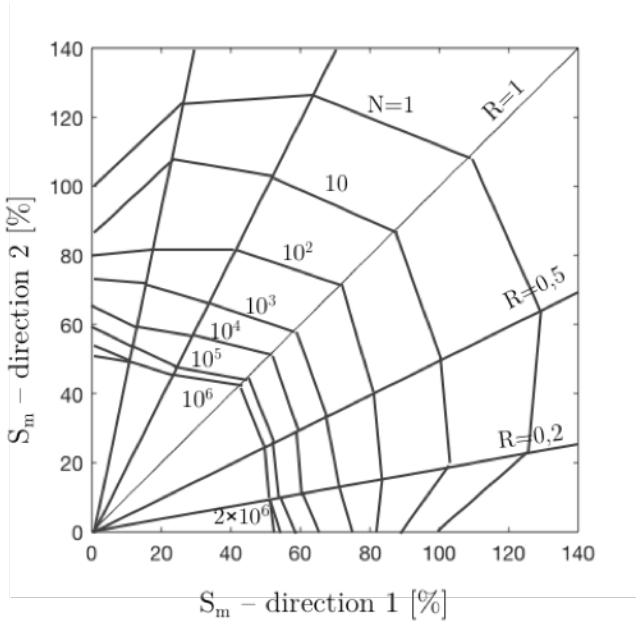

Figure 2.5-4 *Fatigue life under biaxial loading, reproduced from Petkovic [13]*

2.5.2 Microstructural Analysis

Some microstructural analysis is performed on different grout mixes as will be subsequently detailed. The main analysis consists in SEM observations coupled to EDS analysis for mixes with different aggregates. Two methods are presented likewise to characterize the porosity of the grouts. Finally, X-Ray CT is used only to limited extent for observations of crack evolution in fatigue and crack paths.

2.5.2.1 Petrographic observations

Petrographic observations and analysis are conducted in a Scanning Electron Microscopy (SEM) and Energy Dispersive X-ray Spectroscopy (EDS). SEM investigations were used to analyze the cracking generated from fatigue and quasi-static loading. In addition, mixes with different microstructures were used in this thesis. Therefore, SEM was used to analyze interface properties complementary to EDS, where linescan and mapping procedures were performed. Two types of observations are used depending on the target required. Firstly, most of the observations are made using Secondary Electrons (SE), which according to Scrivener [145] have a lower energy than the incident electrons and are detected from a thin layer at the surface of a specimen. Other observations are made using Backscattered electrons (BSE) which have a similar energy to the incident electrons and are detected from greater depths than the secondary electrons.

The first series of specimens observed did not need a particular preparation, because the observations were made on the fracture surfaces after failure. The purpose was mainly to observe the crack shape and location, the presence (or not) of friction areas and distinguish crack failure between specimens from quasi-static and fatigue loading. In terms of preparation only a carbon coating was used and a sample was extracted from the fractured surfaces.

Other specimens were used in order to analyze the microstructure of cement paste, aggregates and ITZ. Specimens in intact state and others stopped before failure were cut in slices, which were later used for analysis. A few steps for preparations were followed in order to obtain the best quality images, where a few are shown in photos in figure 2.5-5. Firstly, the specimens were placed in an oven at 60°C for one week in order to remove moisture. The complete drying would need more time, however this was not a mandatory step and seven days could be considered sufficient as seen from previous work in literature review [146]. Afterwards, the samples were epoxy resin impregnated in a vacuum chamber. Subsequently, they were polished finely and coated with carbon.

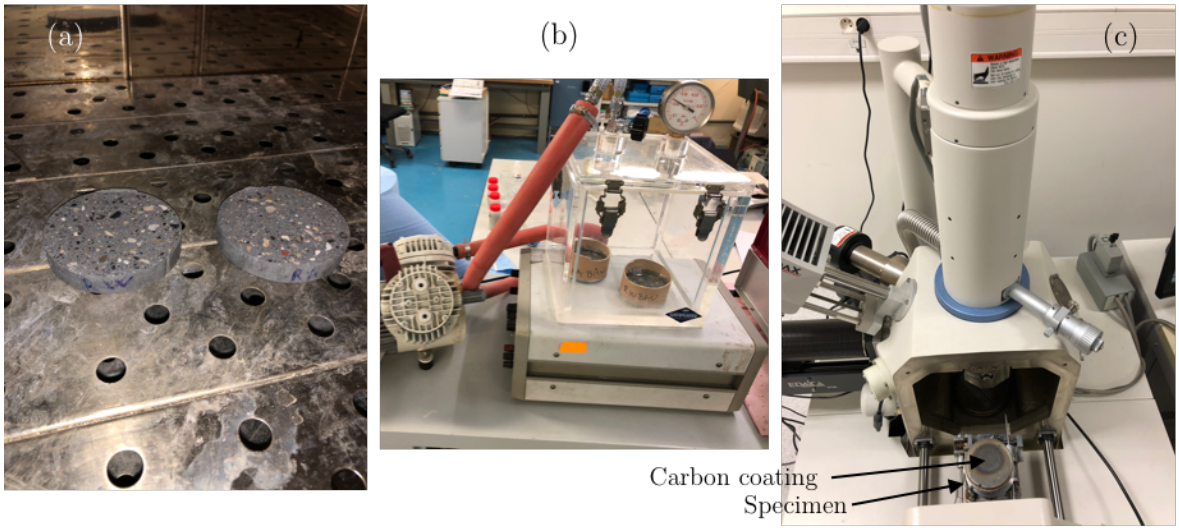

Figure 2.5-5 *Steps for SEM observations - Specimen drying (a) ; Epoxy resin impregnation (b) ; Carbon coating on a specimen placed in the microscope (c)*

In general, a working distance of 5 mm is set for observations and 10 mm when EDS analysis is used. Several levels of magnifications are recorded, up to hydrate observation scale. Finally, most observations are conducted with a 15 kV voltage.

2.5.2.2 Mercury Intrusion Porosimetry

In part 2.3.3 it was presented that a study is conducted on the influence of porosity on the fatigue damage process and fatigue life. The increased porosity is in the form of added water and air-entrained with the means of an air-entraining agent.

In order to characterize the porosity and the distribution of pores, the mercury intrusion porosimetry (MIP) is used and the test of total water porosity, which will be explained in the next part. This is a common method used in cement-based materials, but also a controversial one, especially because it involves addition and removal of water, which can affect the hydrated cement paste according to Feldman [147]. However, according to Cook [148] with certain assumptions, the technique can give a good representation of the porosity and the pore size distribution.

The technique consists in applying controlled increments of pressure to the mercury, which allows its penetration to a sample and the volume introduced is measured. Therefore, different pore sizes can be reached depending on the pressure applied. The method is based on Laplace law and the equation 2.3 gives the relation between the pressure that forces the intrusion and the pore size :

$$d = \frac{-4\,\gamma\,cos\theta}{p} \tag{2.3}$$

Where, d is the equivalent diameter of the intruded pores [m], γ is the surface tension of mercury [N/m], θ is the angle of contact between mercury and the pore walls and p is pressure which causes the intrusion [Pa].

Pore size between 0,003 µm and 100 µm can be given by this method. It is worth noting that this method gives only information on the open porosity and pores with higher diameter than 100 µm cannot be measured. However, the MIP technique will be used in a comparative scale between specimens with different mixtures. Furthermore, 3 measurements are made on specimens from the reference mix. The first is made on an initial intact state and two others after fatigue loading is applied. Samples from these specimens were used for MIP measurements, in order to evaluate if a different evolution of the pore size distribution is present.

2.5.2.3 Total water porosity

The total porosity of the specimens accessible to water is measured as a complementary technique to the mercury intrusion porosimetry. The measures are based on the French standard NF P18-459 [149]. However, a few modifications were applied, in order to make the technique more suitable to grout materials.

The samples used for the measures are cylinders similar to the initial specimens and the dimensions are $D = 60$ mm and $H = 120$ mm. At 8 weeks after the grout mix (the same time as the tests) the specimen were dried in an oven at 60°C for 10 days and not 105°C as suggested by the standard. High temperatures as 105°C can be damaging to the cement

paste and the aim of this study was to influence as less as possible the microstructure. At 10 days, the weight loss was considered to be constant and the mass m_{sec} is determined. However, small variations after 10 days can still be expected. Moreover, the oven was not controlled in humidity, but doors of the oven were constantly opened, in order to let the air circulation.

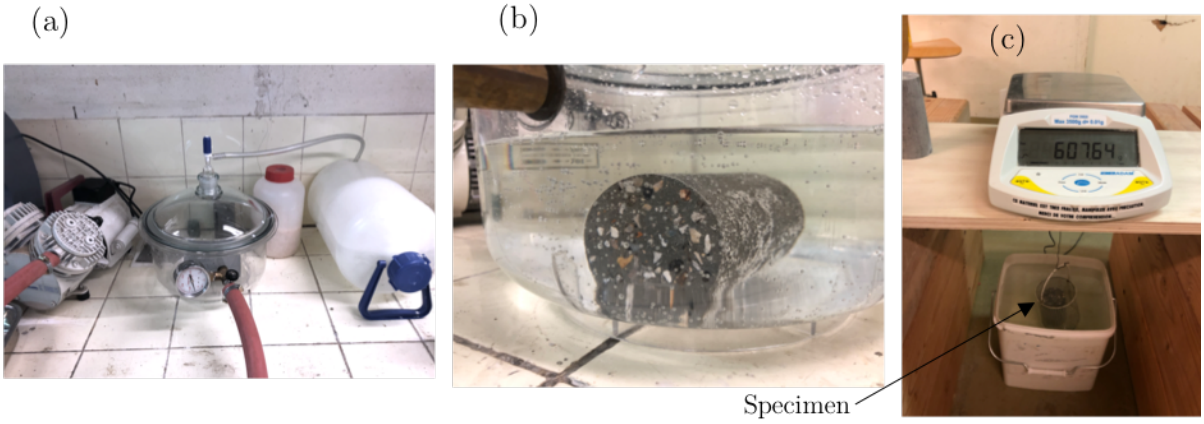

Figure 2.5-6 *Total water porosity measuring system, vacuum pump and desiccator (a) ; Specimen in the desiccator under water (b) ; Hydrostatic weighing (c)*

Afterwards, the specimens were disposed in a desiccator under vacuum for 16 hours in order to evacuate the air in the sample as shown in figure 2.5-6 (a). Once the time is finished, water is introduced up to 2 cm more than the sample's height for total immersion and left in these conditions for 24 hours (see figure 2.5-6 (b)). The following step consisted in stopping the vacuum and proceed with mass measurements. The mass of the saturated specimen is expressed as m_{air} and the hydrostatic mass as m_{eau}. They are measured in a balance with a precision of ± 0,01g. The total water porosity is given from the following expression :

$$\phi\,[\%] = \frac{m_{air} - m_{sec}}{m_{air} - m_{eau}} \qquad (2.4)$$

2.5.3 Flexural Tests

A few flexural tests in quasi-static and fatigue loading are also carried out during this thesis. Nonetheless, this part is not as exhaustive as the comprehension achieved from fatigue in compression. Only few data is collected, essentially for the reference grout. The intent was to compare fatigue life between the two testing methods and make observations on crack initiation and propagation during fatigue. The Digital Image Correlation (DIC) technique is used for this purpose.

2.5.3.1 Test procedures

All specimens tested have dimensions of 40 x 40 x 160 mm^3 and are notched in the mid-span. The notch height is of 10 mm and the width around 1,5 mm, which depends on the width of the blade. The notch is performed after hardening, the day before carrying out the test. The specimens are previously marked in order to ensure that the notch is created in the middle for all specimens (see figure 2.5-7). The span has a length of 10 cm and the areas where the lower supports are placed, are also previously marked. The marking also helps to ensure that no rotation takes place in the z-axis.

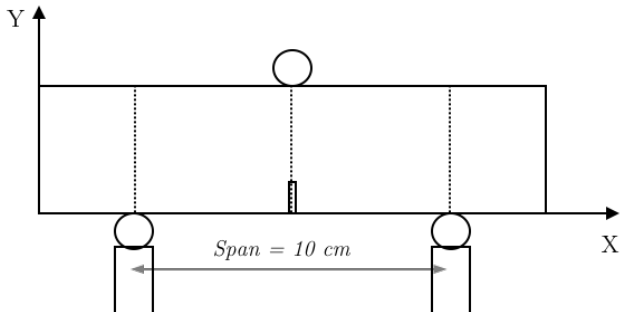

Figure 2.5-7 *Schematic representation and marks of the specimen in the 3-point bending test*

Test procedures in flexural tests are similar to those described in part 2.5.1.3, despite a few changes. 6 quasi-static tests are conducted at 10 weeks, in a 3 point bending test and in a displacement controlled mode, with a constant rate at 2,2 x 10^{-3} mm/s. After the mean quasi-static strength is determined, some specimens are tested at three stress levels at $S_{c,max}$ = 0,80 ; 0,75 and 0,70, where 6 specimens are used for each stress level. The experiments are operated primarily at f = 10 Hz and five more specimens are tested at f = 1 Hz. Comparatively to fatigue in compression, for flexural tests the load is applied in force-controlled mode. Firstly, a monotonic load increase up to the mean value between $S_{c,max}$ and $S_{c,min}$ is performed and subsequently the specimen is submitted to fatigue, up to failure.

2.5.3.2 Digital Image Correlation

The displacement field in 3-point bending tests is measured with the DIC technique. The in-house correlation code Correli RT3 [150] is used for the post-treatment of the images and the calculation of local and mean strains in the utility zone. Moreover, the crack initiation can be detected thoroughly with the correct camera installations. The concept behind this technique is to compute the difference between a reference image and a deformed one. Both are given as functions describing the grey level of every pixel. The displacement field *u(x)* is obtained by minimization of the following equation :

$$f(x) = g(x + u(x)) \tag{2.5}$$

Where, x is the pixel location, f and g are the reference and deformed images, respectively.

In quasi-static tests a CCD PCO PixelFly scientific camera (1400 × 1040 pixels) is used with a telecentric lens x0,125. This camera has been successfully used in our lab for strain field measurements during fatigue loading in steel materials such as in [151]. A region of interest is selected (ROI) in the central part of the specimen with a length of 70 mm and covers the total height of 40 mm. One image is acquired automatically every two seconds during the test and no shutter lag is present. A Labview routine for both quasi-static and fatigue measurements is implemented in order to trigger the camera as defined before the test by the user. The cameras are firstly triggered before the test, where 10 images are taken in order to verify the uniformity of the painted speckle on the specimen's surface generated by a black and white matte paint. Secondly, a contact force of 100 N is applied to the specimen and 10 images are taken as reference. The mean of these images is considered the reference for all other measurements.

During fatigue loading, a different camera is used. Indeed, the CCD camera is not adapted for fatigue loading, unless the acquisition is made in a stroboscopic mode. Therefore for more accurate measurements obtained by avoiding resting periods originally necessary for image acquisition, a high-speed camera is used : Photron SA5. The images are not taken on the entire length of the specimen, but only close to the notch area, where the crack is supposed to be initiated. The image resolution is 1024 × 1024 pixels. All these tests are carried out on a 50 kN machine capacity at LMT Cachan. The complete set-up is given in figure 2.5-8.

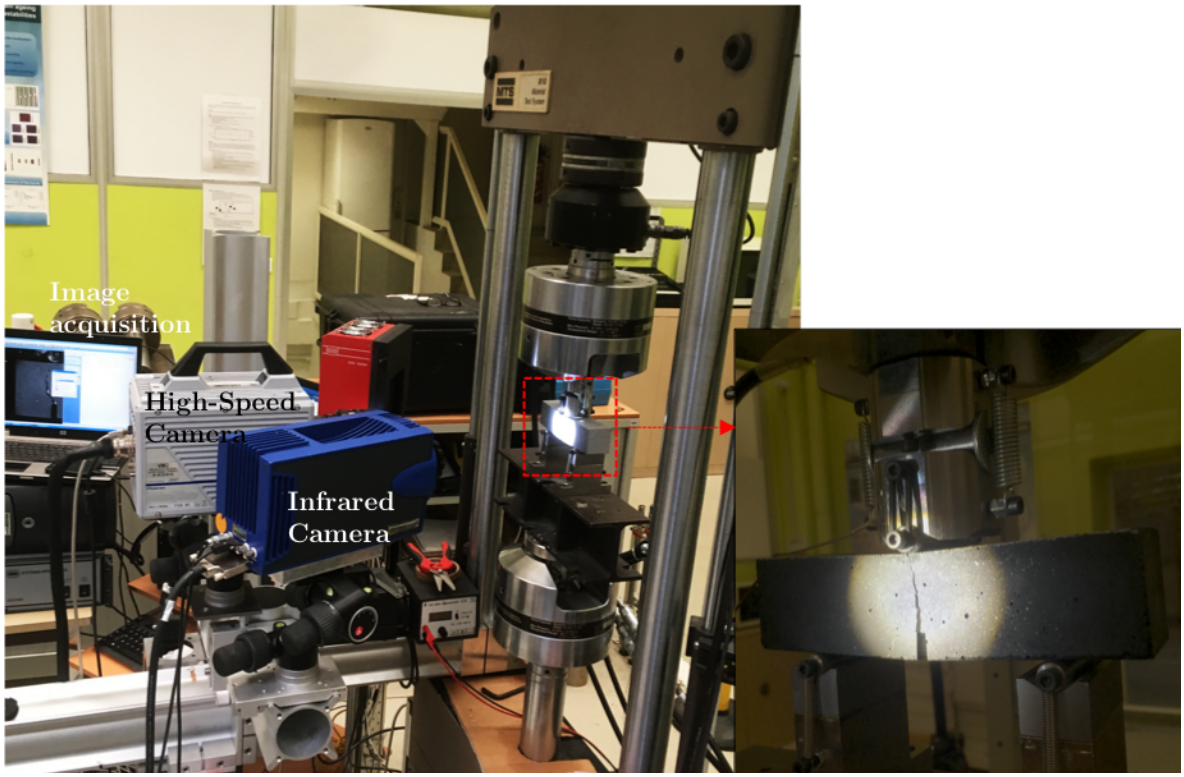

Figure 2.5-8 *Test set-up in 3-point bending tests*

In fatigue, the reference image is acquired when the a small force is applied to the specimen, as well. The high-speed camera has an impressive acquisition frequency of 150K fps. However, this is more adopted to fast dynamics and exceeds our goal, hence a much lower acquisition is adopted. The loading frequency is 10 Hz and an acquisition of 250 Hz is considered sufficient. Therefore the camera is triggered for one second and 250 images are saved on a dedicated computer. A total of 25 images are used to describe one complete cycle. Due to limited space, the camera is triggered once every 1 000 cycles. Once 30 000 cycles are reached, a trigger is configured every 10 000 cycles up to failure. Hence, the high acquisition frequency of the camera allows image capture continuously during the test, with no resting periods involved (which could alter the fatigue life).

From the acquired images and by the means of DIC, the displacements at different ratios of fatigue life can be determined. Thus, the displacement acquisition in the flexural tests is slightly different from the acquisition with laser sensors used in the compressive tests. As previously described, the displacement is measured continuously in compression at a rate of 600 Hz up to the failure of the specimen. Whereas in flexural tests, intermittent acquisitions are carried out. The acquisition program is given schematically in figure 2.5-9.

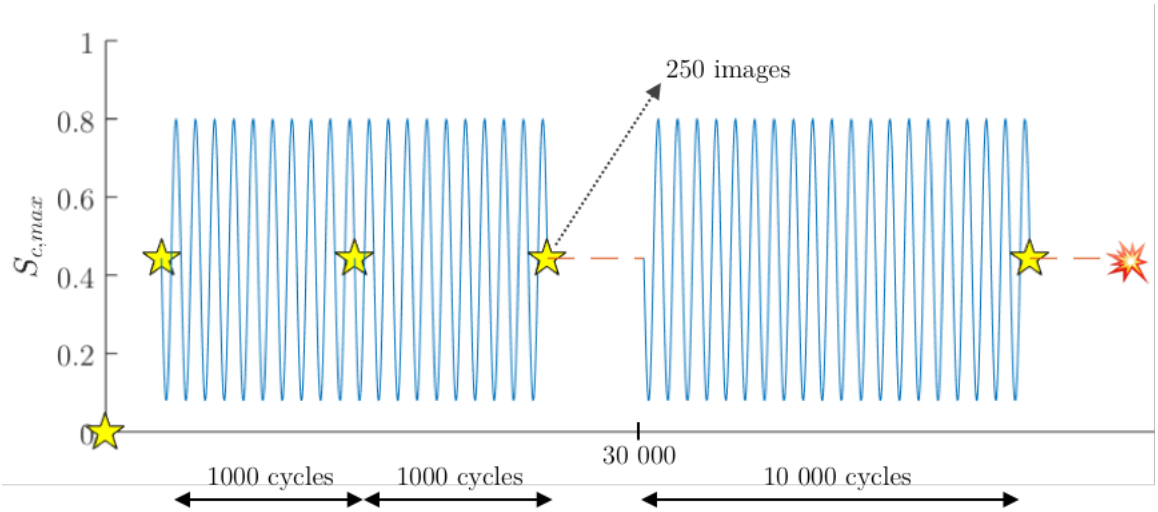

Figure 2.5-9 *Schematic representation of image acquisition in fatigue in 3-point bending tests*

2.6 Conclusions

This chapter gave an outline of the methods followed for establishment of a high-strength grout, which is commonly called "reference" throughout this manuscript. Other grout mixes are also presented and are developed mainly to establish a relation between different mix components and the fatigue life in addition to damage mechanisms during compressive fatigue. Table 2-3 gives an overview of the mixes analyzed and the corresponding number of tests carried out.

A total of approximately 300 specimens will be presented and analyzed throughout the manuscript. Another 200 specimens were tested during this thesis for complementary data, understanding and optimizing the current testing methods presented. Indeed, a large amount of preliminary tests were carried out in order to optimize the measuring techniques, the set-up for a good specimen centering, data acquisition and data processing, as the fatigue tests resulted in large data files.

Thus, it can be noticed that the experimental work was the main focus of this work, in order to give a better description of the fatigue behavior. Different measuring techniques are used for this purpose and presented throughout this chapter.

Table 2-3 *Summary of the main experimental program*

Test type	Specimen size	Conservation	Time of Test	Mix	Number of specimens
Compression	ϕ 60 × 120 mm	Sealed until testing	8 weeks (and >)	R-Bau*	50
				Qua*	30
				Tab*	30
				Bau-G*	30
				Qua-G*	30
				A-Bau*	30
				W-Bau*	30
	ϕ 60 × 180 mm			R-Bau	30
Flexion	40×40×160 mm			R-Bau	30

** Note : Details on the meaning of these abbreviations can be found in "Nomenclature" page XII*

Chapter 3
Mechanical behavior of reference high-strength grout in compression

3.1 Introduction

Considerable studies in the literature are focused on the number of cycles to failure for different concrete types and definition of fatigue strength. Some of these studies have investigated the influence of loading frequency, but contradictory results are reported. However, these results are not often analyzed further in terms of strain and stiffness evolution, but reported only in terms of fatigue life. Nonetheless, they are the basis indicators for a damage mechanisms oriented review. Furthermore, the few hypothesis presented in the literature based on correlations in strain development between quasi-static and fatigue behavior are not verified. In practice, this lack of analysis can lead to unreliable application and structural deficiencies. Additionally, most of the tests are carried out on normal strength concrete and an equivalence between normal strength and high or ultra-high strength concrete/grout is not often examined.

This chapter aims to give a complete analysis of the fatigue behavior of high-strength grouts in compression by the aforementioned indicators and answer some of the questions addressed in the conclusions section of chapter 1. For this purpose, extensive experimental investigations are carried out on a reference high-strength grout, which represents the main part of the current work. Initially, the quasi-static strength is examined and it provides the first step for all further fatigue tests. Subsequently, the fatigue life is presented followed by the effects of some influencing factors, such as loading frequency and temperature generation. Based on the knowledge gained from the tests, a description of the damage evolution in the material is given. In accordance with previous objectives, the strain and stiffness development are analyzed for the corresponding stress level and also given in relation to the intact state. Comparisons between quasi-static and

fatigue tests are consistently developed. This subsection is finalized by alternative methods for fatigue life estimation and endurance limit.

The behavior of specimens tested in compression is not influenced only by the loading and intrinsic properties, but also by specimen size. Therefore, specimens with larger dimensions, but in the same shape were firstly considered for estimating the level of influence on the fatigue life and deterioration process. Due to a lack of capacity of the testing machine, only specimens with larger elongations are examined. The purpose is to provide at least a small indication to what extent the size has an impact.

In order to contribute to a better understanding of the microcrack state development and a better description of the damage evolution at meso-scale level, techniques such as digital image correlation, total water porosity and mercury intrusion porosimetry are employed. Finally, this chapter is concluded with post-mortem observations coupled with SEM analysis.

It should be noted that a particular attention was related to determine the most adapted displacement measuring technique during fatigue in compression and after our trials it resulted to be the laser distance sensors. Additionally, the appropriate acquisition frequency involved an important step in order to give a good description of the hysteresis. The choice of a high acquisition frequency in a continuous and uninterrupted way up to failure of the specimen, resulted in large size data files. Therefore, all data processing in the two following chapters are performed with Matlab.

3.2 Quasi-static behavior

The mix composition of the reference high-strength grout, to which this chapter refers to, can be found in table 2-2 in chapter 2. The methodology followed for the mix establishment is also presented, in addition to the composition of aggregates in table 2-1.

Quasi-static tests for the reference mix are carried out on 7 specimens and the mean value is considered as the compressive strength of the grout. All stress-strain relations are given in figure 3.2-1 (left) and are expressed as the mean value from measurements of 3 laser sensors. A mean compressive strength of 168 MPa is reached and a high Young's modulus of 54 ± 1,8 GPa. The maximum strain at peak load ε_u is between 3,66 and 4,15 ‰. Additionally, the specimens manifest an elastic behavior up to 71 % of the total strength. This value is also calculated individually for each test by evaluating the levels when the linear regression in the elastic phase and the individual curve do not intersect.

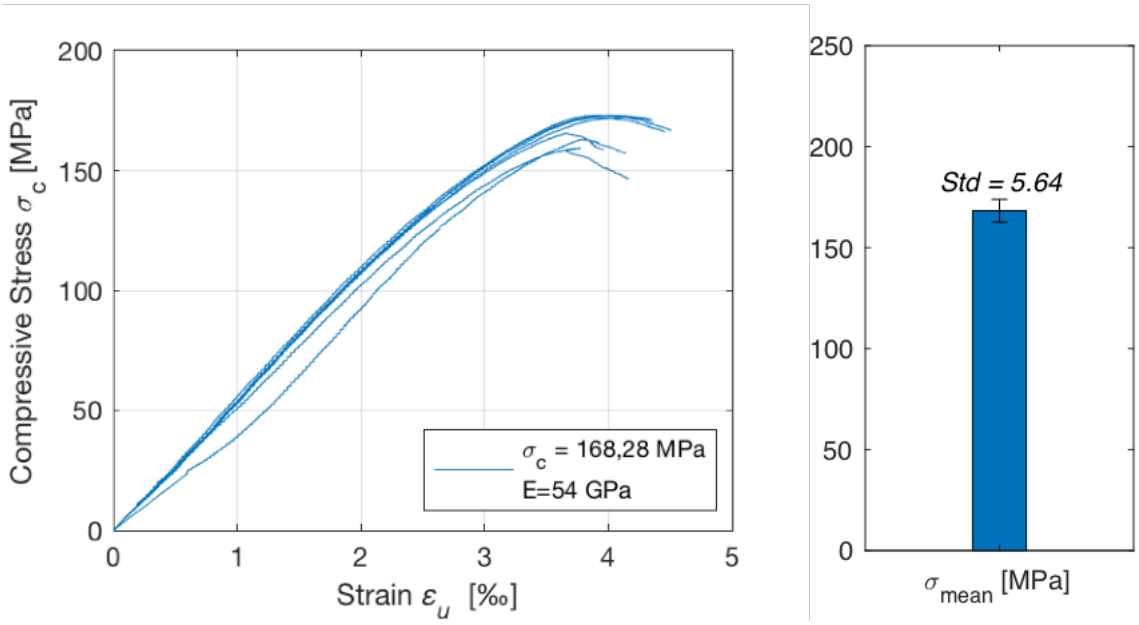

Figure 3.2-1 *Stress-strain relation for all specimens (left) ; Mean strength and standard deviation (right)*

It is worth noting that the specimens are chosen from five different batches. Generally, experimental tests on concrete are performed on specimens of the same batch. In fatigue research, a large number of specimens is required due to different stress levels and large data scatter. However if the number of specimens is large, differences can also be present after the grout mixing between the first and the last specimen poured. For this reason, and due to limited number of molds, the choice is led to use different batches. Nevertheless, a strict mix protocol was followed in order to minimize the differences between each batch. In fatigue tests, specimens from the same batches as in quasi-static are used.

It can be seen from quasi-static tests here that the standard deviation is of ± 5,64 MPa. For a high-strength grout with a quasi-static strength at 168 MPa, this scatter is acceptable. Prior tests carried out in fatigue from different batches and within the same batch did not show significant differences in terms of standard deviation. Therefore, five different batches are used for the experimental tests shown hereafter.

The quasi-static tests are carried out in a displacement controlled mode at 0,003 mm/s as explained in chapter 2. In chapter 1.4.2 from literature review, it was shown that cement-based materials are strain-rate dependent due to Stefan effect. The equivalent strain rate in the quasi-static tests conducted here is in the range of $\dot{\varepsilon} = 10^{-5}$ /s, while in compressive fatigue, as will be shown in next section, strain rates are much higher and reach values up to $\dot{\varepsilon} = 10^{-2}$ /s. Therefore, a strength increase due to dynamic effects can be expected. This increase according to CEB-FIP 2010 [46] is expressed as :

$$\frac{f_d}{f_{cm}} = \left(\frac{\dot{\varepsilon}}{\dot{\varepsilon}_{c0}}\right)^{0,014} \quad (3.1)$$

Or,

$$\frac{f_d}{f_{cm}} = \left(\frac{\dot{\sigma}}{\dot{\sigma}_{c0}}\right)^{0,014} \quad (3.2)$$

where, $\dot{\varepsilon}_{c0}$ is the rate during compressive quasi-static tests and f_{cm} the corresponding strength. f_d is the dynamic compressive strength measured at the $\dot{\varepsilon}_{c0}$ strain rate. The strain rate expressed as $\dot{\varepsilon}_c$ corresponds to the strain rate applied during fatigue loading. The same statements are valid for equation 3.2, where the increase of strength is given in terms of stress rates.

Therefore, an increase up to 10% of the compressive strength can be expected from calculations shown in equation 3.1. Attempts were made to determine this level of increase experimentally. However, the margin between the measured strength and the capacity of the testing machine is limited at approximately 5%. Thus, two specimens tested at a strain rate equivalent to fatigue loading at 10 Hz, did not fail and exceeded the machine capacity. Therefore, it can be admitted that an increase takes place and it is higher than 5%.

3.3 Compressive fatigue behavior

The compressive fatigue behavior of the reference grout is thoroughly analyzed in this part. Firstly, the number of cycles to failure are given at different stress levels and two loading frequencies. The effect of loading frequency is given not only in terms of fatigue life but also as a factor of influence on deterioration mechanisms. Different damage indicators such as the strain development, secant modulus evolution and energy dissipation are considered for this purpose. Whereas, the number of cycles to failure are fitted to the Weibull distribution in order to characterize the probability of failure and establish an estimation of the fatigue life. Other methods based on experimental data are also used for this scope. Therefore, the fatigue life is also described in terms of strain evolution, measurements based on temperature increase and finally a predictive model is developed based on the creep behavior related to fatigue.

3.3.1 Estimation of number of cycles to failure

The number of cycles to failure are recorded for different stress levels and expressed in a Wöhler curve, commonly used in fatigue of materials. As it was previously mentioned, the only guideline for fatigue in grout is given by DNV [1], and the current fatigue lives

are systematically confronted to. The coefficient C_1 is defined at 12, according to recommendations for tests in air conditions (see equation 1.5). All data will be also compared to CEB-FIP [46] as shown in figure 3.3-1.

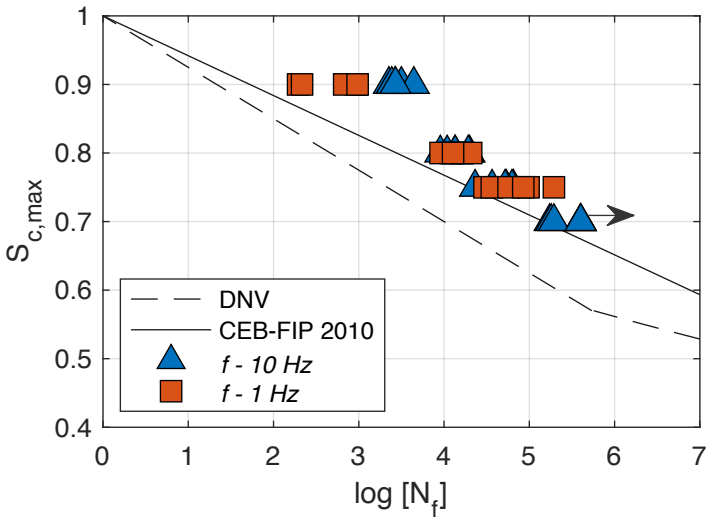

Figure 3.3-1 *Number of cycles to failure for the reference grout for different maximum stress levels at two loading frequencies*

As expected, higher number of cycles to failure are attained for lower stress levels. Indeed, due to a higher maximum force applied, more damage is generated within the material leading to a faster damage accumulation and to earlier failure. The compressive tests are shown for $S_{c,max} = 0{,}90$, $0{,}80$, $0{,}75$ and $0{,}70$. Three specimens at $S_{c,max} = 0{,}70$ did not fail at 4×10^6 cycles and are plotted with an arrow. They will also be considered as "run-outs". Due to laboratory time restrictions, the specimens could not be tested further. However, when the tests were stopped, the specimens did not show any significant ongoing deterioration. This will be demonstrated in section 3.3.5. The run-out specimens are not considered for the linear regressions (which will be displayed graphically in section 3.3.2). Therefore at $S_{c,max} = 0{,}70$ only three specimens are included for this purpose. The linear regression giving the relation between the number of cycles to failure and the stress level applied for both loading frequencies is obtained as follows:

$$S_{c,max} = -0{,}11 \, log \, N_f + 1{,}27 \qquad (f = 10 \text{ Hz}) \qquad (3.3)$$

$$S_{c,max} = -0{,}07 \, log \, N_f + 1{,}07 \qquad (f = 1 \text{ Hz}) \qquad (3.4)$$

These equations allow to give an estimation of the fatigue life and identify the material parameter β as given in the Aas-Jakobsen equation 1.2.

From observations in figure 3.3-1, it can be noticed that the fatigue life at lower stress levels than $S_{c,max} = 0{,}75$ does not accurately follow the regression curve obtained at high stress levels. Indeed, at $S_{c,max} = 0{,}70$, three specimens did not fail and therefore if they are taken into account, the mean number of cycles would be shown as shifted in the figure. A second curve with a smaller slope is to be expected for lower stress levels. Indeed the two standards, recommend this change at approximately log (N_f) = 5.5 and 8, for DNV and CEB-FIP respectively. Very few arguments are given in the literature, in order to explain this change in behaviour, where a much longer fatigue life is obtained after a certain threshold and whether this threshold is variable between different mixes. In the compressive tests carried out in section 3.2, the elastic limit $\alpha_{c,el}$ is determined at 71 %. Therefore, when fatigue tests with a higher maximum stress level than 70% are carried out, plasticity is created very rapidly within the material with a dense microcracking from the first cycles. The damage level is higher and the evolution faster, leading to earlier specimen failure. At stress levels below the elastic limit, the repeating loads do not create deterioration as rapidly. Slower evolution of the damage is manifested by the creation of micro-plasticity zones and when they are intensified, coalescence of micro-cracks takes place. Therefore, the deterioration occurs mostly in an evolution process, whereas at higher stress levels damage is created from within the first cycles.

All data respect both standards and are closer to the CEB-FIP curve. The fatigue life estimation given from the DNV guidelines, seem to underestimate the fatigue life of high-strength grout. These results also show that the grout can be comparable to fatigue in concrete.

The number of cycles to failure presented graphically in figure 3.3-1 show some scatter. The individual values can be found in table A-1 appendix A and figure 3.3-2 in the form of mean values with bar errors. Overall, the scatter seems to be less large than many results reported in the literature review. A particular attention was given before the tests, to a good centering of the specimen. Indeed eccentricity can have a high impact on the mechanical strength in quasi-static or fatigue tests. Moreover, the same operator prepared all the batches in the reference mix and carried out all tests. The present data scatter is of course related to the inevitable heterogenous nature of the material, which is nevertheless lower in grout than in normal-strength concrete (lower aggregate size [7]).

This heterogeneity is manifested in an initial scatter during quasi-static tests. However, in order to determine the stress levels to be applied in fatigue, only the mean value is taken into account in the calculations. As an example, the quasi-static measurements showed a standard deviation of approximately 5 MPa for a mean compressive strength of 168 MPa. Therefore, by supposing that the strength of a specimen tested in fatigue will be comprised within the standard deviation previously measured, it can be expected to obtain specimens with a strength of 160 MPa, which is the minimum value obtained

during quasi-static tests. However, this presumed specimen is tested at stress levels based on the 168 MPa value. The actual equivalent stress level at $S_{c,max} = 0{,}75$ would be approximately 0,77 and thus an earlier failure is to be expected. Even if the difference seems small at first, the relation between stresses applied and the number of cycles is logarithmic in nature, as presented in figure 3.3-2. Therefore the impact on the number of cycles is higher and the scatter is inevitable. Nevertheless, improvement of test conditions showed a good improvement of the data distribution. Figure 3.3-2 demonstrates as error bars in y-axis, the minimum and maximum stress levels to be expected, calculated from the minimum and maximum strengths obtained in quasi-static tests. A variation of 2% in the maximum stress level applied takes place. The error bars given in the x-axis, are the experimentally obtained minimum and maximum number of cycles to failure for the loading frequency $f = 10$Hz.

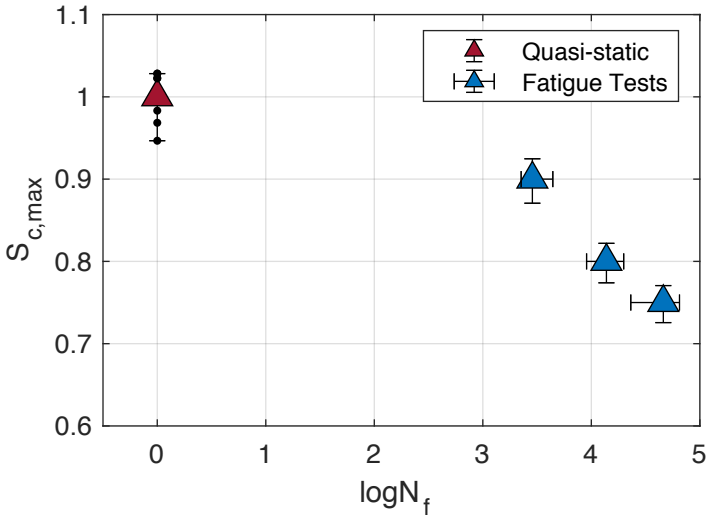

Figure 3.3-2 *Mean quasi-static strength with minimum and maximum values ; mean fatigue life plotted with error bars with minimum and maximum number of cycles to failure and the estimated stress levels applied error*

In order to understand the fatigue behavior of grout, the number of cycles to failure is not a sufficient parameter, due to the scatter presented and also the lack of information in the evolution process. Therefore, information from strain measurements is necessary for the comprehension of the deterioration mechanisms as will be presented in part 3.3.3.

3.3.2 Influence of loading frequency

From literature review it was shown that low frequencies typically lead to lower number of cycles to failure. In general, this seems true for concrete and grout despite the strength, mainly in flexural tests, but also in a few compressive fatigue tests. However, when the influence of frequency is experimentally studied, many authors tend to carry out tests at

many loading frequencies, but at only one stress level, mainly a high one. This analysis is legitimate under the hypothesis that when tested at different stress levels, the specimen will show the same behavior. Nevertheless, we also demonstrated from literature review, that conflicting results have shown a different behavior depending on the stress level applied. Indeed, the difference in number of cycles to failure between two loading frequencies can be reduced and resulting in a similar fatigue life. Moreover, in some cases even a higher fatigue life can be expected for higher frequencies (see section 1.4.3.4 for references). Finally, many studies are carried out on normal strength concrete and the data available on higher strength concrete and grout is rather limited.

In order to assess the effect of loading frequency on the fatigue life and damage process, tests are performed at two loading frequencies, for three different stress levels. The mean number of cycles to failure for each loading frequency, with the corresponding regression lines are given in figure 3.3-3.

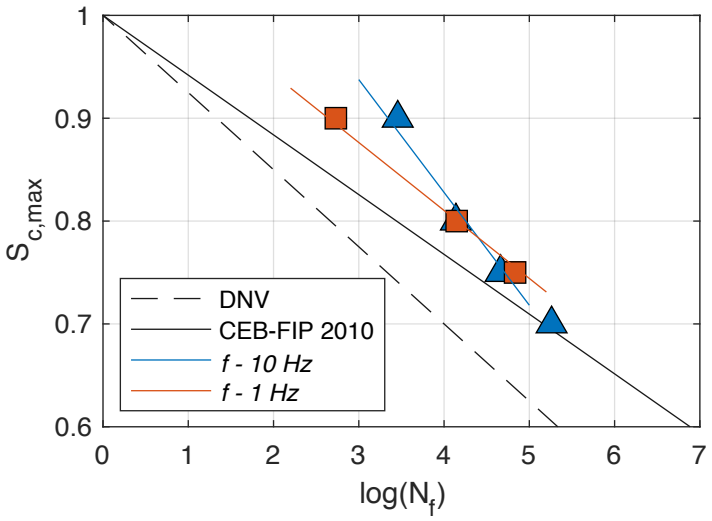

Figure 3.3-3 *Mean number of cycles to failure at two loading frequencies and respective regression lines*

At $S_{c,max} = 0{,}90$ a higher fatigue life is obtained for higher frequency, confirming most of the statements in concrete fatigue. However, at $S_{c,max} = 0{,}80$ the disparity fades and a slightly higher fatigue life is obtained at 1Hz. Finally, at $S_{c,max} = 0{,}75$ a higher fatigue life is achieved at $f = 1$ Hz. These results are in accordance with the fatigue compressive tests reported from Elsmeier [65], Hümme [97] and Hohberg [152]. Very recently in [102] similar results were found, nonetheless only three specimens or less for a stress level were used. No other reports are found in the literature describing this change in behavior, except partially in [98] between 5 Hz and 10 Hz. In [65,97] it is explained that the reason for this behavior could be due to temperature increase within the specimens, which reduces the fatigue life at $f = 10$ Hz and the evaporation of water due to the temperature

increase, creating a high water pressure. This detrimental effect of the temperature increase has also been noticed in other materials, as shown in [153,154]. It is noted that two effects are in competition at higher frequencies : the strength increase due to viscous phenomena and the increased temperature inducing a strength decrease.

Based on these literature discussions in relation to strength increase, the following remarks can be pointed out :

⇒ The cement matrix has a viscous nature, and the increase in strength observed in dynamics is due to the presence of water in the nanopores of cement paste (see sections 1.4.2 and 3.2). This dynamic effect has commonly been accepted to be valid in fatigue.

⇒ However, fatigue loading is a much more complex phenomenon. Many authors have shown that the presence of water or moisture content decreases fatigue life. Therefore, there seems to be a contradiction regarding these phenomena that has not been fully discussed and understood in the literature. The following part attempts to clarify the role of water in the mix during fatigue.

In [152] the changing point is estimated at $S_{c,max} = 0{,}75$ but no explanation is advanced for the differences in the fatigue life. The changing point for the high-strength grout tested here, seems to be around $S_{c,max} = 0{,}80$.

Affected strength and stiffness

Before synthetizing the final mechanisms, in relation to different number of cycles for different stress levels at two different loading frequencies, it is firstly presented to what extent the strength and stiffness are affected by this loading type.

Standards suggest to take into account the stress rate effect, with a linear relation given between the stress rates applied and the frequency of loading as shown in equation 3.5.

$$\dot{\sigma}_D = 2f\,\Delta\sigma \tag{3.5}$$

where $\Delta\sigma$ is the difference between the maximum and minimum stress level.

By including this equation to 3.2, previously presented, an increase in dynamic strength f_d is obtained as follows:

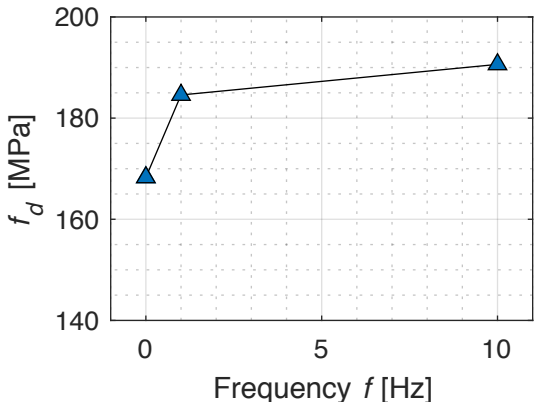

Figure 3.3-4 *Calculated strength increase f_d at two loading frequencies*

From tests showed in figure 3.3-3, and regarding results from literature review, it is concluded that dynamic effects take place in high-strength grouts at high stress levels, and they lead to very high values of $\dot{\sigma}_D$ according to equation 3.5. However, not only the strength is affected by the high rates applied, but also the stiffness. This can be verified by comparing the stiffness between quasi-static and the beginning of fatigue tests. In the next figure, it is demonstrated that the stiffness measured during quasi-static tests is different compared to the stiffness at the first cycles during fatigue loading. Indeed an increase is observed at both loading frequencies, with a higher increase at $f = 10$Hz. The first cycles do not follow the quasi-static stress-strain curve and are distinguished by a higher slope.

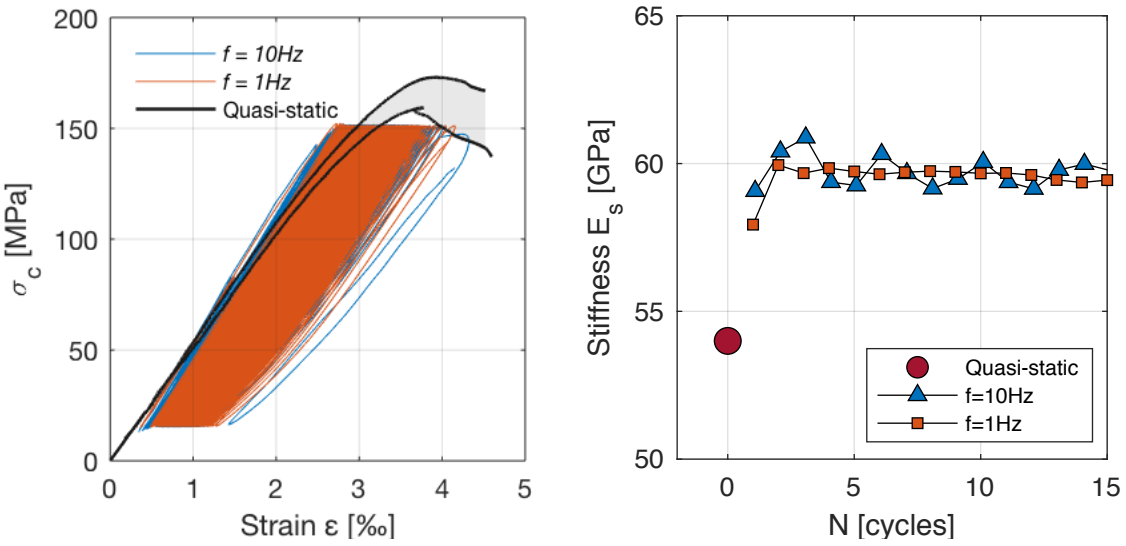

Figure 3.3-5 *Maximum and minimum stress-strain relation in quasi-static tests and examples in fatigue tests at two loading frequencies (left) ; Increase of stiffness within the first cycles for the curves shown in left figure (right)*

An increase of 9,4% takes place at $f = 10$ Hz in the first cycle and 7,3% at $f = 1$ Hz, compared to the Stiffness E_0 measured during quasi-static tests (figure 3.3-5 (right)).

Even higher values are reached at the second and third cycle. A more detailed analysis of stiffness evolution and the method used for the calculations will be described later in section 3.3.5.

Final discussion

High stress levels

Based on the present observations and literature review, there seems to be a contradiction regarding the presence of water at high loading frequencies, that has not been fully discussed and understood in the literature.

Hence, it was presented that the Stefan effect is exerted in the free water and is manifested by a strength increase, due to the delayed appearance of microcracks [25], resulting in an increase of stiffness. However, this effect is exerted only in the free water in the nanopores of the cement paste, and not in the capillary pores [93]. It has been demonstrated that the internal viscosity of the material is related only to the porosity of hydrates (here mainly C-S-H), and not the capillary pores. Therefore, it can be concluded that water in the cement paste has a "beneficial" effect at high loading frequencies, but high moisture content present in the capillary pores creates a detrimental effect.

Afterwards, when the cyclic loading is applied continuously for a longer period, similarly to creep behavior shown in section 1.4.1, the water from adsorbed layers can diffuse to the capillary pores, which creates deformation of the solid skeleton.

In addition, at high stress levels high local pressures are exerted onto the aggregates, conducting to the early appearance of microcracks at $f = 10$ Hz, therefore reducing the fatigue life. Overall, we demonstrated that stress rates at 1 Hz tend to be lower, thus the "beneficial" effect coming from viscous phenomena is less present at $S_{c,max} = 0{,}90$. Therefore, for a low frequency in compression earlier failure is expected at high stress levels.

Low stress levels

In lower stress levels the reduced fatigue life at 10 Hz is overlapped by the presence of very high temperature gradients. The temperature itself does not create the detrimental effect, but it induces physical changes in the microscale level (explained further in part 3.3.3) which leads to a shortening of fatigue life.

Finally, especially at lower stress levels, tests at 1 Hz last to a greater extent, leading to the drying of the specimen during the test. Even if the number of cycles to failure is the same, the time of test is 10 times longer at 1 Hz. Therefore, water diffusion facilitated by the microcracks during loading can help in the hydration of anhydrous cement

particles. This might cause a strengthening of the material and therefore the damage process would occur at a lower rate. It results in less moisture being present leading to an increased strength.

In conclusion, the frequency of loading in compression has an influence on fatigue life due to dynamic effects, creep effects and temperature gradients. A few test conditions can be modified in order to avoid or limit these effects. As an example, only tests at lower testing frequencies could be considered. Furthermore, flexural tests have been carried out, where the specimen is not subjected to temperature increase. This will be part of additional analysis in the last chapter.

Note*
From figure 3.3-3 it is noted that in both standards, including Eurocode 2, the regression in the S-N curve passes through the value 1 in the ordinate axis. Theoretically, this is correct as a result of the $S_{c,max}$ calculated based on the static strength. Nevertheless, in experiments the linear regression does not go through the value 1, which is reflected by supposedly low number of cycles to failure. This can be due to the scatter in quasi-static tests as shown in the previous part. However, another reason could be the stress rate effects leading to an increased strength when high loads are applied. Indeed, two experiments conducted at $S_{c,max} = 1$, did not immediately break and endured a few cycles before failure. Therefore, a revision of the standards is encouraged, where the behavior between $S_{c,max} = 0{,}90$ and 1 should not be considered linear, but polynomial in the semi-log scale.

According to [46], there is little information regarding the effect of high stress or strain rates on the shape of the stress-strain diagrams. The frequency has an effect not only in terms of fatigue life, but also is manifested by different damage mechanisms. For this reason and due to the lack of information in the damage process when considering only the number of cycles to failure, the strain evolution needs to be further analysed. These investigations will be presented in part 3.3.4, after discussing the temperature increase in the specimens during compressive fatigue loading, the mechanisms involved and the possible influence on the number of cycles to failure and the strain development.

3.3.3 Temperature Increase

In chapter 1.4.5 from literature review, it was reported a particular heating of the specimens tested in compression during fatigue loading. These levels of increase can reach very high values, which could be detrimental to the fatigue life and the damage process.

Therefore, judiciously the temperature evolution of all the specimens during the tests was recorded. For further analysis the temperature measured at the specimen's surface at mid-height will be used. In a few cases the temperature at the upper and lower part of the specimen close to the plates is also recorded. These measures can give information on the temperature gradient. However, in analysis only the temperature at mid-height is considered. An example of temperature evolutions measured by each thermocouple is presented in the following figure :

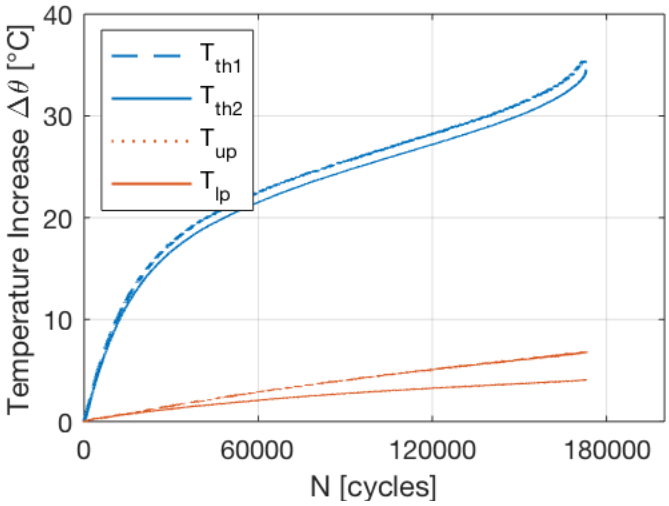

Figure 3.3-6 *Example of temperature evolution of the specimen and the machine plates*

In order to provide only the intrinsic temperature of the specimen, independently of the ambient temperature and the heating of plates during the tests, all following temperatures will be expressed by :

$$\Delta\theta\,[K] = \frac{T_{th1} + T_{th2}}{2} - \frac{T_{up} + T_{lp}}{2} \tag{3.6}$$

Therefore the temperature increase $\Delta\theta$ is given as the difference of the temperature measured in the mid-height of the specimen surface by the means of two thermocouples and the temperature of the plates. The temperature increase inside the specimen, was not recorded as this requires to place a thermocouple during the batches. Therefore, the presence of the thermocouple, even in very small dimensions, creates a flaw within the specimen and therefore might be a source for stress concentrations. Thus, the fatigue life but also the damage process could be altered.

3.3.3.1 Temperature levels at high loading frequency

High temperature levels were reached during tests at load frequency $f = 10$Hz. The temperature increase evolution for all the specimens at three stress levels is given in

figure 3.3-7. Temperature evolution for specimens at $S_{c,max} = 0{,}70$, are not shown due to longer number of cycles, resulting in a unclear representation in the figure. However, these evolutions can be found in appendix B-1.

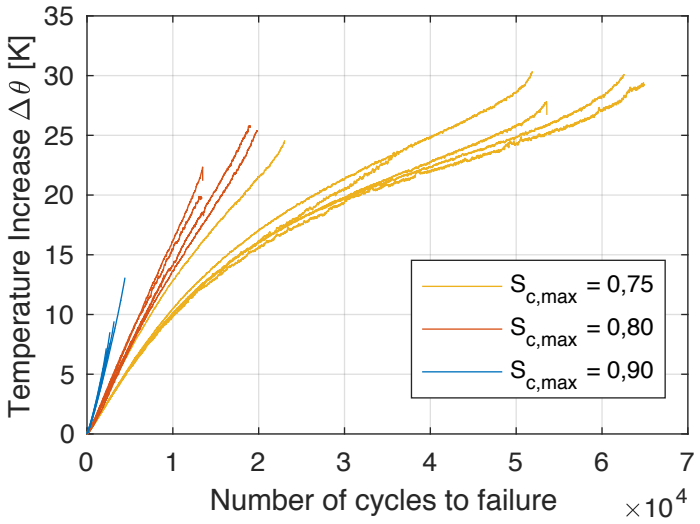

Figure 3.3-7 *Temperature increase with respect to number of cycles to failure at three stress levels (f = 10 Hz)*

As can be seen from this figure, for lower stress levels, higher temperature values are attained. At $S_{c,max} = 0{,}75$ the surface temperature at mid-height is up to $\Delta\theta = 30$ K. The warming of the specimen is also dependent on the duration of the test. Specimens that failed earlier within the same stress levels, had a lower temperature increase. Maximum mean values of temperatures obtained are approximately 28K, 21 K and 9K for $S_{c,max} =$ 0,75, 0,80 and 0,90 respectively. Despite the substantial level of increase in these tests, even higher values are reported in the literature. In [65] $\Delta\theta = 45$ K was reached for $S_{c,max}$ = 0,60 after approximately 59.000 cycles. For a similar fatigue life in the tests from figure 3.3-7, the temperature is recorded around 30K. However, in the reported values the maximum grain size used is 2 mm, whereas in these tests is 5 mm. It can be assumed that when smaller aggregates are used, higher warming levels can be expected. This is also confirmed in recent results in [102] for UHPC.

In [67] the temperature increased approximately to 20 K after 38000 cycles, whereas in our tests this level of temperature was reached after 14000 cycles. In this case the aggregate size is higher (16 mm), which explains the lower warming rate, but also the specimen size is different. A higher specimen length is used in both studies in the literature presented here, with H = 180 mm, instead of 120 mm in our tests for the same diameter length. Therefore, an influence of the specimen size could be pointed out, where for a higher specimen size, lower warming rates might be obtained. However, this is not conclusive and tests of different specimen sizes need to be carried out. Further in section 3.4, the influence of the specimen size on the temperature increase is analyzed.

It should also be reminded that the strength and mix composition is very different between the mixes from literature and the reference mix shown here. Different aggregates and different matrix composition lead to different thermal conductivities and specific heat capacities, therefore modifying the rate of heat exchange with the ambient temperature or machine plates. These parameters are not mentioned in the articles mentioned earlier and direct comparisons cannot be made. Moreover, the mix composition can also modify the intensity of heating sources depending on the mechanism involved. Finally, in [102] where also longer specimens are tested with a UHPC mix, 25K is reached for a fatigue life at approximately 20.000 cycles, which is in the same range of the values obtained in our tests. Thus, it appears that mixes with higher strengths might undergo higher temperatures, depending on the microstructure.

Therefore, this is another argumentation why this thesis will be also focused on the influence of microstructure on the fatigue behavior, by taking into account not only the number of cycles to failure, but also relating the fatigue life to other parameters including the temperature increase. This is subject of further analysis in chapter 4.

3.3.3.2 Comparison of temperature evolution at two loading frequencies

It was mentioned earlier that in tests at lower frequencies, temperature rises to a smaller amount. Indeed in figure 3.3-8, the temperature evolution at $S_{c,max} = 0{,}80$ for $f = 10$Hz and 1Hz is presented as an example. Comparisons of temperature evolution at other stress levels for both loading frequencies can be found in appendix B-2. On one side, the temperature increases almost linearly for a high frequency, up to the failure of the specimen. The mean maximum increase is approximately 21 K. The linear increase is observed for all tests at this stress level. On the other hand, at $f = 1$Hz a small increase takes place at the beginning of the test for approximately 2000 cycles. Afterwards, the temperature reaches a steady-state at 4 K and hardly increases with a very small slope. Only before failure during the last cycles, another rise to a small amount is manifested and reaches a mean maximum increase of approximately 4,5K.

Despite the fact that the temperature increases to a significantly inferior level for the smaller loading frequency, the rate of increase is higher. The image on the right of figure 3.3-8 shows a fraction of the fatigue life during the first cycles and can be clearly observed, that the temperature increases more rapidly. This rapid increase in the first cycles, can be due to the dynamic effects explained earlier, which induce a stiffening of the grout at a higher frequency. Whereas, at 1Hz this increase takes place to smaller extent. Thus, more damage is created at the beginning of the test (at 1Hz), thereby releasing more heat. An analysis of the dissipated energy will be conducted further.

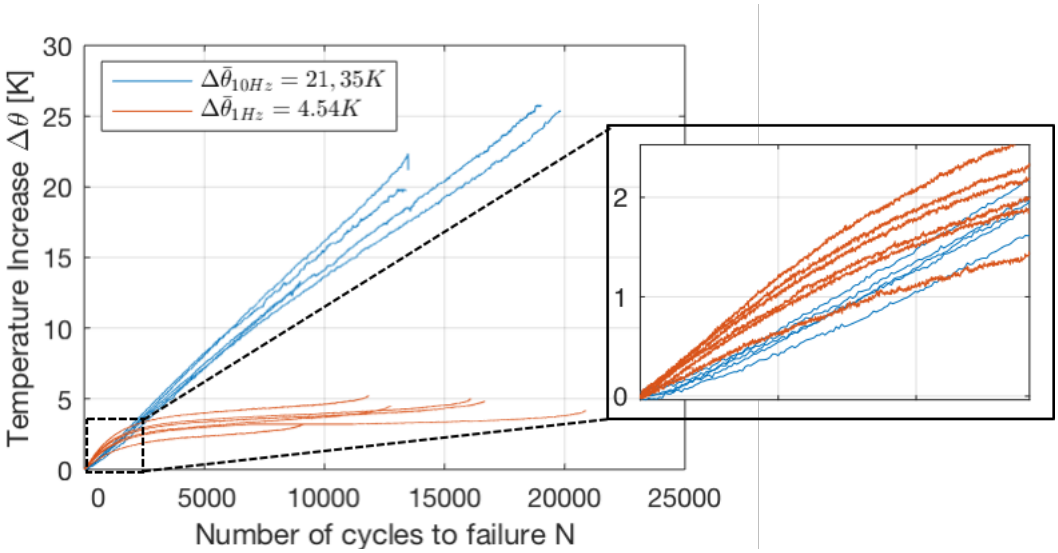

Figure 3.3-8 *Temperature evolution at two load frequencies for $S_{c,max}$ = 0,80*

In order to simplify the observation of the heating rate, the temperature curves have been derived with respect to the number of cycles, as shown in figure 3.3-9. In addition, only two curves are chosen to allow a better distinction. The curves in this figure manifest a fatigue life close to the mean value. Due to some noise in the signal, these curves are averaged by using the Savitsky-Golay method.

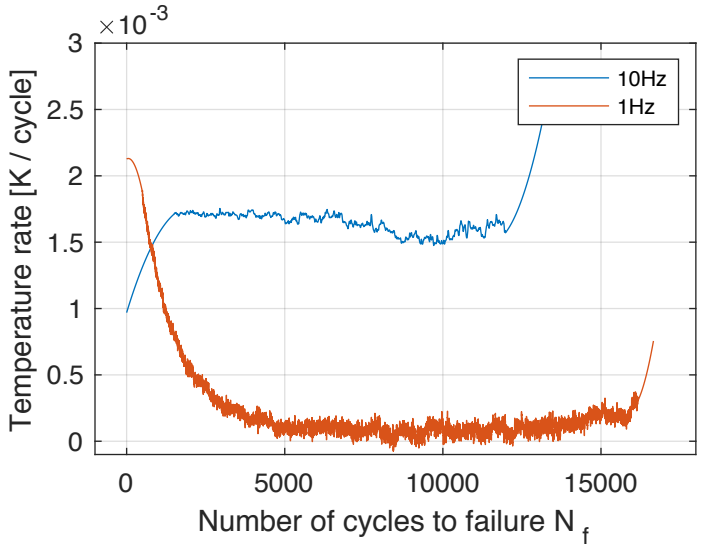

Figure 3.3-9 *Heating rates for two load frequencies at $S_{c,max}$ = 0,80*

This figure shows a heating rate two times higher for the low frequency, at the beginning of the test. Subsequently, the rate decreases close to zero, which means that no evolution is present within the material. Finally, an increase is observed when approaching failure. At a higher frequency, the temperature rate continued to evolve and only decreases to a much smaller amount, meaning that the heating is continuously increasing.

Overall, higher temperature rates are observed at higher stress levels. In figure 3.3-7 it can be observed that the temperature increases more rapidly at $S_{c,max} = 0{,}90$ compared to the other stress levels. In this stress level, higher damage is generated during fatigue loading. Therefore, an hypothesis can be emitted that the heating is the result of two mechanisms, generation and friction of microcracks. The next paragraph explains the origin of this hypothesis, and the tests carried out for its verification.

3.3.3.3 Origin of the heating process

Firstly, when the loading is applied on the specimen, the energy is dissipated in the form of damage and heating (see equation 1.6) and at high stress levels, an increased level of both heating and damage is generated. The same observation is noticed for both loading frequencies. Moreover, the microcracks already present in the grout due to autogenous shrinkage and the microcracks created during the first phase, which can be within the matrix or the aggregate-matrix interface, continue to propagate. During the loading-unloading process, friction is present in crack interfaces. In figure 3.3-10 (b) is schematically presented that during loading, crack opening takes place which further closes due to unloading. Therefore due to continuous loading-unloading the friction between the crack interfaces generates heating. Due to a more dense level of microcracking at high stress levels, more friction is produced and therefore higher temperatures are reached. This is in accordance with the higher temperature rates observed for higher stress levels. Finally in a micro-scale level, when compressive forces are transmitted to the aggregate, tension forces are generated in the transverse direction, thereby creating shear forces in the interface (figure 3.3-10 (c)). The presence of shear forces can be another heating source within the specimen, which also explains the higher temperature increase reached for mixes with smaller aggregate size as observed in the literature. The use of smaller aggregates, conducts to less microcracks in the ITZ area, as we showed from literature review in [7]. However, more numerous grains are present and therefore a higher specific surface, where more shear forces are created and they generate more temperature.

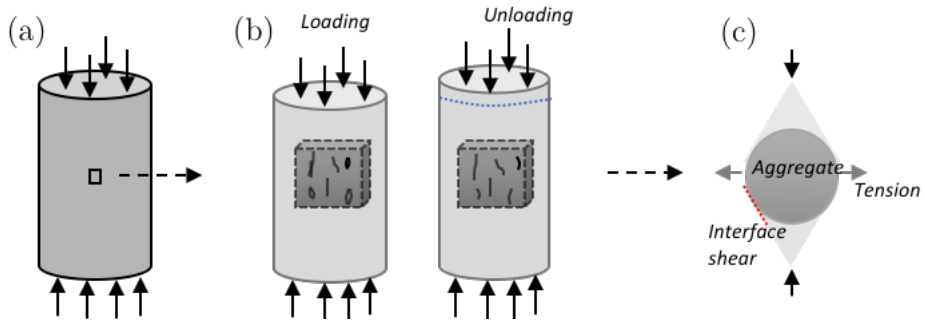

Figure 3.3-10 *Possible heating sources during fatigue in compression ; friction between crack interfaces (b) ; shear forces in the ITZ (c)*

The hypothesis that the specimen warming originates from friction between the microcracks has been advanced in the research articles listed previously. However, no tests have been found in order to verify this assumption. Thus, a simple test is conceptualized for this purpose. It is based on the idea that a denser microcrack state within a specimen leads to a higher temperature increase than an intact specimen.

Therefore the test presented here consists in generating cracks throughout the specimen and observe at the specimen's surface if the heating in a cracked specimen, "pre-damaged", is higher than the "intact specimen".

⇒ The "pre-damaged" specimens were firstly loaded under compressive fatigue during 5000 cycles at σ_{max} = 110MPa with a stress ratio R = 0,1 (see figure 3.3-11 (a)). This stress level applied for 5000 cycles, which normally consists in the completion of phase I in traditional fatigue tests, is sufficient to generate micro-cracks within the specimen. The specimen warming was measured with thermocouples. After this first loading step and when the temperature decreased to ambient temperature, the same specimens were loaded in fatigue with a maximum stress σ_{max} = 60MPa and a stress ratio R = 0,1 during 60000 cycles. Thus, the micro-cracks were generated by a high stress level fatigue loading and afterwards the specimen is loaded under a lower stress level, where the temperature evolution is measured.

⇒ The next type of specimen called "intact specimen" was directly loaded in fatigue at a maximum stress σ_{max} = 60MPa during 60000 cycles. The temperature measurements, are made on 5 specimens for each loading type and the comparison is carried out for the loading under 60MPa.

The figure 3.3-11 (b) demonstrates that higher temperatures are reached for the pre-damaged specimens. This tendency is clearly observed, in spite of two specimens that overlap. The maximum stress applied in the tests (60 MPa) is significantly lower than the elastic limit, which justifies the maximum temperature rise to a smaller extent than in previous tests and the temperature stabilization after a certain amount of cycles. The heating observed in the intact specimens, is mainly due to the friction of microcracks already existing within the material before the loading such as cracking due to shrinkage or drying. The pre-damaged specimens have an preliminary more intense microcracking. Therefore, the heating increases much more rapidly and stabilizes to a higher value than the intact specimens.

It can be concluded from this test, that in a specimen with a more dense state of microcracking, more heating is released during fatigue loading due to friction within the microcrack interface.

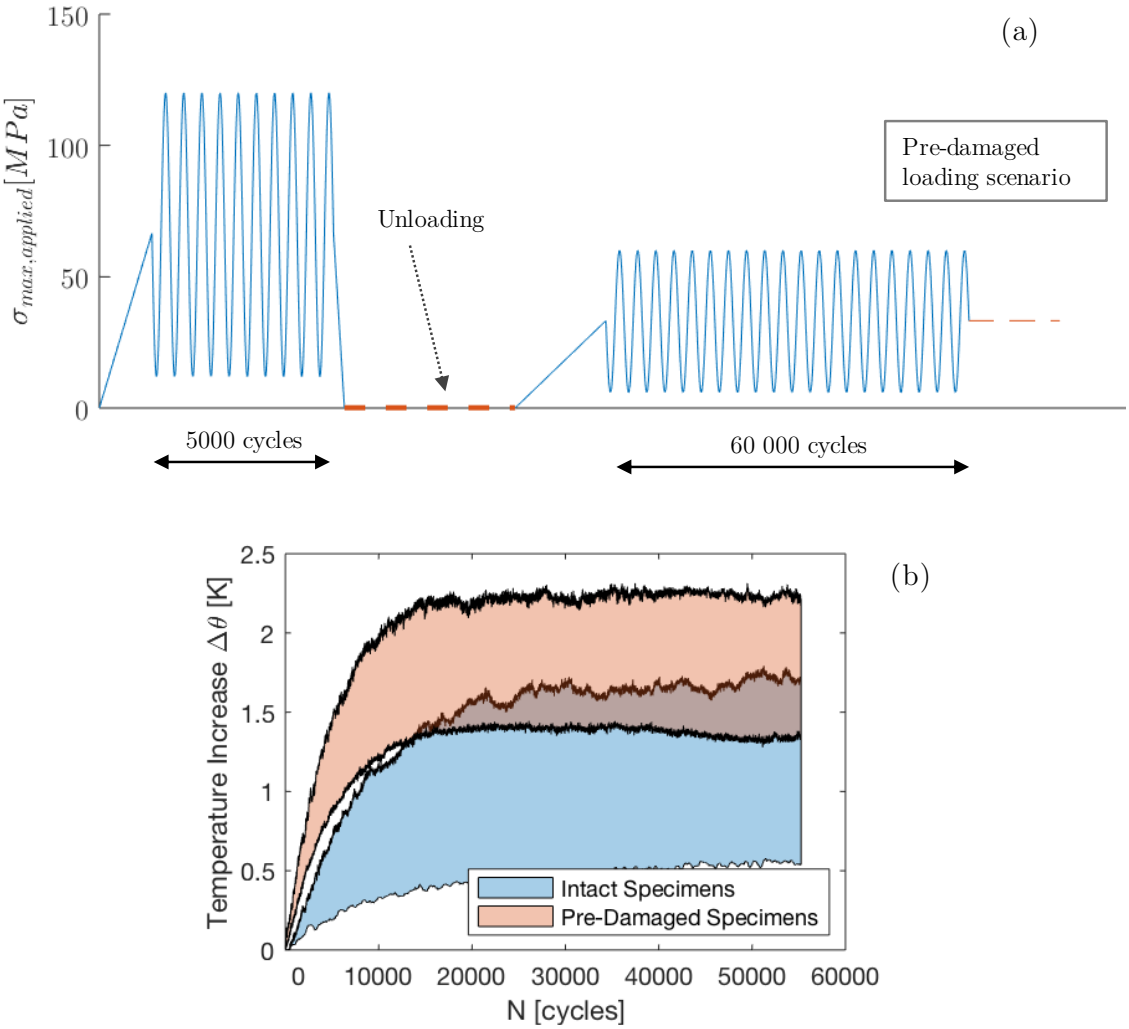

Figure 3.3-11 *Loading scenario in the case of pre-damaged specimens (a) ; Range of temperature increase with minimum and maximum evolution for intact and pre-damaged specimens (b)*

3.3.3.4 Description of damage-induced mechanisms due to temperature increase

This chapter demonstrated very high temperature levels attained during compressive fatigue loading at higher frequencies and the origin seems to be mainly the friction between microcracks and the aggregate-matrix. It was also demonstrated that shorter fatigue life is obtained at 10Hz for a lower stress level and the temperature increase is a factor of influence for the life shortening, among others. Therefore, it is important to determine the nature of the damage that is induced by the temperature on a microscopic scale and the mechanisms which take place in modifying the behaviour of the grout.

The surface temperatures measured reached values up to 55°C. In the core of the specimen even higher values are expected (up to 60°C or higher). Indeed, the temperature inside the specimen was intentionally not measured, due to local damage that could create the placement of a thermocouple. In [65] the temperature within the core and surface of the specimen was measured. It was reported that when the specimen reached 65,9°C in the surface at mid-height, a temperature of 81,6°C was recorded in the core.

Based on these values of temperature rise, it was firstly considered that changes of *chemical origin* could take place, i.e. phase changes in the cement paste could take place and therefore alter the strength of the material. When exposed to 60°C ettringite loses water molecules and therefore becomes unstable [155]. Other authors [156] define the decomposition of the ettringite at 80°C or even at higher temperatures than 100°C [157]. However, the decomposition goes through different phases by losing the water molecules continuously at different temperatures up to total decomposition.

Therefore, the XRD technique was used on the cement matrix of a specimen in the intact state and compared to specimen which submitted fatigue loading. A powder sample was extracted after grinding the grout and using a fine sieve in order to avoid the presence of aggregates. However, small grains could still be present in the powder due to the usage of grains under 200 microns in the mix. Subsequently, a sample which was submitted to fatigue loading and had reached a surface temperature of approximately 54°C was also tested with the XRD. The sample was extracted close to the specimen core. The purpose of this analysis is mainly in order to observe if any phase change takes place which could modify the grout strength.

The results presented in figure 3.3-12, show that the curves from both specimens match almost perfectly. No phase changes take place at this level of temperature. Therefore the nature of the strength degradation, does not seem to have a chemical origin. It can be assumed that a phenomenon of a mechanical origin creates physical changes at the microscale level.

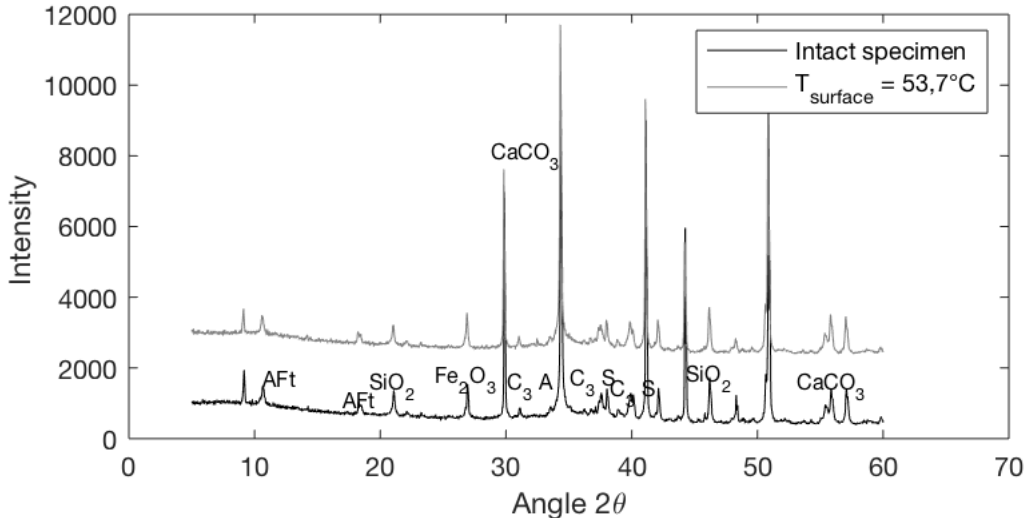

Figure 3.3-12 *XRD of two specimens in intact state and after fatigue loading at f = 10Hz*

The temperature levels reached during the tests at $f = 10$Hz do not create chemical alterations in the matrix at the hydrate scale. However at a micro-scale level, the temperature has an effect due to the presence of water within the grout. The water is present under four forms : free water, capillary water, adsorbed and chemically bound water. The latter has been consumed during the hydration of cement and is combined with other components in the hydrates [156]. It can be considered as non-evaporable and it is not influenced by the temperature increase in the range obtained during the tests. However, according to Noumowé [158], free water and a part of the adsorbed water evacuate from the high-performance concrete in the range of 30°C to 105°C. The capillary water fills the porous volume beyond the adsorbed layer and is separated from the gas phase with a meniscus. While the free water, is not on the influence of the superficial forces and is in equilibrium with the gas phase by the means of a plane interface. Therefore the free water represents a particular case of the capillary water according to [156], and they are often confused in the literature.

Surface temperatures up to 55°C were reached and from literature comparisons, the temperature inside the specimen can rise up to 60°C and higher. Thus, a part of the capillary water is situated in the form of ***water vapor****, resulting in increased pressure* and generating residual stresses. These stresses induce local damage and therefore shorten the fatigue life at 10 Hz.

Moreover, thermal cracking can also take place due to ***different thermal expansions*** *between the aggregates and the matrix*. Indeed, a different chemical composition and different elastic properties lead to distinct coefficients of thermal expansions. In general this coefficient is higher for the cement paste than the aggregate, for temperatures up to 150°C according to [159]. Therefore, thermal stresses are present on the aggregate or the

matrix, which can cause microcracking. As reported by Hettema [160], in a spherical inclusion model, when $\alpha_m > \alpha_i$ the inclusion detaches from the cement paste when the radial stress exceeds the bond strength and therefore microcracking develops in the ITZ (see figure 3.3-13). If $\alpha_m < \alpha_i$ a tensile crack is initiated when the tangential stress is higher than the strength of the matrix, thus microcracks will be formed in the cement paste.

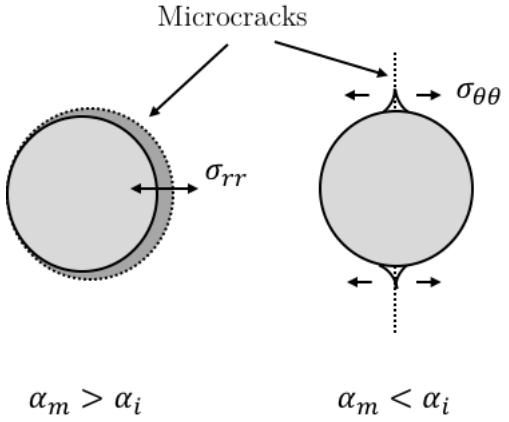

Figure 3.3-13 *Microcracking around an inclusion in the presence of a compressive thermal stress, reproduced from* [160]

Therefore, incompatibilities in the coefficients of thermal expansion lead to microcracking in the ITZ or cement matrix, which contributes to a fatigue life shortening.

Finally, heat exchange takes place with the surrounding air and the machine plates. At the specimen scale macroscopic temperature gradients are firstly observed by the means of an infrared camera. Figure 3.3-14 shows the temperature evolution along the height of the specimen. The length observed is 80 mm instead of the total height 120 mm and the displayed temperature is measured along the dotted line (c). The figure shows a temporal evolution at different stress levels applied (1 to 7) during the self-heating tests which will be explained later. Therefore this is not a traditional fatigue test as previously described under one stress level up to failure. However, it is sufficient to illustrate that the temperature distribution is not uniform in the material.

The stresses applied were much lower than the stress levels showed earlier, which explains the lower temperature values reached. Nevertheless, temperature gradients are obvious when comparing the evolution during the beginning of the test (dark red lines) and during the last stress levels applied (yellow line). The thermal images are also shown in figure 3.3-14 (b) and (c).

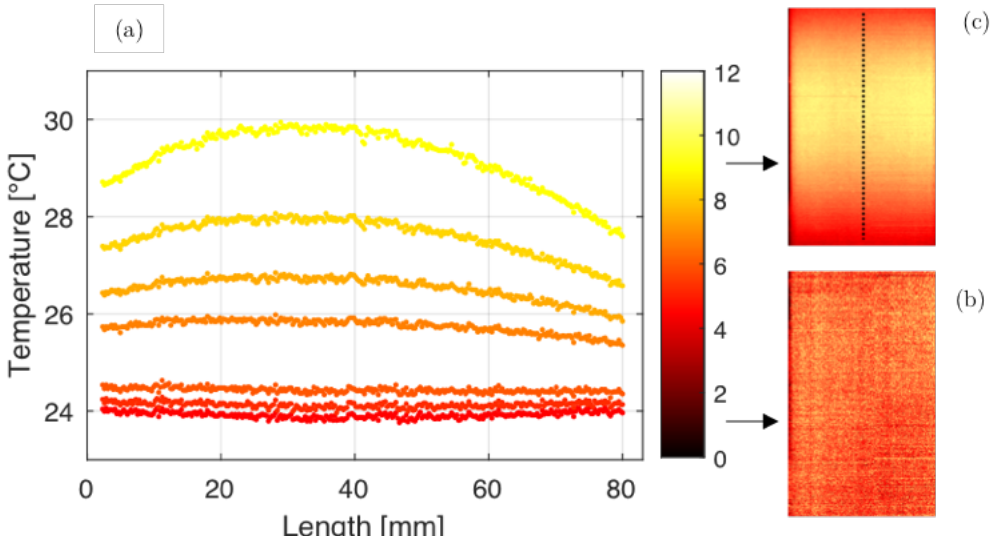

Figure 3.3-14 *Temperature gradients at different levels of fatigue life (a) ; Thermal image at the beginning of the test (b) ; Thermal image at the end of the test (c)*

The ***thermal gradients*** induce restrained differential strains and consequently compressive and tensile stresses within the specimen. Due to high gradients between the core and the surface area in addition to the local tensile stresses which could be larger than the tensile strength of the grout, cracking appears within the specimen. These gradients which do not occur under fatigue at low frequencies, may lead to a reduced fatigue life.

The cracking due to thermal gradients can also be associated with ***drying gradients***, due to the evaporation of a part of the capillary water. This leads to the appearance of microcracks at the surface. The total level of drying of the specimen should be lower at the end of tests at 1 Hz (no measurements of intrinsic HR are carried out), due to a longer testing time. However, the gradients are higher at tests carried out at $f = 10$Hz. Thus, it is the gradients and not the level of drying which causes the detrimental effect in fatigue life.

To summarize the effects explained in this section, the reduction of fatigue life at 10Hz for lower stress levels can be explained by an overlap of four elements : the increased water vapor pressure and the incompatibility of the coefficients of thermal expansion in a microscale level. Secondly at the specimen scale, the presence of thermal and drying gradients. It should be noted that these four factors, have a high influence on concrete or grout strength at high temperatures, as shown from the literature review cited during this section. Certainly their effects at temperatures lower than 100°C are lower. However a combination of these four eventualities, is considered sufficient to create additional damage during compressive fatigue loading and result in a fatigue life shortening.

3.3.4 Strain Evolution

The first sections of this chapter were focused on the analysis of the number of cycles to failure for the reference grout and factors influencing the fatigue life, such as the load frequency and the temperature increase observed during the tests. However, in order to provide a better understanding of the damage mechanisms, the number of cycles to failure is not a sufficient parameter. The strain and stiffness evolution is essential for a macroscale comprehension and produce a better understanding on how the behavior of the grout is modified during the fatigue process. Therefore all tests are analyzed for this purpose. This section includes an analysis of the strain evolution for each stress level applied, at two loading frequencies. Indeed, the previous sections demonstrated that the loading frequency has an effect on the number of cycles to failure. Accordingly, it is necessary to understand whether an influence takes place in terms of strain development. Moreover comparisons with strain behavior in quasi-static tests are also performed.

3.3.4.1 Strain development during compressive fatigue loading

All strain values presented henceforth are determined by computing the mean values measured by three laser distance sensors. Thus, if any lack of surface flatness still exists after the use of the grinding machine, the strain value is corrected by the employment of the three measuring lasers. In a few cases, in order to provide a more clear comparison between the tests, the number of cycles to failure can be normalized in relation to the last cycle to failure, expressed as N/N_f and commonly used in the literature. However, this way of presentation can alter the "real" evolution of the strain development. Therefore, most of the data will be expressed in terms of N_f. When presented as N/N_f it means that prior verifications have shown that no changes in behavior take place. Furthermore, all strains are expressed in [µm/mm] shown as [‰].

The data post-processing includes the definition of the strain peaks at maximum and minimum stress levels applied, which is commonly used in further analysis. Therefore, sufficient data points needs to be available for a good definition. In section 2.5.1.1 it was mentioned that the acquisition of displacements during fatigue loading is made continuously, in most cases at a frequency of 600 Hz for loading frequencies of $f = 10$ Hz. This acquisition frequency allows a good description of strain peaks at maximum and minimum stress levels with 60 data points for each cycle. Attempts at applying lower acquisition frequencies have also been made, in order to reduce the size of final data files. Indeed, for high number of cycles to failure the size could be large and require more time for the post-processing. However, attempts at an acquisition of 10 points for each cycle, as observed in some cases in the literature [49], have been made and they do not give a sufficiently good description of the strain evolution peaks. In figure 3.3-15 it is shown an example of data acquisition at 100 Hz (upper part) and at 600 Hz (lower part) for a

loading frequency of $f = 10$ Hz. The peak detection algorithm is applied in both cases shown in black circles on the figures on the left. From the figures on the right, it can be observed that strain peaks at 100 Hz do not show a good description of the evolution, which can alter the calculations carried out later. Thus, acquisitions at 60 points per cycle are necessary and are used throughout the thesis, despite the large data files in a some cases.

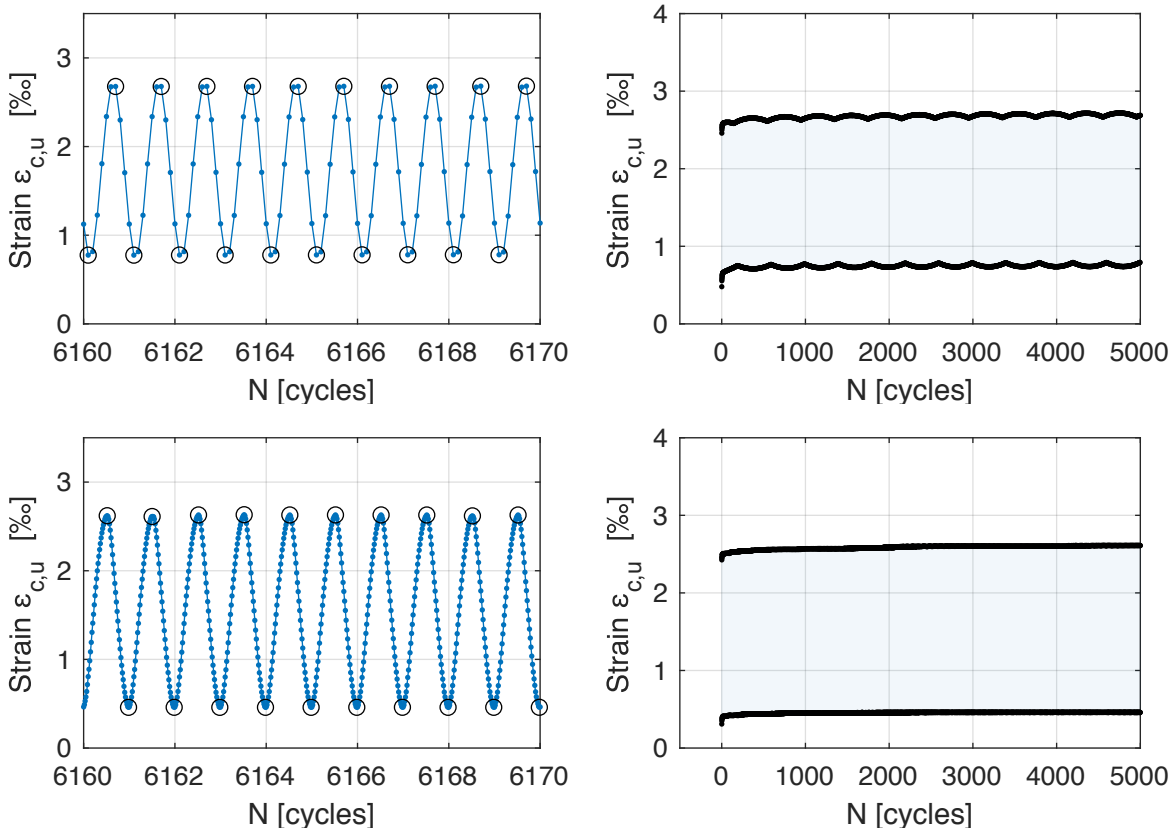

Figure 3.3-15 *Example of displacement acquisition at 100Hz (upper left) for a loading frequency of f = 10 Hz ; Corresponding strain evolution and peak detection at 100Hz (upper right) ; Example of displacement acquisition at 600Hz for a loading frequency of f = 10 Hz (lower left) ; Strain evolution and peak detection at 600Hz (lower right)*

The upper stress level applied in fatigue expressed at $S_{c,max}$ has a corresponding strain evolution expressed as $\varepsilon_{c,max}$, which is the maximum strain development and will be used for most of the analysis (see figure 3.3-16). Accordingly, the minimum stress level applied $S_{c,min}$ has a corresponding strain evolution expressed as $\varepsilon_{c,min}$. It is worth noting that overall, the compressive strains in mechanical annotations are expressed as negative values and tensile expansion as positive values. However, for simplicity reasons, all strains in compressive tests will be expressed as positive values throughout the manuscript.

A typical strain development monitored during the tests is shown in figure 3.3-16 . The curve shows the strain evolution for a fatigue test carried out at $S_{c,max} = 0{,}80$ for a load frequency of 10 Hz. The evolution manifests the three phase curve as mentioned in literature review during section 1.4.3.5. The first phase involves an accelerated increase of strain. It is followed by a second phase where the strain increase has a linear shape. Finally, the strains increase very rapidly leading the specimen to failure. The mechanical mechanisms behind these commonly observed phases are the creation of microcracks in the first phase, the stable propagation and finally coalesce leading to the development of a macrocrack.

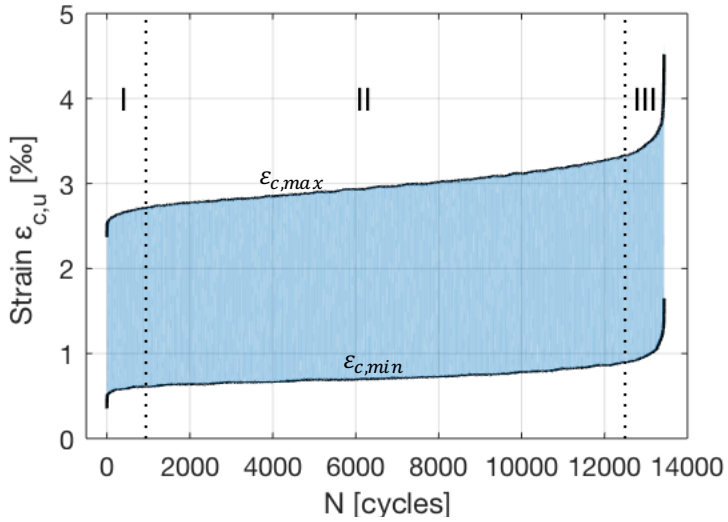

Figure 3.3-16 *Typical strain development at $S_{c,max} = 0{,}80$ with detected minimum and maximum peaks and the three stage damage mechanism*

Influence of the maximum stress level

This type of evolution is qualitatively similar for all tests which submitted failure. However, depending on the stress level applied, the course of the evolution can be distinct. A comparison of all curves within the same figure, makes the data very hard to distinguish. Therefore, median strain curves for each stress level are compared in the following figure. Despite the fact that some scatter also exists in the strain evolution, as observed for the number of cycles to failure, the median curves represent well the strain development occurring for each stress level.

It can be seen from figure 3.3-17 that all curves follow the inverse "S-shaped" evolution, nevertheless the curves are impacted by the maximum stress level applied. Firstly, at $S_{c,max} = 0{,}90$ the strain develops from higher values at the beginning of the test. This is partly due to the applied monotonic loading at a higher stress value before initiating the fatigue loading. Indeed, it was explained earlier that the procedure of a fatigue test consists in applying a quasi-static loading up to the mean value of the amplitude applied,

before the fatigue loading is initiated. Therefore, as the amplitude at $S_{c,max} = 0{,}90$ is higher than in the other stress levels, it implies the application of a monotonic loading to a higher level and as a result the strain evolution starts at a higher value.

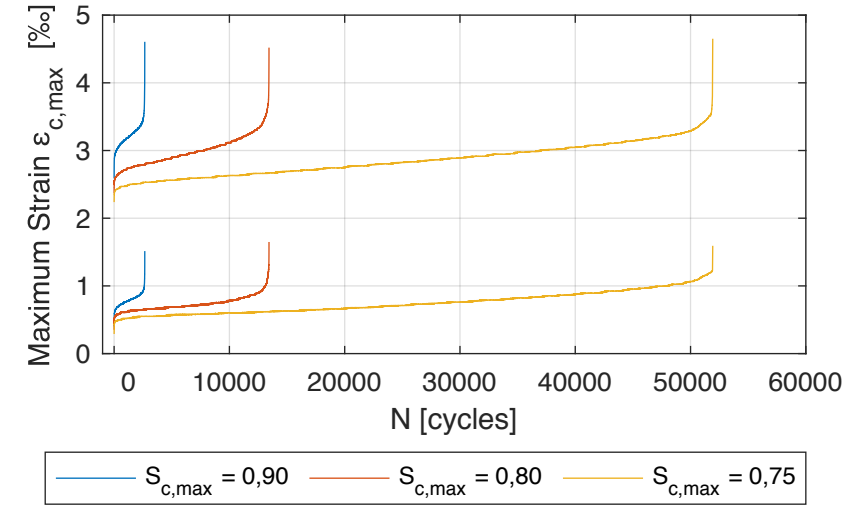

Figure 3.3-17 *Maximum and minimum strain evolutions at three stress levels*

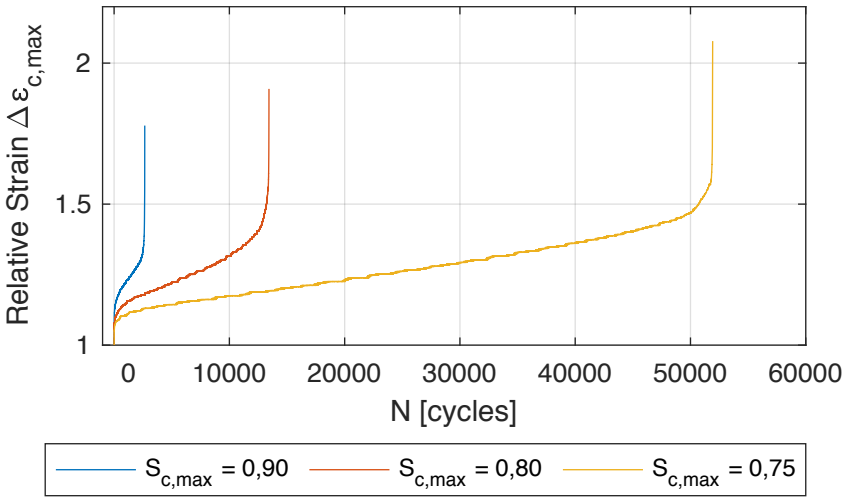

Figure 3.3-18 *Normalized maximum strain evolution at three stress levels*

Consequently, it is reasonable to give a normalization of the data in order to provide a better understanding on the final strain values reached at failure and isolate the strain evolution only due to fatigue loading. Therefore, after normalization in relation to the strain value in the first cycle of the fatigue loading, it is noticed in figure 3.3-18 that the specimens undergo more deformation with decreasing maximum stress level. The strain at failure ε_f at $S_{c,max} = 0{,}75$ has increased by a factor of 2,08 whereas at $S_{c,max} = 0{,}90$ the increase factor is 1,78.

Nonetheless, the rate of strain increase during the second phase is higher for a higher stress level applied. This phase consists in propagating the cracks formed in phase I or already existing within the specimen. As a result of a higher loading, the cracks are propagated more quickly and the coalescence is much faster. Thus, this also illustrates the reason of a lower increase in total strain during fatigue. In a further section (3.3.7.2), it will be demonstrated that a link can be given between the rate of crack propagation during the second phase and the number of cycles to failure.

Overall, these observations show a stress-dependent behavior of the grout. A cycle-dependent (or time-dependent) behavior is also observed during the compressive fatigue tests. Indeed, specimens submitted to the same stress levels, but reached higher number of cycles to failure, tend to reach higher strains at failure. Viscous deformations are produced in the cement matrix due to continuous loading applied (similarly to creep), thereby inducing increased strain development, when the loading is applied for a longer period.

The strains at the minimum stress levels $S_{c,min}$ also show a faster increase with increasing stress level. Even though the specimen is not entirely unloaded at this stress level (small stresses are applied at R = 0,1) it means that irreversible deformations have taken place within the specimen and increase more rapidly when a higher loading is applied.

Influence of the loading frequency

The strain development during compressive fatigue loading is also dependent on the loading frequency applied. Figure 3.3-19 displays a comparison of all tests carried out at both loading frequencies (10 Hz and 1 Hz) at the maximum stress level $S_{c,max} = 0{,}80$. The values of strain at failure are similar for both loading frequencies and this is due to almost identical number of cycles to failure. Therefore a cycle-dependent behavior seems to take place in this case, and regardless of the loading frequency applied, the strain at failure reaches similar values. Strain developments at other stress levels can be found in appendix B-3 and B-4.

However, it appears that in some specimens the crack propagation takes place at a higher rate per loading cycle in the case of loading frequency1Hz, despite similar number of cycles to failure. A first reason to explain this difference can be related to the strain rate effects being higher at 10Hz and thus creating a stiffening in the material. Therefore, it leads to a crack propagation developing at a lower rate. In addition, the lower loading rate during tests facilitates the movement of free water leading to more deformations of the solid skeleton. Nevertheless, it should be noted that the difference in the strain rate in the second phase, is not very significant.

Furthermore, the transition phase from I to II is harder to distinguish for tests at 1Hz (for further analysis on transition phases see next section). This indicates that a longer phase I may occur leading to a higher level of damage generated in the specimens. Therefore the higher strain rate at the low loading frequency, is influence also by a more dense level of damage created during the first phase. The strain development here seems to be in accordance with the explanation given in section 3.3.3.2 for the comparison of temperature increase between 10 Hz and 1 Hz, where within the first cycles a higher temperature increase was observed at $f = 1$ Hz.

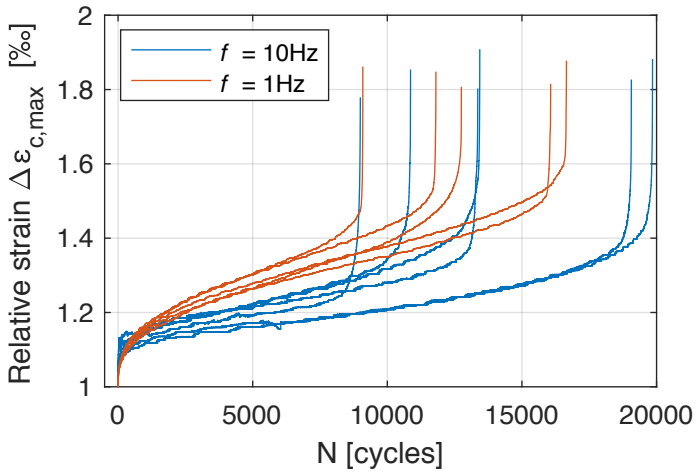

Figure 3.3-19 *Strain development for all compressive tests at $S_{c,max}$ = 0,80 and at two loading frequencies*

Finally, the third phase seems to be similar for tests carried out at both loading frequencies, despite different strain developments during the test. This phase is developed due to the unstable state of microcracks resulting in a localized crack and to failure of the specimen. A similar 3-phase strain development has been found in creep tests from different authors. Although in some research the presence of a tertiary creep has not been proven to take place, other authors indicate its presence at high stress levels, when exposing specimens to coupled basic and desiccation creep [161]. This supports the similar behavior manifested between fatigue and creep, mentioned earlier in chapter 1.

At other stress levels, the third phase develops differently depending on the frequency applied, as shown in appendix B. The strains at failure will be analyzed in more detail in section 3.4.3.3.

3.3.4.2 Transition phases

The level of transition phases from I – II and II – III, is generally considered independent of the stress level applied. In many cases, this analysis is neglected, nonetheless if

variations take place, it can be a relevant factor in a better explanation of the fatigue process.

During the first chapter, in table 1.2, a comparison of the transition phases was made between research articles from different authors and for different concrete strengths. The comparison showed a tendency, where in general the first and last phase seem to be for a higher strength concrete. The transition I-II overall takes place at 10%, however for a UHPC the transition level was estimated at 5%. No reports are found in the literature on whether the maximum stress level applied has an influence on the transition phases.

In order to allow an easier estimation, the strain curves are derived with respect to the number of cycles. Thus the strain rate per cycle can be obtained. Considering the linear increase of strain in phase II, a horizontal evolution close to zero is obtained. An example of the maximum strain evolution $\varepsilon_{c,max}$ during a compressive fatigue loading and the corresponding derived curve are shown in figure 3.3-20.

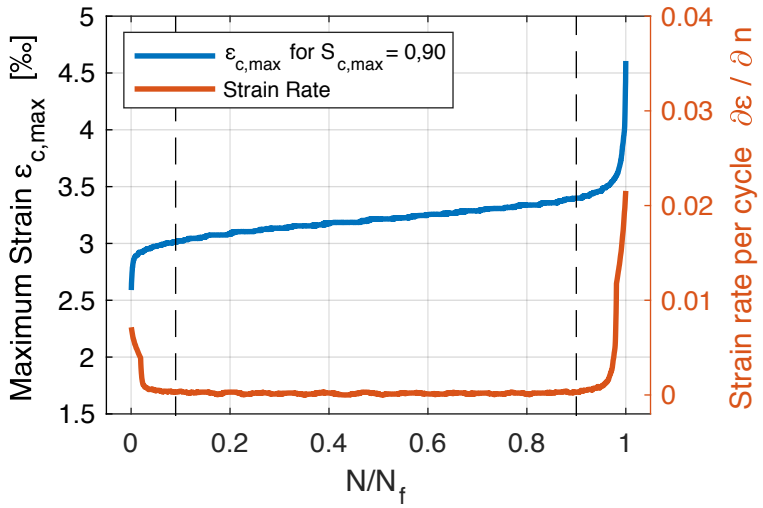

Figure 3.3-20 *Typical evolution of the maximum strain at $S_{c,max} = 0{,}90$ and the corresponding derived curve*

The inflection point is considered the level of the transition phase. The values of transition between phases I-II and II-III are determined individually for each test and the median curves are presented in figure 3.3-21.

In figure 3.3-21 (a) it can be noticed that the first transition phase occurs at a higher value for a higher stress level.

⇒ The first phase is linked to the creation of microcracks. Therefore at a higher stress level, more damage is created within the first cycles. The phase of

microcrack creation lasts longer than at $S_{c,max} = 0{,}75$ where the damage mechanism is essentially due to the propagation of microcracks.

Indeed, higher stresses cause more internal damage resulting in the transition phase at $S_{c,max} = 0{,}90$ estimated approximately at 9 - 10% of the fatigue life and at $S_{c,max} = 0{,}75$ it is estimated in the range of 3%. Another reason for this difference is due to more damage created during the quasi-static loading, applied before fatigue. As shown earlier, a monotonic force is applied up to the mean value between the stresses applied in fatigue and therefore it is higher for a higher stress level. These results seem to be different with the few reports available in the literature [53,96], where no relation between the stress level and the transition phases were found.

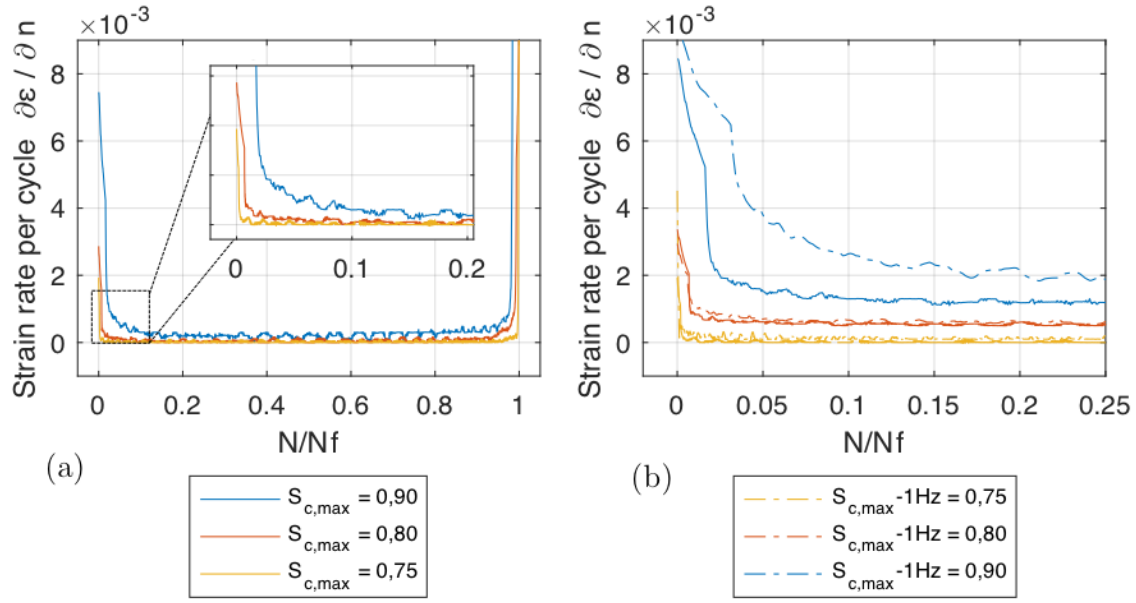

Figure 3.3-21 *Derived median strain curves at different stress levels (a) Derived strain curves at two loading frequencies with respect to normalized fatigue life up to 0,25 (b)*

The explanation given here, helps with the understanding of shorter transition phase I-II for a high performance concrete compared to normal strength, shown in table 1-2 and also observed by Kim in [77]. A higher strength concrete or grout has a better optimization of the particle packing and cement matrix, thus it has less initial flaws. Consequently, the phase of microcrack creation is shorter. This is confirmed for most of the data shown from literature research although some exceptions can be found. The data differing from these results can be due to different geometries of specimen or different loading conditions applied between researchers. More experimental testing between different strengths of concrete or grout under the same experimental conditions need to be carried out to confirm these discussions.

In figure 3.3-21 (b) a comparison of the strain rate evolution up to 25% of the fatigue life is given for a more clear observation, at three stress levels and at two loading frequencies. At $S_{c,max} = 0{,}90$, the difference between the values of transition phases for the two loading frequencies can be observed more clearly. A longer phase I is noticed for a low loading frequency. Indeed, as mentioned in 3.3.4.1 :

⇒ this may be linked to the stiffening of the grout at a higher frequency, which is accompanied by a smaller damage level at the beginning of the fatigue test. Whereas, at a low frequency the stiffening takes place to a smaller extent, thus resulting in more damage creation. This theory can be supported by the higher rates of temperature increase during the first cycles at $f = 1$Hz.

In figure 3.3-21 (b) the difference between the transition phases for lower stress levels $S_{c,max} = 0{,}75$ is of a lower amplitude than the observed difference in $S_{c,max} = 0{,}90$. It is possible that the cause is the stiffening occurring to a smaller extent at $S_{c,max} = 0{,}75$ than at $S_{c,max} = 0{,}90$.

In all tests, the strain rates at the second stage have a slow evolution close to zero, however for all stress levels the curves at 1Hz show higher level of strain rates. This will be analyzed further in section 3.3.7.2.

3.3.4.3 Strain at failure : Comparison quasi-static and fatigue

The third phase consists in an unstable crack growth and the strain at failure can be difficult to define. In the post-processing, the ε_f was defined as the following point recorded after the completion of the last hysteresis cycle. Thus, the strains at failure obtained for all fatigue tests in both loading frequencies are shown in figure 3.3-22 and are compared with the quasi-static curves. All strain development curves can be found in appendix B-3 and B-4.

A general tendency is observed at both loading frequencies : higher strains at failure are obtained after fatigue loading, when lower stress levels are applied.

At $S_{c,max} = 0{,}90$ and 0,80 comparable strains to failure are obtained between $f = 10$ Hz and 1Hz, despite obvious distinctions in the first and second evolution phase. Nevertheless, at $S_{c,max} = 0{,}75$ the strains at failure are particularly higher for the low frequency. This can be accorded to viscous strains developing in the specimen, due to a longer testing time. The difference between the time of test at higher stress levels is not as substantial as at $S_{c,max} = 0{,}75$. Therefore, the strains at failure are similar.

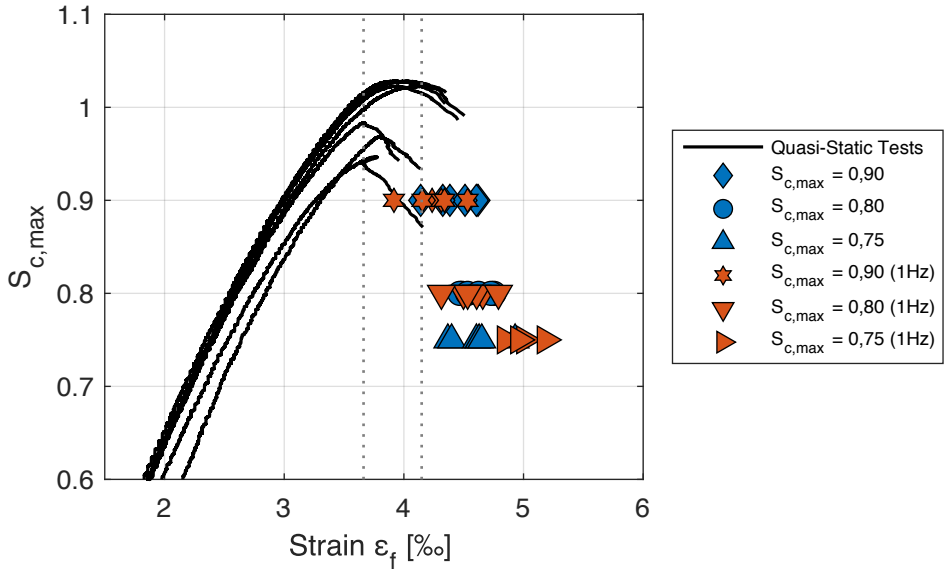

Figure 3.3-22 *Quasi-static tests and strains at failure in fatigue tests at both loading frequencies*

From literature review in section 1.4.3.5, it was shown that a few authors suggest that fatigue failure in concrete occurs when the hysteresis loops reach the negative branch of the envelope curve from quasi-static tests and have developed prediction models based on this assumption. This was disapproved by other research carried out on concrete more recently [67,96]. The compressive fatigue tests carried out on the reference high strength grout, showed that the grouted materials do not follow this assumption and despite an expected more brittle behaviour compared to concrete, strains to failure tend to be higher than the envelope curve.

3.3.5 Energy dissipation and stiffness evolution

So far, the analysis of fatigue damage was focused on the strain evolution in relation to time or fatigue life. The centre of attention in this section is the stress-strain relation, where it is attempted to evaluate the damage evolution in the grout, based on stiffness measurements.

When a specimen is submitted to external loads, damage occurs due to heterogenous local forces and creation of microcracking, therefore energy is released. The grout in the same way as concrete, is characterized by a viscoelastic behaviour, where when loading is applied, the strain increases and after unloading a part of strain is recovered but some residual deformation remains [162]. During this loading and unloading process hysteresis loops appear, due to different paths (see figure 3.3-23). As mentioned in section 1.4.4 the area of the hysteresis loops (equation 1.7) indicates the energy dissipation, which is

composed of the energy released in the form of heating (E_H) and energy due to damage (E_D).

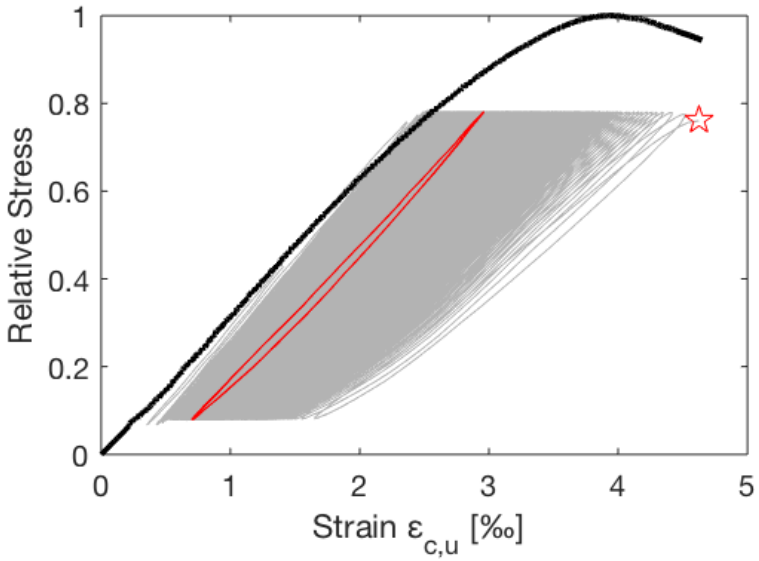

Figure 3.3-23 *Hysteretic behavior during fatigue loading and comparison with a quasi-static test*

Figure 3.3.23 demonstrates that permanent damage takes place with the evolution of fatigue process. Due to increased strain during fatigue tests and therefore damage increase, the energy dissipation should also increase. Therefore, a particular attention was given to the analysis of the hysteresis evolution in order to estimate the energy dissipation and the stiffness evolution.

Firstly, in order to estimate the evolution of energy dissipation, the hysteresis loops are defined from the experimental tests in the stress-strain curves. An acquisition of 60 points per cycle at tests at 10 Hz was sufficient to give a good description of the loops. The limits of the hysteresis are defined within these points and subsequently the area is calculated by numerical integration with the trapezoid method.

In the next figure it is presented an example of the points of data acquisition and the corresponding contour definition for calculation of the hysteresis area. For all tests, the calculations start at the second cycle and the last loop is considered at N_f -1. This choice is made due to unstable first and last cycle, which can alter the comprehension of the phenomenon. The figure also gives the evolution of the hysteresis loops at every 10% of the number of cycles to failure obtained for this specimen.

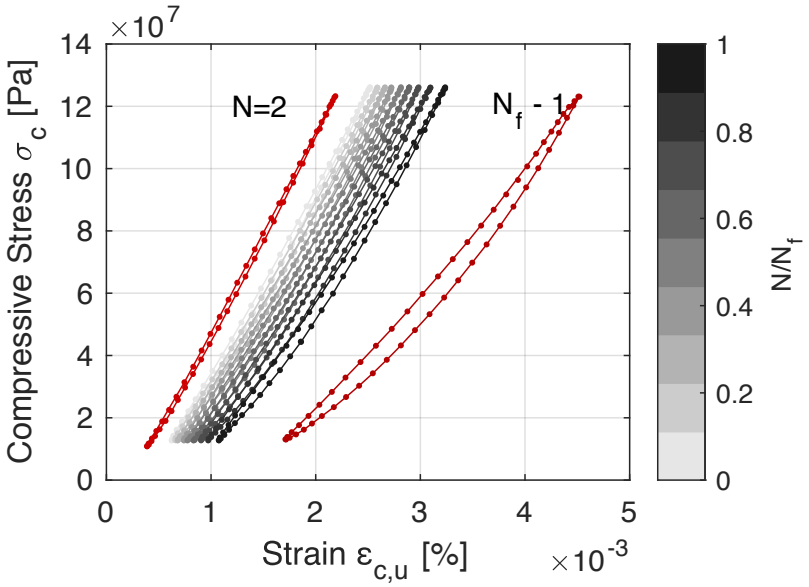

Figure 3.3-24 *Example of hysteresis evolution every 10% of the fatigue life, second and penultimate cycle*

An increase hysteresis loops area can be observed with increasing fatigue life, which is due to an increased level of damage. The loops between $N/N_f = 0{,}1$ and 0,9 (see colorbar on image) are remarkably close, showing of a small and progressive evolution. Nevertheless, a larger difference takes place between the second cycle and at $N/N_f = 0{,}1$. This difference becomes even larger when considering the distance between the penultimate cycle and at 90% of the fatigue life. This shows that during this last phase, a high level of permanent strain and damage occurs in the specimen. The half of the total strain evolution takes place in this phase, which also corresponds to the third phase in the strain evolution curves demonstrated in previous sections. A dense level of microcracking develops, resulting in an increased level of energy dissipation.

It should also be noted that the first hysteresis roughly follows the linear elastic deformation, whereas after the fatigue evolution the hysteresis are shifted towards the right, due to plastic strains generated in the material.

Evolution of energy dissipation

The levels of the energy dissipation per cycle (W) at each step of the fatigue life are calculated for all specimens and at different stress levels for both loading frequencies. However, in order to simplify the comparison between the curves, the mean values of the calculated hysteresis areas every 10% of the number of cycles to failure are displayed in figure 3.3-25. The results are presented separately for each stress level, but for both loading frequencies 1Hz and 10 Hz. In appendix B-5 a different presentation of the energy dissipation is given, where the three stress levels are presented within the same figure.

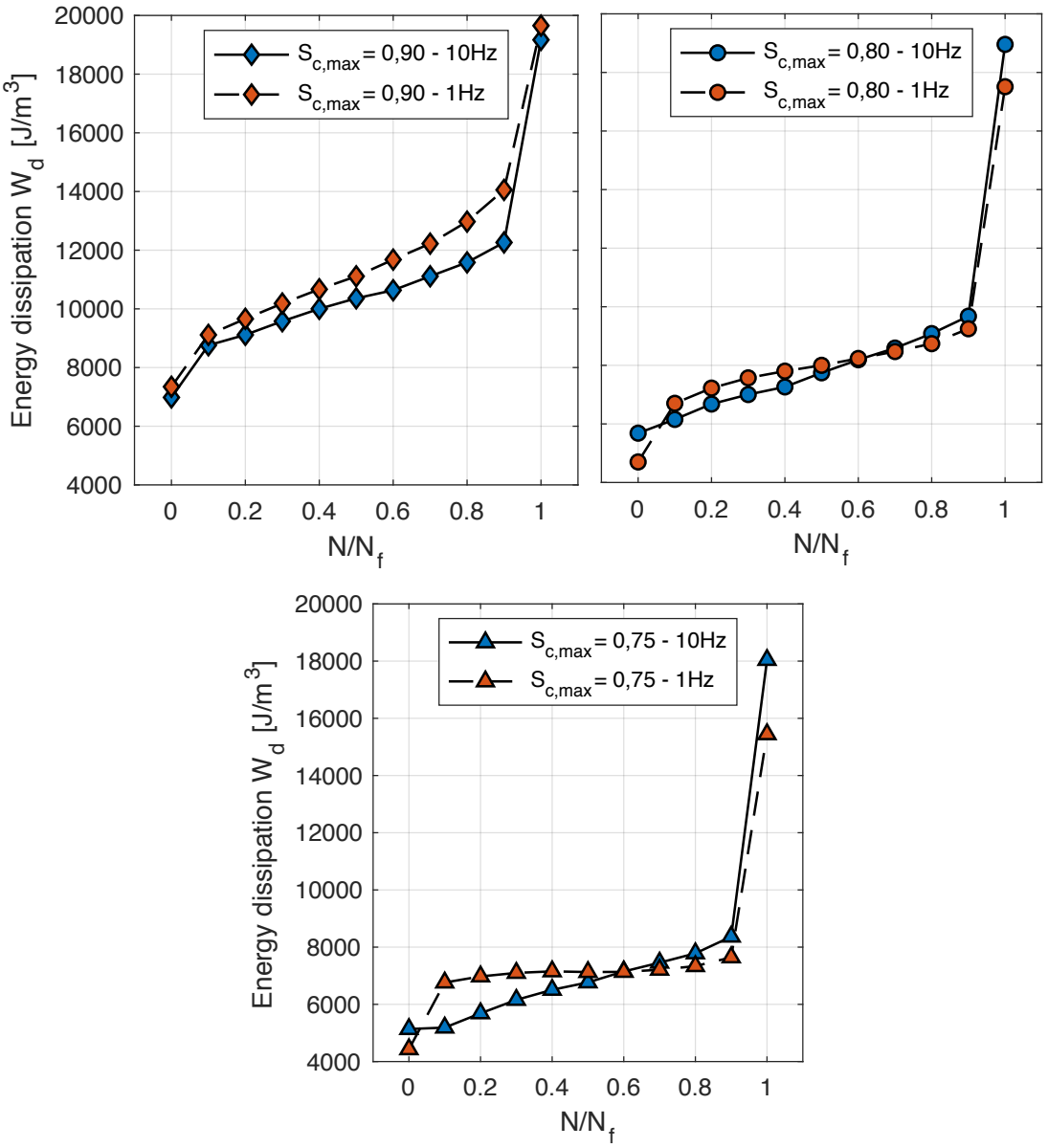

Figure 3.3-25 *Mean curves of energy dissipation at f = 10Hz and 1Hz at three stress levels*

The charts in figure 3.3-25 and from observations in appendix B-5, show that for all tests and at both loading frequencies, more energy is dissipated for a higher stress level. This is clearly noticed from the estimation of energy in the second cycle, but also in the evolution process and the last cycle. Indeed as the energy is calculated from the stress-strain curves, it is expected that the application of a high stress level would result in higher levels of energy dissipation. Some authors [99,100] suggest an exponential relation between the single cycle dissipated energy and the stress level applied. When considering the evolution for each test under the same stress level, more energy is dissipated when a specimen reaches lower number of cycles to failure. This result seems in accordance with recent reports from Bode [163]. Both these evolutions are obviously interpreted by the higher damage induced from the beginning of the test, resulting in higher values of dissipated energy.

Furthermore, particularly at $S_{c,max} = 0{,}90$ the energy dissipation shows a three phase evolution analogously with the longitudinal strain evolution. It means that the energy dissipation due to damage increases continuously up to failure. However, at $S_{c,max} = 0{,}75$ for $f = 10$Hz a very small decrease of energy is observed between the second cycle and the life ratio at 0,1. This is also notices for other specimens at stress level. According to Lei [100] when the load applied is low, the energy due to damage is small comparing with the heat energy dissipation, thereby the total energy decreases in the first stage.

Energy dissipation in relation to loading frequency

When comparing the behavior between 10Hz and 1Hz, it can be noticed from 3.3-25, that at a lower frequency, more damage is generated especially at $S_{c,max} = 0{,}90$. This is in accordance with the analysis of the stiffness evolution in the first cycles, where a higher increase is observed at 10Hz. Moreover, higher temperature rates are also noted for a lower frequency. Thus, these two phenomena help to justify the shorter fatigue life obtained at 1Hz for a high stress level. In [99] is also suggested that a lower loading frequency leads to higher hysteresis areas and therefore to more damage generated.

However, a slightly different behavior can be noticed at $S_{c,max} = 0{,}80$ and 0,75. The energy dissipated in the second cycle (first point on chart) is larger at 10Hz than in 1Hz, but during the first phase the intensity of increase is higher for the low frequency. After the first phase, a higher damage is induced at tests with the low frequency up to approximately 50% of the fatigue life and subsequently the tendency changes. Indeed, the evolution of the energy dissipation is faster at the high frequency, which can be due to the fact that the energy is dissipated in the form of damage and heating. Thus, due to more significant temperature increase at 10Hz, higher values of total energy dissipation are reached. Whereas at 1Hz it was shown that after the first phase, the temperature stabilizes up to the third phase close to failure and an almost steady-state is reached with the generated temperature and the ambient temperature. Therefore the energy presented at 1Hz is mainly the energy dissipation due to damage and at a higher frequency a large amount of the energy is dissipated in the form of heat.

For all tests it can be noted, that after a life ratio of 0,9 the energy dissipation increases very rapidly, approximately two times higher than the evolution observed between the second cycle up to 90 % of the fatigue life. The energy dissipation in the last cycle is up to 4 times higher than the value measured in the second cycle.

Thus far, the “single-cycle” evolution of the energy dissipation is considered. However, due to the additivity of energy, the accumulated dissipated energy was also examined according to equation 1.8 given in the first chapter. In figure 3.3-25 the calculated W_d is

presented for all tests at $S_{,max} = 0{,}80$ – 10Hz. The evolution in relation to the number of cycles is linear up to failure and the final value varies according to the fatigue life obtained.

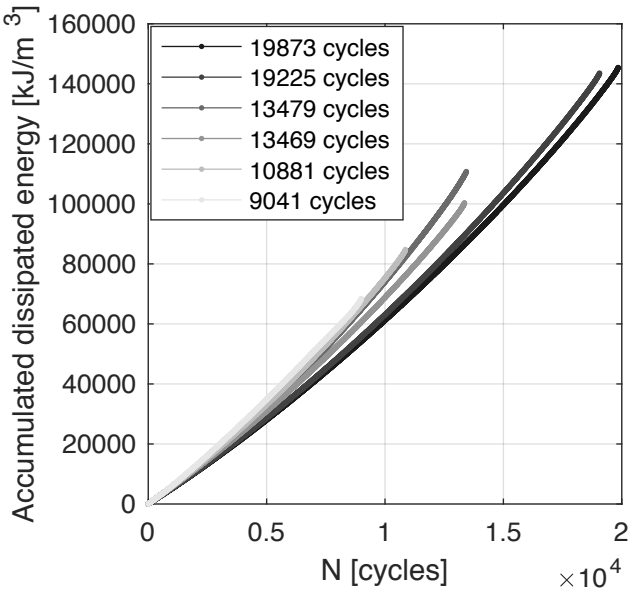

Figure 3.3-26 *Accumulated dissipated energy at $S_{c,max} = 0{,}80$*

Moreover, the final accumulative dissipated energy also varies according to the stress level applied (evolution can be found in appendix B-6). A similarity in the final energy dissipation between stress levels could only be observed when considering the single cycle evolution w_d, during the last cycle at 10Hz (appendix B-5). However, this does not take place for the lower frequency. Therefore, the hypothesis of using a critical dissipated energy W_{dc} (independent of the stress level) as a failure criterion to predict the fatigue life as shown for concrete in [99,100] does not seem to be valid for the high strength grout tested here. Indeed a dependency on the stress level applied takes place, which is in accordance with recent work in [101].

Finally, if we consider adiabatic conditions or a scenario where the heat exchange with the environment is very slow compared to the internal changes, the temperature increase can be given as follows:

$$\int \sigma \, d\varepsilon = c_p \, \Delta T \tag{3.5}$$

Where, σ ; ε are the stress and corresponding strain, c_p is the specific heat considered 2.4×10^6 [J/m^3.K] and ΔT the total temperature increase. Therefore, the temperature increase is calculated individually for each test at $S_{c,max} = 0{,}80$. This would give a mean temperature increase of 45 K, whereas from experiments presented in section 3.3.3.1 it was shown that the temperature increase at this stress level is approximately 21K.

Stiffness Evolution

In damage mechanics the variable D is used to describe the state of deterioration in concrete between 0 and 1, where 0 is the initial state. In equation 1.17 in the first chapter, the variable is introduced as a loss of the elastic stiffness E_0. Thus an evolution of the stiffness, helps describe the damage degree in the material. For this analysis, the secant modulus E_s is calculated at every cycle, between the minimum and maximum values in the stress-strain curve according to equation 3.6.

$$E_s = \frac{\sigma_{c,max} - \sigma_{c,min}}{\varepsilon_{c,max} - \varepsilon_{c,min}} \tag{3.6}$$

Firstly the peaks of the evolution are detected, and afterwards the regression line is plotted between two consecutive points in upper and lower stress levels. The method is schematically presented in figure 3.3-27.

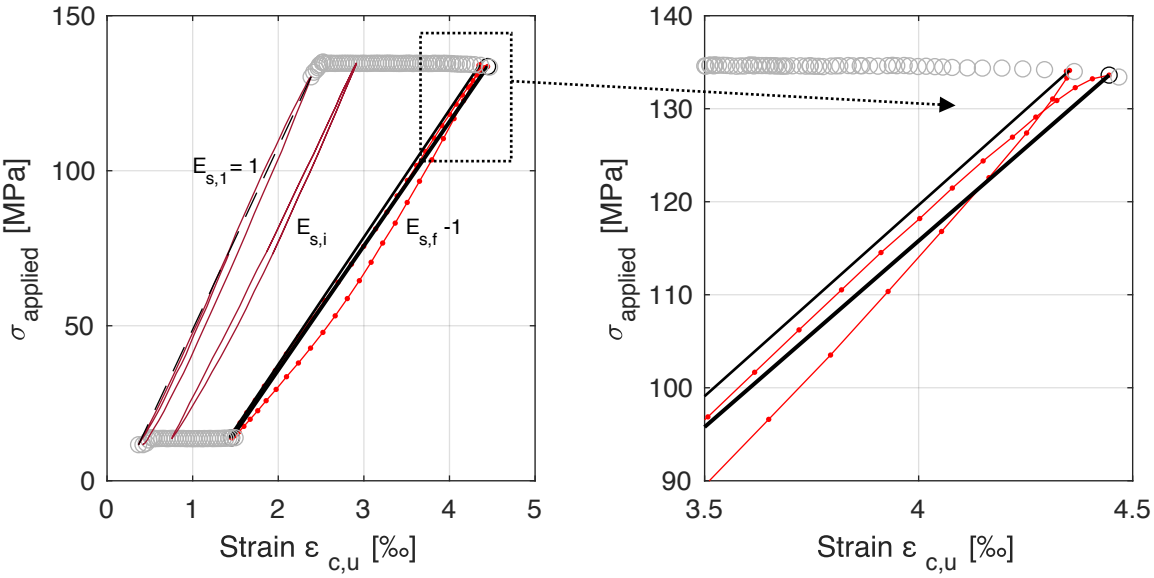

Figure 3.3-27 *Secant modulus E_s calculation method*

The secant modulus evolution is calculated for all curves, however consistently with the previous figures, only the median curves are presented in order to simplify the analysis. The median curves chosen have the closest number of cycles to failure with the mean values for each stress level. Therefore, in figure 3.3-28 the median curves for each stress level at 10Hz are presented. In appendix B-7, comparisons with the loading frequency 1Hz can also be found.

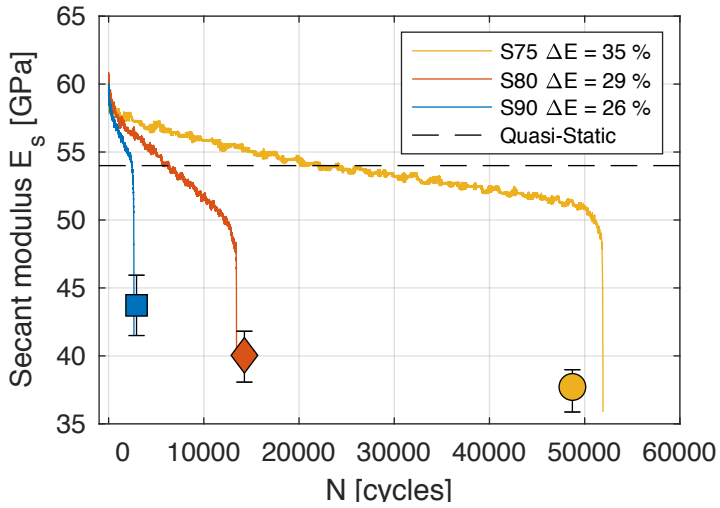

Figure 3.3-28 *Secant modulus E_s evolution at three stress levels and mean final values with bar errors ; Comparison with stiffness E_0 measured from quasi-static tests*

The evolution of the secant modulus shows a three phase development similar to longitudinal strain and decreases with increasing number of cycles for all tests. In addition, correspondingly to the strain evolution, the gradient in the second phase is smaller for the lower stress level, confirming a slower decrease of the stiffness when lower stress are applied. This seems also valid from results in appendix B-7, where smaller gradients are determined for the lower frequency at $S_{c,max} = 0{,}80$; 0,75. However, at 1Hz the gradient is higher compared to 10Hz at $S_{c,max} = 0{,}90$. This means that the stiffness degradation might be independent on the frequency applied, but is dependent on the number of cycles to failure or the test duration.

Moreover, the mean value of stiffness measured from quasi-static tests is also plotted in the figures. It is remarkable that all tests show a significant increase of the stiffness during fatigue loading compared to quasi-static tests. As explained in section 3.2.2 this is due to strain rate effects occurring during fatigue loading, creating a stiffening of the material. At $S_{c,max} = 0{,}90$, the stiffness decreases below the quasi-static level only at 90% of the total fatigue life, consistent with when the third phase occurs. Up to this point, the secant modulus has higher values than the stiffness in quasi-static tests. The total loss in stiffness (ΔE) in this case is approximately 26% and is calculated as a ratio in relation to the stiffness measured in the first cycle. At $S_{c,max} = 0{,}80$ and 0,75 the secant modulus decreases below the quasi-static value at approximately 50% of the total fatigue life and has a higher total decrease. These evaluations seems consistent with results from Oneschkow in [66] for a high-strength concrete.

In table 3-1 the mean values of stiffness loss for every stress level in both loading frequencies are shown. Only at $S_{c,max} = 0{,}90$ a large difference in total loss between 10Hz and 1Hz is observed. Additionally, it is noticed that similar values are reached at lower

stress levels. Nevertheless, *overall* the decrease of stiffness reaches higher values for the higher loading frequency, despite the similarities at the lower stress levels. Similar results have also been reported in [66].

Therefore, a limit value of total stiffness loss in order to describe the fatigue damage close to failure, can hardly be given. Nevertheless, a range of values could be compiled. A conflicting suggestion is given recently in [164] where it is proposed to use the critical damage values from the secant modulus, under the hypothesis that E_s does not deteriorate to zero and the final value is independent on the frequency applied. However, in these reported tests, only one stress level is tested. Therefore, the proposed model is questionable.

Table 3-1 *Total stiffness loss after fatigue loading in relation to the first cycle*

Stress Levels	**Frequency [Hz]**	**ΔE [%]**
0,90	10	26
	1	17
0,80	10	29
	1	28
0,75	10	35
	1	32

The table 3-1 shows the total decrease for the specimens which failed at a certain number of cycles. Three specimens at $S_{c,max} = 0{,}70$ – 10Hz were stopped at 400.000 cycles and did not go up to failure, due to time restriction issues. However, the stiffness evolution and the corresponding energy dissipation for these tests have been determined and an example is given in figure 3.3-29.

From the beginning of the test up to 90.000 cycles, a decrease of the secant modulus takes place up to approximately 10% of the first value. Subsequently, a very slow decrease takes place linearly, which during the end of the test can be considered as a quasi-absence of evolution. A similar development is observed in the energy dissipation, assessed it different "N/N_{lc}" ratios. The ratio in x-axis is calculated in relation to the last cycle, when the test stopped. Despite a few cycles around 60% of the total number of cycles, which showed a decrease in energy dissipation (mainly due to some noisy data and are considered as an artefact), almost no increase in energy dissipation takes place between 200.000 and 400.000 cycles. For comparison, at $S_{c,max} = 0{,}75$ – 10Hz, an increase of 70% takes place between 0,1 and 0,9 of the total fatigue life. However, for the test shown in the following figure, the increase between 0,1 and the total energy dissipation at the last cycle, is approximately 10% and almost no damage is generated. Moreover,

in appendix B-8, the hysteresis cycles are displayed and almost no evolution in irreversible strains occurs. It can therefore be assumed that the dissipative phenomena, which takes place during the first 100.000 cycles, are reduced and probably cancelled if the test would continue up 2.000.000 cycles, which often is considered as the endurance limit. Regrettably, these specimens could not be tested up to this point.

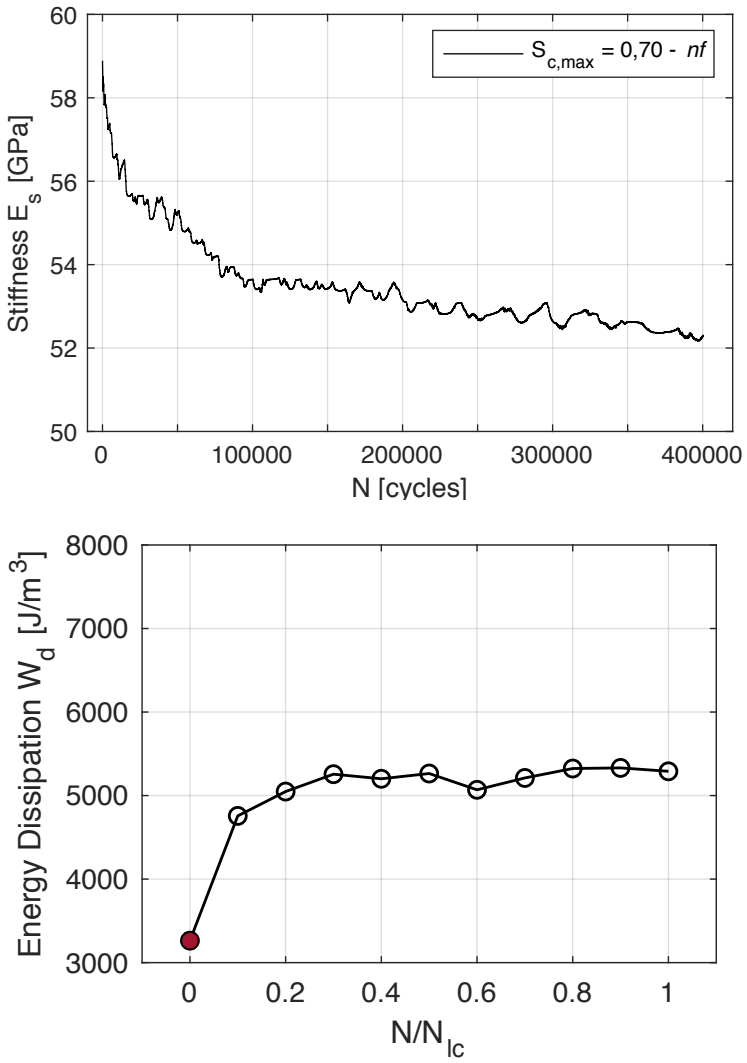

Figure 3.3-29 *Secant modulus evolution and energy dissipation for a specimen at $S_{c,max}$ = 0,70 stopped at 400.000 cycles without failure*

Lateral strains and damage estimation with ultrasonic measurements

Ultrasonic measurements are widely used for in-site monitoring of the degradation in structures or in laboratory conditions. However, not many research has been found using this technique in order to monitor the degradation during fatigue loading. The benefit in the implementation of this technique is firstly the supplementary information on material damage by measuring the ultrasonic velocity passing through the specimen. Indeed, the

creation and propagation of microcracks, should result in a decrease of the ultrasonic velocity.

In addition, another interest in this method is also to define whether a correlation with the stiffness degradation takes place. The stiffness degradation is expressed as the evolution of the secant modulus. However, the assessment of the ultrasonic velocity can also be implemented in equation 2.2 in order to estimate the dynamic Young's modulus. As previously mentioned this equation is based on a hypothesis that the Poisson's ratio is a constant parameter, which is expressed as the ratio between lateral and longitudinal strains. Nevertheless, this is not applicable to fatigue loading and in this part attempts were made to measure the lateral strains, in order to evaluate the evolution of Poisson's ratio.

Consequently, in addition to longitudinal strains presented up to this point, the lateral strains were also measured by the same type of laser distance sensors. All sensors had the same accuracy, whereas the lateral strains are approximately 5 times smaller than the longitudinal strains. Therefore, these measurements resulted to be not as accurate. An example of the lateral and longitudinal strain evolution is shown in the next figure.

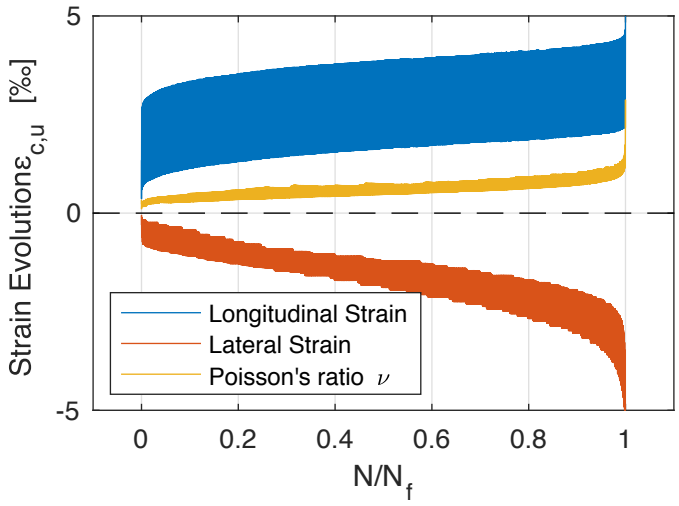

Figure 3.3-30 *Example of longitudinal and lateral strain development and assessed Poisson's ratio evolution*

Despite the imprecise values due to a bad signal obtained, the course of evolution is found to be in a similar shape for all tests and is thus considered to be representative. However, it should be noted that the lateral strain values are not accurate. Therefore, it is demonstrated that the lateral strains also show a three-phase shape, where a smaller first phase, compared to longitudinal strains, seems to take place. This behaviour, leads to an evolution of the Poisson's ratio mostly with a constant rate of increase up to the third phase, where the strain increases to large values until failure. The significant

increase in lateral strains is due to critical crack opening. The microcracks during compressive fatigue develop parallel to the direction of loading and the opening in the lateral direction results in increased lateral strains.

Due to inaccurate Poisson's ratio values in the evolution, the equation 2.2 for the assessment of the dynamic stiffness could not be used. Therefore, it was agreed to evaluate only the change in the ultrasonic velocity and not the dynamic stiffness.

An acquisition program in Labview was developed for this purpose. Due to very noisy data during the test, thresholds had to be inserted within the program. Moreover, in the post-processing, a first filter is applied which removes measurements differing by ± 5% compared to the moving average, calculated with a window size of 30. Subsequently, smoothed curves are given for comparison. Moreover, as briefly explained in chapter 2, the experimental set-up chosen for continuous measurement of the ultrasonic signal during the test implied using a sealant with good adhesive properties. Two other systems for a better fixation were used in a few tests, which implied fixating the transducers by two metallic rods and springs in order to allow lateral deformations to occur. Another more simple method was also used by simply holding the transducers with an elastic band, in addition to the adhesive sealant.

However, in all these cases the third phase was difficult to record. This can be due to the fact that sealants tended to detach and higher adhesive properties should have been used. Nevertheless, in a few cases microcracks develop in the specimen surface on the area of adhesion, therefore this can cause a detachment of the transducers. Two examples of measurements are shown in figure 3.3-31 in two y-axis curve. The ultrasonic evolution is given in the right y-axis and is expressed in relation to the measurement of the first cycle. In the left figures the ultrasonic velocity is given in comparison with the evolution of the secant modulus, also expressed in relation to the first value measured in the first cycle. In the figures on the right, the ultrasonic velocity is given in comparison to the strain evolution in order to indicate more clearly, the stage when the transducers stopped recording. All figures are shown in relation to the relative number of cycles ratio.

Therefore, it can be noticed that in these two cases (also in all other tests not presented here), that when the evolution of the ultrasonic velocity approaches the third phase, the signal is lost. Thus, no conclusions can be drawn about the total loss or the behavior in the third phase. However, a few conclusions can be given with the available evolution. Mainly, when comparing the ultrasonic velocity to the strain evolution, the first transition phase occurs at the same level. This supports the statement that different damage mechanisms take place between the first and second phase.

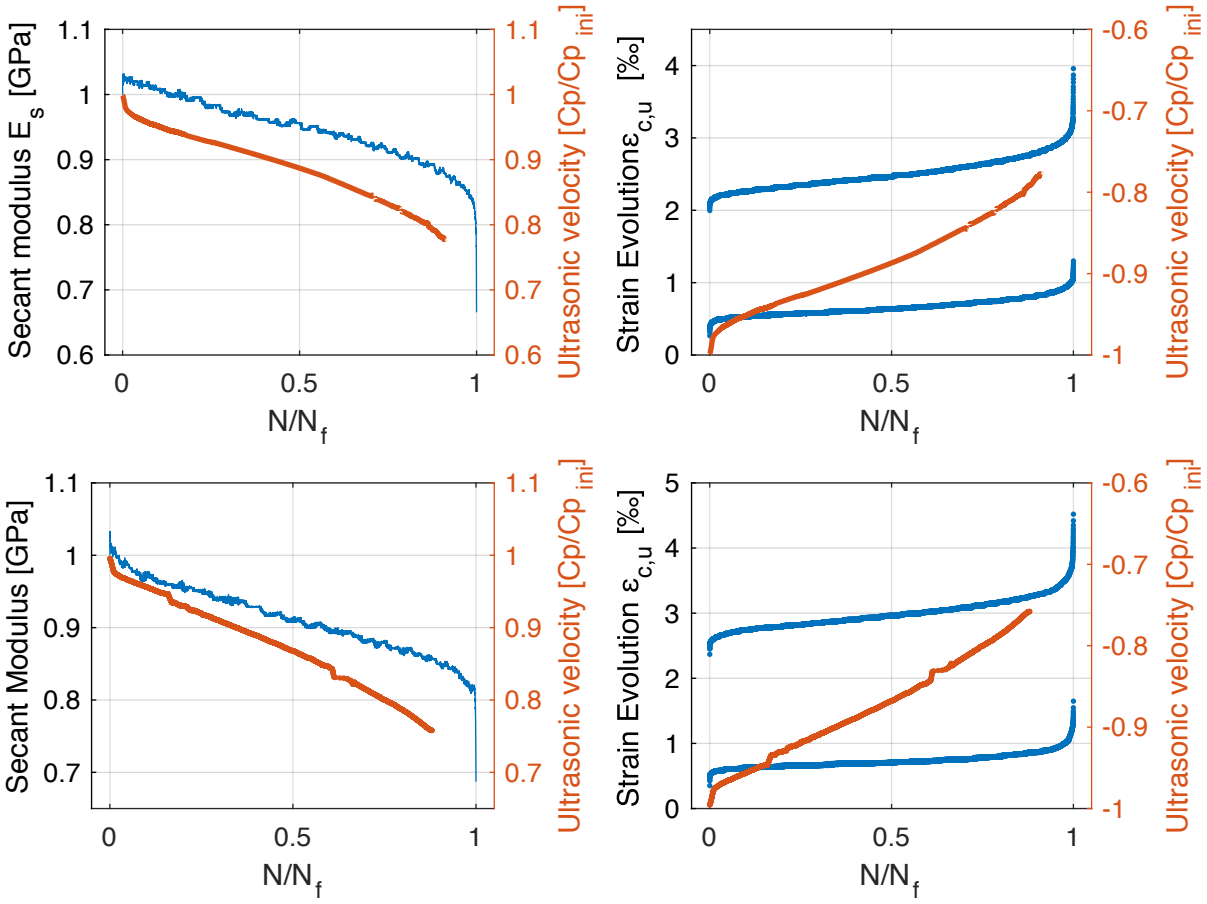

Figure 3.3-31 *Comparison of two different compressive fatigue tests (upper, lower) ; Comparison between the evolution of the secant modulus and the ultrasonic velocity (left) ; Corresponding strain development and evolution of the ultrasonic velocity (right) ;*

The velocity decreases very rapidly in the first phase (see left figures), meaning that a high damage is induced in the material. Subsequently, the evolution is slower and almost linear. In comparison to the evolution of the secant modulus, it seems that overall the ultrasonic velocity decreases more quickly and for the same number of cycles higher damage is recorded from ultrasonic measurements, approximately 10% higher. It is suggested that this is due to the fact that US measurements are made on the lateral direction and are highly influenced by the crack opening. Indeed it is supposed that cracks develop parallel to the direction of loading, which will also be demonstrated in section 3.5. Whereas, the secant modulus is given from measurements in axial direction.

This implies the anisotropy of damage generated during compressive fatigue loading. Moreover, on a microscopic perspective, local increase of stiffness may take place, due to the strain rate effects described previously. Therefore, this can lead to a decrease of stiffness at a lower rate, whereas in the lateral direction this has a minor effect on the ultrasonic velocity.

3.3.6 Estimation of endurance limit from self-heating measurements

At a given stress level, microplastic zones are activated, which generate microcracking and therefore result in dissipated heat. The infrared thermography uses a detector to convert the radiated energy on the specimen surface to a thermal image. A calibration phase is necessary to establish the relation between surface emissivity and temperature, by the means of a black body in the temperature range required. This allows to convert the digital signal coded in digital level (DL) to temperature values (°C) and is dependent on the temperature range, integration time and frame size. For these fatigue tests the range defined is relatively large, within 10-70°C, as it was estimated that these are possible values to be reached during tests. Nevertheless, a shorter range, would improve the precision of the measurements. In order to increase the emissivity of the surface of the specimen, a black matte paint should be used. However, preliminary tests showed flaking due to temperature increase, which distorts the measurements. Therefore, no paint is used in the following tests presented below. An infrared camera and four thermocouples are used for temperature measurements in these tests as complementary measuring methods. Indeed, the advantage of the infrared camera lies on the provided spatial information.

A few challenges are faced in applying the self-heating method based on temperature measurements. Firstly, these challenges are addressed in the following section and subsequently the estimation of the endurance limit is presented.

3.3.6.1 Challenges of self-heating method application on cementitious materials

The good correlation of the endurance limit estimated by the self-heating curves and the traditional fatigue tests for multiple materials, but also the short time required to conduct these tests (literature review in section 1.4.5.2), made this method very "appealing" to apply for the characterization the grout. But one question arises : can all materials be potential candidates for of the self-heating test in order to estimate the endurance limit ?

As explained earlier, the method is based on the appearance of microplasticity areas, which after a few cycles lead to the creation of microcracks, i.e. this microplastic activity occurs before the appearance of microcracks. Due to heterogenous nature of grout and concrete compared to steel, aluminum or alloys, multiple flaws are existent within the material. When the loading is applied, microcracks can be initiated in these areas and not from a microplastic activity as suggested by the self-heating method.

Moreover, the previously mentioned materials have a higher thermal conductivity coefficient compared to concrete and grout (about 10 times higher), resulting to a quicker stabilization between dissipation and heat loss during loading steps. Additionally, the specimen size used in these tests is relatively small, for example in [107] used a specimen with a length of 120mm but composed by a width corresponding to a sheet steel. For the current grout material studied, the maximum aggregate size is 6mm and the specimen dimensions are: ϕ = 60mm and H = 120mm, sufficiently high regarding the microstructure. Thus, more time is needed for the temperature to reach a steady state (if present) than in steel specimens, due to lower conductivity and bigger specimen size.

On the other hand, the last step applied in self-heating tests is defined as the last step during which the temperature does not reach a stabilization. However in some tests, it can be tricky to determine whether a certain step has reached a steady state temperature. The estimation of the endurance limit is carried out from the last 3 points of the self-heating curve, and therefore it can be inaccurate if the operator stopped the test earlier.

The final challenge consists in defining whether there exists an endurance limit for concrete and grout. Literature research shows a disagreement on this point. In model code [46] as described in chapter 1, it is assumed for log $N_f > 8$ that the S-N curves asymptotically approach the minimum stress level of the respective curve. However, the endurance limit is generally considered when a specimen does not fail at 2 x 10^6 cycles.

Based, on these challenges and method descriptions, a few objectives arise. Firstly, to investigate the feasibility of the method on cementitious materials. If it is applicable, establish a test protocol adapted to concrete and grout. In addition, estimate the endurance limit and identify the heating sources.

3.3.6.2 Empirical estimation of the endurance limit

In section 1.4.5.2 the concept and the testing method was briefly described. Based on the same methodology, a few adaptions were carried out, compared to the cited tests in the literature carried out on steel materials. The self-heating method consists in applying successive loading steps with increasing amplitude, but the stress ratio and the loading frequency are kept constant (R = 0,1 ; f = 10Hz) similar to traditional fatigue tests. During one loading step, the temperature increases rapidly and when a thermal equilibrium is reached, the temperature stabilizes at $\bar{\theta}_{sf}$. The time definition of each loading step depends on the time required to reach a steady-state $t_{0,sf}$. Due to the large specimen size (relative to steel specimens) a stable value is reached after 55000 cycles, i.e. 5500 seconds. In figure 3.3-22 (d) is demonstrated an example of the temperature evolution during one loading step, where the temperature shows an increase up to 40000 cycles and subsequently a quasi-absence of evolution take place up to 55000 cycles. The

temperature is measured within the area presented in figure (b) and (c) in the center of the specimen. The presence of a temperature gradient can be observed in figure (c) along the height of the specimen, which takes place due to heat diffusion.

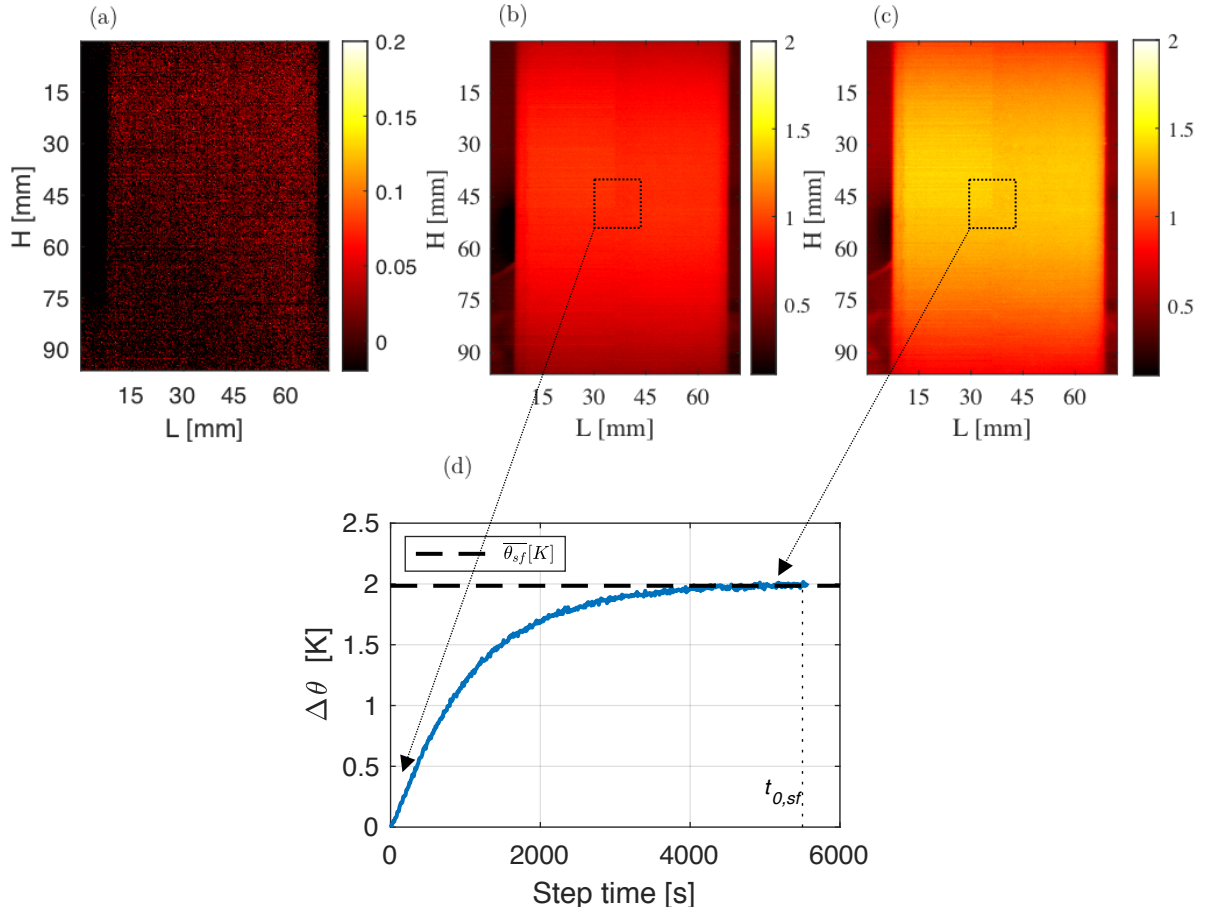

Figure 3.3-32 *Thermal image before self-heating tests (a) ; thermal images at the beginning and the end of a loading step (b) and (c); Estimation of the mean steady-state temperature (d)*

The step time is relatively large when compared to steel specimens. Indeed due to the homogeneous microstructure of steel, specimens used for self-heating tests have a maximum width in the order of one mm. The heat exchange with the environment occurs at a higher rate due to the smaller specimen size and the higher thermal conductivity. Thus, loading steps necessary to reach a steady state for the grout are approximately at least 10 times longer than for steel. This has an impact on the total time required for the test. For steel specimens it can be carried out within two hours, as reported in the literature [107], whereas for the present specimen size and by optimizing the number of steps, at least 12 hours are necessary.

The relatively long loading steps applied, led to the implementation of preliminary tests for optimizing the number of loading steps with increasing amplitude. The interval of amplitude must not be too low, as this would increase the total number of steps. The lowest stress applied is 25Mpa and an increase of 10Mpa is imposed between each step.

This allows the acquirement of approximately 8 different points in the self-heating curve, which resulted to be sufficient. For more accurate results in further applications in concrete or grout, it should be considered using smaller specimens in size and applying more loading steps for a better accuracy. According to [106] the history of loading and the number of steps do not have an influence on the final thermal activity.

It was previously mentioned that the last loading step is considered when the temperature does not show a stable evolution. The concept of the method is based on the increase in energy dissipated in local areas generated by progressive increase of stress levels. Therefore, when the temperature reaches a stable evolution for lower stresses applied, the heating source is constant and no further damage is generated in the material. An increase of the stress applied up to 95MPa or higher (which consisted in the last loading step for these tests) results in a continuous increase of the temperature and a variable heating source. Thus it can be considered that damage grows within the material and the endurance limit is exceeded.

Based on these steps, the self-heating tests are carried out on 5 specimens between 8 loading steps, starting from 25MPa. The self-heating curve is given as a relation between the mean stabilized temperature over a few cycles and the related maximum stress applied. Figure 3.3-33 shows an example of the self-heating curve for one of the specimens.

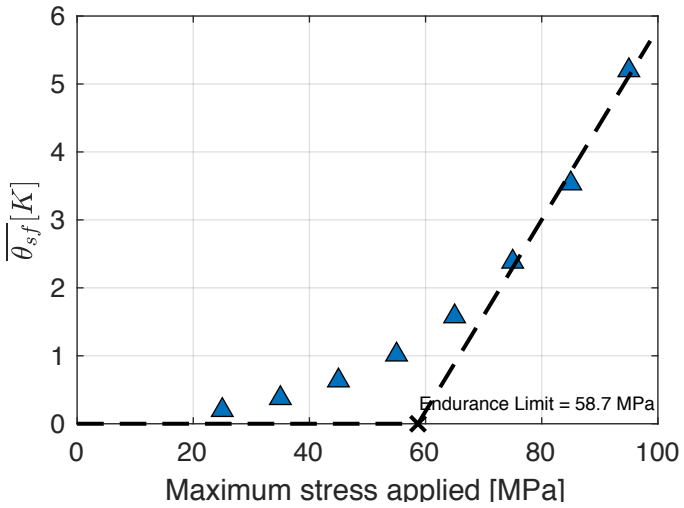

Figure 3.3-33 *Self-heating curve for the reference high-strength grout and estimation of the endurance limit*

The curve in figure 3.3-33 presents clearly the presence of two different regimes. The first regime between the first three points corresponds to a low intensity zone, where the temperature stabilizes quickly at low values. The increase of temperature in the second regime, originates from a higher microplastic activity leading to the creation of microcracks and to higher probability of failure. Thus, in order to identify the endurance

limit, a linear regression is carried out between the last three points of the self-heating curve. The intersection of this regression and the abscissa axis represents the endurance limit. Other authors [165] suggest the evaluations of the endurance limit as the intersection between the linear regression between the last three points and the first three points. Due to a small slope of the first regime, both methods are commonly accepted. In the tests carried out on grout, this second method is not applied, as the first slope would be overestimated. This would be due to the choice of the first step applied at 25MPa, defined to optimize the testing time. For a better estimation, lower stresses in the first loading step can be considered.

Therefore, the endurance limit is estimated at 58,7MPa for the presented test, which correspond to a maximum stress level of $S_{c,max} = 0{,}35$. An estimation from the intersection with the first linear regression would result in an endurance limit of $S_{c,max} = 0{,}39$.

By applying this method for 5 specimens, the endurance limit is identified for each test and presented in the following table in an ascending order.

Table 3-2 *Endurance limit estimated from self-heating tests*

Specimen no°	$\boldsymbol{\sigma_{\infty}^{S-H}}$ **[MPa]**	$\boldsymbol{S_{c,max,\infty}^{S-H}}$ **[-]**
1	53,4	0,32
2	55,8	0,33
3	56,8	0,34
4	58,3	0,35
5	58,7	0,35

The potential of the infrared thermography lies beyond the application showed, by defining the crack initiation in stress concentration zones caused by thermo-mechanical coupling. Indeed, from temperature fields and the assessment of thermal properties, the heat sources can be determined by incorporating the heat equation, in order to evaluate locally the energy dissipation. However, a few adjustments on measurement conditions should be carried out compared to the presented tests, such as a shorter temperature range, with an increase of the integration time, which can reduce the temporal noise. Moreover, the area observed should be reduced or the specimen dimensions. Due to small aggregate size used in grout, it can be considered a reduction of the specimen size, while keeping the volume as representative (REV). In addition, extended work carried out on steel materials suggest the application of a negative stress ratio (R =-1), i.e. alternate loading in traction-compression. Finally, possible applications can also be carried out in quasi-static tests, where heat areas can be identified before the appearance of cracks.

3.3.7 Fatigue life estimation

3.3.7.1 Probabilistic analysis and fatigue life distribution

Section 1.4.3.2 referred to different approaches for the analysis of fatigue behaviour and probabilistic methods are relevant in order to give a better understanding of the fatigue life distribution, due to high scatter in number of cycles to failure. Previous studies [50,166] successfully used the two-parameter Weibull distribution to describe the fatigue behaviour from flexural tests in plain and fibre reinforced concrete. However, its application in compression and in grouted materials, is not commonly found in the literature. For instance, in [58] the three-parameter Weibull distribution is used in compressive tests for cube-shaped specimens or in [167] for polymer fibre concrete.

Due to common use of Weibull distribution in fatigue analysis, the method is adopted for the life distribution of the reference high-strength grout. Obviously, higher number of specimens are necessary in order to give a more reliable description and ensure an appropriate fatigue resistance in structures. Nevertheless, 6 specimens is considered as a sufficient low boundary in order to perform the analysis. Indeed in [48], 5 specimens resulted in an optimum number for most practical purposes. The three parameter Weibull distribution includes a location parameter, which physically represents the endurance limit at a certain stress level. However, in order to give a better reliability, this parameter is not taken into account and the two-parameter Weibull distribution is adopted. Based on equation 1.3 and 1.4, the failure probability is expressed as follows :

$$PF(N_f) = 1 - \exp\left\{-\left(\frac{N_f}{\alpha}\right)^{\beta}\right\} \tag{3.7}$$

Different methods can be used in order to estimate the two distribution parameters scale α and shape β. Firstly the graphical method is used to show if the data follows the Weibull distribution and afterwards the parameters are estimated with the maximum likelihood method. Therefore the survival probability function is given by :

$$L(N_f) = 1 - PF(N_f) \tag{3.8}$$

By introducing equation 3.8 in 3.7 and taking the natural logarithm twice on both sides, a linear relation between $ln(N_f)$ and $ln\ [\ ln\ (1/L(N_f))\ ]$ is expressed as follows :

$$\ln\left[\ln\left(\frac{1}{L(N_f)}\right)\right] = \alpha \ln(N_f) - \alpha \ln(\beta) \tag{3.9}$$

Thus, if for a certain stress level all data follow the linear relation, it is assumed that the Weibull distribution may be applied. The empirical survival function is calculated as follows [166] :

$$L = 1 - \frac{i}{k+1} \tag{3.10}$$

where, i is the failure order number and k the total number of data at a certain stress level. Therefore, based on the experimental number of cycles to failure at $f = 10$Hz, the data is plotted in figure 3.3-34 for each maximum stress level applied ($S_{c,max} = 0{,}70$ is not included due to three specimens which did not undergo failure).

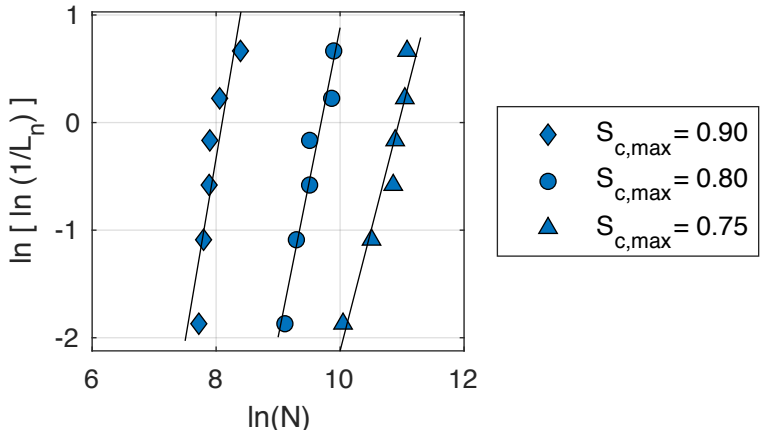

Figure 3.3-34 *Graphical method for fatigue life distribution at each stress level*

Fairly good correlation coefficients of $R^2 = 0{,}94$ and 0,93 are obtained at $S_{c,max} = 0{,}80$ and 0,75 respectively. However, at $S_{c,max} = 0{,}90$ the correlation coefficient is estimated at 0,80, which shows a relatively poor relation. It is therefore questionable whether the data follows the distribution and what are the lower boundaries of acceptable correlation coefficients. Moreover, the number of specimens tested is relatively low for a rigorous probabilistic analysis and more specimens should be used. The Weibull distribution is highly sensitive of the number of specimens uses. In some of the tests cited earlier, approximately ten specimens are used for each stress level. Nevertheless, due to good correlation at $S_{c,max} = 0{,}80$ and 0,75, it was decided to proceed with the estimation of the probabilities of failure.

The probability density function is given in chapter 1 equation 1.3, where x = N_f and the maximum likelihood is used to determine the scale and shape parameters. The number of cycles to failure are used for the calculations and not the logarithmic values, as this would modify the evaluations. Therefore, the parameters estimated for each stress level are shown in table 3-3 below.

Table 3-3 *Values of parameters in Weibull distribution*

Frequency f (Hz)	$S_{c,max}$	**Scale parameter α**	**Shape parameter β**
10	0,90	3225	4,060
	0,80	15851	3,989
	0,75	54015	4,087

A smaller shape parameter indicates a larger variability in the distribution of fatigue life. From data in table 3-3, the values of the shape parameters are very close and no significant change is observed for the three stress levels. These results differ from most of the articles cited in this section, where a larger scatter is reached for lower stress levels [54,166]. The corresponding probability density function is plotted in figure 3.3-35 (left). The scale parameter increases with increasing stress levels. This was expected as this parameter indicates the average of the distribution and therefore should be close to the mean number of cycles to failure. The failure probability estimated with the parameters of the Weibull distribution is shown in figure 3.3-35 (right).

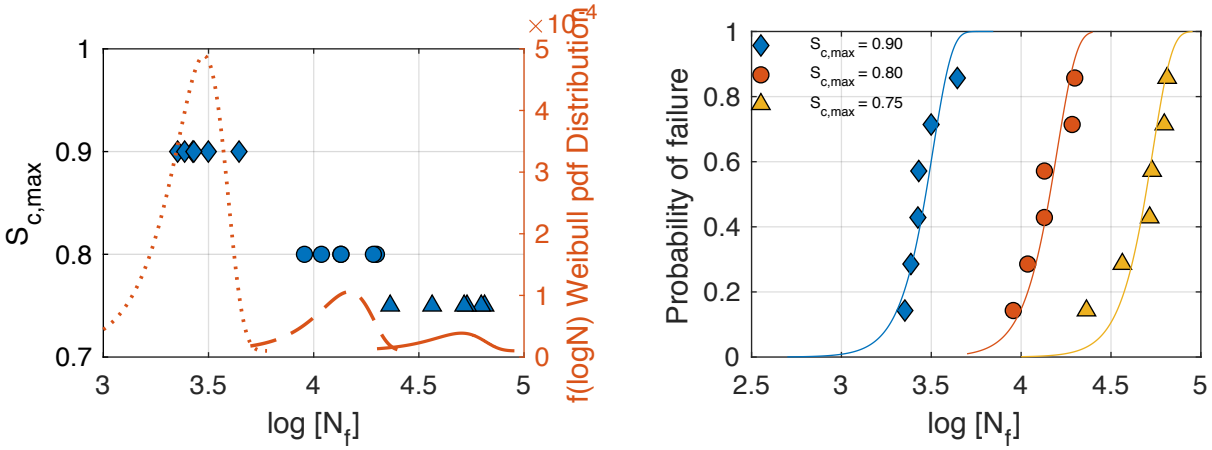

Figure 3.3-35 *Probability density function for each stress level (left) ; Cumulative Distribution Function(cdf) of experimental tests and the fitted Weibull distribution (right)*

Estimation of endurance limit

The values of the design fatigue life can be calculated for different probabilities of failure required, by rearranging equation 3.7 as follows :

$$N_D = \alpha \left[\ln\left(\frac{1}{1-PF}\right)\right]^{\frac{1}{\beta}} \tag{3.11}$$

For a better reliability, low probabilities of failure should be chosen in order to estimate the fatigue life for a corresponding stress level. Moreover, the endurance limit can be determined from equation 3.11 at a low PF. The probability of failure is chosen at 5% and the design fatigue life is estimated for each stress level due to different Weibull parameters. Therefore, the regression curve (equation) can be obtained between the three calculated data at PF=0,05 (or any chosen PF) and a relation between $S_{c,max}$ and the number of cycles is achieved.

$$S_{c,max,PF05} = -0{,}123 \log (N_D) + 1{,}289 \tag{3.12}$$

Thus, from equation 3.12 and by supposing that the endurance limit corresponds to 2.000.000 cycles, the endurance limit is estimated at 51% of the compressive quasi-static strength with a failure probability of 5%. This value determined by the probabilistic distribution can be confronted to the endurance limit calculated according to equation 3.3 in section 3.3.1, which represents the linear regression in the Wöhler curve (as traditionally determined). By considering the same number of cycles as endurance limit, i.e. 2.000.000 cycles, a limit of 58% is obtained. According to these results, the S-N relation incorporating the failure probability leads to more conservative results. Hence these relations should be considered in design, for a better predictability.

Overall, the probabilistic distribution can be modelled by the two parameter Weibull distribution and allows an estimation of the endurance limit. However, whether this method is appropriate in grouts is still questionable, due to one low correlation coefficient at the high stress level. In addition, the results are not conclusive due to limited number of tests which increase the estimated error. Tests with at least ten specimens for each stress level should be carried out in further research.

3.3.7.2 Secondary Strain Rate

The slope of the second phase in the maximum strain evolution is called secondary strain rate and will be noted $\dot{\varepsilon}_{max,II}$ in further analysis. In section 1.4.3.5 it was mentioned that a few authors, found a linear relation between the secondary strain rate and the number of cycles to failure in a double logarithmic scale. All authors report good correlation coefficients. However, no research has been found in the literature, whether this relation intervenes in high-strength grouts. The benefit of the linear relation, lies in the fact that despite different final or initial strains values, when one disposes the gradient of the strain evolution after the initial phase, the fatigue life of a material can be determined, independently of the stresses applied.

For this purpose, gradients of the second phase for all tests up to failure have been evaluated. In order to avoid any possible inaccuracies due to an imprecise definition of the transition phases, the slopes were calculated for all tests between 20% and 80% of the total number of cycles to failure. The transition phases for the reference grout were defined occurring at a maximum ±10% and 90%. Therefore, the chosen levels for the calculation are undoubtedly within the second phase. Firstly, the results are presented separately for each loading frequency, in order evaluate whether a possible influence takes place. The secondary strain rates in relation to the number of cycles to failure in the double-logarithmic scale are shown in figure 3.3-36, where one can notice that a linear relation is achieved. The corresponding equations for each loading frequency and the correlation coefficient are given in the following equations :

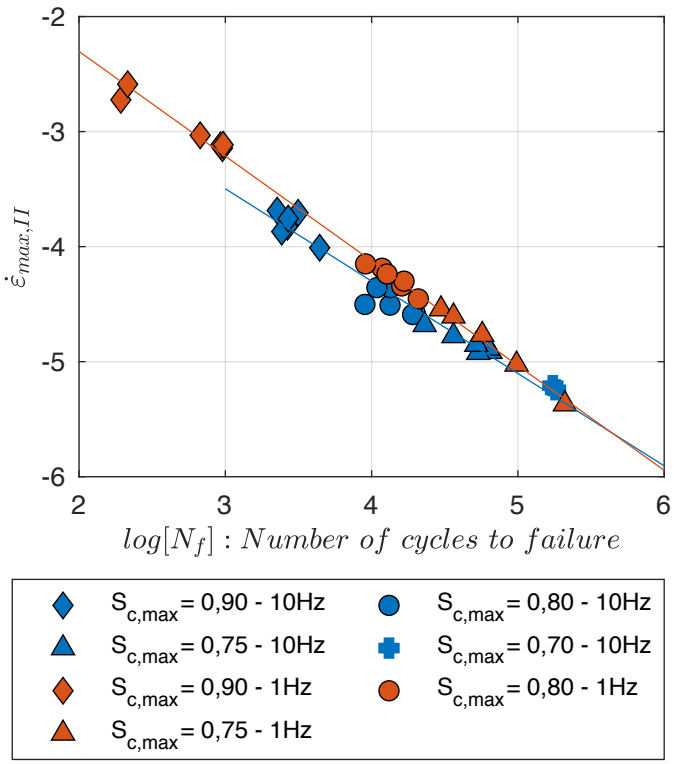

Figure 3.3-36 *Secondary strain rate in relation to the number of cycles to failure for all tests up to failure and regression curves for both loading frequencies separately*

$$\mathrm{f} = 10\mathrm{Hz}: \ \log\left(\dot{\varepsilon}_{max,II}\right) = -0{,}803 \log N_f - 1{,}088 \qquad R^2 = 0{,}966 \qquad (3.13)$$

$$\mathrm{f} = 1\ \mathrm{Hz}: \log\left(\dot{\varepsilon}_{max,II}\right) = -0{,}910 \log N_f - 0{,}483 \qquad R^2 = 0{,}995 \qquad (3.14)$$

Firstly, it is remarkable that a lower scatter is achieved, compared to results presented in the form of Wöhler curve. This can be due to the fact that the second phase represent the crack propagation and therefore is a real indicator of damage within the material

[168]. Overall, for lower stress levels and higher number of cycles to failure the gradients of phase two are smaller and less damage is generated within one cycle. Moreover, the first and last phases in the strain development within these stress levels were demonstrated in section 3.3.4.2 to be shorter. Whereas, the total strain at failure is higher for the lower stress levels. Indeed, the damage progress occurs at a lower rate and in addition, a time-dependent mechanism related to viscous deformations occurs leading to higher strains.

The values of the secondary strain rates between 10Hz and 1Hz, compared at a fixed number of cycles are very similar, nevertheless the gradients at 1Hz reach slightly higher values. It suggests a more rapid crack propagation at the lower loading frequency. This result is in analogy with the analysis carried out 3.3.4.1 for Sc,max = 0,80. *However*, it is noticed that at higher number of cycles to failure, the difference between the regression lines is smaller and tend to overlap. A small change of tendency should also be expected for even higher cycles. This is can be seen for the specimen tested at $S_{c,max} = 0{,}75$ – 1Hz, which failed at approximately 200.000 cycles and has a similar slope to one test at $S_{c,max} = 0{,}70$ – 10Hz, which failed at 180579 cycles. Therefore, these results led to consider that the loading frequency might not have a significant effect in the secondary strain rate, especially for low stress levels. For this purpose, the regression between all tests is also plotted in figure 3.3.30.

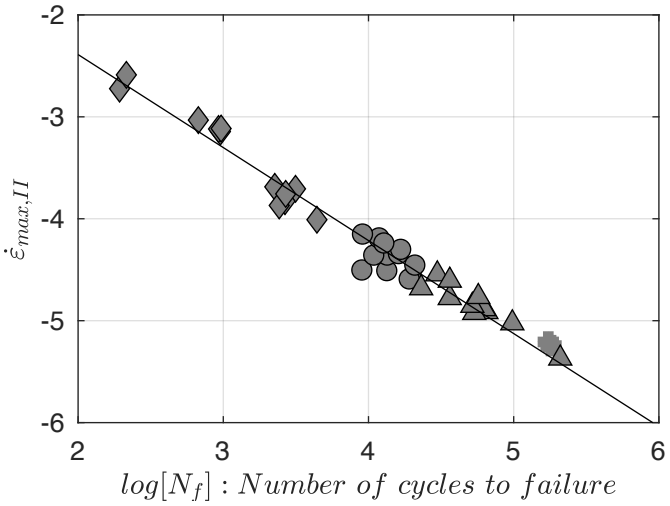

Figure 3.3-37 *Secondary strain rate in relation to the number of cycles to failure and regression curve for all tests*

$$\log(\dot{\varepsilon}_{max,II}) = -0{,}912 \log N_f - 0{,}565 \qquad R^2 = 0{,}9703 \qquad (3.15)$$

The highest correlation coefficient is determined when the regression between all tests is considered. This shows that the slope in the second phase in not dependent on the stress level applied, nor the loading frequency, but only related to the fatigue life. These results

seem in accordance with reports from [96] for a high-strength concrete, where all tests seemed to follow the same regression line independently on the loading frequency.

However, these results differ from the evolutions in [62], where lower number of cycles to failure are reached for a lower frequency. The regression curve for lower frequencies are situated in the left (shifting parallel) and different regression curves are obtained much more distinctly. It is worth noting that the specimen geometry in this case is cubic of 100mm and the strength 56 MPa. It is possible that the specimen geometry has a high influence on the damage mechanisms in compressive fatigue. Thus this is a factor which should be investigated in further research.

Despite eventual size influences, this method can be used to predict the failure of specimens at lower stress rates, which did not fail and need to be stopped due to time restrictions. Indeed, a specimen can be submitted to fatigue loading up to a certain number of cycles, in order to properly evaluate the second phase and the corresponding slope. Subsequently, the fatigue life can be calculated according to equation 3.15. This method might produce a more accurate prediction than the Wöhler curves, partially due to less scatter. In addition, according to [64], this method could be used in fatigue-damage monitoring for structures, but other factors such as the age of concrete and stress distribution should be taken into account.

3.3.8 Modelling based on creep behavior

When high constant compressive stresses are applied on concrete, a non-linearity in the relation creep strain and stress is manifested. A review of the related micro-mechanisms is given in section 1.4.6. The deterioration of concrete during creep tests is characterized by a reduction of stiffness and increase of inelastic strain. Additionally, the strain evolution shows a three-step mechanism similar to the damage mechanisms occurring during fatigue. The analogous response of concrete and grout under creep and fatigue motivated the present work, which consists in predicting the strain development and failure of the specimens, based on models proposed for basic creep. Nevertheless, a few substantial differences take place, which will be discussed further.

Equations (1.9) to (1.19) in chapter 1 describe the basic creep model used, coupled with damage based on previous work from [121,122]. The total strain is obtained as an addition of the elastic strain ε_{el} and basic creep ε_{bc}. The elastic strain is calculated with Hooke's law, whereas the total basic creep strain is given as the sum of all elementary basic creep strains $\varepsilon_{bc}^{i}(t)$:

$$\varepsilon_{bc}(t) = \sum_{i} \varepsilon_{bc}^{i}(t) \tag{3.16}$$

In a Kelvin-Voigt unit i, the basic strain evolution is obtained in the following relation:

$$\tilde{\sigma}(t) = k_{kv}^{i}\, \varepsilon_{kv}^{i}(t) + \eta_{kv}^{i}\, \dot{\varepsilon}_{kv}^{i}(t) \tag{3.17}$$

$$\dot{\varepsilon}_{am} = \frac{\tilde{\sigma}\,(t)}{\eta_{am}^{i}}\,\frac{t_n}{t} \tag{3.18}$$

In the numerical algorithm the effective stresses $\tilde{\sigma}(t)$ are linearized for each time step :

$$\tilde{\sigma}(t) = \tilde{\sigma}_n + \Delta\tilde{\sigma}_{n+1}\frac{(t - t_n)}{\Delta t_n} \tag{3.19}$$

With $t \in [t_n\,,\ t_{n+1}]$, $\Delta t_n = t_{n+1} - t_n$, $\Delta\tilde{\sigma}_{n+1} = \tilde{\sigma}_{n+1} - \tilde{\sigma}_n$ and t_n is the time at time-step number n.

Subsequently, the equivalent strain is computed according to equation (1.18) and by introducing the parameter β. In addition, the computations of the damage criterion and damage variable are carried out.

The stress-strain curves from compressive tests carried out for the reference mix are used for the identification of the mechanical parameters according to equation (1.19) and are presented in table 3-4.

Table 3-4 *Values of the mechanical parameters used in the simulations*

A_c	B_c	κ_0	ϑ	E_0 [Gpa]
2,5	853	7×10^{-4}	0,2	53

The parameters from table 3-4 are introduced in the model, however a slight difference is performed for the stiffness. This is due to the strain rate effects occurring in fatigue loading, which do not necessarily take place during creep. Based on the experimental data, these effects are manifested by an increase of stiffness up to 10%, compared to the quasi-static tests (depending on the stress level applied). Thus, a variation of the stiffness up to 10% is allowed in the identification process.

The basic creep parameters k_{kv} , η_{kv}, η_{am} and β are identified from a fatigue test carried out at $S_{c,max} = 0{,}80$ and $f = 10$ Hz. This choice is mainly due to lower scatter in number of cycles to failure at this stress level, compared to $S_{c,max} = 0{,}75$ and 0,90. In the model the stiffness is increased by 5 % at this stress level (compared to experimental quasi-static value), which is a similar level of increase to the mean secant modulus

determined in the first cycle for all tests. The parameters in table 3-4 are kept constant, therefore the main characteristics of basic creep are modelled by the means of 4 parameters. The age of loading is established at 56 days, corresponding to the time of experimental loading carried out at 8 weeks. It should be noted that the identification process does not have a unique solution and different combination of parameters can be adapted to describe the strain evolution. However, the identified parameters are the outcome of the fitting between the model and the compressive fatigue test at $S_{c,max}$ = 0,80 resulting in the lowest error. These parameters are shown in table 3-5.

Table 3-5 *Parameters of basic creep*

k_{kv} [Gpa]	η_{kv} [s]	η_{am} [Gpa]	β	E [Gpa]
350	50	1×10^5	0,4	55,7

Subsequently, the total strain evolution is simulated for the stress level $S_{c,max}$ = 0,80. For $\beta = 0$ when no interaction between creep and cracking is considered, the strain evolution is slightly underestimated and characterized by a linear relation in the second phase without reaching failure. This is graphically presented in figure 3.3-38. It can be noticed that the first phase and the linear relation is relatively correctly reproduced, with the current parameters.

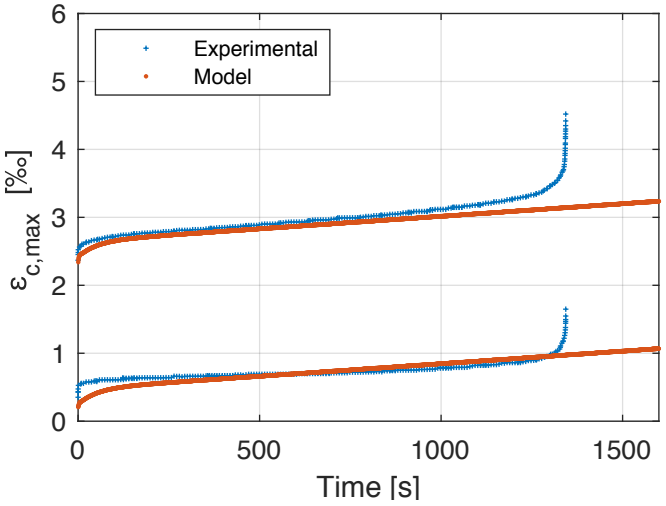

Figure 3.3-38 *Strain evolution at $S_{c,max}$ = 0,80 for β = 0*

The next step consists in adding the cracking interaction in order to predict the strain evolution more accurately and predict the failure of the specimen. If the parameter β is considered equal to 1, early failure occurs. Therefore it is possible to estimate its value by identification with the experimental tests and it lies between 0 and 1. The best fit is obtained for β = 0,4 and the experimental curve with the model are presented in figure 3.3-39. This parameter is larger than the reports in [122], however the same value has

been determined in [169]. It should be noted that this coefficient is a tool introduced for adapting a damage model, which was not initially intended to take into account the creep.

The strain evolution is given in relation to the testing duration despite the t_0 being considered at 56 days.

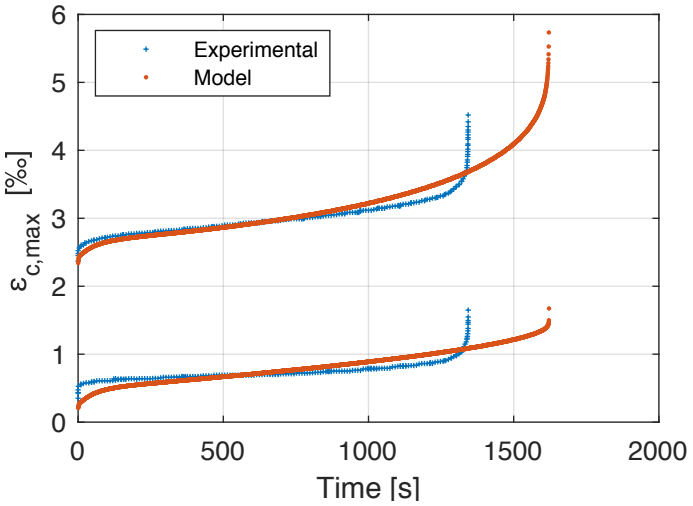

Figure 3.3-39 *Strain evolution at $S_{c,max}$ = 0,80 in compressive fatigue : comparison of the experimental test and simulation for β = 0,40*

The figure 3.3-39 presents a comparison of the experimental test and the simulation after introducing $\beta = 0{,}40$. The simulation fits relatively correctly the strain development in the present compressive fatigue test with a prediction of non-linearity in the third phase. Similar to the previous simulation with $\beta = 0$, the simulated strain is lower than the test in fatigue, especially up to 50% of the total life. This can be due to the fact that, as previously presented, friction between microcracks adds additional damage in fatigue and this is not significant for creep. After approximately 50% of the total life, the simulated strain presents a more rapid kinetics up to failure. The latter increase can be due to the fact that the model is based on basic creep and the interaction creep-cracking is introduced as a scalar value. Considering the scatter in the experimental fatigue tests, the predicted time of failure is in good agreement with the mean time of failure obtained for this stress level.

Based on the identified parameters, simulations are carried out for stress levels at 0,75 and 0,90 and are presented in figure 3.3-40 (left figures). It can firstly be noted that the three-step mechanism is well predicted, but the time of failure presents a few differences. At $S_{c,max} = 0{,}90$ the time of failure is overestimated, whereas at $S_{c,max} = 0{,}75$ failure occurs earlier. As mentioned previously, this is possibly due to the fact that β is a scalar value and the hypothesis that this parameter can predict the failure despite the stress level

applied is questionable. In practice, temperature increases within the specimen and in addition, drying occurs during test. Both these phenomena are not taken into account. The limited results in the literature do not allow a good understanding of a possible evolutions law for this parameter. Moreover, the strain rates occurring in fatigue are taken into account by an increase of the initial Young's modulus. However other parameters such as the Poisson's ratio are also altered during loading and this is not considered in the simulations. Thus, the current model can be considered as a first step in reproducing the strain development during fatigue, however other phenomena occurring in practice should be considered in further research.

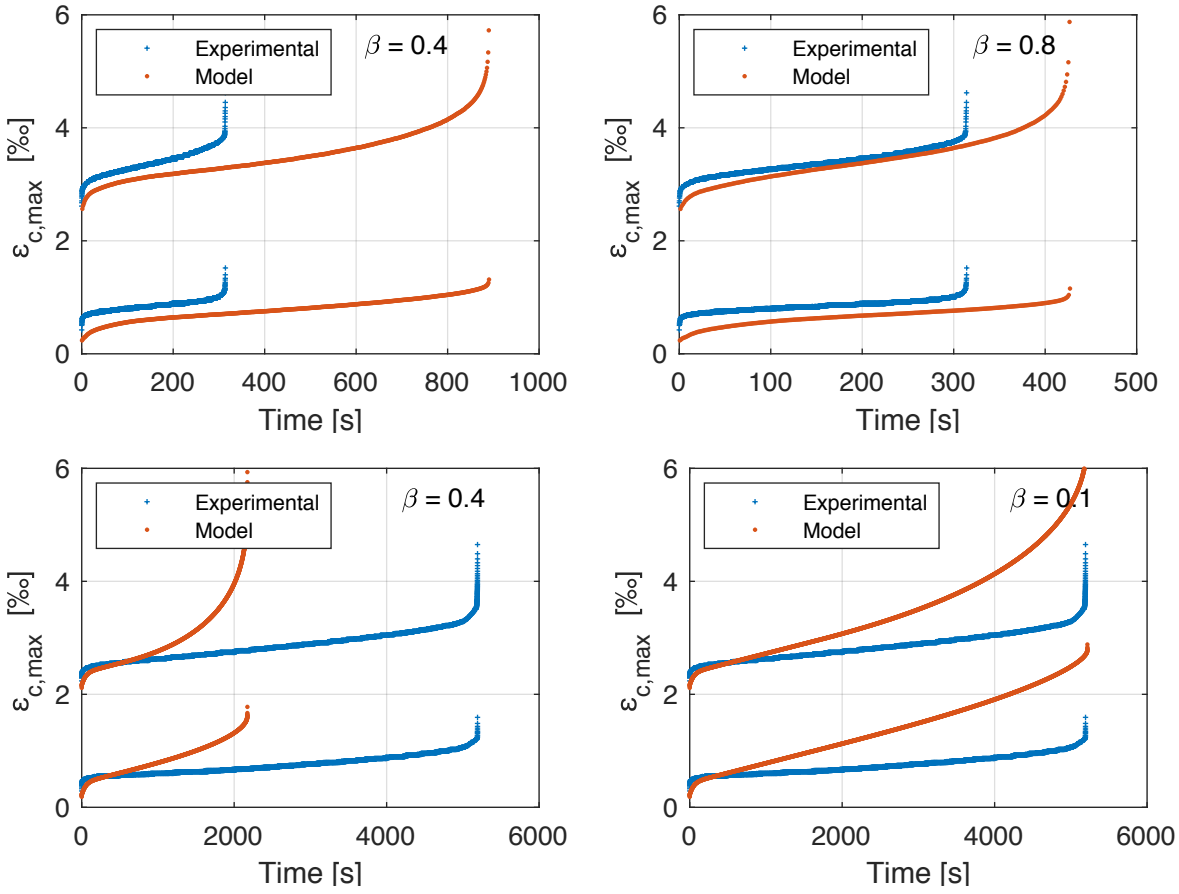

Figure 3.3-40 *Experimental and simulated strain evolutions for stress levels $S_{c,max} = 0{,}75$ (lower-left) and $S_{c,max} = 0{,}90$ (upper-left) for $\beta = 0{,}40$; Strain evolutions and adjusted parameter β for $S_{c,max} = 0{,}75$ (lower-right) and $S_{c,max} = 0{,}90$ (upper-right)*

An attempt is conducted to adapt the parameter β for the present tests at the stress levels 0,90 and 0,75, presented in the right figures 3.3-40. A coefficient of 0,8 and 0,1 respectively is achieved, which allows in a better description of the time of failure. Nevertheless, the variation of this parameter depending on the stress level applied is a strong hypothesis and has not been proposed in the literature.

Overall, the present model is able to simulate the three-step damage mechanism observed in compressive fatigue. Moreover, for higher stress levels, failure occurs earlier. This is resumed graphically in figure 3.3-41, where the time of failure for the three stress levels simulated with $\beta = 0{,}4$ is presented. Additionally, the mean time of failure for each stress level with all data values obtained experimentally are also plotted. It should be noted that the fatigue tests in concrete and grout are characterized by scatter in terms of time of failure, which is mainly due to the heterogenous nature of the material. Therefore, not only the mean values should be considered in the analysis. In figure 3.3-41 the mean values are presented with a larger font than the time of failure for each test.

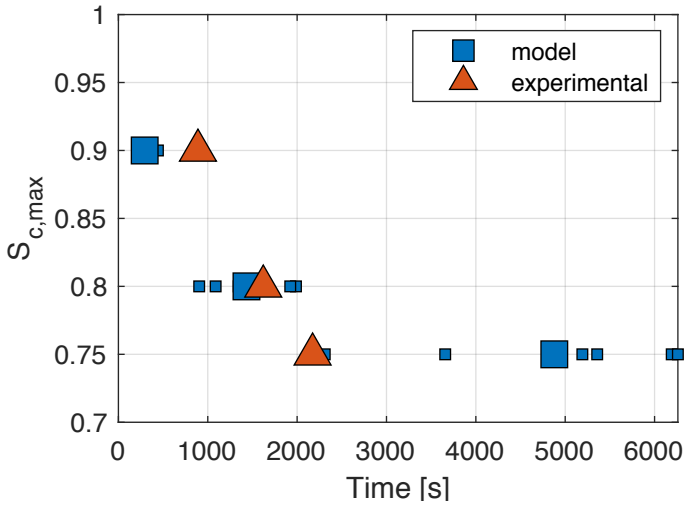

Figure 3.3-41 *Time of failure for all tests with mean values for each stress level and the time of failure for $\beta = 0{,}40$*

This section highlighted the similar behavior manifested in fatigue and creep, both being time-dependent. The fatigue loading as conducted in these tests consists in applying a sinusoidal evolution between two constant stress levels. Whereas, creep is manifested as the deformation under a sustained load. The related damage mechanism is similar, with the secondary phase dominating the most of lifetime. However higher rates tend to take place in fatigue, due to additional effects occurring during loading such as temperature increase, early microcracking, friction between microcracks and drying. The proposed rheological model is able to reproduce the non-linearities observed in the strain development for different stress levels, however the time of failure is not quite accurately predicted. Additionally, a few differences in the secondary strain rates can be observed. An evolution law of the coupling creep-damage parameter should be considered and additional effects occurring during fatigue loading should also be included.

Therefore, despite similarities between creep and fatigue, a few differences take place. It should not be neglected that during fatigue, microcracks are generated early when the loading is applied and this does not seem to take place in creep. For future work, it could

be considered to carry out experimental tests in both fatigue and creep with similar specimen dimensions and estimate the difference in strain development or stiffness deterioration.

3.4 Size effect on fatigue behavior

All the current fatigue analysis in this thesis and the study of influencing parameters for high-strength grouts are based on experimental tests carried out on cylindrical specimens with D/H=1/2 and a diameter of 60mm. This choice was partially conditioned by the DNV guideline [1], where a D/H ratio of ½ is suggested. Nevertheless, a higher specimen size is recommended in this guideline : 150/300 mm. Due to machine capacity limits and the relatively high strength of the grout tested, experiments with these dimensions could not be carried out. One can question the suitability of using smaller specimens, not only in terms of strength and number of cycles, but also whether the damage mechanisms are independent on the specimen size or shape. Indeed, it is commonly observed in the literature, the implementation of fatigue tests on cube specimens or cylinders with higher slenderness. Moreover, additional knowledge on the influence of the size effect is necessary for a better prediction of the grout behavior for structures *in-situ*, where inevitably higher dimensions than in laboratory conditions are employed.

Subsequently, this work was oriented towards the investigation of this parameter and an increased slenderness is adopted in this regard. Thus, specimens with D/H = 60/180 mm are tested in quasi-static and fatigue tests and are confronted to the reference specimens in terms of fatigue life and damage evolution. Ideally, other shapes of specimens and higher diameter dimensions should also be considered for a more complete analysis. However, due to time restrictions and machine capacity limits this could not be carried out within the timeline of this thesis. Nevertheless, the study on the influence of increased slenderness is a legitimate choice, due to a common application of grout in offshore wind turbines, typically characterized by an elongated shape.

It is worth noting that the molds used for these specimens are composed of the same material as the reference specimens and the mixing protocol is strictly followed identically. The protection and fixation plates for the laser sensors are adapted for the longer specimens. Small variations could be induced as a result of different batches used between specimens of both lengths. In the following figures specimens with lengths of 120mm and 180mm will be referred to H120 and H180, respectively. Firstly, the quasi-static strength is measured based on 6 specimens. The stress-strain evolution curves for H180 in comparison with the specimens H120 are presented in figure 3.4-1.

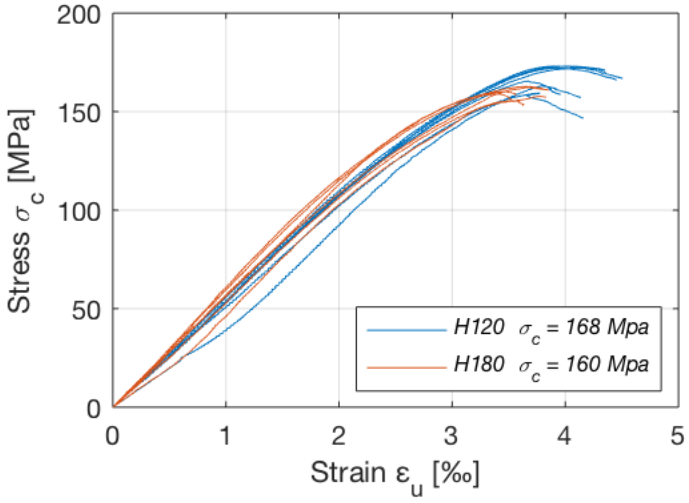

Figure 3.4-1 *Quasi-static tests for the reference grout at two different specimen lengths (H=120mm and H=180mm)*

A decrease of 4,8% in the compressive strength is observed from figure 3.4-1. Moreover, the increase in specimen slenderness resulted in a slight increase of the stiffness from 54GPa to 57GPa, however the pre-peak regime is very similar. After reaching the peak load, a more sudden drop takes place up to the failure of the specimen. This behavior seems in accordance with reports from Van Mier [170] where it is suggested that a higher slenderness leads to a lower ductility. Moreover, a snap-back behavior is produced in the post-peak regime, which can be expected for specimens with higher slenderness. The decrease in strength can be explained by the frictional restraint created due to mismatch in lateral expansion between loading platens and the specimen [171]. The unrestrained areas are therefore larger for specimens with a higher slenderness.

Fatigue tests

Based on the compressive strength measured on the specimens with a height of 180mm, it was proceeded to the definition of maximum stress levels applied for the compressive fatigue loading, where the test procedure is the same as for H120. The tests are carried out at three stress levels and at a loading frequency of f =10 Hz. Overall, smaller number of cycles to failure are reached for the specimens with a higher slenderness, as presented in figure 3.4-2 and in appendix B-9. This is valid for the three stress levels tested here. Indeed, as suggested in the literature for quasi-static loading, the presence of a higher specimen size represents an increased likelihood to attain the weak link and thus results in earlier failure. This effect and the presence of lower frictional restraint leads to a reduced strength and lower number of cycles to failure.

A larger difference is noticeable for a higher stress level, which is different from reports in [73] where a much larger difference in terms of number of cycles is reached for a lower stress level. Moreover, the number of cycles to failure present a larger scatter compared

to smaller size specimens. In comparison with the fatigue life standards, all specimens are above the recommendations from the DNV guideline [1]. Two specimens at $S_{c,max} = 0{,}75$ and one specimen at $S_{c,max} = 0{,}80$ are situated below the recommended curve from fib [46]. Overall, the number of cycles to failure for D/H = 1/3 respect the Model code 2010 standard and are closer to the prescribed estimation of number of cycles to failure, whereas tests on specimens with a length of 120mm tend to overestimate the fatigue life.

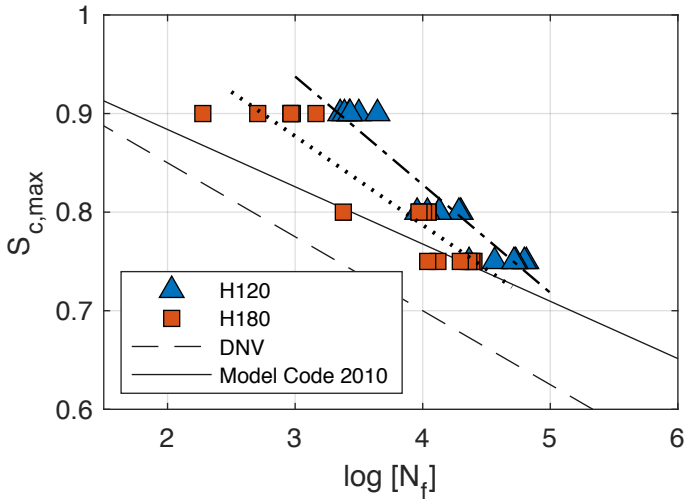

Figure 3.4-2 *Number of cycles to failure for the reference grout at two different specimen lengths (H=120mm and H=180mm) ; f = 10Hz*

A less ductile behavior was highlighted for the quasi-static tests. Therefore, the strain development and the strains at failure are also considered in the assessment of size effect. Figure 3.4-3 resumes all strains at failure ε_f and the quasi-static stress-strain curves for the specimens H180.

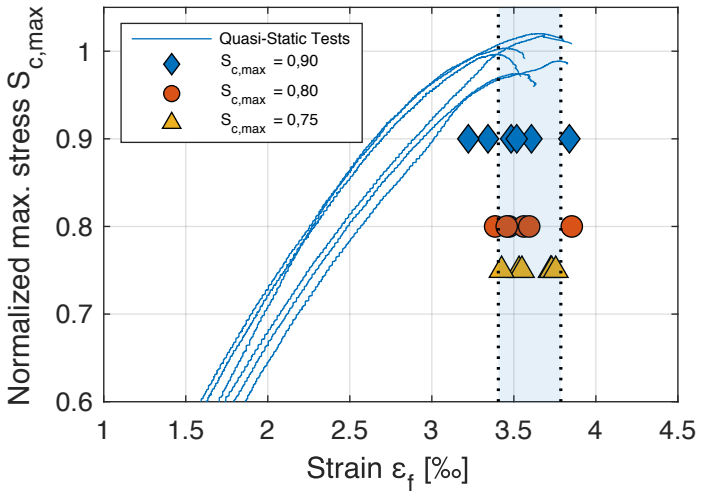

Figure 3.4-3 *Quasi-static tests and strains at failure in fatigue tests for H = 180mm*

It is promptly obvious that lower final strains are attained, compared to reference tests at H120, which was previously shown in figure 3.3-22. Not only the values are lower, but

also most of the data are included within the ranges of strains at peak load from quasi-static tests, contrarily of results for H120 specimens. In the softening regime a lower ductility with increasing slenderness is found, and this regime is associated with the coalescence of microcracks and the capacity to undergo plastic deformation without failure. Therefore, the lower strains at failure in fatigue can be related to the lack of capacity to deform, when the strain development reaches the phase transition II-III. For this reason, strain evolutions for all tests are analyzed.

In order to give more accurate evaluations of the size effect on the damage behavior of the grout, specimens which endured similar number of cycles to failure within the same maximum stress level are confronted. Therefore, in figure 3.4-4 (b) to (f) one specimen of each length is compared in terms of energy dissipation, strain development and temperature increase for $S_{c,max} = 0{,}80$ (left figures) and $S_{c,max} = 0{,}75$ (right figures). Similarly to strains at failure, the initial strains ε_i are smaller for all tests carried out on specimens with a higher length. It is possible that the observed increase of brittleness noticed in quasi-static tests is an influencing factor on the lower initial deformation observed. Moreover, the evolution of phase II is very similar for these tests indicating a similar damage evolution. This is also verified when the gradients of the second phase of all tests at H120 and H180 are compared (figure 3.4-4 (a)). No significant differences are observed and the regression lines are almost overlapped. The main distinction between the curves in strain evolution in (c) and (d) occurs after the transition phase II-III, where microcracks start to connect and the failure is reached more rapidly. Thus, due to a less ductile behavior, a more rapid failure will occur in phase III and lead to lower strains at failure, for a higher specimen length.

Moreover, the energy dissipation in figure 3.4-4 (b) at $S_{c,max} = 0{,}75$ shows a very similar evolution, but with a slightly higher slope for the H180 specimen which might be due to the higher temperature increase. Indeed, the assessment of energy dissipation is carried out from the hysteresis $\sigma - \varepsilon$ at each cycle, where smaller strains measured led to lower values. The evolution of temperature during the test is also displayed for the same tests at $S_{c,max} = 0{,}80$ (e) and $S_{c,max} = 0{,}75$ (f). The temperature increases at higher values and with higher rates for specimens with a higher length at similar number of cycles to failure. Indeed, comparing the mean total temperature attained for all specimens between the two lengths has no sense, due to different test durations, which conditions the total increase. Therefore, only tests with comparable number of cycles to failure are presented. Thus, at $S_{c,max} = 0{,}75$ a total temperature rise of 33 K and 24 K, is reached for H180 and H120 respectively and at $S_{c,max} = 0{,}80$ the increase is 22 K and 13 K. The higher temperature increase for a larger specimen is to a certain extent due to slower heat transfer with the environment leading to higher temperature gradients. It is possible that additional damage is induced due to this effect as presented, in the energy dissipation evolution.

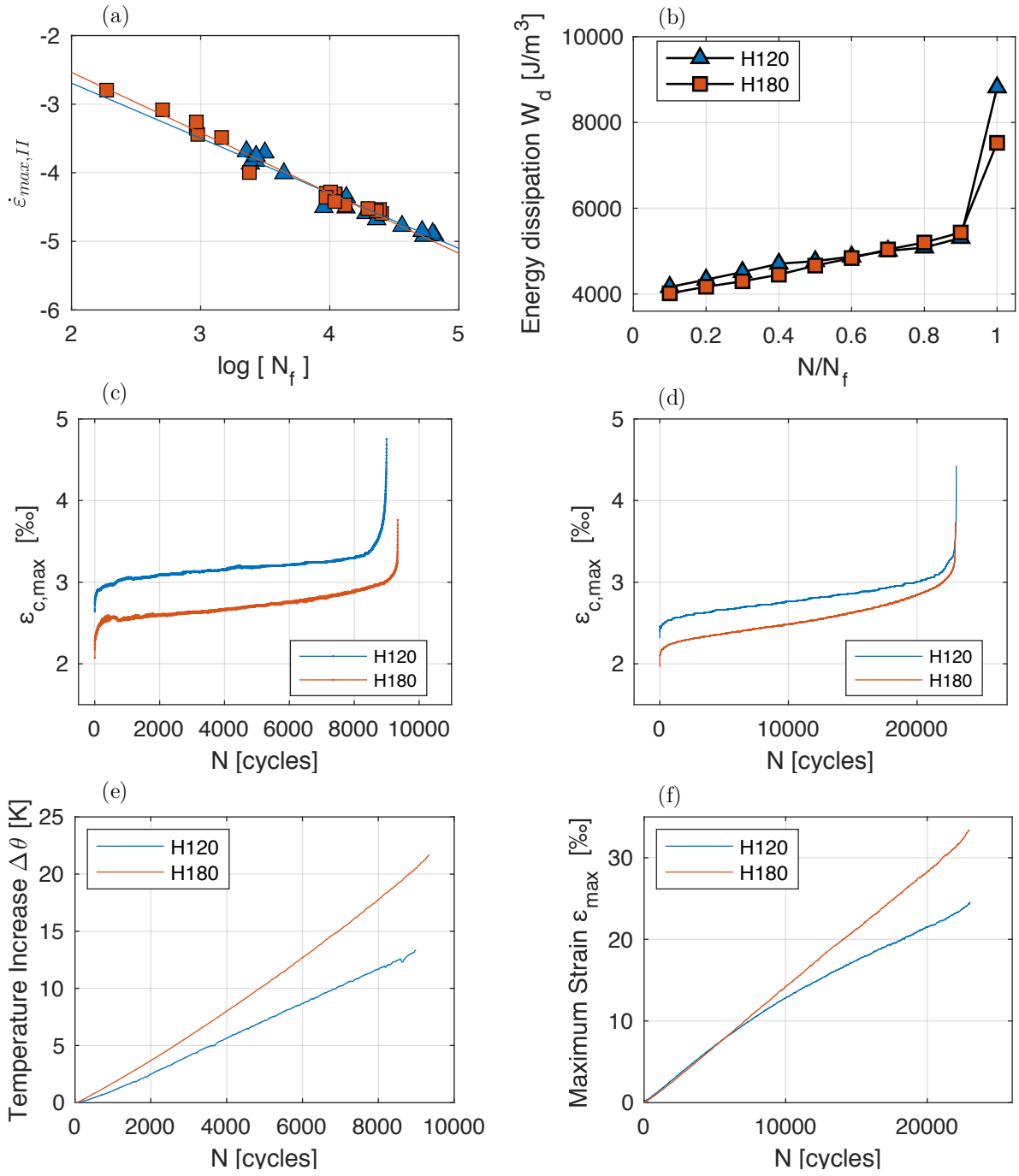

Figure 3.4-4 *Secondary strain rate for all specimens of two different lengths 120mm and 180mm (a); Comparison of two specimens with different lengths at similar number of cycles to failure ((b)-(f)) at two stress levels, $S_{c,max} = 0{,}75$ (right figures) $S_{c,max} = 0{,}80$ (left figures)*

The stiffness for the large specimens slightly increased in quasi-static tests. The same tendency is observed when comparing the secant modulus at the first cycle of fatigue loading, where $E_{s,1} = 58$ GPa for H120 and $E_{s,1} = 62$ GPa for H180. The evolutions curves of the secant modulus can be found in appendix B-10. The total loss of stiffness is much lower for the larger specimens as presented in table 3.6. It can be due to the increased brittleness observed for these specimens.

Table 3-6 *Comparison of total stiffness loss in fatigue in relation to the first cycle*

Stress Levels	**ΔE** [%]	
	H 120	*H 180*
0,90	26 ± 4,2	14 ± 5,9
0,80	29 ± 5,5	23 ± 6,5
0,75	35 ± 2,4	39 ± 3,5

From all the data analysis in this section, it can be concluded that overall similar damage mechanisms take place in specimens with different slenderness. However, clear differences are shown when analysis of strain and stiffness is carried out. A lower quasi-static strength and lower number of cycles to failure are reached for the specimens with a larger D/H ratio. The increased stiffness in quasi-static tests and in fatigue during the first cycle (compared to the reference specimens) lead to lower initial and final strains. In addition, these specimens are characterized by a lower ductility. The higher temperature increase per cycle also resulted in slightly higher rate of energy dissipation. Nevertheless, the rates in the second phase for energy dissipation or strain development are very similar.

3.5 Damage assessment in relation to microcrack development

The aim of this section is firstly to suggest a qualitative assessment of the damage evolution occurring during the three phases of compressive fatigue loading. Thus far, it is concluded from analysis of the strain, stiffness development and energy dissipation that microcracks are initiated very early in the fatigue process and stable crack growth takes place up to failure. However, very rare attempts have been found in the literature to use image analysis, such as Digital Image Correlation on the surface of the specimen [74] or X-ray CT scan [172], in order to show the crack state in the specimen. For the compressive fatigue tests, both methods were tested. However, only results obtained from DIC are presented, as the resolution from CT scan used did not allow a proper detections of microcracks.

3.5.1 Qualitative microcrack state with DIC

The DIC technique is presented in chapter 2 for the purpose of use in flexural tests for strain field measurements. For tests in compression, the goal was mainly to give a qualitative description of the microcrack state within the specimen. Therefore only one digital camera is used. For a cylindrical shaped specimen, at least three cameras should

be used to reconstruct a three-dimensional strain field by the means of the stereo-correlation technique. Nevertheless, this was not the purpose of this test and one single digital camera resulted to be sufficient in order to capture the crack evolution within the specimen.

The method used for image capturing is different from the one followed in flexural tests. The camera used is a Canon EOS 60D with a lens 18-55mm. The loading is stopped for 1 minute in the upper and lower stress level in order to allow the image capture. The capturing method is shown in the following figures, where blocks of different load cycles are applied to the specimen. The first image is taken when the machine plates are in contact with the specimen prior to the test and at a low force applied of approximately 100N. The first blocks of cycles are carried out at regular intervals such as 3 000, 20 000, 40 000 and 100 000 cycles and afterwards the intervals are regulated depending on the evolution of the test. The measurements are carried out for two tests at $S_{c,max} = 0{,}70$ and at $f = 10$ Hz.

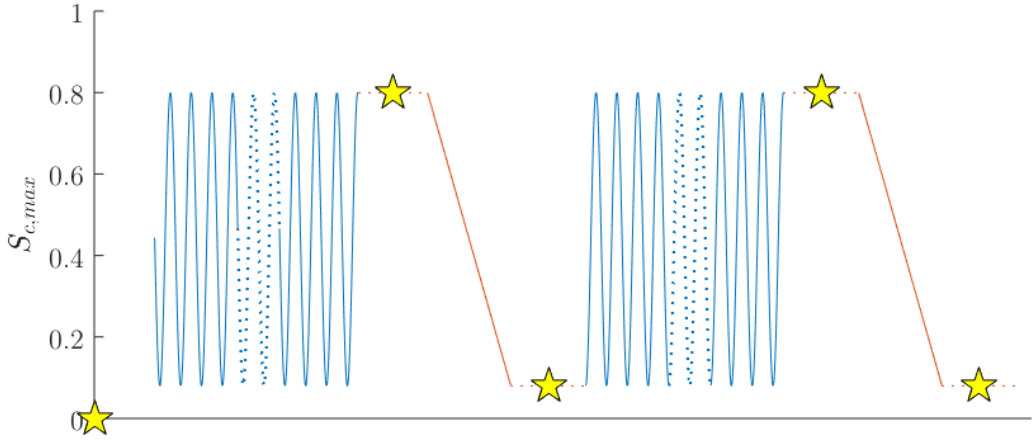

Figure 3.5-1 *Schematic representation of image acquisition in fatigue compressive tests*

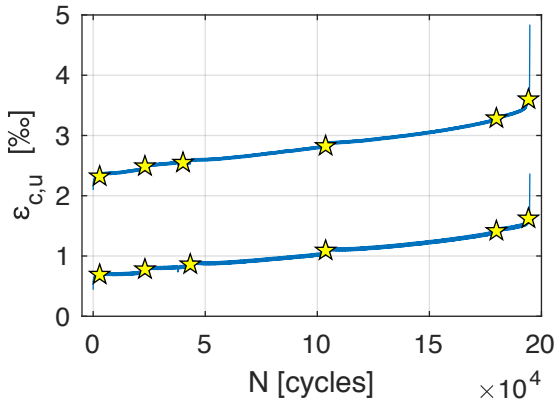

Figure 3.5-2 *Strain evolution for one specimen at f=10Hz and levels of image acquisition*

In order to correctly use the DIC technique, it is important to assess the uncertainty of the ROI area. The definition of the ROI is shown in figure 3.5-3 (a). This image and the resulting ones from DIC are presented in a reversed direction. Due to the cylindrical shape of the specimen, approximately 5 mm on each side is omitted from the analysis. The histogram of the gray level of the speckle (see figure 3.5-3 (b)) and the standard deviation are analyzed. Two successive images before loading are used for this purpose, and the standard deviation is 0,02 pixels which is relatively low. It can be seen that the histogram covers all levels.

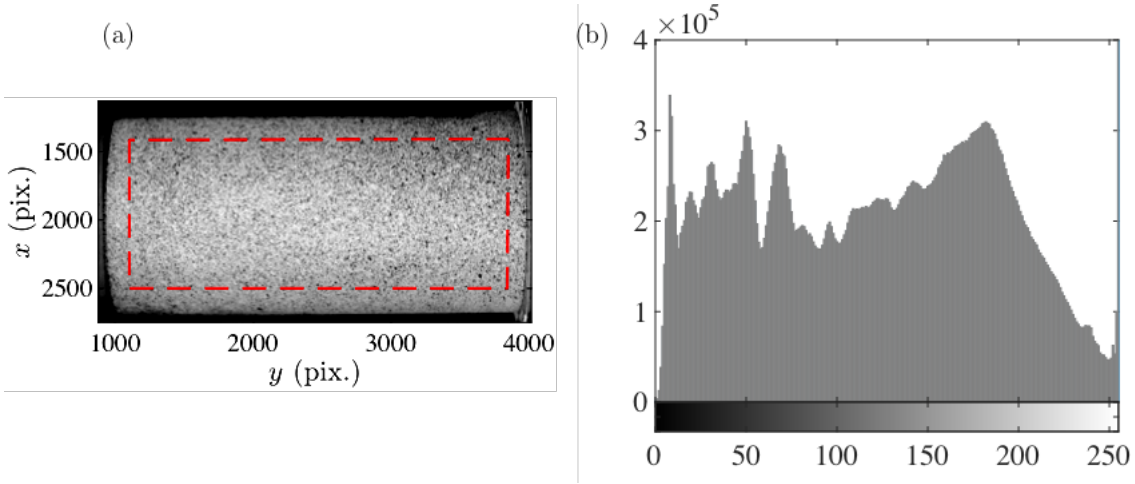

Figure 3.5-3 *Definition of the Region of Interest (a) ; Histogram of the grey level (b)*

The image correlation is carried out with the correlation code RT3, developed in LMT Cachan, between the initial and the deformed images. The discontinuities in the field indicate the presence of cracks. In figure 3.5-4, the evolution of the microcrack state in the surface of the specimen is displayed for different ratios of fatigue life. All images shown coincide with capturing at the maximum stress level $S_{c,max}$. The scale for images acquired after 50% of the fatigue life has been slightly changed in order to allow a better observation. It is worth noting that the state of the surface reflects the state of the specimen only to a limited extent, however it allows a first comprehension of the concentration areas and the evolution of cracks.

Both tests show an evolution of the microcrack state with increasing number of cycles and the orientation is parallel to the loading direction. The crack length and opening increase progressively. In specimen 2 an image is acquired at 3000 cycles corresponding to approximately 2% of the fatigue life, which is situated within the first phase of the strain development. When compared with the reference image and at the same scale, small activity areas can be observed. It confirms that during this phase, small cracks are initiated in the specimen. In reality, the density of these microcracks could be larger, but microcracks with a small length could not be detected with the camera and lens used here. Moreover, it was decided to observe the entire length of the specimen (120mm) in

order to give a global evolution of the microcrack state. Therefore, the pixel size is 0,04 mm. A smaller area with a higher image resolution could be observed in order to have a better estimation of the first microcracks appearing within the specimen.

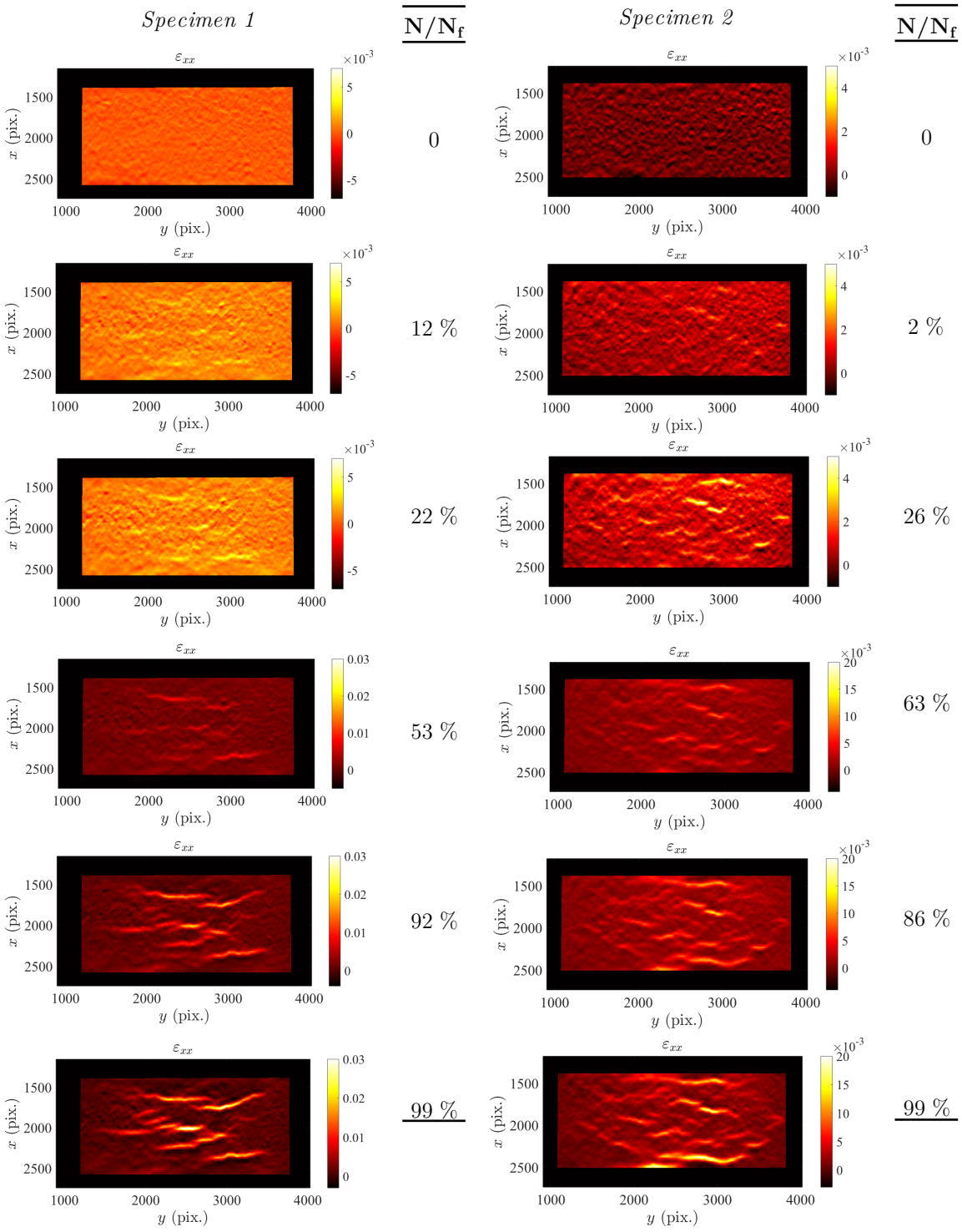

Figure 3.5-4 *Crack state evolution in a fatigue loaded grout for different ratios of fatigue life at the maximum stress level*

More microcracks are observed in specimen 1 at 12% of the fatigue life, which corresponds to the first part of phase II. The cracks observed in the first images continue to grow in size in the following, especially in the last three images. Moreover, crack branching can be observed in the extremities of some cracks, which may due to the presence of high-strength aggregates. This is not to be confounded with the crack coalescence which is observable at 92% or higher. The crack state in a microscale level will also be analyzed further by means of SEM observations.

For both specimens it was possible to obtain images close to failure, corresponding to 99% of the total fatigue life. In both cases, "long" and "wide" microcracks are observed in a relatively homogenous distribution. However, close to the extremities along the height of the specimen (horizontal axis), less microcracks are present. This can be due to the lateral boundary restraint near the edges, which is also observed in post-Mortem specimens in a cone shape. The images in figure 3.3-4 displayed the crack evolution at the maximum stress level applied. The images taken at the minimum stress level can be found in appendix B-11. Most of the microcracks are still visible, however due to crack closure during unloading, which implies a smaller observable width, they appear at a lower intensity.

In the transverse direction, only a few cracks are visible close to failure at 99% of the total fatigue life. An example is shown for the specimen 2, in figure 3.4-5. The observed microcracks in the transverse direction are much smaller in size. Indeed, similar to compression in quasi-static tests, cracking occurs parallel to the direction of loading. However, close to failure, due to tensile forces in the transverse direction, horizontal cracks may appear.

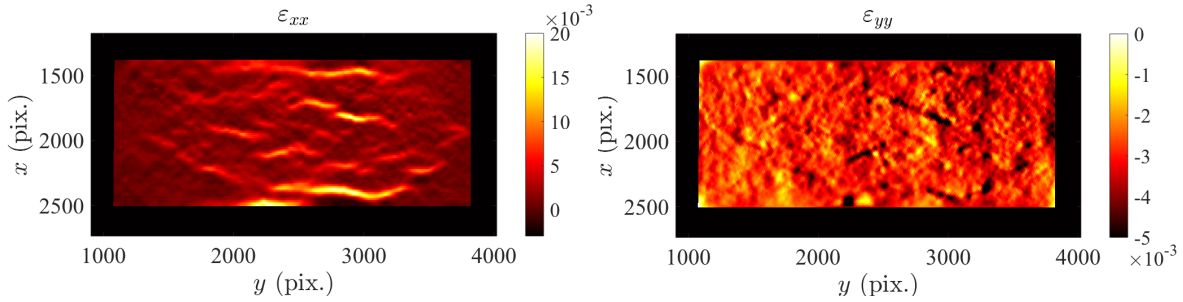

Figure 3.5-5 *Longitudinal crack state (left) ; Transverse cracks (right) for specimen 2*

The evolution of the microcrack state from the images by the means of the DIC technique seem to be in correlation with the strain development and damage mechanisms mentioned previously. The appearance of microcracks is detected during the first phase and they increase in length in the following cycles. Close to failure, the propagated microcracks connect and lead the specimen to failure.

3.5.2 Damage state evaluation with porosity measurements

Two methods are commonly used in cementitious materials for the assessment of the total pore volume : the mercury intrusion porosimetry and total water porosity. When the grout or concrete specimens have an increased state of damage, especially in fatigue loading close to failure, it is possible to expect a higher level of interconnected porous network. For this reason the two techniques are combined to give an assessment of the total porosity and the distribution of the pore volume.

3.5.2.1 Mercury Intrusion Porosimetry (MIP)

The Mercury Intrusion Porosimetry technique gives the pore size distribution of pores with a size up to 116 µm. The outcome of this method is complementary to the DIC technique aforementioned, where microcracks showed a relatively larger size. Moreover the MIP technique can overestimate the total volume of small pores, nevertheless in this analysis the absolute values are not required, but a relative analysis of the evolution of the pore size after damage in relation to the initial state.

Therefore, from an intact specimen after 8 weeks of curing, a cubic sample of 10mm in length is extracted from the core of the specimen. Two other specimens from the same batch were tested under compressive fatigue and the tests were stopped shortly before failure at transition phase II-III and approximately at the first transition phase I-II. A sample was extracted from these specimens and analysed with MIP, in order to estimate an eventual evolution of the pore size distribution.

In figure 3.5-6, the results for the three specimen types are displayed. The pores with a diameter between 6 –116 µm demonstrate an increase in the distribution, when comparing the intact state up to the damaged state II-III. Indeed, the z-axis represents the distribution [%] for each group of pores. The pores within this size group represent approximately 6 %, 12 % and 37 % of the total porosity for the intact state, transition I-II and transition II-III, respectively. The fatigue loading has generated an increase of pores with a larger size than 6 µm, which is due to crack propagation and connection leading to an increase of the open porosity. In previous section it was shown that the nucleated microcracks during the first phase, propagate with the evolution of the fatigue loading. Therefore, this seems to be correlated with the results from the MIP technique.

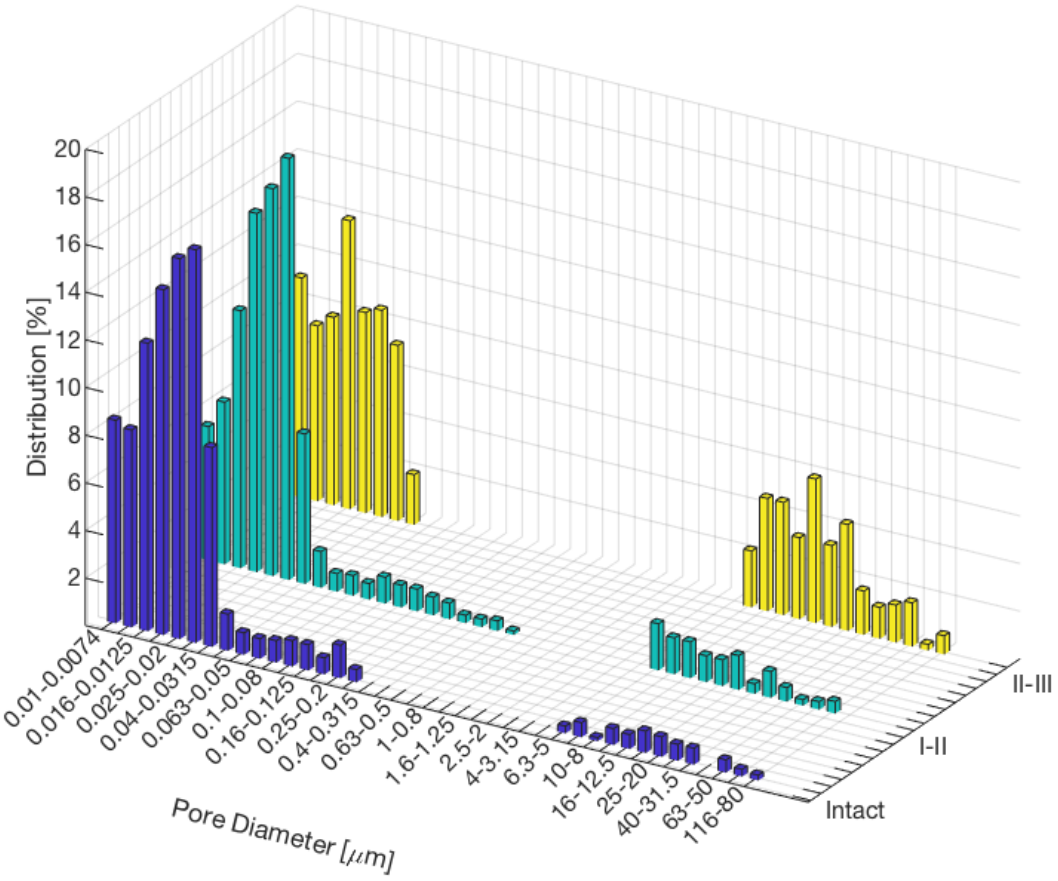

Figure 3.5-6 *Pore size distribution for specimen in intact state and at transition phases I-II and II-III*

3.5.2.2 Total water porosity

The total water porosity is also assessed for specimens in the same scenario as in MIP technique. Nevertheless, the specimens are evaluated as a whole and no samples are extracted from the specimens. The testing method is described in section 2.5.2.3 and the test results are summarized in table 3-7.

Table 3-7 *Total water porosity for specimens in intact state and in transition phases I-II and II-III*

	Intact state	**Transition I-II**	**Transition II-III**
Total water porosity [%]	2,2	2,3	3,1

Firstly, the values of the total water porosity are very low. For a high strength concrete these values are situated between 8-10%, according to results reported in the literature. Due to an optimized microstructure, the grout should have a lower porosity than concrete. Nevertheless, these values are lower than expected and it might be related to

the test conditions. The specimens were dried only 10 days at 60°C in order to avoid additional damage at 105°C, as suggested in the standard. This outcomes only to a partial drying and therefore the water is not totally impregnated. However, if the results of the damaged specimens are considered in relative values to the intact specimens, a total increase of porosity is observed with increasing damage. The increase in total porosity, is related to the coalescence of microcracks leading to the appearance of macrocracks and increase in open porosity, as demonstrated from mercury intrusion porosimetry measurements and images during fatigue loading with the digital image correlation.

3.6 Post-Mortem examinations

All previous sections were focused on the analysis of damage mechanisms in a high-strength grout mix based on quantitative and qualitative measurements during the compressive fatigue loading. In this section, observations are carried out after the failure of the specimens in quasi-static and fatigue, in order to estimate if any differences take place in failure modes. In addition, microscopic observations with Scanning Electron Microscopy are carried out for crack pattern investigations.

3.6.1 Macroscopic observations

In quasi-static tests, the irreversible deformations and stress concentrations are distributed over the entire sample and do not result in localization before reaching the peak. However, in the post-peak regime the microcracks connect to form a macrocrack and the damage is localized [170]. It results in a “hour-glass” type of failure as shown in figure 3.6-1.

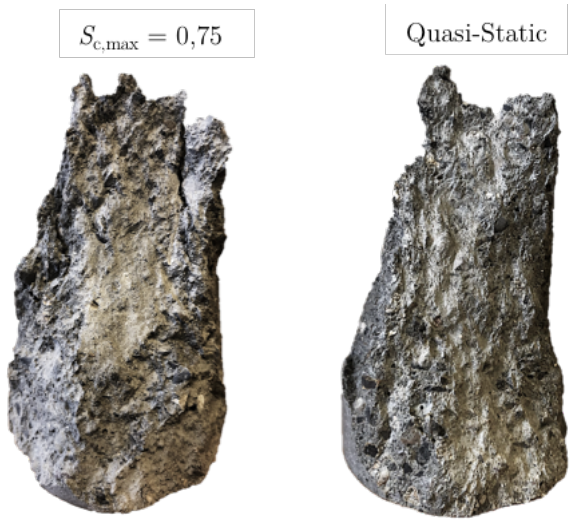

Figure 3.6-1 *Hour-glass type of failure in fatigue and quasi-static test*

This type of failure has been observed for all quasi-static and fatigue tests. However, a main difference can be pointed out with a closer observation in the remaining cone-shaped component. Some friction traces are observable with the naked-eye on the fracture surface from fatigue tests. These are local areas observed in different parts of the fracture surface and characterized by a light color. It was suggested earlier that the temperature increase in the specimen is the outcome of friction in the microcracks and the interface aggregate-matrix. Therefore the parallel traces, similar to fatigue striation in steel materials, might be linked to friction and crack propagation. They are located mainly in central part of the specimen. A closer observation is given in the next section, by SEM images.

One should not confuse these local areas, with long vertical traces along the fracture surface (observable also from quasi-static tests), which occur mainly just before failure due to sliding between two sections. Indeed, these vertical traces are longer, located in a larger area and are not characterized by a light color.

3.6.2 Microscopic observations – SEM

Scanning electron microscopy is used for closer examinations of the fracture surface in specimens submitted to quasi-static and fatigue tests, mainly for determining crack patterns. In a sliced sample as shown in figure 3.6-2 (a), different crack paths are observed macroscopically: around the aggregates in the ITZ area, crack branching when a microcrack reaches an aggregate and through the aggregate. The crack paths cannot be clearly observed on the fracture surfaces, thus SEM images are used for a more accurate investigation.

In images (b) and (c) cracks within the cement matrix are presented. Friction traces are also present in figure (c) and shown more closely in (d). These traces are presented as parallel and smooth lines, which form during crack propagation. Figures (e) and (f) represent a macrocrack going through an aggregate and in (g) and (h), crack branching occurs in the interface and through the aggregate. These types of cracking are also observed in other areas of the specimen. Thus, it can be concluded that different types of crack patterns occur during fatigue loading for a high-strength grout. Moreover, they can be considered as macrocracks created during fatigue loading. Indeed, in the observation of *micro*cracks it can be arduous to distinguish whether they result from specimen shrinkage, drying, during preparation process or from fatigue loading. For the images presented here and from observations with the DIC technique in the surface of the specimen close to failure, it is assumed that cracking due to fatigue loading is in the form of long cracks and with a relatively large width. Whereas, in cracking due to hydration process microcracks are diffused and shorter in length and therefore are not considered in this section.

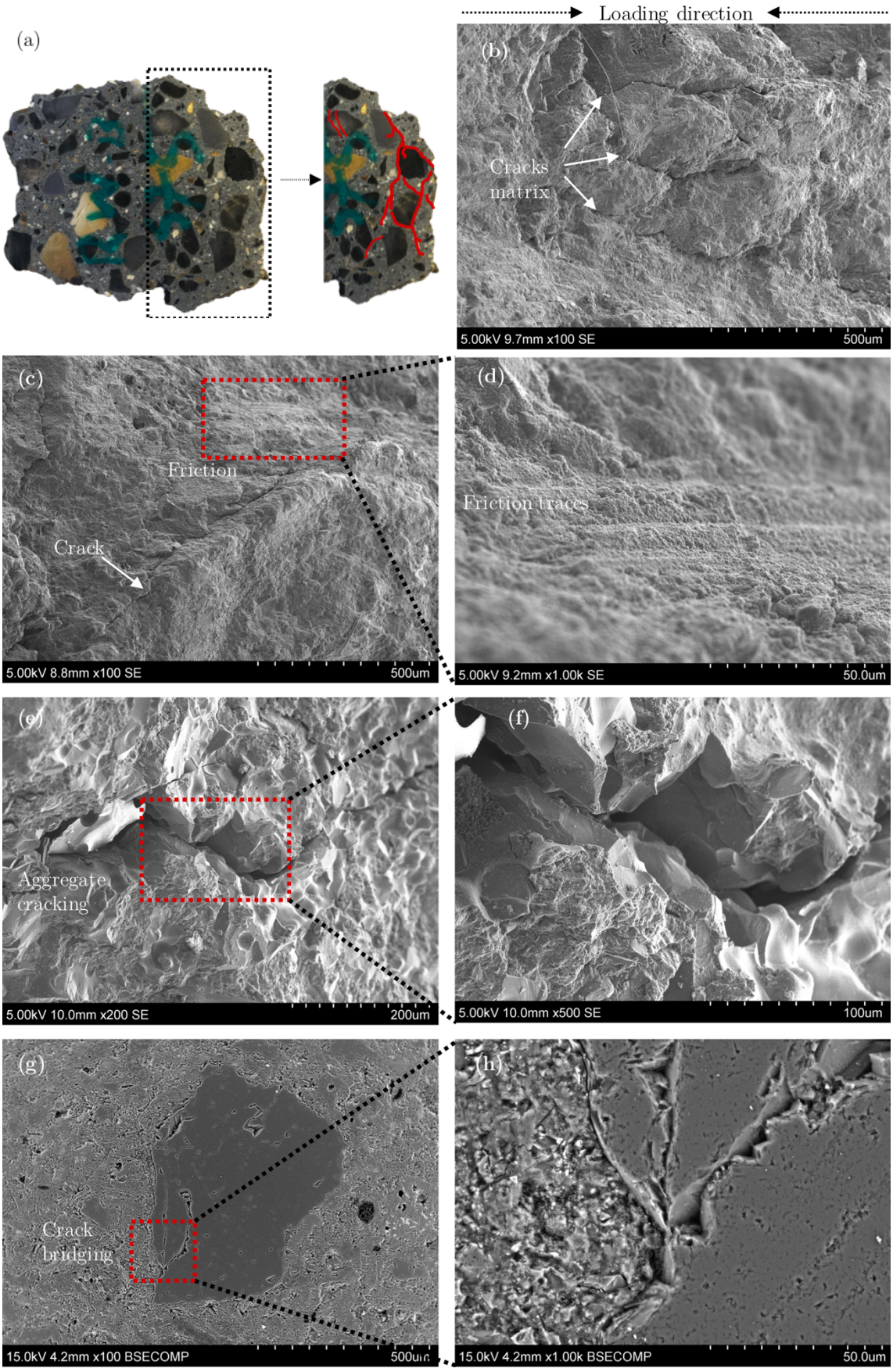

Figure 3.6-2 *SEM images of different crack types (b)-(h) ; Macroscopic observation of crack development in a plane cut of a specimen (a)*

3.7 Conclusions

Reminder of objectives

The aim of this chapter was essentially to provide a detailed description of mechanisms occurring during compressive fatigue of high-strength grouts. Despite recent studies in the literature on fatigue behavior of cementitious materials, some questions have not found consensus. The current work was mainly experimental and aims to give a thorough analysis of involved mechanisms in the damage process and the influencing factors. A few questions were addressed in the conclusions section of the first chapter, resulting as an outcome of literature review. They are related to the affected material properties during fatigue process, changes in stress-strain relation compared to quasi-static, appropriate indicators reflecting the deterioration, involved structural changes and differences between creep and fatigue. Some of the these issues are discussed below.

Main influencing parameters on fatigue life

Firstly, the fatigue life according to Wöhler curves is investigated, where despite data scatter a linear relation seems to take place in a semi-logarithmic scale. However, it appears from the current tests, that when specimens are tested at a maximum stress level below the elastic limit, the number of cycles to failure do not follow the same regression and a *bilinear relation* takes place. For these stress levels, the deterioration occurs in an evolving process with low damage created in the first phase. Overall, higher stresses applied lead to lower number of cycles to failure, due to higher local stress concentrations exceeding locally the material capacity. Whereas at lower stress levels, time-dependent viscous components develop.

One main influencing parameter on fatigue life and behavior of the grout is the loading frequency and as a result the *temperature* generation. Indeed, due to stress rate effects a higher fatigue life is expected, for a higher loading frequency applied. Nevertheless, a competing phenomenon occurs at lower stress levels, where high levels of temperature are generated at 10Hz, thereby shortening the fatigue life. This leads to shorter fatigue life for a higher loading frequency. The change of tendency can be explained by an overlap of four mechanisms : the increased water vapor pressure and the incompatibility of the coefficients of thermal expansion in a microscale level. Secondly, the presence of thermal and drying gradients. A new test type was conceived in order to define the origin of the temperature generation. Indeed, specimens with a “dense” microcrack state and

specimens in intact state were compared under the same fatigue loading conditions. The temperature increased to a higher level and with a higher rate for the damaged specimens. This demonstrated that the temperature is generated by friction in the microcracks. SEM observations in the failure surface of specimens submitted to fatigue loading also showed the presence of friction traces.

An influencing factor on both static and fatigue strength is the *specimen size*. Larger specimens could be tested within this work only by increasing the elongation and not the diameter. At first, a similar behavior seems to take place with increasing the specimen length. However from measurements, significant differences can be noticed. A decrease in strength by 4,8% takes place for the larger specimens, with a lower ductility in the post-peak. The decrease in strength is explained by the frictional restraint created due to mismatch in lateral expansion between loading platens and the specimen. The unrestrained areas are therefore larger for specimens with a higher slenderness. For this reason and due to an increased likelihood to attain the weak link in larger specimens, the number of cycles to failure is lower. However, the fatigue life obtained for these tests is closer to the curves defined from FIB and DNV standards, whereas tests on specimens with a length of 120mm might overestimate the fatigue life of the grout. Overall, an increase of brittleness is observed for the larger specimens leading to lower initial and final strains, in addition to a lower total loss of stiffness.

Main mechanisms occurring during compressive fatigue loading

The main focus of this work was to give a better understanding of the involved mechanisms during fatigue, by considering different indicators.

The presence of water has been often considered in the literature, nonetheless some confusion is perceived. Hence, on one side the presence of water in the mix is considered to be detrimental to fatigue life, whereas a strength increase is reported to take place due to stress rate effects, which is an outcome of high loading frequencies applied. Nonetheless, a description of the role of water in this chapter is provided by a distinction between water in the capillary pores and water in the porosity of hydrates. A strength increase takes place in fatigue when high loading frequencies are applied due to the presence of water in the hydrates. However, the internal viscosity of the material is related only to the porosity of hydrates, and not the capillary pores. Thus the presence of water in the form of moisture content present in the capillary pores creates a detrimental effect to fatigue life.

The material properties measured during this work were affected by fatigue loading. The strain and stiffness showed a three-phase evolution related to the creation of microcracks,

propagation and coalescence up to failure. Firstly a stiffening of the material occurs compared to quasi-static measurements and subsequently the decrease takes place from the beginning of the test over the entire service life. A correlation in the time of phase transition takes place between strain and stiffness. However, the continuous decrease of stiffness does not correlate well with the measured ultrasonic signal. A faster evolution, indicating a higher damage level results from US evaluations. The main reason seem to be the measurements carried out in different axis, which demonstrates an anisotropic distribution of damage during compressive fatigue. The DIC used on the surface of the specimen also verified the heterogenous strain distribution. Microcracking mainly develops parallel to the applied loading.

The transition phases are developed at different life ratios depending on the stress level applied. Overall, specimens with longer fatigue life and higher strength tend to have a longer second phase. The assumption in the literature regarding an independency on the stress level and the material strength is not valid for the studied grout.

The loading frequency does not affect only the fatigue life, as described in the previous section of conclusions, but also the strain, stiffness and energy dissipation. At a lower frequency, more damage is generated during the first phase of strain development. This is demonstrated by higher temperature rates during the first cycles, lower stiffening than at 10Hz and higher strains developed. During the second phase, overall, lower rates are determined for the lower loading frequency, nonetheless the difference is very small. In addition, for lower stress levels, the secant modulus evolves at a lower rate and less energy is dissipated. Indeed, this is due to the shortening of fatigue life at 10Hz, due to temperature increase.

> Therefore, the evolution phase of these parameters is directly related to the fatigue life of the specimen and the stress level applied, rather than the loading frequency. However, the total stiffness loss is dependent on loading frequency applied. Thus, a few proposed models developed in the literature based on a critical value of secant modulus as an indicator used in order to predict the fatigue life cannot be applied.

The *strains at failure* are different between quasi-static and fatigue tests. The results showed a dependency on the stress level applied, where higher strains are reached for lower stress levels. Overall, a larger fatigue life is associated to higher strains due to viscous deformation development, as a time-dependent phenomenon. Therefore, despite a stiffening of the grout when fatigue loading is applied, the strains at failure (especially at low stress levels) tend to exceed the envelope curve of quasi-static tests. This is also confirmed at the lower stress level between two loading frequencies and similar number of cycles to failure, i.e. despite a similar fatigue life, tests at 1Hz last longer and larger

viscous deformations occur leading to higher strains at failure. A few theories in the literature developing this hypothesis on the basis of equality of damage states and energy inputs between the two loading types for fatigue life prediction cannot be confirmed.

Microcracking develops in all fatigue tests since the first phase of loading, which is manifested in a decrease of load-bearing capacity of the material. As a result, the stiffness decreases and permanent deformations are created during the test. Several microcracks were detected by DIC at different fatigue life ratios. Furthermore, measurements of MIP and total water porosity demonstrated an increase of "large" pore size and total porosity with increasing number of cycles, respectively. Indeed, pores with a diameter between 6 –116 µm presented a significant increase between the intact state and a damaged specimen. SEM observations on the fracture surface of specimens showed development of cracking around the aggregates in the ITZ area, crack branching when a microcrack reaches an aggregate and through the aggregate.

Alternative methods for estimation of the endurance limit

Alternative methods describing the fatigue behavior and particularly the endurance limit, were considered in this chapter. *The self-heating test*, commonly used in steel material, resulted to be applicable to grout, after some test optimizations. Nevertheless, it should be noted that the interest of this method lies on the limited amount of time and number of specimens to identify the fatigue strength. Indeed, in the literature it reported approximately 2 hours of testing, whereas for the grouted material in these tests, at least 12 hours were necessary. Therefore, the benefit of this method is more limited. However, by applying this method on 5 specimens an endurance limit of 0,34 was obtained. It is unclear to what number of cycles this method refer to as an endurance limit. In further work which could be carried out by optimizing some test conditions, the heating sources could be detected in the surface of the specimen. This can give an additional information on the microplasticity zones and a better indication of the crack localization.

Three other methods were essentially based on predictions from the analysis of traditional fatigue tests. Firstly, the S-N curves jointly used with *failure probabilities* resulting from the Weibull distribution lead to an estimated endurance limit at $S_{c,max} = 0{,}51$. These calculations are carried out under the hypothesis that the endurance limit coincides with 2000000 cycles, as commonly considered in the literature. This result is confronted to calculations based on the regression given from the Wöhler curve, where the endurance limit is predicted at 0,58. According to these results, the S-N relation incorporating the failure probability leads to more conservative results. Therefore, this relation should be considered for a better predictability depending on the failure probability determined by the designer. Nevertheless, it should be noted that the data was rather limited for a

probabilistic analysis and more specimens would be necessary to confirm these results. Additionally, the Weibull parameters are highly dependent on the stress level applied.

The analysis of the *secondary strain rate* showed more pertinent results with a significantly lower scatter than in Wöhler curves. The reason seems to be the direct relation of the rate in the second phase with the crack propagation. Furthermore, a linear relation is obtained with the number of cycles to failure in a double-logarithmic scale and the influence of loading frequency is not significant. Therefore, this method can be useful to estimate the fatigue life at low stress level, which due to time restrictions cannot undergo failure. It can also be useful for on-site monitoring.

With regard to the description of the fatigue mechanisms presented and the time-dependent phenomena a few analogies can be conducted between *fatigue and creep*. The related damage mechanism is similar, in a three-phase evolution process with the secondary phase dominating most of lifetime. However higher rates tend to take place in fatigue, due to additional effects occurring during loading such as temperature increase, early microcracking and friction between microcracks. The proposed modified rheological model is able to reproduce the non-linearities observed in the strain development for different stress levels, however the time of failure is not quite accurately predicted. In addition, it should not be neglected that during fatigue, microcracks are generated early when the loading is applied and this does not seem to take place in creep. Thus, a distinction between the two phenomena can be made in future work by considering experimental tests in both fatigue and creep with similar specimen dimensions and estimate the difference in strain development or stiffness deterioration.

The analysis in this chapter leads to a better comprehension of the fatigue behavior of high-strength grouts. The influencing parameters in both fatigue life and damage process were described. All current methods resumed here for alternative fatigue life analysis and prediction can be complementary in terms of fatigue life description in cementitious materials. Therefore, the next chapter will have a different focus, compared to this work. Different elements in the mix composition were modified, in order to estimate their impact on the fatigue deterioration process and the analysis is carried out based on the knowledge acquired in this chapter.

Chapter 4
Influence of mix composition on the compressive fatigue behavior

4.1 Introduction

Following a better comprehension of damage mechanisms during compressive fatigue loading developed in the previous chapter, the current work was oriented towards an analysis on the influence of microstructure on the fatigue life and deterioration mechanisms in high-strength grouts. The literature review in chapter 1 demonstrated, that different mix components can affect differently the fatigue behavior. However, relatively low number of reports can be found on examinations of these parameters. In addition inconsistent results are reported, which is often due to limited number of specimens tested.

Therefore, this chapter is subdivided in three main parts, where initially the influence of aggregate type on the compressive fatigue life and damage mechanisms are evaluated. A relation with differences in microstructure is also established. In the second part, tests on the effect of two aggregate types at different fractions are carried out. Lastly, the porosity increased in the form of added water content and induced air is measured and its possible effect on fatigue life is analyzed. Based on the gained knowledge from the tests, a description of the damage process involved in high-strength grout with possible influencing factors is given.

4.2 Influence of aggregate type on the fatigue behavior

In the first chapter, a description of the influence of distinct mix components on the fatigue behavior of concrete and grout is given. A particular focus is also directed towards aggregate properties, which can affect the strength (flexural or compression), the fatigue life and the related damage mechanisms. This is due to initial differences in mineralogical composition, surface shape and texture, which can impact the microcrack development areas. In addition to the reference grout composed of bauxite aggregates, two other types of aggregates are analyzed in terms of fatigue behavior, quartz and tabular alumina. The three chosen aggregates are very distinct in shape, strength and compatibility with the cement matrix. A general description is given in section 2.3.1.1.

This section provides the strength and fatigue life of three mixes with different aggregate types, followed by analysis of damage mechanisms. In addition a particular interest is given to petrographic analysis by means of SEM and EDS, at a microscale level of the aggregates and the ITZ.

4.2.1 Strength properties

The difference between bauxite and tabular alumina is firstly on the composition. Tabular alumina has a high chemical purity and is composed of 99,5% Al_2O_3, whereas bauxite is composed of 70% Al_2O_3 and the remaining is mainly SiO_2, Fe_2O_3 and TiO_2. The choice of the tabular alumina, is supported by the homogenous microstructure of the aggregates, which could possibly result in a reduced scatter of number of cycles to failure. In contrast, bauxite aggregates have a higher apparent porosity and a slightly lower stiffness. The hardness in Mohs scale differs between the three aggregates, and it is 9, 8,5 and 7 for tabular alumina, bauxite and quartz, respectively. These data are provided by the suppliers and no tests of hardness on aggregates are carried out. Bauxite and quartz aggregates differ in chemical composition, hardness and shape. Indeed, quartz is composed mainly of SiO_2 ($> 98\%$) has a lower porosity and the surface texture is relatively smooth.

These are general properties provided to justify the choice of aggregates and expedite the comprehension of test results. In section 4.2.5 the aggregate shape and interface properties will be further analyzed with SEM.

After mix establishment according to the methods described in 2.3.1, the quasi-static tests are carried out at 8 weeks, similarly to the reference grout. The subsequent fatigue tests are conducted with an identical testing method and the same number of specimens.

It should be noted that all fatigue tests carried out for the two mixes with quartz and tabular alumina aggregates are performed only at one loading frequency ($f = 10$ Hz).

Minimum and maximum stress-strain curves from quasi-static tests are presented in figure 4.2-1 for the three mixes (R-Bau : mix with bauxite aggregates ; Qua : mix with quartz aggregates ; Tab : mix with tabular alumina aggregates).

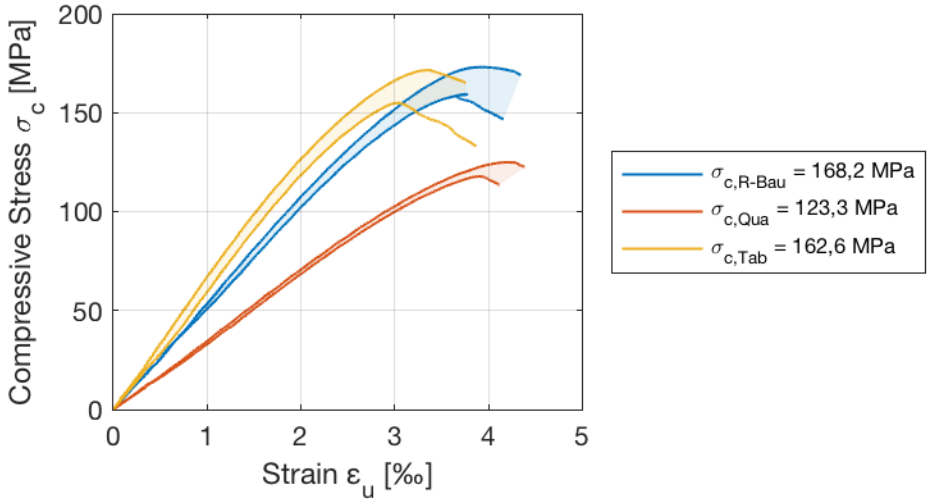

Figure 4.2-1 *Quasi-static tests with minimum and maximum evolutions for three grout mixes with different aggregates*

The highest strength is reached for the bauxite mix and the lowest for the quartz mix, where the aggregate hardness is the lowest. Moreover, the stiffness is higher for the tabular alumina mix ($E_{Bau} = 54$ GPa, $E_{Qua} = 36$ GPa, $E_{Tab} = 64$ GPa), analogously to the elastic modulus of the aggregates. Indeed, the cement matrix is kept the same in terms of composition and the water quantity has remained unchanged in terms of volume. Therefore, the difference in elastic modulus is attributed to the aggregate stiffness.

It is often suggested in the literature that the failure in a higher strength concrete is more brittle than for a lower strength. However, when the peak was reached in the stress-strain curve for the quartz mix, the failure occurred vary rapidly in a brittle manner. Whereas, in tabular alumina and bauxite specimens, a higher bearing capacity occurs in the post peak regime. These aggregates, are subject to mechanical interlocking in the interface with the matrix, resulting in a better bonding, compared to quartz. Therefore, when cracking occurs, the aggregates have a bridging effect which leads to different types of cracking (matrix, interface and through aggregate). For the specimens composed only of quartz aggregates, the cracking develops more rapidly due to a facilitated path through the aggregates, which present a relatively low hardness.

4.2.2 Fatigue life

Based on previous measurements of grout strength, compressive fatigue tests are conducted at three stress levels and loading frequency $f = 10$Hz. The number of cycles to failure are summarized in table 4-1 in an ascending order and a graphic presentation can be found in appendix C-1.

Similarly to the reference mix, the two other mixes also show some scatter in terms of number of cycles to failure. The scatter is surprisingly high when considering $S_{c,max} = 0{,}75$ for the quartz mix, but also for the tabular alumina. An initial effort was made to reduce possible scatter in fatigue tests, not only by following a strict mix protocol, but also by selecting mix components with a better homogeneity, when possible. This conditioned the choice of tabular alumina, as relatively homogenous aggregate. However, no improvement of scatter resulted from fatigue tests compared to the reference mix. Meanwhile, a slight improvement resulted when compared to quartz mix, where the data at $S_{c,max} = 0{,}75$ and 0,80 is very dispersed.

Table 4-1 *Number of cycles to failure for three mixes at three stress levels and corresponding mean values (f = 10Hz)*

Mix	Stress Level $S_{c,max}$	Number of cycles to failure N_f						Average
R-Bau	0,90	2255	2435	2664	2693	3156	4417	2937
	0,80	9041	10881	13469	13479	19225	19873	14328
	0,75	23098	36572	51918	53577	62609	64915	48782
Qua	0,90	1989	2034	2350	2425	2801	2924	2421
	0,80	8724	12324	13188	13888	19185	29756	16775
	0,75	17212	21269	61125	73528	101414	165023	73262
Tab	0,90	62	534	727	2067	2542	4560	1749
	0,80	9050	14879	15540	16517	16556	17617	15026
	0,75	18176	73488	78003	83034	97065	112868	77106

4.2.2.1 Sources of data scatter

A surprisingly larger scatter can be observed in the number of cycles to failure for the Qua mix in particular at $S_{c,max} = 0{,}75$. When comparisons of fatigue life between different mixes are carried out, only the mean values are often considered. Nevertheless, if the values are very dispersed, the sources of the scatter should firstly be investigated, to allow a better comparison.

Despite the lower scatter obtained in tabular alumina compared to quartz, the scatter is significant. In chapter 3, it was demonstrated by SEM observations that cracking occurs through the aggregate, but also in the cement matrix and the interface. Therefore, despite a more homogenous aggregate, the reason for the existing scatter in Tab mix, might be the development of microcracking only in the ITZ and matrix, where the composition has not changed. In the mix with tabular alumina the aggregate stiffness is higher compared to the two other aggregates. It is possible that in this mix cracking occurs mainly in the ITZ and the cement matrix and therefore the presence of homogenous aggregates but with a very high stiffness, do not add a beneficial effect.

The scatter observed in fatigue life (see table 4-1) for Qua mix is also reflected on strain and secant modulus evolutions during the first cycles. In figure 4.2-2 (left), it is presented the strain at maximum stress levels for the first 10 cycles at $S_{c,max} = 0{,}75$, where the initial strains for specimens of Tab and Bau mix are within the same range. However, specimens from the Qua mix show a very large scatter in initial strains, i.e. four specimens have higher strains than the two other mixes, whereas two are much lower.

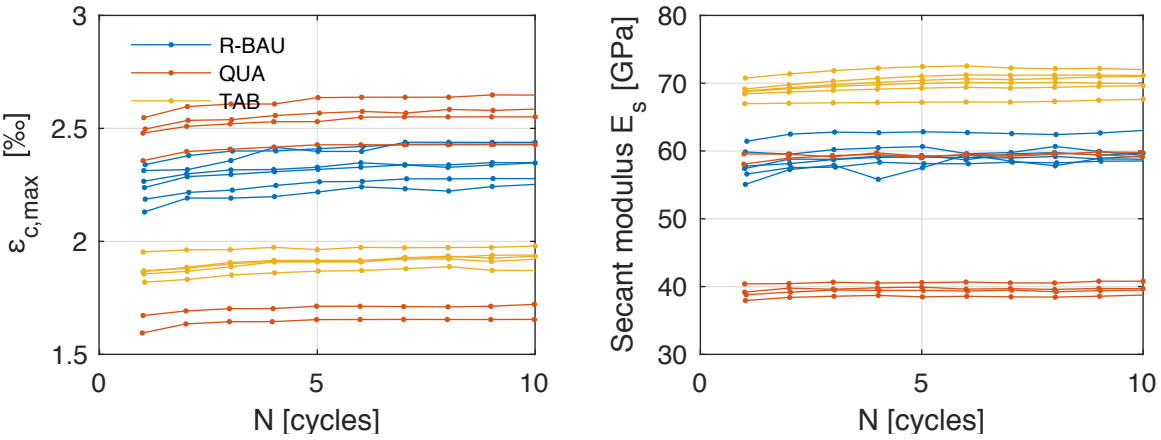

Figure 4.2-2 *Strain and secant modulus evolution for all specimens during the first 10 cycles of the three mixes with different aggregate types at $S_{c,max} = 0{,}75$*

The origin of the high scatter in number of cycles to failure and initial strain for this mix comes from an initial difference at a microstructural scale, reflected in a large variation of the secant modulus (see figure 4.2-2 right). The stiffness of the two specimens is much higher than expected, with similar values to the bauxite mix. It should be noted that the Young's modulus of this mix is estimated at 36 GPa. The high secant modulus for these two specimens resulted also in surprisingly high values of number of cycles to failure at $S_{c,max} = 0{,}75$. If these tests were excluded, the average fatigue life would be slightly lower for the quartz mix compared to bauxite. Therefore, a direct comparison of mean fatigue lives should not be considered sufficient to determine the effect of aggregate type on fatigue behavior.

One question may arise on why the mix with quartz aggregates presents more variability than the one with bauxite aggregates. Despite tested specimens being from the same batch, different microstructural arrangements can take place for certain specimens, which lead to different strengths. Moreover, as the cement matrix does not have a significant change compared to the reference mix, the scatter should come mainly from aggregates. The quartz aggregates do not manifest a higher strength compared to the cement matrix and thus they represent the weakest link, where microcracking possibly develops to a high extent. Whereas, in the reference mix cracking seems to occur in the aggregate, ITZ and cement matrix combined. The quartz aggregates have no cleavage and exhibit a conchoidal fracture. Thus, the fracture for this aggregate type generally occurs in an irregular manner and in all directions, leading to a possible higher scatter during fatigue loading.

This section demonstrates that a comparison only in terms of mean number of cycles to failure as often is carried out in the literature is not sufficient to investigate the effect of aggregate type on fatigue loading. Damage mechanisms should be analyzed macroscopically and also in relation with the mixture microstructure. For this reason, next sections will attempt to evaluate these parameters.

4.2.3 Influence of temperature between the three mixes

The number of cycles to failure between the three mixes in table 4-1 indicates that at $S_{c,max} = 0{,}90$ higher number of cycles to failure are reached for the bauxite mix and the lowest for the tabular alumina mix. It is possible that the higher stiffness of tabular alumina compared to the two other aggregates results in large microcracking in the interface and matrix, due to incompatibilities in stiffness with the cement paste. Therefore, in this mix the weakest link would be the ITZ and the cement matrix, where cracking develops rapidly.

Nevertheless, this tendency is reversed for $S_{c,max} = 0{,}75$ where the lowest number of cycles are reached for the bauxite mix. In order to understand why this change of behavior takes place, we established in chapter 3 an inverse relation between temperature increase and fatigue life. Therefore, temperature evolutions should be analyzed, firstly. In figure 4.2-3 the temperature increase $\Delta\theta$ in relation to the number of cycles is presented for three stress levels with a comparable fatigue life for the three specimens.

The number of cycles to failure at $S_{c,max} = 0{,}90$ are relatively low, therefore no significant differences are noted in the temperature increase. Nevertheless at $S_{c,max} = 0{,}80$ and 0,75 due to a larger fatigue life, a difference in the temperature evolution appears between the three mixes at approximately 20% of the total fatigue life. The highest temperature increase takes place for the bauxite mix, where the rate of increase per cycle is also

higher. Therefore, the detrimental effect on the bauxite mix is higher. This can help explain partially, a shortening of the fatigue life to a higher extent compared to the two other mixes, mainly at $S_{c,max} = 0{,}75$. However, it is not a sufficient parameter, as the difference in temperature is not too critical. Therefore, the next sections will evaluate damage mechanisms based on strain and stiffness development.

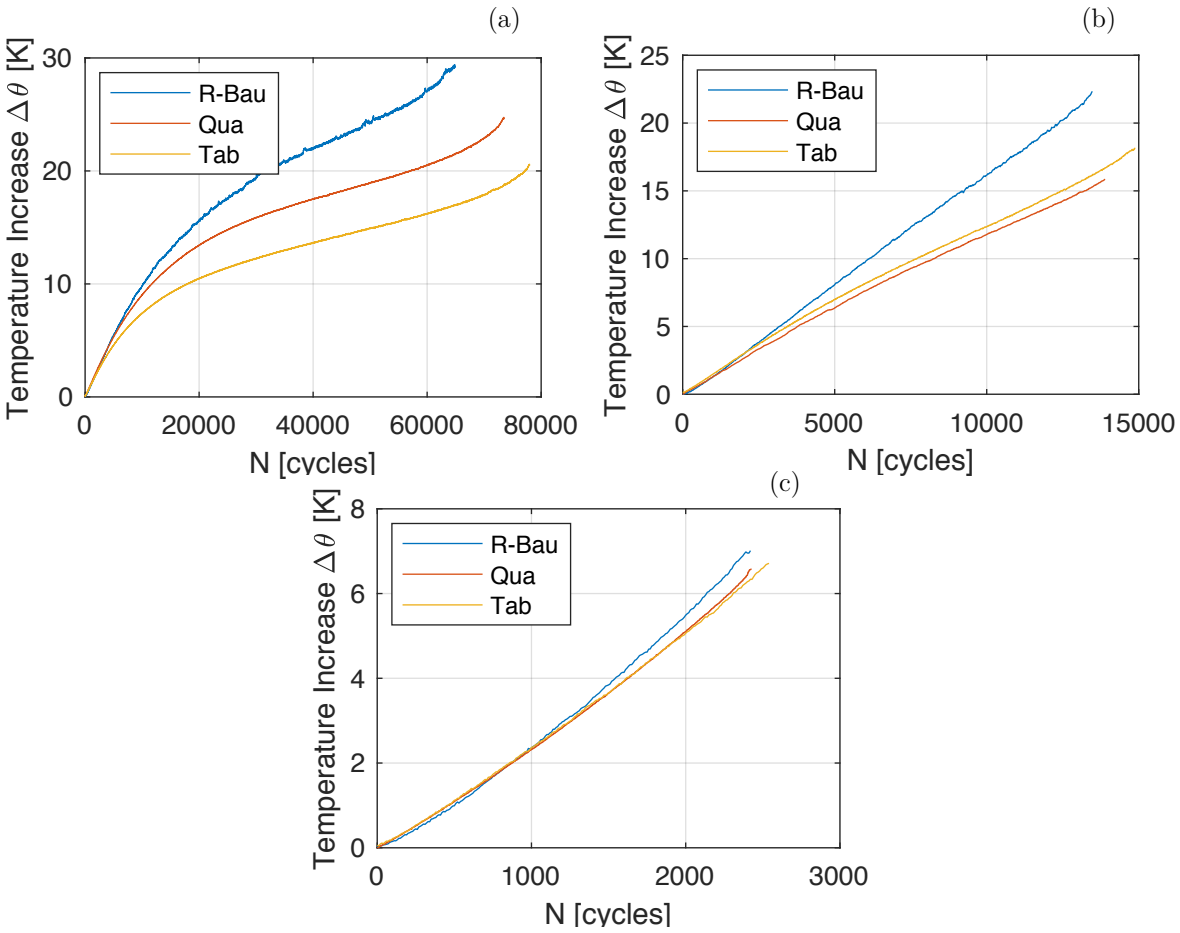

Figure 4.2-3 *Temperature evolution for three mix compositions with comparable number of cycles to failure $S_{c,max} = 0{,}75$ (a); $S_{c,max} = 0{,}80$ (b) and $S_{c,max} = 0{,}90$ (c)*

In the previous section, it was suggested that microcracking in the mix with quartz aggregates is very present within the aggregates. In chapter 3, it was demonstrated that the specimen heating is produced by the friction between microcracks. Less friction occurs when microcracks are situated within the aggregates compared to cement matrix, which it would result in a lower temperature increase in the quartz mix. Whereas, in the bauxite mix microcracking occurs also in the interface and matrix. Additionally, bauxite aggregates have a higher thermal conductivity coefficient compared to quartz. As the temperature is measured on the surface of the specimen, the heating generated within the specimen is conducted with a higher rate to the surface. Thus, even for similar number of cycles during fatigue, the measured temperature in the surface is higher for a mix with higher thermal conductivity.

4.2.4 Damage based on strain and stiffness development

The *secondary phase* in the strain development during fatigue loading is found to be related to crack propagation. It is therefore appropriate to pursue the analysis by a comparison of rates in this phase between the three mixes. The secondary strain rates are calculated for each specimen individually, between 20% and 80% of the total fatigue life. The estimated values are given in relation to number of cycles to failure (both presented in logarithmic values) in figure 4.2-4 for the three mixes, where a linear relation achieved. It is remarkable that the linear regression between mixes with bauxite and tabular alumina aggregates overlap almost perfectly. This implies that despite differences in number of cycles to failure, the crack propagation occurs in a similar way. Thus, the difference in fatigue life between these two mixes should be related to differences during phase I and/or III. The next section will attempt to establish a possible relation.

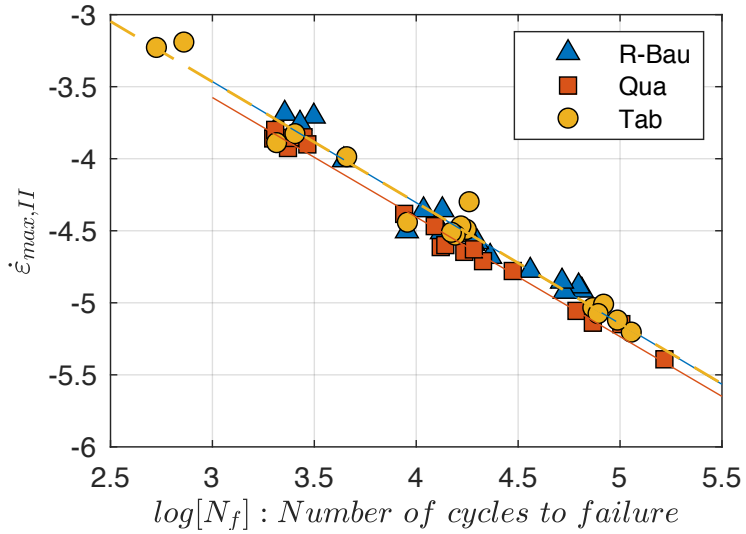

Figure 4.2-4 *Secondary strain rate in relation to number of cycles to failure for all specimens tested at f = 10 Hz for the three mixes with different aggregates*

For a given secondary strain rate, lower number of cycles are to be expected for the quartz mix, where the regression lies almost parallel to R-Bau. It also implies that overall a lower strain rate is expected for this mix. However, in order to explain the variations in terms of fatigue life for Qua mix, mainly at $S_{c,max}$ = 0,90 and 0,75 compared to the bauxite mix, analysis of stiffness evolution and strain development should be carried out in the first phase.

Section 4.2.2.1 showed an evolution of the *secant modulus* during the first 10 cycles. It was demonstrated that aggregates with higher stiffness resulted in grout mixes with higher stiffness in quasi-static and in fatigue. This part will attempt to investigate the evolution of the secant modulus during fatigue loading at different stress levels, but also

evaluate the increase in stiffness due to dynamic effects. Indeed, in chapter 3 was indicated that an increase occurs in the secant modulus measured in the first cycles, compared to the Young's modulus from quasi-static tests. Therefore in table 4-2, the stiffness increase measured in the first cycle $E_{s,0}$ is calculated for all tests at the three stress levels and expressed in relation to the Young's modulus E_0.

At $S_{c,max} = 0{,}90$ similar levels of increase in stiffness are manifested between Bau and Qua mix. Surprisingly low values are reached for the tabular alumina mix at this stress level. At lower stress levels, mainly at $S_{c,max} = 0{,}75$ the increase in stiffness for the quartz mix is particularly high. An increase of approximately 27% is reached, compared to the reference mix where the increase is 7%. The high level of increase is due to the two specimens mentioned earlier which manifested a much higher stiffness compared to the other specimens. If they were excluded, an increase of 9% would take place which is still higher than the two other mixes at $S_{c,max} = 0{,}75$. At $S_{c,max} = 0{,}80$ the strain rate effects are also higher for the quartz mix.

Table 4-2 *Mean values of stiffness increase in relation to the static tests ($E_{s,0}/E_s$) and total stiffness decrease during fatigue ΔE for each mix*

Stress Levels	***BAU***		***QUA***		***TAB***	
	$E_{s,0}$ / E_0 [%]	ΔE [%]	$E_{s,0}$ / E_0 [%]	ΔE [%]	$E_{s,0}$ / E_0 [%]	ΔE [%]
0,90	10	26	9	20	2	25
0,80	4	29	9	25	6	33
0,75	7	35	27	35	7	33

Therefore, the Stefan effect exhibited in the three mixes, derives to an increase of stiffness observed mostly for the Qua mix. A similar review is suggested from Sparks [64], where three aggregates with different stiffnesses were used and the stiffest aggregate produced the lowest strength increase. However, the reason for this effect is not provided. This effect initially occurs due to the presence of free water in the hydrates. Nevertheless, the three mixes have been developed with the same water quantity in terms of volume and the binder composition is not changed. Thus, theoretically the increase in stiffness should be similar. It is possible, that bauxite aggregates which are more porous consume locally the water in the matrix. Therefore a better bond is created in the interface and less water is locally present. In quartz aggregates, no absorption takes place and is possible that more water is present resulting in a mix more prone to dynamic effects. Hence, the difference in relative stiffness increase, might be related more to the aggregate capacity of absorption and not the aggregate stiffness.

The levels of stiffness increase and the evolutions can be found graphically in figure 4.2-5 (right) for $S_{c,max} = 0{,}80$ and for similar number of cycles to failure between the three mixes. The dotted lines represent the mean Young's modulus measured from quasi-static tests. Evolutions for other stress levels can be found in appendix C-2. To simplify comparison between phases, in the left figure the secant modulus is expressed in relation to the first cycle. The strain evolutions corresponding to the same specimens from these mixes can be found in figure 4.2.6.

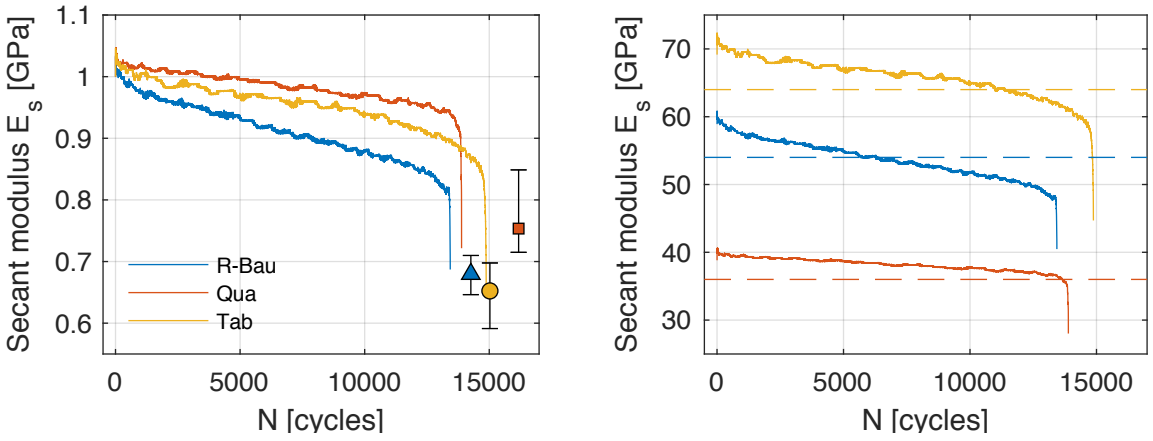

Figure 4.2-5 *Relative secant modulus evolution for specimens of each mix with similar number of cycles to failure at $S_{c,max} = 0{,}80$ (left) ; Corresponding absolute values of secant modulus and comparison with the elastic modulus (right)*

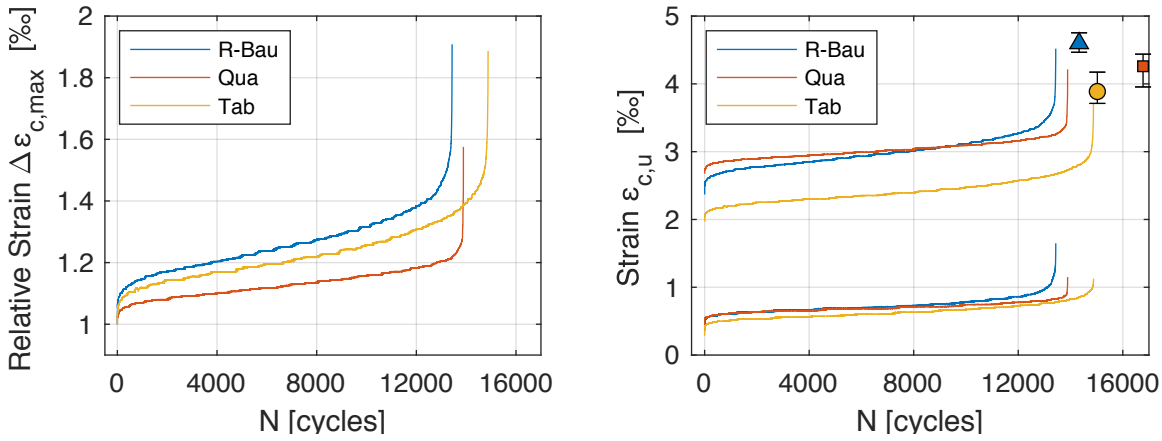

Figure 4.2-6 *Relative maximum strain evolution for specimens of each mix with similar number of cycles to failure at $S_{c,max} = 0{,}80$ (left) ; Corresponding minimum and maximum strain evolutions and mean values of strain at failure (right)*

The quartz mix has a lower stiffness, compared to the two other mixes as shown in quasi-static tests and also during fatigue (figure 4.2.5 right). Consequently, higher maximum and minimum strains are reached for the quartz mix, especially up to 50% of the total fatigue life (figure 4.2.6 right). This is also observable for the other stress levels shown in appendix C-3, where strain development and the secant modulus seem in correlation.

However, the total strain increase relative to the first cycle is lower in the quartz mix (figure 4.2-6 left). Based on these observations, the following mechanisms seem to be related to the *first phase* :

⇒ It can be assumed that the quartz mix undergoes more deformation during the monotonic force (applied before the fatigue loading initiates), leading to higher initial strains ε_i when the fatigue loading starts. This is due to a lower stiffness of the aggregate.

Subsequently, the first phase is shorter and the crack propagation is slower for the quartz mix compared to the reference, as also presented in figure 4.2-4. The third phase seem to occur more rapidly, leading to a sudden failure and lower loss of stiffness. Despite, higher deformations in the elastic phase, the failure was more brittle for the quartz mix when the peak was reached in quasi-static tests and almost no strain softening occurred. This seems likewise to be reflected in fatigue.

Furthermore, it should be noted that the stiffness degradation also occurs at a lower rate for the quartz mix (figure 4.2-5 left), similar to strain development. Additionally, for most of the fatigue life, (approximately 90% for all tests), the secant modulus is higher than in quasi-static tests (figure 4.2-5 right). Therefore failure occurs rapidly when the secant modulus decreases below the elastic modulus. The lower damage induced in the second phase might also be related to the larger stiffening compared to the other mixes. For the bauxite mix, despite decrease below the elastic modulus at approximately 50% of fatigue life, the specimen does not fail and degradation continues to develop.

In a few studies such as [13,81], is assumed that higher strength concrete with a higher stiffness, shows a less steep evolution in the secondary phase of the strain development. However, based on the strain and secant modulus evaluations carried out in this research, the mix with quartz aggregates showing a lower stiffness and lower strength, is subjected to a slower damage evolution in the second phase and it becomes more brittle during the fatigue process, despite higher strains in quasi-static. Therefore, from these previous analyses, it can be concluded that in the *second and third phase* the following mechanisms take place :

⇒ the strain development between mixes with different strengths and different aggregates is more dependent on the post-peak behavior of quasi-static tests, where plasticity occurs. In fatigue, rapid development of plasticity occurs after the first transition phase. Thus, the mix with quartz aggregates resulted to become more brittle and the bearing capacity seems lower, when plastic strains develop. Therefore the rate in the second phase is lower for the quartz mix, which presented a sudden failure in quasi-static tests.

⇒ Due to small strain development during fatigue and the abrupt failure, the internal damage is greatly localized. As a result, the total loss of stiffness is also lower, despite the higher initial strain values which are a result of the monotonic force applied before the fatigue loading.

In addition, different microstructural changes can occur due to the different nature between aggregates. Thus, it is necessary to observe more closely the shape of the aggregates and the interface with the cement matrix.

4.2.5 Petrographic Analysis with SEM and EDS

Scanning electron microscopy is used for observations of aggregate shape and interface properties between the aggregates and the matrix. The Energy-dispersive X-ray spectroscopy is also employed for analysis of aggregate composition and the interface thickness with a relatively detailed microstructure investigation. This section will focus only on observations in samples with quartz and bauxite aggregates, which have the most disparities at a micro-scale level.

4.2.5.1 Aggregate shape

In figure 4.2-7, two selected images of bauxite and quartz aggregates are presented. The images are shown with back-scattered electrons, reflected by elastic scattering. They emerge from a higher depth in the specimen and the signal is related to the atomic number. Elements with a higher atomic number appear brighter in the image. Therefore it is relevant to use BSE for detection of contrast in areas with different chemical composition, as is the case of aggregate-matrix.

Bauxite aggregates in figure (a) and (b) have a more angular shape, than quartz in (c) and (d), where aggregates appear to be more smooth and in a rounded shape. Furthermore, bauxite is more porous, but not at the same level of porosity for all aggregates (figure 4.2-7 (a) shows two aggregates with different porosity levels). The porosity of quartz aggregates can hardly be detected. However, the surrounding cement matrix seems to be more porous. It is possible that during hydration and due to a higher open porosity for bauxite aggregates, the water in the cement matrix is partially absorbed and hydrates form in the aggregate surface in the form of mechanical interlocking. Thus, interface properties are improved, resulting in a lower porosity. This can also be seen at the image scale 500 µm, where the ITZ can hardly be distinguished, whereas in quartz aggregates darker areas surround the aggregates. In addition to this qualitative analysis, a closer investigation is carried out in the next section.

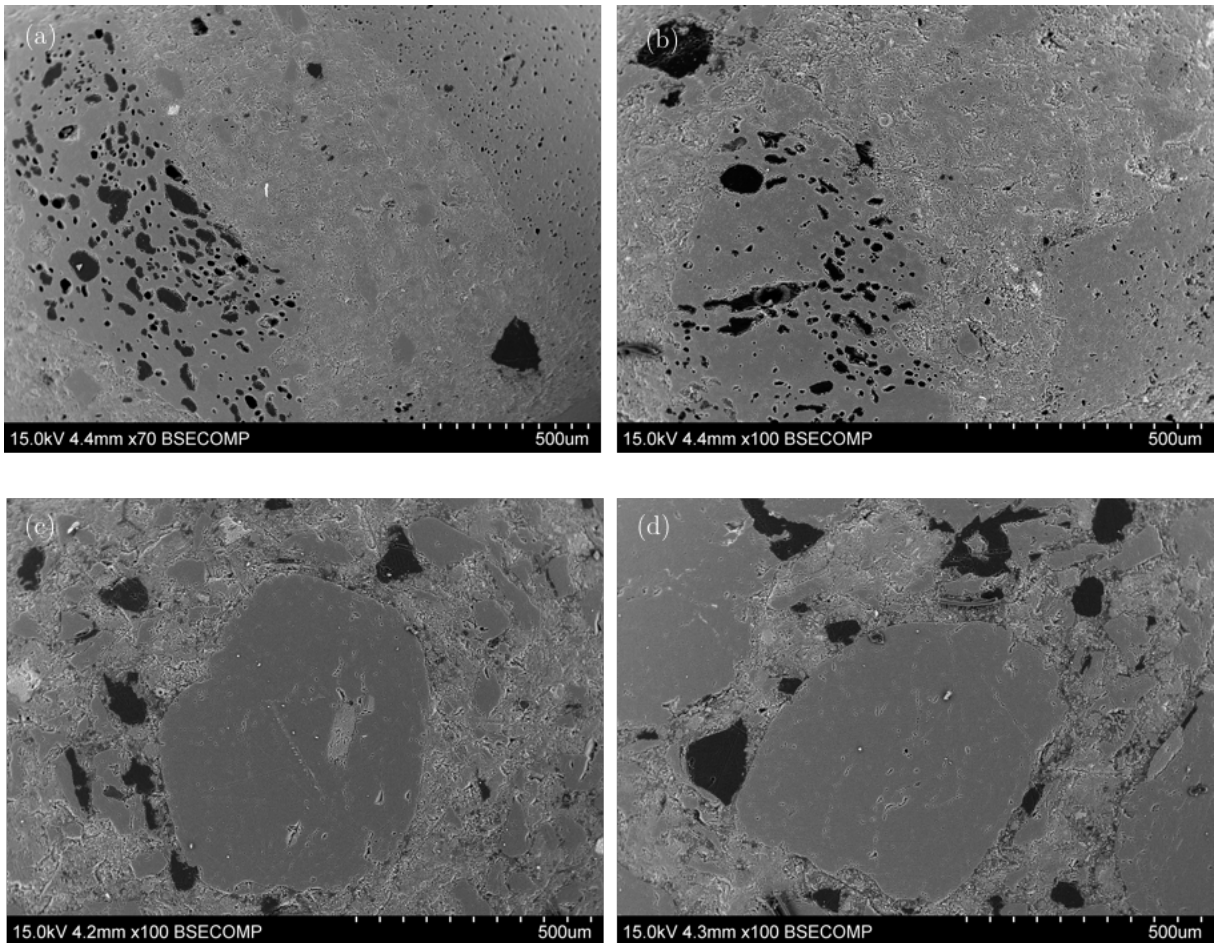

Figure 4.2-7 *Aggregate shape from SEM observations; bauxite aggregates (a)(b); quartz aggregates (c)(d)*

4.2.5.2 Characterization of Interface Transition Zone

Due to a more angular shape of bauxite aggregates, a type of mechanical interlocking occurs with the cement paste. This phenomenon is graphically presented in figure 1.3-3 of chapter 1. Whereas, for specimens with quartz aggregates only a small interaction occurs with the cement paste, thereby suggesting a larger interface zone. The EDS technique is used jointly to SEM, for observations in the interface between the mixes with two aggregates.

Flat polished specimens with epoxy resin are used for these observations and the specimen preparation steps are summarized in section 2.5.2.1. Two procedures are practiced for the analyses : mapping and line scan. The mapping in EDS identifies and quantifies the elemental composition of an area in the sample, by revealing a spatial distribution of each element. The line scan allows the analysis over a selected line. This can be helpful in estimating the width of the interface.

Two interface areas are analyzed with the EDS procedure for two aggregates, quartz and bauxite. This was carried out to determine the composition of aggregates and verify the composition provided by the suppliers. Furthermore, the procedure allows a quantification of the matrix in the interface area and is used for the purpose of comparison if any disparities take place when different types of aggregates are used.

Therefore, in figure 4.2.8 the mapping procedure is used on two different aggregates of the quartz mix and in the following figure 4.2.9 two bauxite aggregates are analyzed. The observation scale is chosen sufficiently low, to allow a better distinction between elements. Images of the chosen areas are presented, in addition to the spatial distribution of the chemical elements present in the micrographs. The elements chosen in the sample during analysis are : Al, Ca, Si, Na, Fe, K, Mg, commonly present in concrete. Nevertheless, for the current grout mixes the highest concentrations are Al, Ca and Si, therefore only these three elements are presented in the following images. The other elements present negligible quantities. An overlap image of all elements can be found in appendix C-4.

In the images (c)and (i), the colors show the different phases detected. The detection depends on the presence and quantities of different elements. The elements composing each phase (corresponding to each color in (c)and (i)) are shown at the bottom of each group of figures. In 4.2-8 (c) it can be firstly noticed, a very uniform red area, which represents the aggregate. A high concentration of silica and negligible quantities of other elements are encountered in this phase. This seems in accordance with the mineralogical composition of quartz. Furthermore, three distinct areas are detected in this image containing Ca and Si. This can be distinguished in other figures likewise. The distinction between these areas in image (c) relies on the ratios between the two elements. Indeed, an increased level of calcium is detected in the blue area of the two aggregates of figure 4.2-8. This can also be seen in the figure (e), where the concentration of calcium differs. Within these blue areas (detected also for the second aggregate figure (i), extremely low quantities of silica are identified. In figures (f) and (l) these same areas result in a quasi-absence of silica.

In order to give a quantitative evaluation of the ratio between calcium and silica, the number of atoms of these two elements concentrated in each area, is given in table 4-3 in [%].

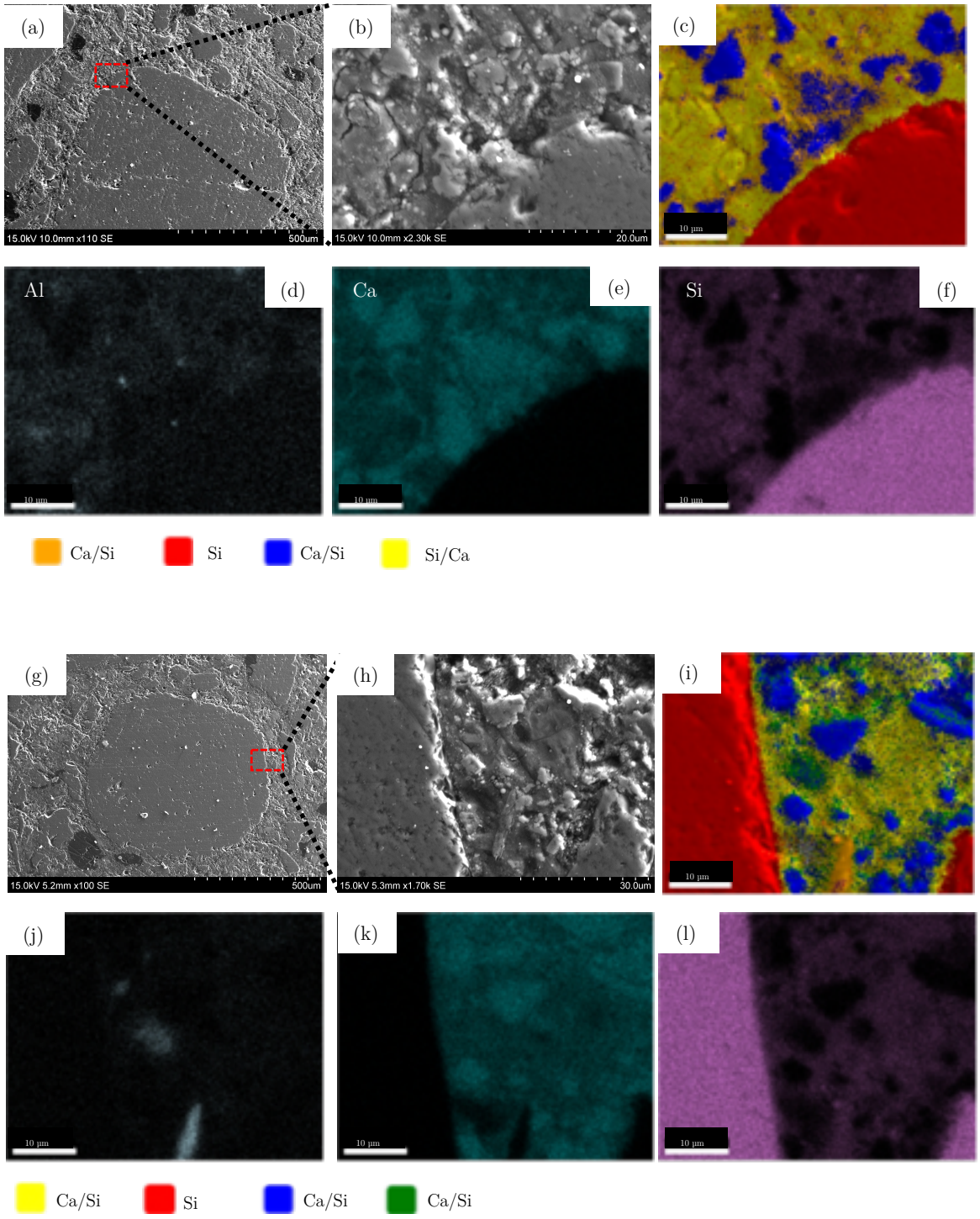

Figure 4.2-8 *Mapping EDS on two quartz aggregates*

Table 4-3 shows phases 1 to 4 in the same order presented in the legend of the figure 4.2-8. Comparable ratios between calcium and silica in phases 1 and 4 are attained. However, a high calcium concentration and an extremely low silica concentration takes place in the third phase, leading to a ratio of 9,8 between the two elements for the first aggregate. It is possible that these areas with a size of 10 µm or lower, represent anhydrous cement particles or amounts of $Ca(OH)_2$ as suggested in [14]. Nevertheless, due to the size of

these elements and the absence of a light color in BSE observations, which characterize the presence of $Ca(OH)_2$ it seems more likely that this phase is related to anhydrous cement particles.

Table 4-3 *Concentration of Ca and Si and corresponding ratios in the detected areas from EDS analysis in the sample with quartz aggregates*

		Atomic [%]			
Quartz aggregate n°	**Element**	**Phase 1 (Ca/Si)**	**Phase 2 (Si)**	**Phase 3 - *blue* (Ca/Si)**	**Phase 4 (Si/Ca)**
1	Ca	23,06	0,72	29,72	17,94
	Si	10,06	40,12	3,03	17,83
	Ratio (Ca/Si)	*2,3*		*9,8*	*1,0*
2	Ca	23,87	0,66	29,57	12,24
	Si	15,27	40,56	4,43	16,51
	Ratio (Ca/Si)	*1,6*		*6,7*	*0,7*

Furthermore, due to the low w/b, the test carried out at 8 weeks and the incorporation of silica fume in the mix, it is unlikely that this phase is related to $Ca(OH)_2$. However, SEM observations in the ITZ, but also in the cement matrix are carried out in order to detect the formed hydrates and will be presented in section 4.2.5.3.

A similar comparison is given for two bauxite aggregates within the same sample. The mapping procedure carried out in the interface zone of the first aggregate, from figure 4.2-9 (a) to (f) is in the same observation scale as the previous quartz aggregates. The observations for the second aggregate in figures (g) to (k) is carried out in a slightly larger scale of 50 µm.

Table 4-4 *Concentration of Ca and Si and corresponding ratios in the detected areas from EDS analysis in the sample with bauxite aggregates*

		Atomic [%]		
Bauxite aggregate n°	**Element**	**Phase 1 (Al/Si)**	**Phase 2 (Si/Al/Ca)**	**Phase 3 (Ca/Si)**
1	Al	28,16	14,86	2,65
	Ca	1,92	4	26,2
	Si	11,32	17,18	5,29
	Ratio (Ca/Si)		*0,2*	*5,0*
2	Al	29,43	12,22	2,21
	Ca	0,62	4,18	23,54
	Si	9,46	15,98	4,85
	Ratio (Ca/Si)		*0,3*	*4,9*

The first mapping procedure is performed in an area, where the aggregate has a rough and angular surface and the it presents a high porosity. The second mapping is performed on an aggregate with a smoother surface. It can firstly be noted, that unlike the quartz aggregates, which had mainly a composition of silica, the bauxite aggregates have a high concentration of alumina (see figure (d) and (i)). Concentrations of silica can also be found in these aggregates. Similarly, to the previous analysis, different phases are detected within the sample depending on the ratio between the three main elements Ca, Si, Al. Nevertheless, for the two bauxite samples, only three phases are detected, presented in figures (c) and (h) with different colors. The composition of these phases can be found in table 4-4.

It should be noted, that in figure (c) the aggregate is presented in blue color whereas in (h) in red. In the first phase corresponding to the aggregate, high concentrations of alumina and silica are detected with a ratio (Al/Si) between 2,5 to 3,2. The yellow (second) phase with high concentration of silica, seems to be related to aggregates, which have a different ratio of Al/Si. Indeed due to the very low quantity of Ca and relatively high concentration of alumina in this phase, it is unlikely that this phase would be a hydration product. Thirdly, the cement paste is composed mainly of calcium and silica and no other phases with different ratios are detected.

From these observations, it can be noted that the cement matrix is more homogenous for the mix with bauxite aggregates, whereas in mix with quartz aggregates, anhydrous cement particles can be found. The exact reason for this cannot be fully given here, as the cement matrix is kept unchanged in terms of volume between mixes and the mixing protocol is the same. Nevertheless, it is possible that the round shape of aggregates participates in the packing of more unreacted cement grains against the aggregate surface.

Furthermore, from figure 4.2-9 (e), there seems to be a small area of calcium diffusion in the interface. This can also observed in figure (c) where no abrupt line separates the aggregate from the matrix, as is the case in quartz aggregates (see figure 4.2-8). It is possible, that due to the open porosity of the aggregate surface, the C-S-H hydrates infiltrate these areas, and thereby creating a better locking. This may result in an “absence” of ITZ or at least a shorter width. The ITZ is not easily distinguished with image analysis, especially for high-strength grout and concrete. The size can vary between 5 to 20 µm for an optimized microstructure and up to 50 µm for an ordinary concrete. Consequently, the line scan analysis in EDS is employed in order to estimate the interface size.

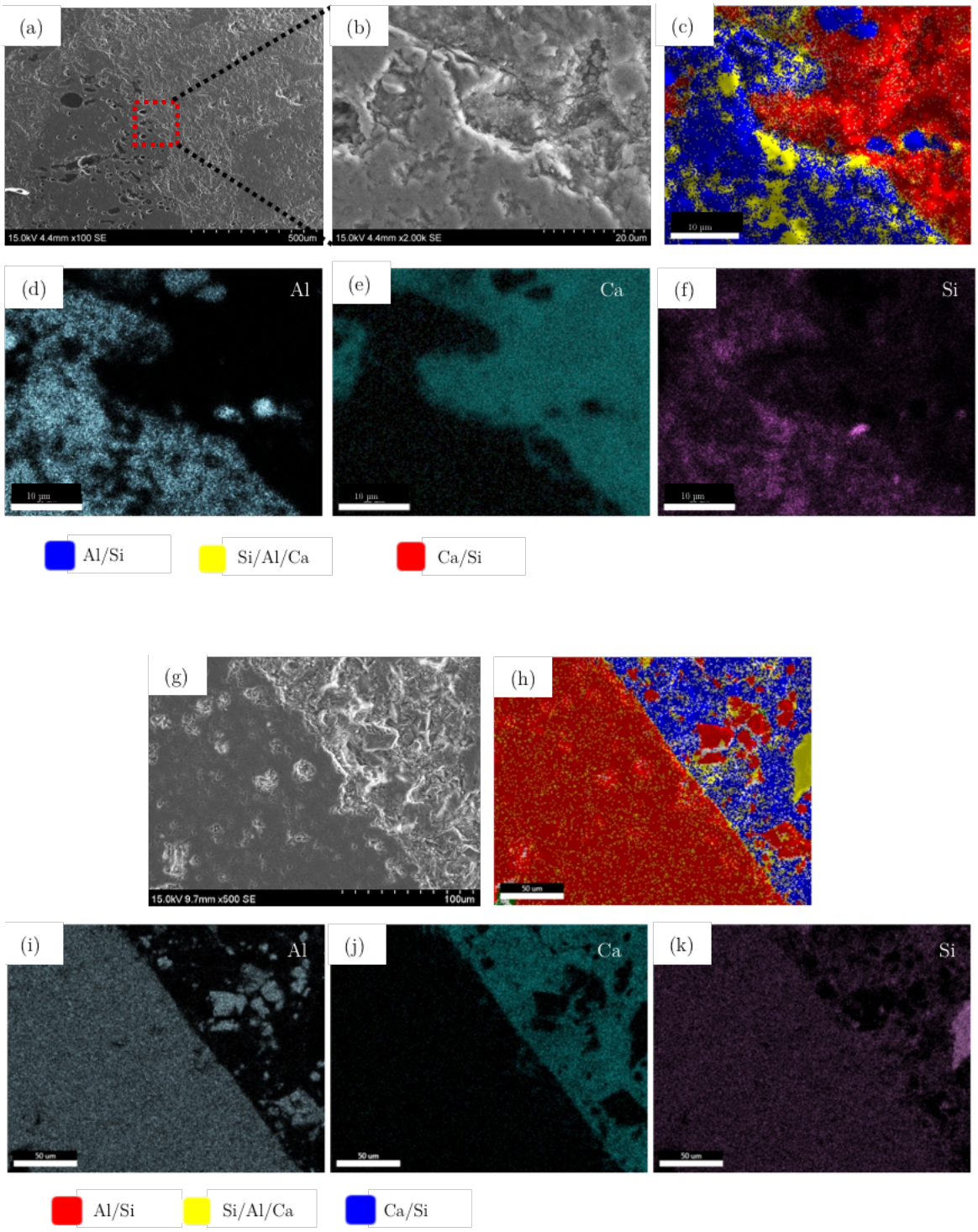

Figure 4.2-9 *Mapping EDS on two bauxite aggregates*

The line scan consists in estimating the composition of the elements along a defined line, starting from the aggregate towards the matrix. This technique is useful, as the ITZ appears as a rapid difference in chemical composition. The results are shown in figure 4.2-10 for the bauxite and quartz specimens.

It should firstly be noted, that the analysis should be carried out in a similar scale of observation, between the two samples. Additionally, the absolute value of the width interface zone measured with this procedure, can be controversial. Indeed, it may be influenced by the specimen preparation step. However, for this study the size of ITZ is not the parameter of interest, but the focus is mainly to give a comparison on how it varies between samples with quartz and bauxite aggregates. Due to similar preparation steps, the specimens are considered comparable and the ITZ size is examined in a relative scale.

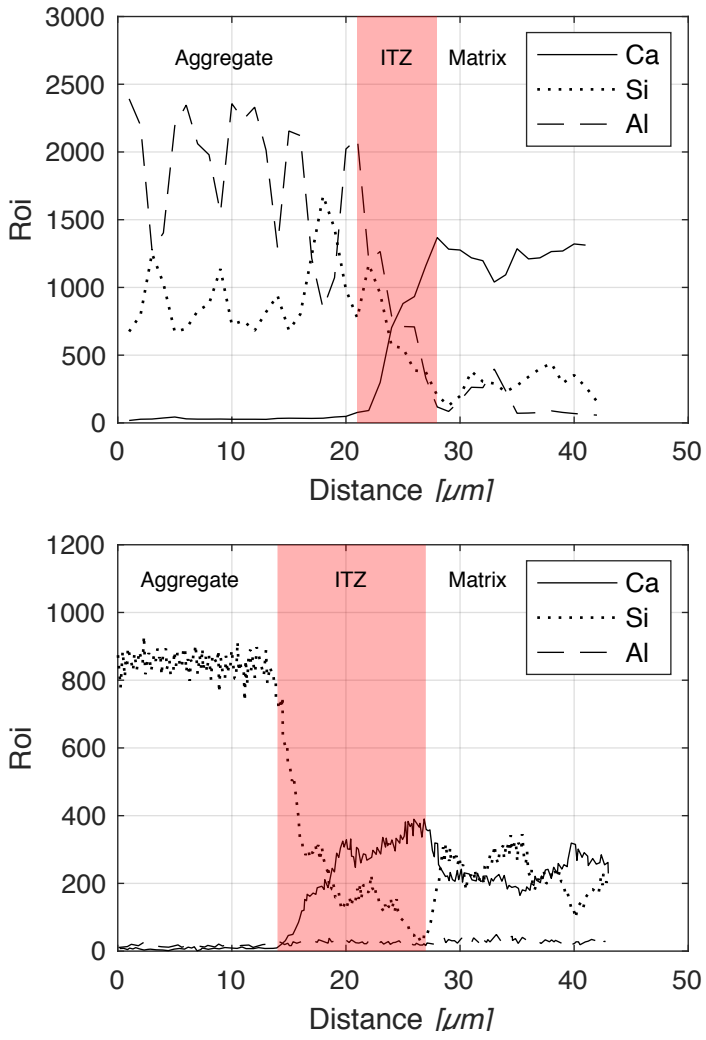

Figure 4.2-10 *Line scanning analysis of ITZ region in grout with bauxite aggregates (upper); with quartz aggregates (lower)*

A line was defined with a starting point on the aggregate and ending point at a distance of approximately 43 μm on the matrix. In the first figure, where the mix with bauxite aggregates is analyzed, relatively high content of alumina and silica are found in the first 20 μm. This area coincides with the aggregate. As the scanning distance increases between 22 and 28 μm, the chemical composition shows remarkable variations. The Al

and Si quantities decrease, while the Ca drastically increases. After 28 µm, the content of these elements can be considered relatively constant. Therefore the width of the ITZ is estimated as the distance over which the chemical composition presents an evolution. For this aggregate it is estimated at 6 µm.

The quartz specimen, had likewise variations of chemical composition along the defined line. Negligible contents of Ca and Al can be found on the aggregate, as previously presented in figure 4.2-8. Nevertheless, an increase of content of Ca begins at 14 µm up to 27 µm. Simultaneously, a sharp decrease of silica takes place. The ITZ width in this sample is estimated at 13 µm. Therefore, the interface transition zone seems to be two times higher in the sample with quartz aggregates.

As mentioned earlier, the absolute measured values can be questionable. However, from SEM observations where larger dark areas are observed in the interface and from the EDS analysis performed in this section, a larger interface zone seems to develop in the mix with quartz aggregates, compared to bauxite. If absolute values were considered, both samples presented a lower ITZ size compared to values of normal strength concrete reported in the literature. The optimized w/b ratio and the presence of silica fume, help improve the interface properties.

4.2.5.3 Microstructure observation of hydrates

The samples above-mentioned are examined for potential presence of various hydration products, due to different Ca and Si ratios. The same mixes are also observed in samples extracted from the fracture surfaces, where no epoxy resin was used.

It is suggested in the literature that the calcium hydroxide is deposited in the open pores and therefore its presence in the aggregate interface has often been reported. It can be detected in SEM images with secondary electrons, due to the shape being easily distinguished from CSH. The calcium hydroxide can be present in many forms, where the most common is as hexagonal platy crystals. The CSH phase can appear in the form of fibrous microstructure at early age, whereas after 28 days, as is the case of observations carried out here (12 weeks), the CSH can appear as equant grains. Therefore, the morphology of the hydration products is observed in the interface area, from samples extracted from fracture surfaces, where the presence of calcium hydroxide is likely to appear. Figure 4.2-11 (a-b-d) shows the same aggregate interface with different magnifications, in order to display clearly the appearance in different scales. Figure (c) is another area on the sample with a large magnification. Additionally, appendix C-5 shows other interface areas in the epoxy impregnated specimens.

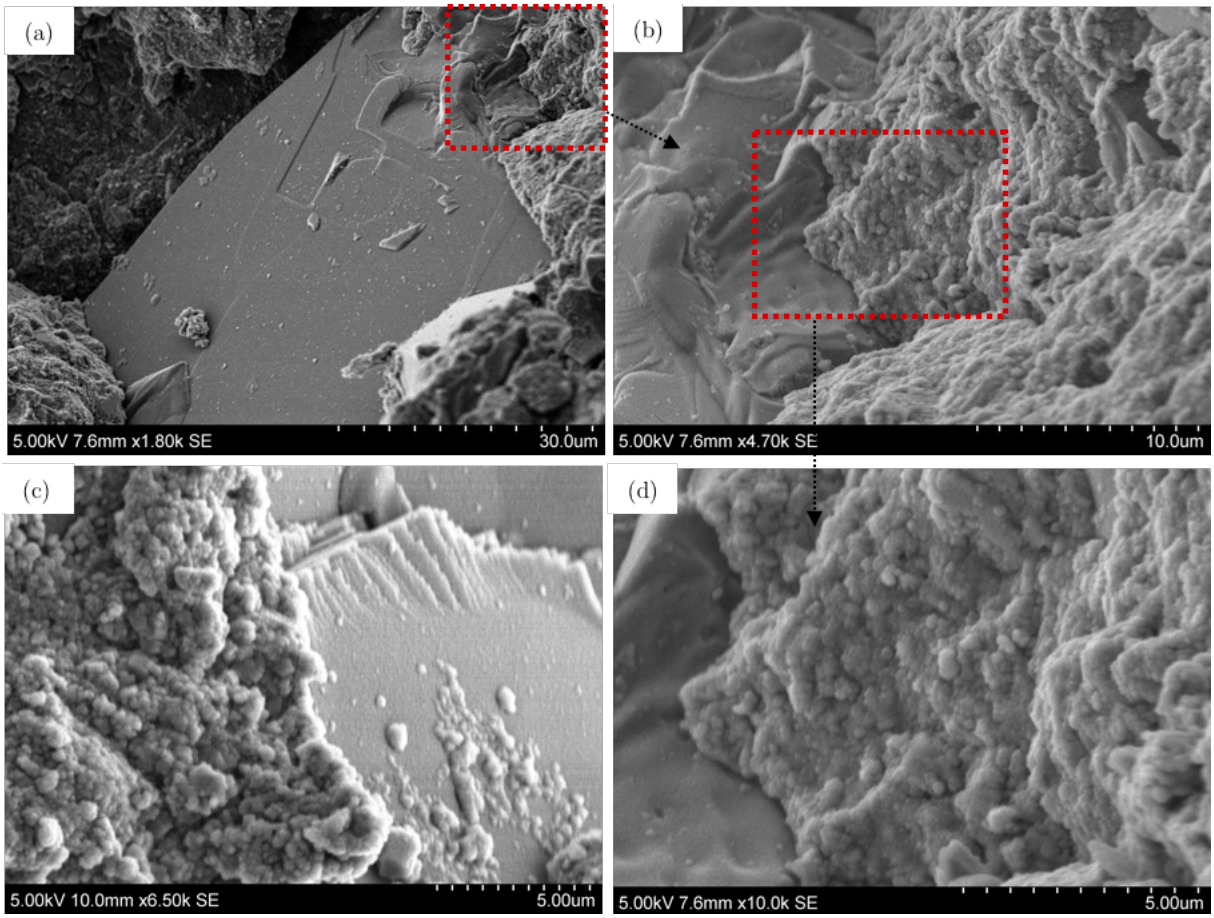

Figure 4.2-11 *SEM images on the fracture surface of a specimen in the aggregate interface area (a-b-d) ; Another area of observation (c) in aggregate interface*

From all figures, a relatively regular and homogenous microstructure is observed. The needle-like crystals or hexagonal plates could not be observed in these images. The matrix phase is very dense, as is often reported in high-strength concrete. The CSH appear in the form of equant grains, due to the late age of observation.

Alternative methods for detecting the presence of unhydrous particle and the calcium hydroxide have been reported in the literature [14,173], based on image analysis of BSE micrographs. It can also allow detecting the ITZ in different samples. This method suggests to threshold the grey-scale image for identification of hydration products. The thresholds are created based on the hypothesis that unhydrated cement particles are in the range 210 to 240 in the greyscale histogram, calcium hydroxide between 160 to 210 and porosity between 0 up 100. This method based on image analysis was also attempted as a complement to the previous technique presented with EDS analysis. However, it resulted that the levels of thresholds and the filtering applied (sharpen masks, opening of objects) have a strong influence in the interface size. Moreover, both unhydrous cement particles and calcium hydroxide resulted to be present in both samples, in very located areas. In contrast, the greyscale histogram presented a uniform distribution with a high

intensity peak only in the range corresponding to CSH, but no peaks corresponding to other hydration products were detected. Therefore, an improvement of thresholding method in addition to multiple observed areas and optimization of sample preparation, might possibly result in more accurate interpretations. As the results were inconclusive and this analysis was intended only as a complementary technique, the results are not further presented.

This section allowed to give a better understanding on the influence of three different aggregate types in hardness, shape and composition. Overall, a more homogenous aggregate does not necessarily improve the scatter in fatigue, when the hardness is significantly higher than the cement matrix. The quartz mix presented a secondary strain rate lower than the two other mixes and this does not necessarily result from lower damage induced in the second phase, as could be firstly supposed. Indeed, the strain development resulted to be more dependent on the ductility of the mix. In fatigue, rapid development of plasticity occurs after the first transition phase. Thus, the mix with quartz aggregates resulted to become more brittle and the bearing capacity seems lower, when plastic strains develop. This mix with rounded shape aggregates presented a more heterogenous matrix around the aggregates and larger interface size, compared to bauxite with a more angular and porous aggregate microstructure.

4.3 Influence of aggregate type in different grain fraction

Mixes with combined aggregate types, bauxite and quartz, at different fractions are established. The procedure and details of these mixes can be found in section 2.3.2. In summary, the first mix which will be named “Qua-G” is composed of quartz as coarse aggregates (≥ 1mm) and bauxite as fine. Whereas the second mix “Bau-G”, bauxite is used in coarse aggregates, and quartz in fine. The volume of the cement matrix is kept unchanged between the two mixes, in addition to the water quantity. The composition is schematically presented in figure 4.3-1.

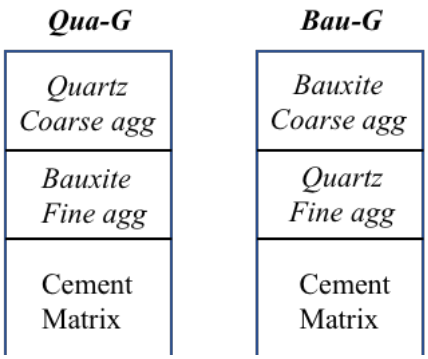

Figure 4.3-1 *Schematic presentation of proportions in mix components*

These two mixes are tested in quasi-static and fatigue and the effect of each aggregate type in the different grain fractions will be analyzed.

4.3.1 Quasi-static behavior

Quasi-static tests are carried out at 8 weeks, similarly to previous mixes. The minimum and maximum stress-strain curves are displayed in figure 4.3-2. The reference mix composed of bauxite aggregates and the mix composed of quartz aggregates are also presented for comparison.

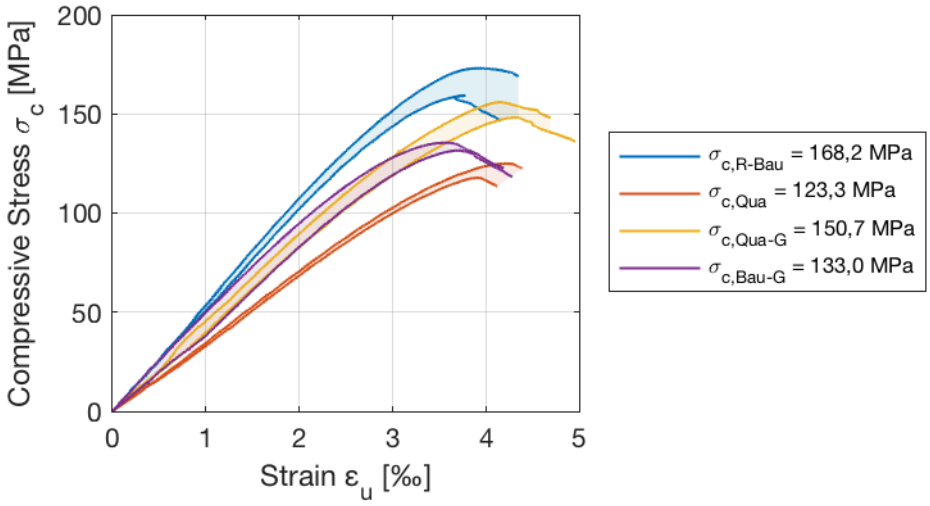

Figure 4.3-2 *Quasi-static tests with minimum and maximum evolutions for three grout mixes with different aggregates*

Mixes with combined aggregate types have a similar elastic behavior. Due to equal proportions of aggregate type (despite different sizes) and the same composition of matrix, the Young's modulus is the same between the two mixes. Table 4-5 summarizes the measurements carried out for these four mixes. A higher strength is reached for Qua-G, (mix with quartz as coarse aggregates) in addition to higher strains at peak load, compared to Bau-G. The post-peak behavior is similar for both mixes. As expected, both mixes are situated between the bauxite and quartz mix in terms of strength and Young's modulus.

Table 4-5 *Summary of measurements in quasi-static tests for four mixes*

Nom	σ_c [MPa]	$\varepsilon_{u,min} - \varepsilon_{u,max}$ [‰]	E [Gpa]
R-Bau	168,28	3,66 – 4,15	54
Qua-G	150,70	4,14 – 4,33	44
Bau-G	133,02	3,40 – 3,85	45
R-Qua	123,36	3,91 – 4,20	36

4.3.2 Fatigue Life

The compressive fatigue tests are carried out at $f = 10$ Hz, on three stress levels for both mixes. The mean number of cycles to failure, and the linear regression curves carried out over all specimens for each mix are presented in figure 4.3-3. A summarized table, with all data values can be found in appendix C-6.

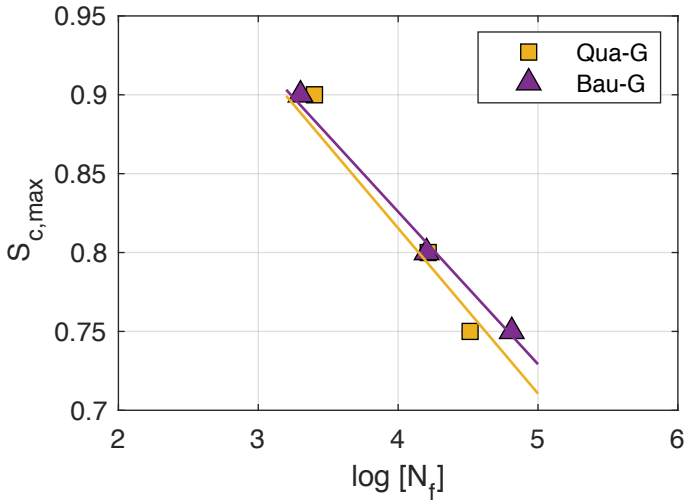

Figure 4.3-3 *Mean number of cycles to failure and regression lines for mixes Qua-G (quartz as coarse aggregates) and Bau-G (bauxite as coarse aggregates)*

At $S_{c,max} = 0{,}90$ a slightly higher fatigue life is produced for the Qua-G mix, compared to Bau-G. This mix also resulted in a higher compressive strength. However, the mean number of cycles to failure are very similar at this stress level and at $S_{c,max} = 0{,}80$. The tendency is reversed at $S_{c,max} = 0{,}75$, where a higher fatigue life is reached for Bau-G mix. The linear regression carried out on all data (not over average values) suggests a higher life to be expected for the mix with bauxite as coarse aggregates for all stress levels.

However, as the quartz aggregates previously showed large scatter, it should be firstly examined to which extent this takes place in the two new mixes. Therefore, in figure 4.3-4 all data are presented and it can be noticed at $S_{c,max} = 0{,}90$, two specimens have a relatively larger fatigue life. Opposingly, four specimens have an overall lower fatigue life than Bau-G at this stress level. Thus, the presence of these two specimens with particularly higher number of cycles to failure, can distort the mean values. This explains the linear regression predicting a higher fatigue life for Bau-G.

Both mixes are composed of quartz and bauxite, in different fractions. Nevertheless, it is clearly observed from figure 4.3-4 that the mix with quartz in coarse aggregates presents a larger scatter, compared to the other mix, where the values are relatively repeatable. It is therefore concluded, that the scatter appearing when quartz aggregates are used,

mainly results from coarse aggregates. The irregularities in type of failure, which characterize this aggregate type, have a higher influence when cracking develops in coarse aggregates.

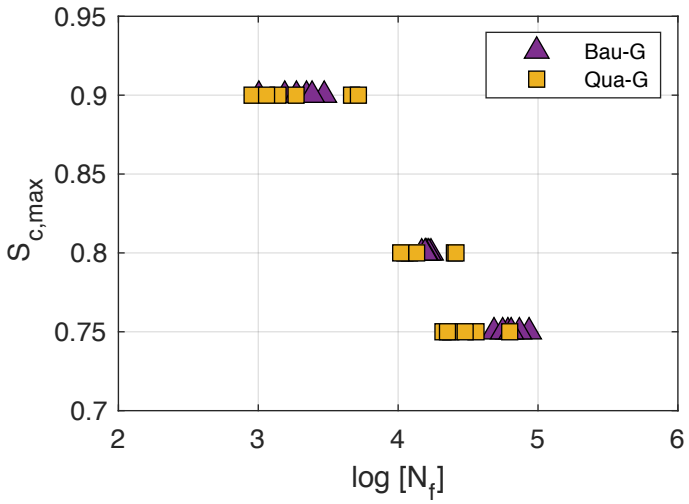

Figure 4.3-4 *Number of cycles to failure for Qua-G and Bau-G at three stress levels*

Based on these observations, it can be concluded that overall a better fatigue life is reached for the mix where bauxite is used in coarse aggregates and quartz in fine. This mix presented a lower strength from quasi-static tests and similar stiffness to Qua-G. In the literature it can often be found reports on a lower fatigue life for a higher strength concrete [77]. The reason is often related to the brittle nature of a higher strength concrete, leading to lower total strains at failure and in a localized internal damage. Conflictual data have also been reported [140] and the absence of influence has also been mentioned [81] (see literature review, chapter 1). Therefore, the strain development should be analyzed before giving a general conclusion. Nevertheless, in these studies the concrete microstructure is greatly modified between the mixes and a link with the microstructure is rarely given. Hence, instead of a direct comparison of strength in fatigue life, the difference in composition, temperature evolution and strain and stiffness development should also be considered.

4.3.3 Damage mechanisms in fatigue loading

In this section, the temperature increase for all tests is firstly evaluated. Additionally, strain evolutions and stiffness degradation will also be estimated for both mixes.

4.3.3.1 Temperature effect

The temperature evolutions for specimens from each mixture and comparable number of cycles to failure are presented in figure 4.3-5 for $S_{c,max}$ = 0,75 and 0,80. The evolutions

for $S_{c,max}$ = 0,90 can be found in appendix C-7. Due to differences in number of cycles to failure, which can influence the total level of increase, the tests which had a similar fatigue life are preferably presented. For all stress levels, a higher temperature increase is manifested for the mix with quartz aggregates used in coarse fraction. For the presented curves, an increase of $\Delta\theta$= 31 K and 22 K occurs at $S_{c,max}$ = 0,75 for Qua-G and Bau-G, respectively. Whereas at $S_{c,max}$ = 0,80 an increase of 26 K and 17 K takes place. The rate of increase is also higher for the Qua-G mix.

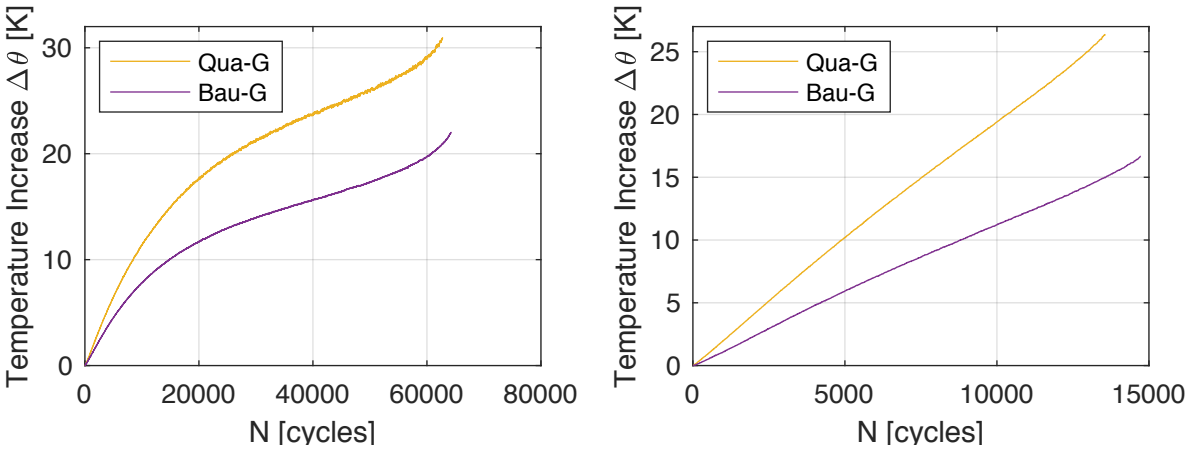

Figure 4.3-5 *Temperature evolution for Qua-G and Bau-G with comparable number of cycles to failure at $S_{c,max}$ = 0,75 (a); $S_{c,max}$ = 0,80 (b)*

This higher level of temperature increase might have an influence on the lower number of cycles to failure reached for Qua-G. Nevertheless, as the previous sections presented, the variation in the temperature ranges observed in these fatigue tests are not the only influencing factor.

4.3.3.2 Strain and stiffness development

The number of cycles to failure between the two mixes resulted to be similar at $S_{c,max}$ = 0,90 and 0,80. However, at 0,75 higher number of cycles to failure are attained for Bau-G mix. The strain evolutions of two specimens with a comparable fatigue life are presented in the upper part of figure 4.3-6. They are presented in relation to the maximum strain in the first cycle (upper-left figure) in order to simplify the comparison of the total strain growth. Whereas the upper-right figure presents the maximum and minimum strain developments. Evolutions for other stress levels and all specimens can be found in appendix C-8.

For all stress levels, Qua-G mix presented higher strains during the monotonic loading before applying fatigue. Hence, in the first cycles higher deformations are attained for Qua-G (upper right). The reason for this, is unclear as in quasi-static tests the linear relation of the stress-strain curve is similar for both mixes. The secondary strain rate for

all tests, resulted in slightly higher values for Qua-G (figure lower left), demonstrating a higher damage occurring in the second phase for this mix. The equations of the linear regression for each mix are also presented (4.1) and (4.2), and indicate a lower correlation coefficient for Qua-G mix, which analogously presented a larger scatter.

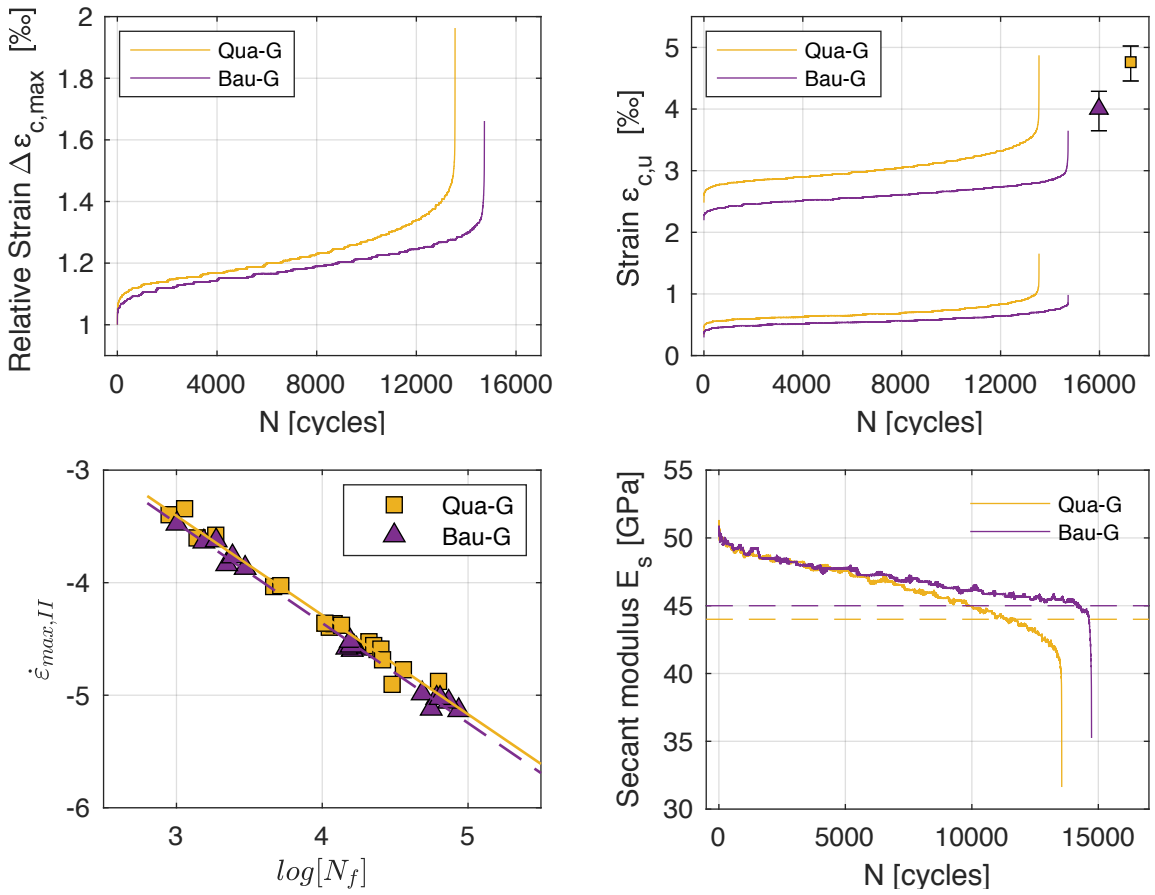

Figure 4.3-6 *Relative maximum strain development for Qua-G and Bau-G at $S_{c,max}$ = 0,80 (upper-left); Corresponding maximum and minimum strain development (upper-right); Secondary strain rate (lower-left) ; Evolution of the secant modulus (lower-right)*

$$Qua\text{-}G: \quad \log(\dot{\varepsilon}_{max,II}) = -0{,}882 \log N_f - 0{,}761 \quad R^2 = 0{,}978 \qquad (4.1)$$

$$Bau\text{-}G: \quad \log(\dot{\varepsilon}_{max,II}) = -0{,}888 \log N_f - 0{,}806 \quad R^2 = 0{,}992 \qquad (4.2)$$

The same indication is given from the evolution of the secant modulus, where despite similar initial values, the Qua-G mix is submitted to more damage in the second phase. It is likely that the temperature increase has an influence on the increased stiffness degradation observed in this phase. However, overall the evolutions of the secant modulus are comparable when other stress levels are considered (see appendix C-9). In order to evaluate if the higher initial strains in Qua-G mix are related to a different increase in secant modulus, the ratios $E_{s,0}/E_0$ are evaluated for each stress level in table 4-6. The

increase of secant modulus in fatigue in relation to the Young's modulus measured in quasi-static is remarkably similar at $S_{c,max}$ = 0,75 and 0,90. Only a slight increase is noticed at 0,90. Overall the strain rate effects seem to act similarly between the two mixes.

Table 4-6 *Mean values of stiffness increase in relation to the static tests ($E_{s,0}/E_s$) and total stiffness decrease ΔE during fatigue for each mix*

Stress Levels	***Qua-G***		***Bau-G***	
	$E_{s,0}$ / E_0	ΔE [%]	$E_{s,0}$ / E_0	ΔE [%]
0,90	14	20	11	26
0,80	12	25	11	33
0,75	10	35	10	36

Based on observations carried out in this section, it can be concluded that despite a higher strength in quasi-static tests, the mix with quartz in coarse gradation and bauxite in fine gradation presented overall lower number of cycles to failure. Nevertheless, the difference in fatigue life is not critical. It is possible that the temperature, which increased at a higher level, has an influence in the reduced fatigue life. This mix also presented higher initial strains, whereas the total strain development during fatigue did not result in significant difference. The reason for the variance in initial strains is hard to identify due to a very similar quasi-static behavior, stiffness and microstructure with the Bau-G mix. Overall, the presence of an aggregate type on a specific fraction does not seem to strongly influence the fatigue behavior in terms of number of cycles or deterioration process. Nevertheless, the scatter should be considered closely, especially for coarse quartz aggregates. If this factor is taken into account, quartz aggregates should be used in fine fractions, and bauxite in coarse gradation, for applications where grout is submitted to fatigue. This result is obviously based on the quartz type selected for these tests, in the specific specimens dimensions.

4.4 Influence of porosity on the fatigue behavior

Porosity in concrete and grout can be manifested in the form of air or free water. For numerous reasons their levels can be purposefully increased or decreased depending on the final application required. Firstly, the air voids can be present as "entrapped" or "entrained" air [87]. The first term is used to characterize pores generated around the aggregate particles and are typically of 1 mm or more in diameter. As a result they have an irregular shape. The size can be lower for high-strength cementitious materials. The

second term describes the added air voids by the means of an air-entraining agent (as used in the current work), where the distribution is relatively homogenous throughout the mix. The particle size is smaller than in the entrapped air and can vary between 0,01 – 0,1 mm. The beneficial effect in using an air-entraining agent consists in improving the freeze-thaw action by allowing the expansion during freezing without fracture. In addition, the workability is improved and segregation is reduced.

In contrast, it has generally been accepted that increased levels of porosity, in different shape or form, (water or air) result in a reduced quasi-static strength. However, the beneficial effects lead formulators to increase the water/binder content or the entrained air in applications subjected to fatigue. Within this framework, the fatigue behavior with increased porosity levels need to be addressed, particularly when very few investigations are reported. How does the material behavior change when similar levels of air and water are injected in the mix? Is the fatigue strength reduced, similarly to the quasi-static strength? And can one form of porosity have a more beneficial effect compared to the other?

4.4.1 Identification of porosity levels

In order to address the issues previously mentioned, mixes with increased levels of porosity are carried out according to descriptions in chapter 2. Firstly, the water content is increased compared to the reference mix. If expressed as w/b ratio, the variation consisted in a growth from 0,26 to 0,31. As specified in chapter 2, a small quantity of viscous agent was used to avoid segregation. Furthermore, in the second mix the porosity is increased by the use of an air-entraining agent. It is recalled that "R-Bau" is the reference mix analyzed throughout this work, "A-Bau" is the same mix as "R-Bau" with increased content of entrained air and "W-Bau" has an increased water content compared to "R-Bau".

The total water porosity technique is used for measuring the open porosity contained within each mix. The measured values are presented in the following table and are carried out on specimens with the same cylinder geometry and dimensions.

Table 4-7 *Total water porosity for the reference mix and mixes with increased air and water content*

	R-Bau	**A-Bau**	**W-Bau**
Total water porosity [%]	2,2	2,8	4,3

Firstly, it should be mentioned that similarly to the total water porosity presented in chapter 3, the values obtained are relatively low compared to tests in the literature. It is possible that the drying of the specimens was not entirely completed when the weight of the specimens was measured. The drying was performed during 10 days.

The use of the air-entraining resulted in an increase of the total porosity as expected. Likewise, the porosity increased with increasing water content, however at a higher level than the mix A-Bau. Indeed, the water evaporation due to drying, results in increase of porosity in the mix compared to the reference, where the water quantity is lower.

The porosity of the three mixes is also characterized by the means of the mercury intrusion porosimetry technique, as shown in figure 4.4-1. It can be noticed that pores with a diameter size between 0,04 up to 0,1 mm increased for the mix with entrained air and increased water quantity. This range is within the expected pore diameters induced by these two methods.

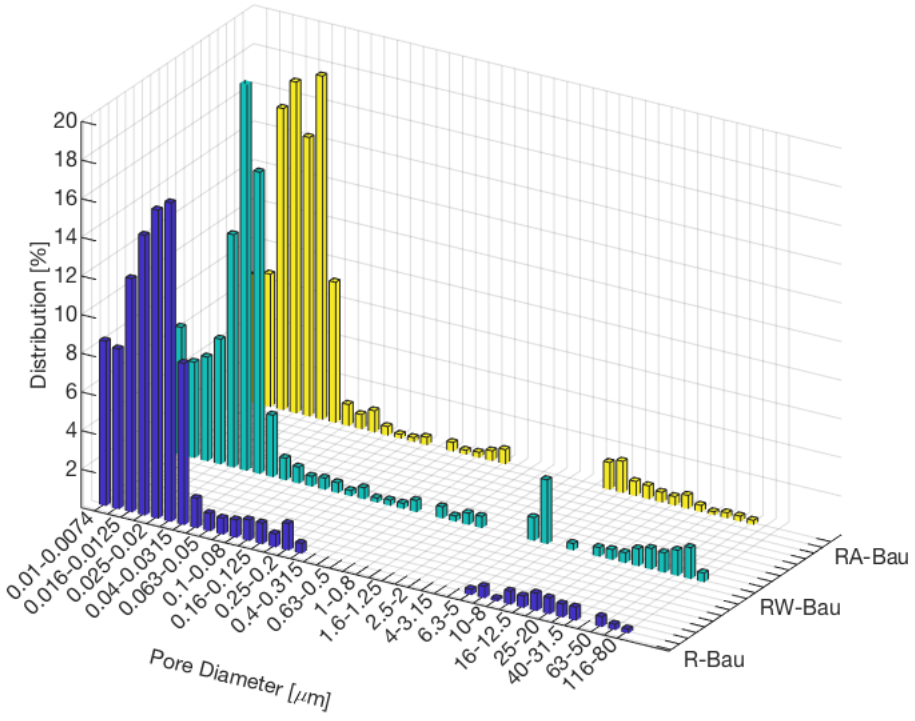

Figure 4.4-1 *Pore size distribution for the reference mix and mixes with increased levels of porosity by means of air-entraining agent and water quantity*

The mixes “A-Bau” and “W-Bau” do not have the same level of porosity. Hence, the porosity induced by water evaporation in the W-Bau mix and induced air cannot be directly compared for identifying which porosity type influences more the fatigue behavior. Nevertheless both mixes will be constantly compared to the reference mix.

4.4.2 Quasi-static tests

Quasi-static tests are carried out for the "A-Bau" and "W-Bau", similarly to the reference mix. Six specimens are used to evaluate the mean quasi-static strength. The minimum and maximum stress-strain curves are presented in figure 4.4-2 for the three mixes.

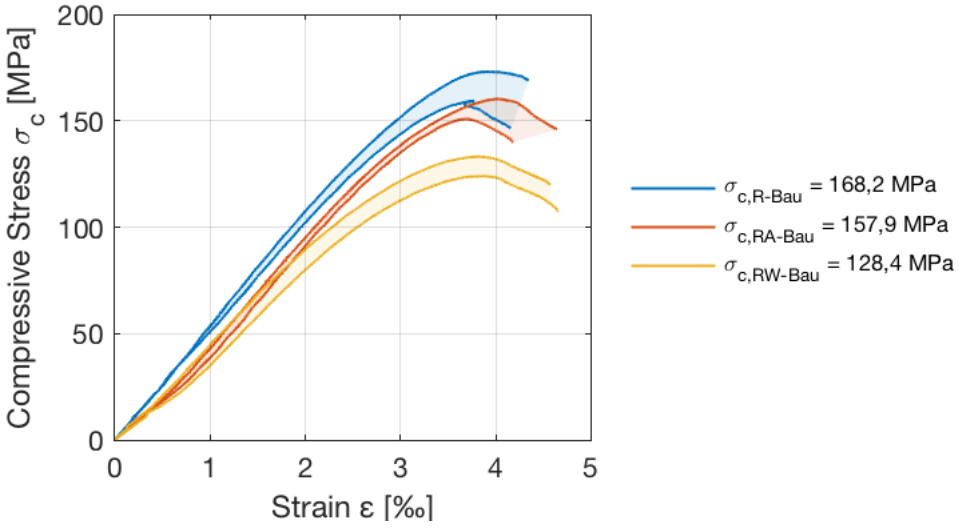

Figure 4.4-2 *Quasi-static tests with minimum and maximum evolutions for reference grout mix and two grout mixes with increased porosity level by means of air-entraining agent and water quantity*

The increase of porosity resulted in a decrease in strength of the grout. The mix with increased water quantity, which presented the highest total porosity measured, resulted in the lowest strength of 128 MPa. Likewise, in the mix with entrained air the measured compressive strength is approximately 158 MPa, compared to the reference mix which had a compressive strength of 168 MPa. Furthermore, the stiffness decreases with increasing porosity as resumed in table 4-8. The measured mean compressive strength is used for calculations of the maximum stress levels applied during fatigue.

Table 4-8 *Mean compressive strength and Young'' modulus for three mixes*

	R-Bau		**A-Bau**		**W-Bau**	
	σ_c [MPa]	E [GPa]	σ_c [MPa]	E [GPa]	σ_c [MPa]	E [GPa]
Total water porosity [%]	168 ± 5,6	54 ± 1,8	158 ± 4,3	51 ± 2,0	128 ± 3,2	44 ± 2,0

4.4.3 Fatigue life

The grout specimens within each series are tested at three maximum stress levels and loading frequency $f = 10$ Hz. Six specimens are tested at each stress level. The number of cycles to failure and the mean fatigue life is given in table 4-9, with a comparison to the reference mix. In appendix C-10, the Wöhler curves with corresponding regression lines are presented. It becomes apparent that overall fatigue life decreases as porosity content increases. However, a slight increase is observed at $S_{c,max} = 0{,}75$ for "W-Bau" compared to "A-Bau". Nevertheless, the mean number of cycles to failure between these two mixes in the related three stress levels, can be considered relatively similar, considering the scatter.

Table 4-9 *Number of cycles to failure for three grout mixes at three stress levels and corresponding mean values (f = 10Hz)*

Mix	Stress Level $S_{c,max}$	Number of cycles to failure N_f						Average
R-Bau	0,90	2255	2435	2664	2693	3156	4417	2937
	0,80	9041	10881	13469	13479	19225	19873	14328
	0,75	23098	36572	51918	53577	62609	64915	48782
A-Bau	0,90	1274	1419	1464	1741	1839	2089	1638
	0,80	8524	9810	10867	11762	12616	14354	11322
	0,75	17401	22634	30416	31325	35128	37599	29084
W-Bau	0,90	431	1258	1656	1768	1796	1913	1470
	0,80	8513	10352	11584	11653	12803	14700	11601
	0,75	23364	27235	30263	31939	46934	50467	35034

Similarly to the analysis methodology followed in the previous sections, the temperature evolution is firstly examined for tests with similar number of cycles to failure for each stress level. An example for $S_{c,max} = 0{,}75$ is shown in the following figure, whereas evolutions for other stress levels can be found in appendix C-11. For all tests, the temperature increase for the reference mix is lower and occurs at a lower rate. It is possible that mixes with increased porosity levels present more initial flaws leading to more rapid cracking and more friction during compressive fatigue loading, therefore leading to a slightly higher rate of temperature. However, one can notice that the difference between the three mixes is not significant. Especially for "A-Bau" and "W-Bau" the curves overlap almost perfectly. Almost no difference can also be observed from evolution in appendix C-11. Hence, it can be assumed that the temperature increase does not have a different effect on the mixes considered in this part.

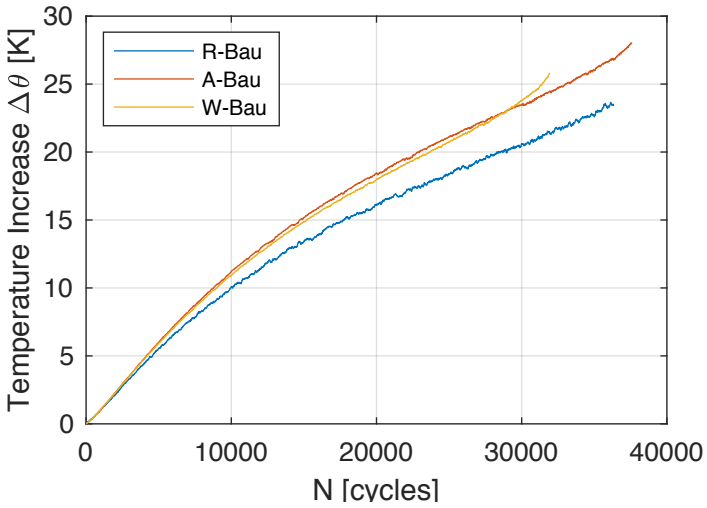

Figure 4.4-3 *Temperature evolution with comparable number of cycles to failure at $S_{c,max} = 0,75$ for the reference mix and mixes with increased porosity levels*

4.4.4 Strain and stiffness development

Current available work on the influence of porosity on fatigue in compression or flexion is mainly focused on fatigue life. However, the strain and stiffness development is as significant, in order to understand the influence in the evolution process in relation to the grout microstructure. Thus, these two parameters have been investigated in the present work.

In previous sections, a strong emphasis was given to the effect of strain rates occurring during fatigue loading, at both levels of frequency tested. Its influence in cementitious materials was reported to take place due to the presence of free water in the hydrates. Therefore, it can be reasonably assumed that increased water content introduced in the mix leads to an increased level of free water during the test and the impact of strain rates would be greater. An indicator of this effect was considered to be the secant modulus measured in the first cycle during fatigue and confronted to the value measured during quasi-static tests. The calculated ratios for each stress level and each mix are presented in table 4-10.

Table 4-10 *Mean values of stiffness increase in relation to the static tests ($E_{s,0}/E_s$)*

	R-Bau	**A-Bau**	**W-Bau**
Stress Levels	$E_{s,0}$ / E_0 [%]	$E_{s,0}$ / E_0 [%]	$E_{s,0}$ / E_0 [%]
0,90	10	15	14
0,80	4	10	17
0,75	7	11	19

One can notice a significant increase of stiffness for the mix with increased water content compared to the reference and this occurs at each stress level. Indeed, the presence of free water delays the appearance of microcracking. Particularly at $S_{c,max} = 0{,}75$ the increase of stiffness is large (19%), which can help explain the slight fatigue life increase at this stress level. Additionally, a higher ratio $E_{s,0}/E_0$ is also manifested for the mix with increased air content. Hence, it can be concluded that the strain rate effect has a higher influence on mixes with increased levels of porosity and as a result the material becomes more rigid, when fatigue loading is applied.

In addition to the stiffness evaluation at the beginning of fatigue loading, the evolution of stiffness and strain during the test is analyzed. In order to simplify the observations, only evolutions with similar number of cycles to failure are presented for each mix at each stress level. In figures 4.4-4 and 4.4-5 the same specimens as presented in figure 4.4-3 are shown. Other evolution curves can be found in appendix C-12 and C-13.

Firstly, it can be noted in figure 4.4-5 right, that for W-Bau mix a large gap exists between the secant modulus and the dotted line which represents the measured stiffness and this gap is larger than for the two other mixes. This can also be found for other stress levels as shown in appendix C-13 and illustrates the previous statement of strain rate effects having a higher influence on this mix. Furthermore, this mix undergoes less strain increase at the beginning of the test (see figure 4.4-4 right), which is related to a higher ratio $E_{s,0}/E_0$. As the brittleness of this mix increases at a higher level than the two other mixes, less deformation occurs. However, during loading the strain increases at a higher rate analogously to the rate of stiffness degradation. Additionally, the total strain growth in relation to the first cycle is higher for W-Bau mix (figure 4.4-4 left). It is possible that the higher porosity facilitates the water movement in the microstructure, which is in the origin of strain increase. Furthermore, after reaching the peak load in quasi-static tests the “W-Bau” mix presented a less brittle behavior, by enduring more strain increase before reaching failure. In the first section of this chapter, it was suggested that mixes which present a more ductile behavior in the post-peak region are more likely to deform more during compressive fatigue. Hence, this hypothesis seems valid for the current mixes likewise.

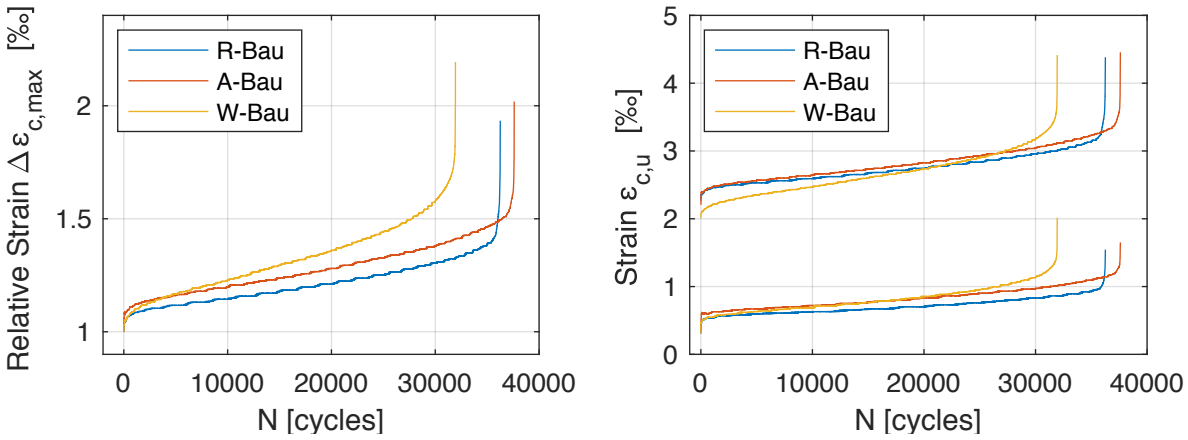

Figure 4.4-4 *Relative maximum strain evolution for specimens of each mix with similar number of cycles to failure at $S_{c,max} = 0{,}75$ (left) ; Corresponding minimum and maximum strain evolutions and mean values of strain at failure (right)*

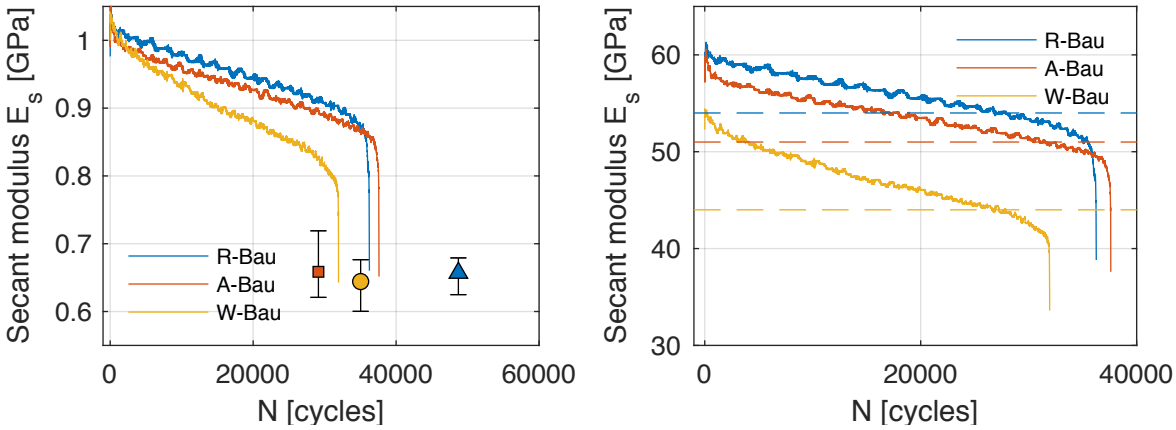

Figure 4.4-5 *Relative secant modulus evolution for specimens of each mix with similar number of cycles to failure at $S_{c,max} = 0{,}75$ (left) ; Corresponding absolute values of secant modulus and comparison with the elastic modulus (right)*

The more rapid development of strain in the secondary phase for “W-Bau” mix is related to the initial microstructure presenting more initial flaws. Microcracks are more likely to develop and connect in the more porous mix. These rates in the second phase of strain evolution are calculated for all tests and for each mix. The regression curves in relation to the corresponding logarithmic number of cycles to failure are presented in figure 4.4-6.

This figure also show higher rates for the mix with entrained air compared to the reference. Nevertheless, the difference becomes smaller for lower stress levels and almost no difference takes place. This suggests that for low stress levels, the damage evolution is similar for small quantities of increased air content.

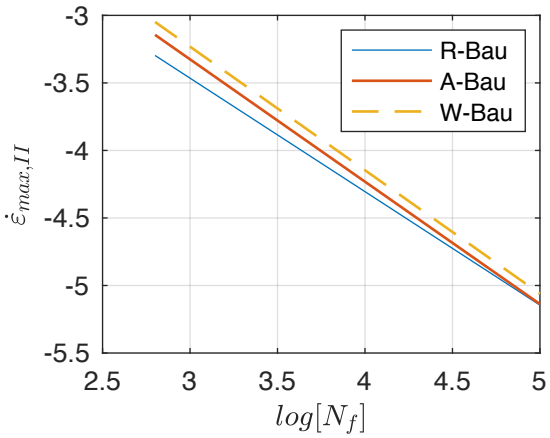

Figure 4.4-6 *Regression curves of the secondary strain rates in relation to the logarithmic fatigue life for each mix*

Observations of the failure surface for different specimens with increased air content, showed an increasing number of microcracks in the interface aggregate-matrix. Lower quantities of aggregates were subjected to cracking or failure. It indicates that increased air content results in a less strong bond between the aggregate and the matrix. This is only a qualitative macroscopic observation. However, a similar examination [87] has been previously reported.

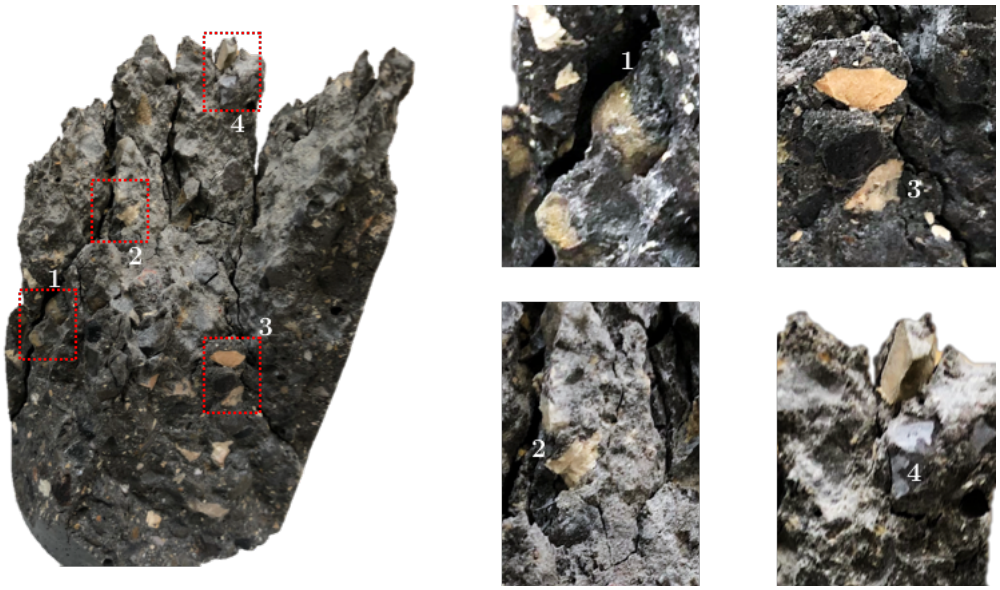

Figure 4.4-7 *Failure surface of a specimen with entrained air and areas with interface microcracking*

4.5 Conclusions

This chapter was divided into three main parts, where some parameters in the mix composition were analyzed and their influence on the fatigue behavior was examined. The focus was not only investigating the fatigue life, but also establish a relation with the microstructure. For this reason, three aggregates types were firstly analyzed. Two of these aggregates with different properties and hardness, were used in different grain fractions. Finally, the porosity was increased compared to the reference mix by air-entrainment agent and water quantity.

Influence of aggregate type

In addition to the reference grout established with bauxite aggregates, two other mixes with quartz and tabular alumina aggregates were developed. The interest in tabular alumina is reflected by its chemical purity, which was initially supposed to result in lower scatter during fatigue testing. Indeed, in chapter 3 it was demonstrated that microcracking can develop through aggregates, in addition to the ITZ and matrix. However, the higher strength and stiffness of this aggregate type led to incompatibilities with the cement matrix and development of microcracking only in the interface and matrix. Therefore, the homogenous microstructure of the aggregates does not add a beneficial effect and large data scatter was still observed. The largest scatter occurred in the mix with quartz aggregates, where both in quasi-static and fatigue tests the cracking tends to develop through the aggregates, due to the lower hardness. Quartz minerals have no cleavage and exhibit a conchoidal fracture. Thus, the fracture for this aggregate type generally occurs in an irregular manner and in all directions, leading to a possible higher scatter during fatigue loading. The presence of microcracking being more present in the aggregates than in the matrix, seemed to lead to lower temperature levels developed during loading, due to lower friction.

Nevertheless, the scatter in the mix with quartz aggregates did not derive only from the type of failure endured by the aggregates, but also an initial uncommon “microstructure arrangement” for some specimens, which was reflected by highly increased stiffness. SEM observations jointly used with EDS, showed the presence of anhydrous cement particles in this mix close to the interface area, which do not seem to appear in the mix with bauxite aggregates, and indicate a more heterogenous matrix. However, from closer observations only CSH hydrates could be found in the cement paste, due to an optimized w/b ratio and the use of silica fume.

The Stefan effect is exhibited in the three mixes, however to a different degree. Bauxite aggregates are more porous as shown from SEM and they locally consume the water in the matrix. Therefore a better bond is created in the interface and less water is locally present. In quartz aggregates, no absorption takes place and is possible that more water is present in the hydrates resulting in a mix more prone to dynamic effects. For this reason, the stiffness increased significantly and the strain development in the first phase is lower compared to the other mixes. The mix with quartz aggregates presented overall a slower evolution in the second phase and this is not due to lower damage occurring in the mix, as can be firstly supposed. On the contrary, lower ductility is observed in quasi-static tests, which is reflected in fatigue by less capacity to deform and endure plastic strains. For this reason, the third phase corresponding to crack coalescence develops very rapidly.

Overall, a better bond is achieved in the mix with bauxite aggregates, in a mechanical interlocking type, due to the rough and porous surface.

Final Note
Based on the presented observations, the mix with bauxite aggregates would be more adapted in applications prone to fatigue loading. Firstly, less scatter takes place, which is a relevant factor. In addition, at high stress levels the fatigue life is larger compared to the mix with quartz aggregates. For lower stress levels, no significant difference in terms of number of cycles to failure can be found (under the condition that the two specimens which resulted in unexpected high stiffness are omitted). In addition, if tested at lower loading frequencies it is highly possible that a higher fatigue life would be reached for the mix with bauxite aggregates. Finally, this mix presented better bonding properties and higher capacity to deform when plastic strains are developed.

Influence of aggregate type in different fractions

Due to the demonstrated influence of aggregate type on static and fatigue behavior, one can question whether implementing different aggregate types on different grain fractions would result in a modified performance. Quartz and bauxite aggregates, which presented large disparities, were used as coarse and fine aggregates with the same quantity in volume. These two mixes resulted in a similar elastic behavior with an approximately equal stiffness and similar post-peak behavior. However, a higher compressive strength resulted for the mix where quartz was used in coarse aggregates and bauxite as fine. In contrast, this mix resulted in an overall lower fatigue life, when comparing the regression S-N curves. Literature review showed that similar results, i.e. a lower fatigue life for a higher strength concrete can be expected and the reason is often related to the brittle nature of a higher strength concrete. Nevertheless, static tests did not necessarily show

a more brittle behavior for the higher strength concrete. On the contrary, this mix presented higher initial strains and a slightly higher secondary strain rate. Furthermore, similar rates in stiffness deterioration and total strain development were attained. In fatigue tests, a slightly higher stiffening could be observed in the first cycles for the mix with quartz as coarse aggregates, however the difference between the two mixes was almost negligible.

Therefore, the reason for an overall lower fatigue life for the higher strength grout cannot be identified. Nevertheless, it should be mentioned that the presence of an aggregate type on a specific fraction does not seem to *strongly* influence the fatigue behavior in terms of number of cycles or deterioration process.

It should be noted, that the scatter should be considered closely, especially for coarse quartz aggregates, as this mix resulted in larger data scatter. If this factor is taken into account, quartz aggregates should be used in fine fractions, and bauxite in coarse gradation, for applications where grout is submitted to fatigue. This result is obviously based on the quartz type selected for these tests, in the specific specimens dimensions.

Influence of porosity on fatigue behavior

The investigations in this chapter aiming to provide an understanding of the influence of different mix components in high-strength grouts were completed by a study of increased porosity levels in two forms : air content and water quantity. Despite a decrease of strength which could be expected for these mixes, numerous on-site applications can condition the use of mixes with a higher porosity content. Therefore, this was an issue which needed to be addressed in fatigue.

The MIP technique showed an increased content of pores with a diameter size between 0,04 mm up to 0,1 mm for the mix with entrained air and increased water quantity. In addition the total water porosity also demonstrated a higher total void content. Therefore, as expected the quasi-static strength and stiffness were lower with increasing porosity, but the mix with increased water quantity presented a less brittle behavior. This mix was particularly interesting as it resulted to be more prone to strain rate effects. An increase of stiffness (ratio between the first cycle in fatigue and the Young's modulus) up to 19% was observed. Indeed, a hypothesis was emitted in the previous chapter, where during fatigue loading the Stefan effect occurs due to larger water content in the CSH hydrates. Therefore, this seems to be validated for this mix.

Hence, this mix firstly became more brittle at the beginning of fatigue test resulting in lower strains. However, with increasing test duration the water freely moves in the microstructure, leading to higher deformations. This phenomenon is also in correlation with the more ductile behavior detected in quasi-static tests.

The variations between the reference mix and the air entrained mix, were not as significant. The main distinction seemed to arise from areas of microcrack development. Indeed, observations of the failure surface for different specimens with increased air content, showed an increasing number of microcracks in the interface aggregate-matrix. Lower quantities of aggregates were subjected to cracking or failure. Thus, it indicates that increased air content results in a less strong bond between the aggregate and the matrix.

Final Note

The conclusions from this chapter help firstly to extend to a better understanding the behavior of different high-strength grouts. More information on the influence of microstructure on the macroscopic behavior is presented. Additionally, the informations gained from this work can be helpful in better formulating grout or concrete mixes adapted to applications situated in a fatigue-prone environment.

Chapter 5
Flexural Fatigue Behavior of High-Strength Grouts

5.1 Introduction

The main focus of this thesis is the comprehension of the fatigue behavior of high-strength grouts in compression. Previous chapters showed a relatively detailed analysis of multiple mixes of the fatigue life and damage mechanisms involved. A *limited part* of the work was dedicated into observations of flexural fatigue, in order to estimate whether any difference takes place in number of cycles to failure between the two different testing methods. Indeed, a few reports in the literature suggested that if identical loading ratios are applied to the material, the S-N relation is independent on the testing type. However, not many reports are found in the literature that examine both flexural and compressive fatigue.

Furthermore, high-strength grouts can be used in road joints or pavements, where flexural stresses are particularly present. For this reason, three point bending tests are carried out this chapter. Similarly to the work in previous chapters, the results from static tests are firstly presented in the scope of this study. Subsequently, another section provides an overview of the results from fatigue tests on notched specimens. It should be noted that these tests were developed mainly to give additional data on fatigue life and estimate whether a distinction takes place with compressive fatigue. Therefore, the analysis of fatigue behavior in flexural tests is not as exhaustive as in previous chapters.

5.2 Quasi-static strength

Flexural tests are often used to assess the tensile behavior of concrete, due to : the practical simplicity compared to direct tensile tests and to the correlation in behavior with the loading conditions encountered in practice. Indeed, especially in fatigue, the flexural tests are the main type of testing used for concrete or fiber reinforced concrete used in bridges or pavements. High-strength grouts can also be used in applications prone to flexural fatigue loading. Furthermore, a few reports [99] indicated that Wöhler curves for tensile and compressive fatigue are identical. Therefore this chapter was developed mainly to determine how the fatigue life changes with changing loading type. For this reason, three point bending tests are carried out in quasi-static and fatigue loading, accordingly to the method presented in chapter 2, section 2.5.3. These tests are carried out only for the reference mix composed with bauxite aggregates. It should be noted that the specimens come from different batches, compared to those used in compressive tests.

All specimens are notched in mid-span as described in 2.5.3.1. The notch represents an initial flaw, which does not take place in applications and it has an influence on the structural behavior. However, the choice was made to carry out tests in these specimens, where the cracking zone is initially known and the crack growth can be easily observed with a camera for image correlation. In addition the presence of the notch, forces deformations to localize and can modify the post-peak behavior. Nevertheless, it is not necessarily located in the weakest cross-section and as demonstrated in [174] the flexural strength remains unchanged between notched and unnotched specimens.

The displacement of the hydraulic cylinder, the number of cycles and the applied force are measured during the test. Moreover, the specimen displacements are measured with the DIC technique.

The flexural strength is calculated at mid-span by the following expression:

$$f_{t,fl} = \frac{3\,F_{max}\,L}{2\,b \times h^2} \tag{5.1}$$

where, F_{max} is the maximum force recorded during the test [N], L is the span length [mm], b is the width of the specimen [mm] and h is the distance between the tip of the notch and the top of the specimen [mm]. From this relation the flexural strength is estimated for 6 specimens. The mean strength is estimated at 15,53 ± 0,65 MPa (see figure 5.2-1). However, it should be noted that the stress distribution is not constant over the section and the value of flexural strength cannot be accurately known, which is the main drawback of this testing method.

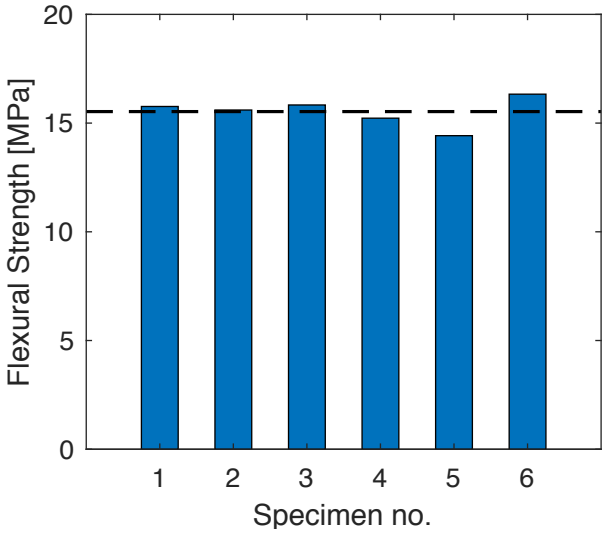

Figure 5.2-1 *Flexural strength of six specimens and the corresponding mean strength*

The specimen displacements are measured over the acquired images during the tests. The observed area is approximately 70 × 40 mm over 1400 × 1040 pixels with a mesh length of 20 pixels (see figure 5.2-3). Therefore, displacements are measured as the mean value over a band of 10 pixels at mid-height on x-axis (U_x) (in the correlation code RT3 used here, the vertical axis is noted x). Initially, the histogram of the grey-level is analysed and adapted. The standard deviation obtained on U_x and U_y images is 0,02 pixels.

The entire force displacement curves cannot be obtained, due to the low acquisition frequency of the camera used for the image correlation in these tests. However, a few acquired data allows to establish the relation. The displacements presented in the following figure 5.2-2 correspond to measurements up to the maximum force applied. Due to the high-strength of the material and the small dimensions of the specimens, the failure occurred in a brittle manner and the post-peak evolution is not acquired. The relation of the stress applied and the produced displacements are presented in figure 5.2-2 for 4 of the specimens (no. 2 to 5 according to figure 5.2-1). An almost linear relation is identified for specimens 2, 3 and 5, however a type of two-slope curve can be observed for specimen 4, which resulted mainly due to a measuring error, rather than the actual mechanical response. In figures 5.2-3 (b) and (c) are presented two results after image correlation between a reference image at the beginning of the test and the last deformed images before reaching the peak. It can be observed that cracking initiates at the notch tip and propagates quickly up to image (d) acquired just after peak force. The crack path developed in the specimen surface can be easily detected. For comparison, an image of the same specimen after failure is shown in figure (e), where the same crack path can be identified. As expected, no other cracks are developed in the surface of the specimen during the flexural test.

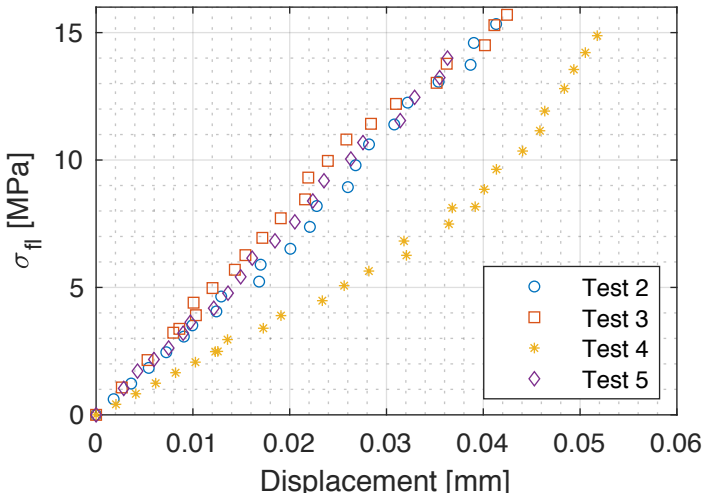

Figure 5.2-2 *Stress-displacement curves in quasi-static tests*

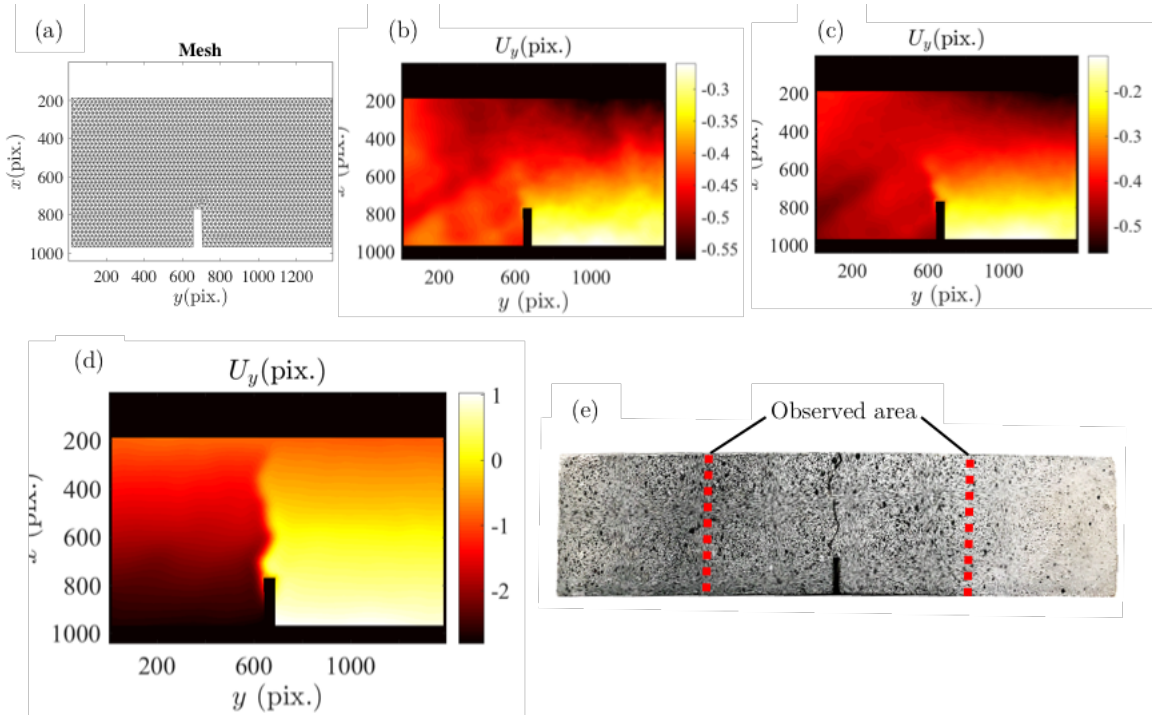

Figure 5.2-3 *Generated mesh with a length of 20 pixels (a) ; Correlation of last images before failure for test 5 (b)(c) ; Crack path in post-peak (d) and the same tested specimen after failure (e)*

5.3 Fatigue life

Based on previous measurements of flexural strength, the stress levels S_{max} are identified at 0,70, 0,75 and 0,80. The loading ratio is kept the same as in the compressive tests at 0,1. Firstly, the flexural tests are carried out at a loading frequency $f = 10$ Hz and only

at $S_{max} = 0{,}75$, five specimens are tested at 1 Hz. Other details on loading conditions are described in section 2.5.3. Table 5-1 gives an overview on the number of cycles to failure for each test and the mean values for each stress level.

Table 5-1 *Number of cycles to failure in notched 3-point bending test for the reference grout at different stress levels*

Frequency [Hz]	**Stress Level S_{max}**	**Number of cycles to failure N_f**						**Average**
	0,80	52	148	540	910	978	3812	1073
10Hz	0,75	272	6222	8746	59482	95404	115664	47631
	0,70	10898	38213	90592	155820	474006	848919	269741
1Hz	0,75	33	210	677	4513	21240		5335

It is particularly striking the scatter obtained in these tests. In compressive tests, the same mix also presented some inevitable scatter (see chapter 3), however not at the same extent as in the flexural tests. This can be seen mainly at $S_{max} = 0{,}75$ and 0,70 and two main reasons are identified. Firstly, it was pointed out in chapter 2 and 3, that a good centering of the specimens is mandatory for repeatable results between different tests. For the testing machine in compression, a set-up was specifically conceived for the current tests in order to ensure that all tests are carried out in the same position. Additionally, the presence of two laser distance sensors helped to determine, whether eccentricity takes place. However, in flexural tests no specific set-up was used. The areas where the lower supports are placed, are previously marked and serve as a guide for the centering. But this type of centering can include an error from the operator. It should be noted that in even in quasi-static tests, the measured strength values are more dispersed with a covariance of 4,2% in flexural tests, in contrast to 3,3% in compressive tests. Furthermore, the second reason identified for the scatter in these 3-point bending tests is related to the notch height. The notch is performed on hardened specimens before the test with a saw configured to execute the same length. Nevertheless, it is not excluded that variations may take place in the actual length performed, which can modify the crack development during fatigue.

Overall, a larger scatter in flexural tests seems to take place compared to compressive tests, also based from literature observations [49,93]. It can be laborious to draw conclusions based on the results obtained in these flexural tests, where the values are very dispersed. However, when the average fatigue life is compared for the same stress level between flexural and compressive tests (see appendix A-1), a larger fatigue life is obtained for tests in compression. The average value is only an indication of the trend in experimental results.

A similar conclusion can be given when comparing the mean fatigue life at the loading frequency of 1 Hz. At $S_{max} = 0{,}75$ larger number of cycles to failure are attained for specimens tested in compression. Only one stress level is tested at 1 Hz in flexural tests and despite the scatter, a decrease by a factor of 9 is manifested compared to tests at 10 Hz. Of course, tests at other stress levels are required to give a general conclusion, nevertheless there seems to be a trend where lower number of cycles to failure are reached for a lower loading frequency. This was also confirmed by other flexural tests carried out in additional mixes, which are not presented here. Furthermore, thermocouples and infrared camera are used for temperature measurements on the surface of the specimen. Specimens tested at 10 Hz showed no temperature increase, even for large number of cycles to failure. Indeed, it was previously concluded in chapter 3, that a temperature increase takes place in specimens where a high loading frequency is applied and it results from the friction between microcracks. In notched 3-point bending tests, only one crack is detected to develop at the notch tip and propagates up to failure of the specimen. Therefore, only crack opening occurs and no friction, which leads to an absence of generated temperature, when comparing to the high levels observed in compression. As a result, only the strain rate effect takes place leading to an increased strength at higher loading frequencies. However, additional data at other stress levels are necessary to confirm these results.

An attempt is made to measure the evolution of the displacement during the fatigue tests by DIC and the use of a high-speed camera, accordingly to descriptions in section 2.5.3.3. The camera is triggered every 1000 cycles and therefore no continuous measurement is made, in contrast to compressive tests. Regrettably, the high-speed camera could not be triggered to register the last cycles before failure. With the considerable scatter in terms of fatigue life, comparisons or a large significant analysis cannot be made. Nevertheless an example of strain evolution is presented in figure 5.3-1. It is related to the specimen, which failed at 10898 cycles at $S_{max} = 0{,}70$. The observed area on the specimen's surface is approximately 52 × 40 mm over 1024 × 1024 pixels. The followed method for measuring the displacement is similar to the one presented for static tests.

The strain increases with increasing number of cycles, however a slower evolution seem to take place in the second phase, compared to evolutions observed in compressive tests. The first and last phases could not be registered, but a three-step damage mechanism seem to take place. Due to the small data acquired during tests and the significant scatter in terms of fatigue life, the analysis of fatigue in flexion in terms of strain or stiffness deterioration could not be analyzed further.

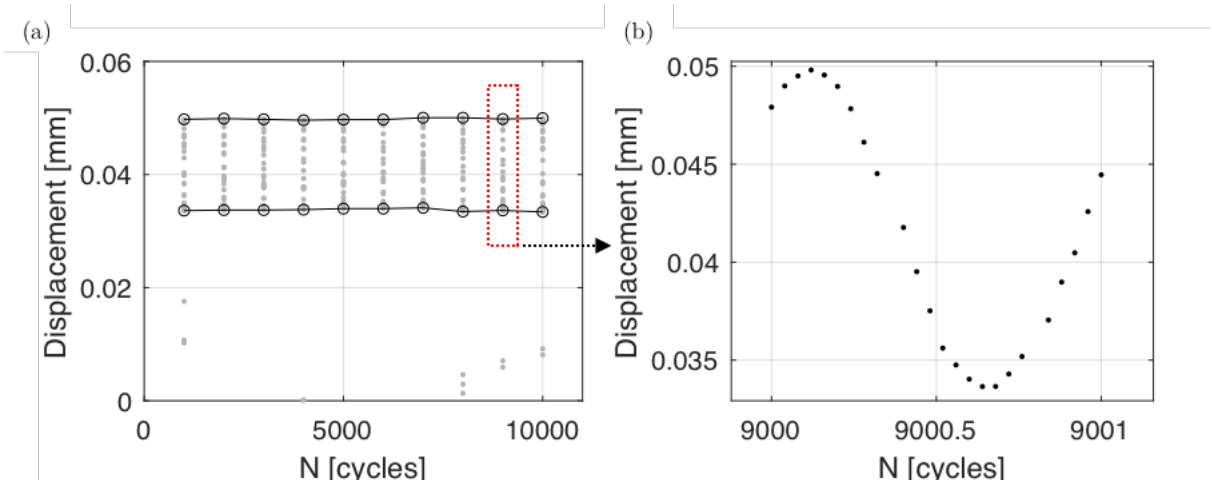

Figure 5.3-1 *Example of displacements evolution at different number of cycles (a) ; Identified displacements from acquired images during one loading cycle (b)*

Finally, the tested specimens in quasi-static and fatigue tests all developed only one single crack up to failure of the specimen, initiated at the notch tip. In fatigue, the evolution of the crack was slow, despite early appearance. Overall, no particular difference can be noted between the crack patterns developed in quasi-static and fatigue tests, as presented in figure 5.3-2 for specimens after failure.

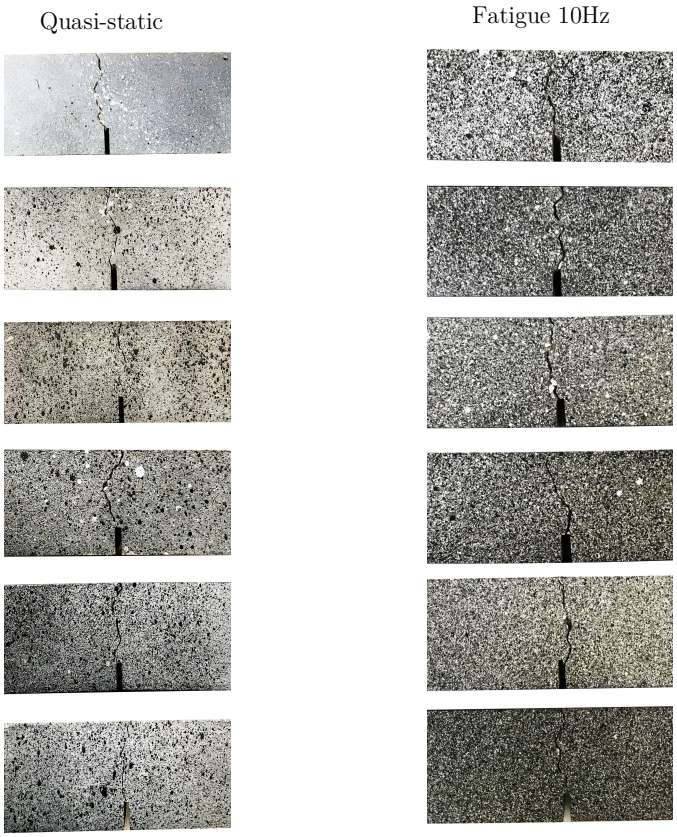

Figure 5.3-2 *Crack pattern in quasi-static and fatigue flexural tests*

5.4 Conclusions

This chapter was focused on 3-point bending fatigue tests on one high-strength grout and evaluating possible disparities with fatigue tests in compression. The same loading ratio was applied in both testing types and the testing methodology is kept unchanged. The first remark to be addressed from these tests is the high scatter achieved in terms of number of cycles to failure, which occurred at each stress level. The data scatter was also present in compressive tests, however to a small scale. The main reasons identified for this outcome are : the test conditions less upgraded, mainly in terms of specimen centering and the notch length which can present a variation between specimens.

Overall, fatigue life in flexural tests resulted to be shorter than in compressive tests, despite the scatter found. Only at $S_{c,max} = 0{,}75$ a similar average fatigue life could be found. The most essential difference resulted for the specimens tested at 1Hz, where the fatigue life was almost 10 times lower than in compression. Along with these examinations, further measurements on fatigue tests showed no temperature evolution during loading. As this phenomenon is an outcome of the friction between microcracks, it can be expected that in bending tests, it occurs to a lower extent or is completely absent. Finally, the tested specimens in quasi-static and fatigue tests all developed only one single crack up to failure of the specimen, initiated at the notch tip. In fatigue, the evolution of the crack was slow, despite early appearance. Overall, no particular difference can be noted between the crack patterns developed in quasi-static and fatigue.

Some additional information was provided from this chapter on the relation between flexural and compressive fatigue life of high strength grout. However, further insight and continuous research is still necessary. Improved tests conditions with improved data acquisition and more specimens tested at lower loading frequencies in different stress levels would be essential for a better understanding of the behavior of high strength grouts in bending. Furthermore, the specimens tested here had relatively small dimensions due to practical convenience. However, larger size specimens should be tested, such as according to Rilem recommendations for concrete beams of 150x150mm in cross section with a minimum length of 550 mm.

Final conclusions

Reminder of objectives

The relevance of a better comprehension of compressive fatigue behavior in concrete and grout, especially in slender structures was developed in chapter 1. From an examination of the current state of the art, a research work was established in order to verify the emitted assumptions, provide more data on the non-consensual issues and clarify some of the many open questions regarding the behavior of high-strength grouts. Against this background, two main directions were pursued :

⇒ Based on extensive experimental tests, providing an analysis and description of involved mechanisms in the damage process during fatigue loading in compression

⇒ Based on the gained information from the first topic, identify how the grout microstructure and the use of different mix components impact the fatigue behavior

Approximately 300 tests are shown and analyzed throughout this manuscript. Another 200 fatigue tests, were carried out during the thesis period which are not presented here. It was the first time this type of test was conducted on grout or concrete at the LMT laboratory. Therefore, a large amount of work was initially implemented into designing the most appropriate measuring techniques, data acquisition devices, defining loading procedures and processing the large amount of data effectively. From the analysis of these experimental tests, the main resulting conclusions are synthetized.

Damage mechanisms resulting from fatigue loading in compression

In spite of an improvement of test conditions and centering of specimens, the scatter in number of cycles to failure is still present due to the heterogenous nature of the material. Random localization of damage occurs in the third phase, leading to large scatter. The use of aggregates with high chemical purity, such as tabular alumina did not necessarily improve the scatter due to the high stiffness of these aggregates, leading to incompatibilities with the cement matrix and to microcracking mostly in the interface or

matrix. Whereas, the reference mix with bauxite aggregates presented microcracking through the aggregates additionally.

The results of the experimental investigations have shown that the compressive fatigue loading modifies the grout behavior in various ways. Non-linear evolutions take place macroscopically, jointly with microstructural changes. Microcracking develops since the first phase in the mix and this was also observed with digital image correlation. In addition, the present microcracks resulting from loading or hydration grow within this phase, both affecting the bearing capacity. Subsequently, a stable crack growth occurs up to an unstable third phase which leads the specimen to failure.

The transition between these phases resulted to be dependent on the maximum stress level applied and the loading frequency. Almost all parameters analyzed presented a strong time and stress dependent relation, in particular the strain and stiffness developments. The strain rate effects seem to have a strong influence in fatigue and the material became more brittle during the first cycles, which was demonstrated by a significant increase of stiffness. The cyclic loading creates a deterioration of stiffness and increase of deformations. At the lower stress levels which resulted in larger number of cycles to failure, strain increased at higher values and more stiffness loss occurred, demonstrating a larger damage state in the material. Indeed, at higher stress levels the damage is localized more rapidly, whereas at lower stress levels is more distributed. The higher deformations reached for a longer testing time (which are even more clearly identified at lower frequencies where the testing time is longer), demonstrated the time-dependent viscous changes in the cement matrix, analogously to creep. Overall, the strains at failure after fatigue loading were larger than the envelope curve from quasi-static tests. Hence, the hypothesis in the literature of an equality of damage states between static and cyclic (fatigue) loads could not be confirmed.

A few questions still remain open on the influence of loading frequency. As aforementioned, at high stress levels a low frequency might have a negative effect on fatigue life. However, at lower stress levels a higher fatigue life was obtained. The main reason for this was attributed to the temperature increase at high loading frequencies which adds additional damage and shortens the fatigue life. Nevertheless, tests at lower stress levels or at lower loading frequencies would be necessary for confirmation. The temperature increase resulted to occur mainly from friction between microcracks.

Different alternative analytical and predictive methods were explored in order to predict the strain development or the fatigue strength. In particular, the secondary strain rate showed a linear relation with the number of cycles to failure and with a very low scatter, which could be useful in terms of prediction. However, for application in structures more analysis would be necessary, especially to establish a link with variable loadings.

Influence of different mix components

It was essential in the current work to test different mixes of high-strength grouts in order to confirm if the previously presented mechanisms are relevant. Additionally, in order to develop a more optimal high-strength grout mix for applications prone to fatigue loading, it was considered relevant to investigate a few aspects of the influence of formulation on fatigue behavior. Furthermore, relatively low research is available on the literature on this subject.

Three aggregate types with very different properties were studied, nevertheless the main focus was directed towards bauxite and quartz, being more susceptible to be used for the current applications. Particularly in the mix with quartz aggregates, more microcracking was present within the aggregates. The fracture for this aggregate type generally occurs in an irregular manner and in all directions, leading to a higher scatter during fatigue loading. This resulted to be more present in the coarse fraction. Furthermore, it was demonstrated that a larger interface size is developed for the quartz aggregates compared to bauxite. Indeed a better bonding with the matrix is achieved for bauxite aggregates which has a rough and porous surface. Additionally, the cement matrix resulted to be less homogenous when quartz aggregates are used, with anhydrous cement particles close to the aggregates, possibly due to a wall effect created by the round shape.

Overall, the strain and stiffness analysis of these mixes showed that the strain development during compressive fatigue loading is strongly related to the ductility of the material. Nevertheless, the fatigue life is not significantly different between these two mixes. However, the mix with bauxite aggregates would be more adapted in applications prone to fatigue loading due to less scatter with a more regular fracture and a higher capacity to deform when plastic strains are developed. These tests also showed that a higher strength cementitious material is not necessarily more brittle as often reported in the literature. The mix with bauxite aggregates showed less brittle failure due to better bond properties. In the literature, reports can be found where it is suggested that a higher strength concrete and grout is less resistant to fatigue, due to the brittle nature. This seemed verified to a small extent for the mix where different aggregate types are used in different fractions. However, this statement should not be generalized for all mixes. Mixes with different aggregates types and increased porosity levels do not validate this affirmation.

The fatigue life decreased with increasing porosity levels by : increased air content or water quantity. The mix with increased air content showed a decreased bond in the interface, where most microcracks developed. In addition, the mix with increased water

quantity resulted to be more prone to strain rate effects due to larger water content in the CSH hydrates. Conjointly, more water was also present within the capillary pores, which resulted in a decreased fatigue life compared to the reference mix. Higher deformations were also reached for this mix, due to the presence of water inducing more viscous effects.

Finally, the developed high and ultra-high strength grouts could have more applications in thin and slender structures with high loads applied in an environment prone to fatigue loading. The statements of a higher strength concrete or grout having a shorter fatigue life are not necessarily verified in these tests. On the contrary, the fatigue behavior is more complex and should be examined in close relation to the microstructure and mix composition.

Outlook

In the present work a large amount of experimental tests was carried out, which answered a few addressed questions regarding the compressive fatigue behavior of high-strength grouts. Nevertheless, a few issues still need to be clarified, in addition to new questions arised.

Firstly, maximum stress levels between 0,70 to 0,90 were applied to the specimens. Lower stresses should be considered in future work, mainly to verify the values of endurance limit estimated from the alternative methods. In the context of loading types, lower loading frequencies would be highly recommended. The frequency effect could not be clearly clarified from these tests, due to high levels of temperature generated at high loading frequencies. Therefore, loading frequencies between 0,1 to 0,3 Hz could be tested and would be more representative for applications in wind turbines. Thus, the effect of loading frequency on fatigue life would be more indicative.

The current work was focused mainly on fatigue loading with a constant maximum stress level applied. In practice, the loadings are variable and randomly applied on the structure. Hence, the behavior of the grout should be examined when submitted to variable loadings. In addition, this would be useful in order to assess more accurately the long-term behavior and the damage accumulation during fatigue. Against this background, a transferability of the results carried out on laboratory conditions onto on-site applications should be considered. The evaluation of stiffness during the fatigue process in the current tests is carried out on well-defined hysteresis stress-strain curves. However, this damage indicator as considered in this thesis could face challenges when applied in practice. In monitoring, the ultrasonic method could be a more appropriate technique, but with a few previous upgrades in the laboratory.

The influence of the specimen slenderness on the fatigue life was discussed in the manuscript. Nevertheless, a larger specimen size should be part of further research.

Digital image correlation showed microcrack activity since the first phase of loading. Nevertheless, these observations were carried out only at one stress level and evaluations of the microcrack state should additionally be conducted at higher stress levels. This would allow a comparison of the crack distribution, depending on the stress level.

Furthermore, X-ray CT scan could be used in order to provide a volume distribution of microcracks. Nevertheless, the size of the specimen should be correctly estimated.

Many similarities in the material response seemed to take place between creep and fatigue, due to the development of viscous deformations for tests with a large fatigue life. Creep tests could be carried out for specimens under the same stress levels and geometries, in order to assess the disparities in strain development and stiffness deterioration between the two loading types. A model developed for predicting the tertiary creep was applied to the current fatigue tests. However, other phenomena occurring during fatigue were not considered. The continuum damage mechanics would possibly give a better description of the material damage.

Based on the analysis methods followed in this work and the gained knowledge on mechanisms related to fatigue, the influence of other mix components on fatigue behavior could be evaluated. The aggregate size or additives such as GGBS, which can improve the durability can be subject of interest. In addition, a better link with normal strength mixes could be provided.

Finally, it would be advisable to carry out more flexural fatigue tests in other loading frequencies and in improved testing conditions. The tests carried out in this work showed an overall fatigue life different for specimens tested in compression and flexion. Nonetheless, this would need further verifications.

REFERENCES

[1] DNV, Offshore Standard: Design of Offshore Wind Turbine Structures, 2014.

[2] S. Anders, L. Lohaus, Polymer-und fasermodifizierte Hochleistungsbetone für hochdynamisch beanspruchte Verbindungen wie "Grouted Joints“ bei Windenergieanlagen, Leibniz Universität Hannover, 2007.

[3] N. Dedic, Analysis of Grouted Connection in Monopile Wind Turbine Foundations Subjected to Horizontal Load Transfer, (2009) 1–114. doi:10.2471/BLT.07.046664.

[4] P. Schaumann, S. Lochte-Holtgreven, S. Steppeler, Special fatigue aspects in support structures of offshore wind turbines, Materwiss. Werksttech. 42 (2011) 1075–1081.

[5] I. Lotsberg, A. Serednicki, H. Bertnes, A. Lervik, Design of grouted connections for monopile offshore structures: Results from two Joint Industry Projects, Stahlbau. 81 (2012) 695–704. doi:10.1002/stab.201201598.

[6] J. Grünberg, J. Göhlmann, Concrete Structures for Wind Turbines, Wiley, Ernst & Sohn, Berlin, Germany, 2013. doi:10.1002/9783433603291.

[7] P. Richard, M. Cheyrezy, Composition of reactive powder concretes, Cem. Concr. Res. 25 (1995) 1501–1511. doi:10.1016/0008-8846(95)00144-2.

[8] L. Lohaus, N. Oneschkow, K. Elsmeier, J. Hümme, Ermüdungsverhalten von Hochleistungs- betonen in Windenergieanlagen, in: Ernst & Sohn Verlag für Architektur und technische Wissenschaften GmbH & Co, Berlin, 2012: pp. 533–541.

[9] S. Brunauer, M. Yudenfreund, I. Odler, J. Skalny, Hardened portland cement pastes of low porosity VI. Mechanism of the hydration process, Cem. Concr. Res. 3 (1973) 129–147.

[10] H. Bache, Densified Cement Ultra-Fine Particle-Based Materials, in: 2nd Int. Conf. Super-Plasticizers Concr., Ottawa, 1981.

[11] J. Birchall, A. Howard, K. Kendall, Flexural strength and porosity of cements, Nature. 289 (1981) 388. doi:10.1016/b978-0-408-15960-9.50075-9.

[12] J. Lewis, W. Kriven, Microstructure Property Relationships in Macro-Defect-Free Cement, IEEE Trans. Appl. Supercond. 3 (1993) 1354–1357. doi:10.1109/77.233648.

[13] G. Petkovic, H. Stemland, S. Rosseland, R. Lenschow, Fatigue of High-Strength Concrete, n.d. doi:10.14359/3740.

[14] K.L. Scrivener, A.K. Crumbie, P. Laugesen, The interfacial transition zone (ITZ) between cement paste and aggregate in concrete, Interface Sci. 12 (2004) 411–421.

[15] M.H. Zhang, O.E. Gjørv, Microstructure of the interfacial zone between

lightweight aggregate and cement paste, Cem. Concr. Res. 20 (1990) 610–618. doi:10.1016/0008-8846(90)90103-5.

[16] P.J.M. Monteiro, P.K. Mehta, Interaction between carbonate rock and cement paste, Cem. Concr. Res. 16 (1986) 127–134. doi:10.1016/0008-8846(86)90128-6.

[17] R. Wasserman, A. Bentur, Interfacial interactions in lightweight aggregate concretes and their influence on the concrete strength, Cem. Concr. Compos. 18 (1996) 67–76. doi:10.1016/0958-9465(96)00002-9.

[18] CEB-FIP, CEB-FIP Model Code, (1990).

[19] R. Kozul, D. Darwin, Effects of aggregate type,size, and content on concrete strength and fracture energy, Lawrence, Kansas, 1997. doi:10.1227/00006123-199401000-00001.

[20] L. Lohaus, N. Lindschulte, S. Anders, Opportunities and risks of steel fibres in grouted joints, Eur. Wind Energy Conf. Exhib. 2010, EWEC 2010. 4 (2010).

[21] DNVGL-ST-0126 Support structures for wind turbines, 2016.

[22] E. Fehling, T. Leutbecher, M. Schmidt, M. Ismail, Grouted connections for offshore wind turbine structures, Steel Constr. 6 (2013) 216–228. doi:10.1002/stco.201310031.

[23] M.K. Lee, B.I.G. Barr, An overview of the fatigue behaviour of plain and fibre reinforced concrete, Cem. Concr. Compos. 26 (2004) 299–305. doi:10.1016/S0958-9465(02)00139-7.

[24] AFNOR, NF EN 12390-3 Testing hardened concrete - compressive strength of test specimens, n.d.

[25] J.M. Torrenti, G. Pijaudier-Cabot, J.-M. Reynouard, Mechanical Behavior of Concrete, ISTE Ltd and John Wiley & Sons, Inc., 2010. doi:10.1002/9781118557587.

[26] A. Neville, Properties of concrete, 5th ed., Pearson, 2011.

[27] J. Mazars, Application de la mécanique de l'endommagement au comportement non linéaire et à la rupture du béton de structure, University of Paris 6, 1984.

[28] S. Shah, U. Gokoz, F. Ansari, An Experimental Technique for Obtaining Complete Stress-Strain Curves for High Strength Concrete, Cem. Concr. Aggregates. 3 (1981) 21–27.

[29] P. Bischoff, S. Perry, Compressive behaviour of concrete at high strain rates, Mater. Struct. Constr. 24 (1991) 425–450.

[30] P. Rossi, Influence of cracking in the presence of free water on the mechanical behaviour of concrete, Mag. Concr. Res. 43 (1991) 53–57. doi:10.1680/macr.1991.43.154.53.

[31] X.X. Zhang, G. Ruiz, R.C. Yu, M. Tarifa, Fracture behaviour of high-strength concrete at a wide range of loading rates, Int. J. Impact Eng. 36 (2009) 1204–1209. doi:10.1016/j.ijimpeng.2009.04.007.

[32] B. Riisgaard, T. Ngo, P. Mendis, C.T. Georgakis, H. Stang, Dynamic increase factors for high-performance concrete in compression using split Hopkinson

pressure bar, Proc. 6th Int. Conf. Fract. Mech. Concr. Concr. Struct. 3 (2007) 1467–1471.

[33] Y.B. Guo, G.F. Gao, L. Jing, V.P.W. Shim, Response of high-strength concrete to dynamic compressive loading, Int. J. Impact Eng. 108 (2017) 114–135. doi:10.1016/j.ijimpeng.2017.04.015.

[34] H.C. Fu, M.A. Erki, M. Seckin, Review of effects of loading rate on concrete in compression, J. Struct. Eng. 117 (1991) 3645–3659.

[35] E. Cadoni, K. Labibes, C. Albertini, M. Berra, M. Giangrasso, Strain-rate effect on the tensile behaviour of concrete at different relative humidity levels, Mater. Struct. Constr. 34 (2001) 21–26. doi:10.1617/13528.

[36] T. Hsu, Fatigue of plain concrete, ACI J. 78 (1981) 292–305.

[37] D.A. Hordijk, H.W. Reinhardt, Numerical and experimental investigation into the fatigue behavior of plain concrete, Exp. Mech. 33 (1993) 278–285. doi:10.1007/BF02322142.

[38] A. Pipinato, E. Brühwiler, Innovative Bridge Design Handbook: Construction, Rehabilitation and Maintenance : Fatigue and fracture, 2016. doi:10.1016/B978-0-12-800058-8.00004-9.

[39] W. Schutz, A History of Fatigue, Eng. Fract. Mech. 54 (1996) 263–300.

[40] J.O. Holmen, Fatigue of concrete by constant and variable amplitude loading, University of Trondheim, 1979.

[41] K. Aas-Jakobsen, Fatigue of concrete beams and columns, Norges tekniske høgskole, Institutt for betongskonstruksjoner, Trondheim, 1970.

[42] T.T.C. Hsu, Fatigue and microcracking of concrete, Matériaux Constr. 17 (1984) 51–54. doi:10.1007/BF02474056.

[43] P. Paris, F. Erdogan, A critical analysis of crack propagation laws, J. Fluids Eng. ASME. 85 (1963) 528–533. doi:10.1115/1.3656900.

[44] Z.P. Bazant, K. Xu, Size Effect in Fatigue Fracture of Concrete, ACI Mater. J. 88 (1989) 390–399.

[45] CEB-FIP, Constitutive Modelling of High Strength/High Performance Concrete : State-of-the, FIB Bullet, 2008.

[46] CEB-FIP Model Code, (2010).

[47] CERIB, G. Bavelard, H. Beinish, Guide de bonnes pratiques des essais de compression sur éprouvettes Guide de bonnes pratiques des essais de compression sur éprouvettes, Epernon, 2006.

[48] T. Paskova, C. Meyer, Optimum number of specimens for low-cycle fatigue tests of concrete, J. Struct. Eng. (United States). 120 (1994) 2242–2247. doi:10.1061/(ASCE)0733-9445(1994)120:7(2242).

[49] P.B. Cachim, Experimental and numerical analysis of the behaviour of structural concrete under fatigue loading with applications to concrete pavements (PhD thesis), (1999).

[50] B. Oh, Fatiguelife distributions of concrete for various stress levels, ACI Mater. J.

88 (1991) 122–128.

[51] S.P. Singh, S.K. Kaushik, Fatigue strength of steel fibre reinforced concrete in flexure, Cem. Concr. Compos. 25 (2003) 779–786. doi:10.1016/S0958-9465(02)00102-6.

[52] H. Li, M. hua Zhang, J. ping Ou, Flexural fatigue performance of concrete containing nano-particles for pavement, Int. J. Fatigue. 29 (2007) 1292–1301. doi:10.1016/j.ijfatigue.2006.10.004.

[53] M.-T. Do, O. Chaallal, P.-C. Aïtcin, Fatigue behavior of High Performance Concrete, J. Mater. Civ. Eng. 5 (1993) 96–111.

[54] J.J. Ortega, G. Ruiz, R.C. Yu, N. Afanador-García, M. Tarifa, E. Poveda, X. Zhang, F. Evangelista, Number of tests and corresponding error in concrete fatigue, Int. J. Fatigue. 116 (2018) 210–219. doi:10.1016/j.ijfatigue.2018.06.022.

[55] D. Zhao, Q. Chang, J. Yang, Y. Song, A new model for fatigue life distribution of concrete, Key Eng. Mater. 348–349 (2007) 201–204.

[56] L. Saucedo, R.C. Yu, A. Medeiros, X. Zhang, G. Ruiz, A probabilistic fatigue model based on the initial distribution to consider frequency effect in plain and fiber reinforced concrete, in: VIII Int. Conf. Fract. Mech. Concr. Concr. Struct. Fram., 2013. doi:10.1016/j.ijfatigue.2012.11.013.

[57] B.T. Huang, Q.H. Li, S.L. Xu, B.M. Zhou, Frequency effect on the compressive fatigue behavior of ultrahigh toughness cementitious composites: Experimental study and probabilistic analysis, J. Struct. Eng. (United States). 143 (2017). doi:10.1061/(ASCE)ST.1943-541X.0001799.

[58] A. Medeiros, X. Zhang, G. Ruiz, R.C. Yu, M. de S.L. Velasco, Effect of the loading frequency on the compressive fatigue behavior of plain and fiber reinforced concrete, Int. J. Fatigue. 70 (2015) 342–350. doi:10.1016/j.ijfatigue.2014.08.005.

[59] AFNOR, NF EN 1992 Partie 2 : Ponts en béton — Calcul et dispositions constructives, LCP-Con. (2006).

[60] J.W. Murdock, A Critical Review of Research on Fatigue of Plain Concrete, Eng. Exp. Stn. Bull. 475. (1965).

[61] E. Soerensen, L. Westhof, E. Yde, A. Serednicki, Fatigue life of high performance grout for wind turbine grouted connection in wet or dry environment, in: EWEA Offshore, Amsterdam, Netherlands, 2011.

[62] A. Medeiros, X. Zhang, G. Ruiz, R.C. Yu, M.D.S.L. Velasco, Effect of the loading frequency on the compressive fatigue behavior of plain and fiber reinforced concrete, Int. J. Fatigue. 70 (2015) 342–350. doi:10.1016/j.ijfatigue.2014.08.005.

[63] B. Zhang, D. V. Phillips, K. Wu, Effects of loading frequency and stress reversal on fatigue life of plain concrete, Mag. Concr. Res. 48 (1996) 361–375.

[64] P.R. Sparks, J.B. Menzies, The effect of rate of loading upon the static and fatigue strengths of plain concrete in compression, Mag. Concr. Res. 25 (1973) 73–80. doi:10.1680/macr.1973.25.83.73.

[65] K. Elsmeier, J. Hümme, N. Oneschkow, L. Lohaus, Prüftechnische Einflüsse auf

das Ermüdungsverhalten hochfester feinkörniger Vergussbetone, Beton- Und Stahlbetonbau. 111 (2016) 233–240. doi:10.1002/best.201500065.

[66] N. Oneschkow, Fatigue behaviour of high-strength concrete with respect to strain and stiffness, Int. J. Fatigue. 87 (2016) 38–49. doi:10.1016/j.ijfatigue.2016.01.008.

[67] C. von der Haar, S. Marx, Strain Development of plain High Strength Concrete under Fatigue Loading, in: HiPerMat Ultra-High Perform. Concr. High Perform. Constrution Mater., 2016.

[68] C. Tomann, N. Oneschkow, Influence of moisture content in the microstructure on the fatigue deterioration of high-strength concrete, Struct. Concr. 20 (2019) 1204–1211. doi:10.1002/suco.201900023.

[69] F. Benboudjema, Modélisation des déformations différées du béton sous sollicitations biaxiales. Application aux enceintes de confinement de bâtiments reacteurs des centrales nucleaires, Université de Marne la Vallée, 2002.

[70] H. Matsushita, K. Onoue, Influence of surface energy on compressive strength of concrete under static and dynamic loading, J. Adv. Concr. Technol. 4 (2006) 409–421. doi:10.3151/jact.4.409.

[71] A. Cheng, S.J. Chao, W.T. Lin, Effects of leaching behavior of calcium ions on compression and durability of cement-based materials with mineral admixtures, Materials (Basel). 6 (2013) 1851–1872. doi:10.3390/ma6051851.

[72] J.R. del Viso, J.R. Carmona, G. Ruiz, Shape and size effects on the compressive strength of high-strength concrete, Cem. Concr. Res. 38 (2008) 386–395. doi:10.1016/j.cemconres.2007.09.020.

[73] S. Schneider, J. Hümme, S. Marx, L. Lohaus, Untersuchungen zum Einfluss der Probekörpergröße auf den Ermüdungswiderstand von hochfestem Beton, Beton-Und Stahlbetonbau. 113 (2018) 58–67. doi:10.1002/best.201700051.

[74] M. Thiele, Experimentelle Untersuchung und Analyse der Schädigungsevolution in Beton unter hochzyklischen Ermüdungsbeanspruchungen, Technischen Universität Berlin, 2015.

[75] R. Lenschow, Fatigue of Concrete Structures, State-of-the-Art-Report, 1982. doi:http://doi.org/10.5169/seals-28890.

[76] S. Kono, H. Hasegawa, K. Mori, Y. Ichioka, M. Sakashita, F. Watanabe, Low cycle fatigue characteristics of high strength concrete, in: 8th Int. Symp. Util. High-Strength High-Performance Concr., 2008: pp. 616–621.

[77] J.-K. Kim, Y.-Y. Kim, Experimental Study of the fatigue behavior of High Strength Concrete, Cem. Concr. Res. 26 (1996) 1513–1523.

[78] Z. Bazant, W.F. Schell, Fatigue fracture of high-strength concrete and size effect, ACI Mater. J. 90 (1993) 472–478. doi:10.14359/3880.

[79] G. Petković, S. Rosseland, H. Stemland, High Strength Concrete SP3 – Fatigue. Report 3.2: Fatigue of High Strength Concrete, Trondheim, 1992.

[80] L. Lohaus, N. Oneschkow, M. Wefer, Design model for the fatigue behaviour of normal-strength, high-strength and ultra-high-strength concrete, Struct. Concr. 13

(2012) 182–192. doi:10.1002/suco.201100054.

[81] Hordijk D.A. & Wolsink G.M. & de Vries, Fracture and fatigue behaviour of a high strength limestone concrete as compared to gravel concrete, HERON. 40 (1995).

[82] T. Scheiden, N. Oneschkow, Influence of coarse aggregate type on the damage mechanism in high-strength concrete under compressive fatigue loading, Struct. Concr. 20 (2019) 1212–1219. doi:10.1002/suco.201900029.

[83] S. Korte, V. Boel, W. De Corte, G. De Schutter, Static and fatigue fracture mechanics properties of self-compacting concrete using three-point bending tests and wedge-splitting tests, Constr. Build. Mater. 57 (2014) 1–8. doi:10.1016/j.conbuildmat.2014.01.090.

[84] K.M.A. Sohel, K. Al-Jabri, M.H. Zhang, J.Y.R. Liew, Flexural fatigue behavior of ultra-lightweight cement composite and high strength lightweight aggregate concrete, Constr. Build. Mater. 173 (2018) 90–100. doi:10.1016/j.conbuildmat.2018.03.276.

[85] K. Onoue, M. Tokitsu, M. Ohtsu, T.A. Bier, Fatigue characteristics of steel-making slag concrete under compression in submerged condition, Constr. Build. Mater. 70 (2014) 231–242. doi:10.1016/j.conbuildmat.2014.07.107.

[86] M.A. Farooq, Y. Sato, T. Ayano, K. Niitani, Experimental and numerical investigation of static and fatigue behavior of mortar with blast furnace slag sand as fine aggregates in air and water, Constr. Build. Mater. 143 (2017) 429–443.

[87] T.L. Thomas, The effects of air content, water-cement ratio, and aggregate type on the flexural fatigue strength of plain concrete, Iowa State Unıversity. (1979) 100.

[88] F.W. Klaiber, D.. Lee, J.W. Coleman, Fatigue behavior of air-entrained concrete, 1977.

[89] S. Seitl, V. Bilek, Z. Keršner, L. Řoutil, Can microsilica improve concrete in terms of fatigue behavior ?, in: Fract. Mech. Concr. Struct. - High Performance, Fiber Reinf. Concr. Spec. Loadings Ans Struct. Appl., 2010: pp. 1776–1781.

[90] H. Zhang, K. Tian, Properties and mechanism on flexural fatigue of polypropylene fiber reinforced concrete containing slag, J. Wuhan Univ. Technol. Mater. Sci. Ed. 26 (2011) 533–540. doi:10.1007/s11595-011-0263-8.

[91] L.P. Guo, A. Carpinteri, A. Spagnoli, W. Sun, Experimental and numerical investigations on fatigue damage propagation and life prediction of high-performance concrete containing reactive mineral admixtures, Int. J. Fatigue. 32 (2010) 227–237. doi:10.1016/j.ijfatigue.2009.05.009.

[92] E. Poveda, G. Ruiz, H. Cifuentes, R.C. Yu, X. Zhang, Influence of the fiber content on the compressive low-cycle fatigue behavior of self-compacting SFRC, Int. J. Fatigue. 101 (2017) 9–17. doi:10.1016/j.ijfatigue.2017.04.005.

[93] E. Parant, Mécanismes d'endommagement et comportements mécaniques d'un composite cimentaire fibré multi-échelles sous sollicitations sévères : fatigue, choc,

corrosion, Ecole Nationale des Pont et Chaussées, 2004.
[94] Y.J. Park, Fatigue of concrete under random loadings, J. Struct. Eng. (United States). 116 (1990) 3228–3235.
[95] G.A. Plizzari, S. Cangiano, S. Alleruzzo, The fatigue behaviour of cracked concrete, Fatigue Fract. Eng. Mater. Struct. 20 (1997) 1195–1206. doi:10.1111/j.1460-2695.1997.tb00323.x.
[96] N. Oneschkow, Analyse des Ermüdungsverhaltens von Beton anhand der Dehnungsentwicklung. Analysis of the fatigue behaviour of concrete with respect to the development of strain, Leibniz Universität Hannover, 2014.
[97] J. Hümme, C. von der Haar, L. Lohaus, S. Marx, Fatigue behaviour of a normal-strength concrete - number of cycles to failure and strain development, Struct. Concr. (2015).
[98] N. Oneschkow, Fatigue behaviour of high-strength concrete with respect to strain and stiffness, Int. J. Fatigue. 87 (2016) 38–49.
[99] R. Tepfers, B. Hedberg, G. Szczekocki, Absorption of energy in fatigue loading of plain concrete, Matériaux Constr. 17 (1984) 59–64. doi:10.1007/BF02474058.
[100] D. Lei, P. Zhang, J. He, P. Bai, F. Zhu, Fatigue life prediction method of concrete based on energy dissipation, Constr. Build. Mater. 145 (2017) 419–425. doi:10.1016/j.conbuildmat.2017.04.030.
[101] Z. Song, T. Frühwirt, H. Konietzky, Characteristics of dissipated energy of concrete subjected to cyclic loading, Constr. Build. Mater. 168 (2018) 47–60. doi:10.1016/j.conbuildmat.2018.02.076.
[102] M. Deutscher, N.L. Tran, S. Scheerer, Experimental investigations on the temperature increase of ultra-high performance concrete under fatigue loading, Appl. Sci. 9 (2019). doi:10.3390/app9194087.
[103] C. Otto, K. Elsmeier, L. Lohaus, Temperature Effects on the Fatigue Resistance of High-Stength-Concrete and High-Strength-Grout, in: High Tech Concr. Where Technol. Eng. Meet, Springer International Publishing AG 2018, Maastricht, Netherlands, 2017: pp. 1401–1409. doi:10.1007/978-3-319-59471-2.
[104] C. Doudard, S. Calloch, P. Cugy, A. Galtier, F. Hild, A probabilistic two-scale model for high-cycle fatigue life predictions, Fatigue Fract. Eng. Mater. Struct. 28 (2005) 279–288. doi:10.1111/j.1460-2695.2005.00854.x.
[105] C. Doudard, S. Calloch, F. Hild, P. Cugy, A. Galtier, Identification of the scatter in high cycle fatigue from temperature measurements, Comptes Rendus Mécanique. 332 (2004) 795–801. doi:10.1016/j.crme.2004.06.002.
[106] M. Poncelet, Multiaxialité , hétérogénéités intrinsèques et structurales des essais d'auto-échauffement et de fatigue à grand nombre de cycles, Ecole Normale Supérieure de Cachan, 2007.
[107] R. Munier, C. Doudard, S. Calloch, B. Weber, Determination of high cycle fatigue properties of a wide range of steel sheet grades from self-heating measurements, Int. J. Fatigue. 63 (2014) 46–61. doi:10.1016/j.ijfatigue.2014.01.004.

[108] E. Dulinskas, V. Gribniak, G. Kaklauskas, Influence of Curing Conditions on the Fatigue Strength and cyclic creep of Compressive Concrete, in: 9th Int. Conf. "Modern Build. Mater. Struct. Tech., Vilnius, Lithuania, 2008: pp. 517–522. doi:10.12783/dteees/peee2016/3878.

[109] Z.P. Bazant, M.H. Hubler, Theory of cyclic creep of concrete based on Paris law for fatigue growth of subcritical microcracks, J. Mech. Phys. Solids. 63 (2014) 187–200. doi:10.1016/j.jmps.2013.09.010.

[110] C.P. Whaley, A.M. Neville, Non-elastic deformation of concrete under cyclic compression, Mag. Concr. Res. 25 (1973) 145–154. doi:10.1680/macr.1973.25.84.145.

[111] P. Acker, De la controverse sur les lois de fluage du beton et des moyens d'en sortir, Cem. Concr. Res. 13 (1983) 580–582. doi:10.1016/0008-8846(83)90018-2.

[112] Z.P. Bažant, A.B. Hauggaard, S. Baweja, F.J. Ulm, Microprestress-solidification theory for concrete creep. I: Aging and drying effects, J. Eng. Mech. 123 (1997) 1188–1194. doi:10.1061/(ASCE)0733-9399(1997)123:11(1188).

[113] F.-J. Ulm, P. Acker, Le point sur le fluage et la recouvrance des bétons. BLPC, 1998.

[114] A. Hilaire, F. Benboudjema, A. Darquennes, Y. Berthaud, G. Nahas, Modeling basic creep in concrete at early-age under compressive and tensile loading, Nucl. Eng. Des. 269 (2014) 222–230. doi:10.1016/j.nucengdes.2013.08.034.

[115] M. Briffaut, F. Benboudjema, J.M. Torrenti, G. Nahas, Concrete early age basic creep: Experiments and test of rheological modelling approaches, Constr. Build. Mater. 36 (2012) 373–380. doi:10.1016/j.conbuildmat.2012.04.101.

[116] J.J. Brooks, 30-Year Creep and Shrinkage of Concrete, Mag. Concr. Res. 57 (2005) 545–556. doi:10.1680/macr.2005.57.9.545.

[117] A. Carpinteri, S. Valente, F.P. Zhou, G. Ferrara, G. Melchiorri, Tensile and flexural creep rupture tests on partially-damaged concrete specimens, Mater. Struct. Constr. 30 (1997) 269–276. doi:10.1007/bf02486351.

[118] M.A. Al-Kubaisy, A.G. Young, Failure of Concrete Under Sustained Tension, Mag. Concr. Res. 27 (1975) 171–178. doi:10.1680/macr.1975.27.92.171.

[119] S. Shah, S. Chandra, Fracture of concrete subjected to cyclic and sustained loading, ACI J. Proc. 67 (1970).

[120] A. Berthollet, Contribution à la modélisation du béton vis-à-vis du vieillissement et de la durabilité: interaction des déformations de fluage et du comportement non-linéaire du matériau, INSA de Lyon, 2003.

[121] C. Mazzotti, M. Savoia, Nonlinear creep damage model for concrete under uniaxial compression, J. Eng. Mech. 129 (2003) 1065–1075. doi:10.1061/(ASCE)0733-9399(2003)129:9(1065).

[122] N. Reviron, F. Benboudjema, J.M. Torrenti, G. Nahas, A. Millard, Coupling between creep and cracking in tension, Proc. 6th Int. Conf. Fract. Mech. Concr. Concr. Struct. - Fract. Mech. Concr. Concr. Struct. 1 (2007) 495–502.

[123] L. Kachanov, Time of the Rupture Process under Creep Conditions (in Russian) Izvestiia Akademii Nauk SSSR, Otdelenie Teckhnicheskikh Nauk, 8 (1958) 26–31. doi:10.4236/as.2011.23023.

[124] J. Lemaitre, Evaluation of dissipation and damage in metals submitted to dynamic loading, in: Int. Conf. Mech. Behav. Mater., Kyoto, Japan, 1971.

[125] A. Neville, P.C. Aïtcin, High performance concrete - An overview, Mater. Struct. Constr. 31 (1998) 111–117. doi:10.1007/bf02486473.

[126] T.C. Holland, Working With Silica-Fume Concrete, Concr. Constr. - World Concr. 32 (1987).

[127] B.S. Al-Azzawi, Fatigue of Reinforced Concrete Beams Retrofitted with Ultra-High Performance Fibre- Reinforced Concrete, (2018).

[128] W. Fan, F. Stoffelbach, J. Rieger, L. Regnaud, A. Vichot, B. Bresson, N. Lequeux, A new class of organosilane-modified polycarboxylate superplasticizers with low sulfate sensitivity, Cem. Concr. Res. (2012). doi:10.1016/j.cemconres.2011.09.006.

[129] K. Yoshioka, E. Sakai, M. Daimon, A. Kitahara, Role of Steric Hindrance in the Performance of Superplasticizers for Concrete, J. Am. Ceram. Soc. 80 (1997) 2667–2671. doi:10.1111/j.1151-2916.1997.tb03169.x.

[130] T.S. Liao, C.L. Hwang, Y.S. Ye, K.C. Hsu, Effects of a carboxylic acid/sulfonic acid copolymer on the material properties of cementitious materials, Cem. Concr. Res. 36 (2006) 650–655. doi:10.1016/j.cemconres.2005.10.005.

[131] B. Łaźniewska-Piekarczyk, Influence of anti-foaming admixture and polycarboxylic superplasticizer type on fresh and hardened properties of self-compacting mortar, Archit. Civ. Eng. Environ. 3 (2010) 61–72.

[132] S. V. Kumar, M. Santhanam, Particle packing theories and their application in concrete mixture proportioning: A review, Indian Concr. J. 77 (2003) 1324–1331.

[133] D.M. Roy, B.E. Scheetz, M.R. Silsbee, Processing of optimized cements and concretes via particle packing, MRS Bull. 18 (1993) 45–49. doi:10.1557/S088376940004389X.

[134] D.R. Dinger, J.E. Funk, Particle-packing phenomena and their application in materials processing, MRS Bull. 22 (1997) 19–23. doi:10.1557/S0883769400034692.

[135] F. De Larrard, T. Sedran, Optimization of ultra-high-performance concrete by the use of a packing model, Cem. Concr. Res. 24 (1994) 997–1009. doi:10.1016/0008-8846(94)90022-1.

[136] J.E. Funk, D.R. Dinger, Predictive Process Control of Crowded Particulate Suspensions, Applied to Ceramic Manufacturing, 1994. doi:10.1007/978-1-4615-3118-0.

[137] H.J.. Brouwers, H.. Radix, Self-compacting concrete: the role of the particle size distribution, in: First Int. Symp. Des. Perform. Use Self-Consolidating Concr. SCC 2005, Rilem, Changsha, Hunan, China, 2005: pp. 109–118.

[138] J.K. Kim, S.T. Yi, Application of size effect to compressive strength of concrete members, Sadhana - Acad. Proc. Eng. Sci. 27 (2002) 467–484.

doi:10.1007/BF02706995.
[139] C. von der Haar, S. Marx, Development of stiffness and ultrasonic pulse velocity of fatigue loaded concrete, Struct. Concr. 17 (2016) 630–636. doi:10.1002/suco.201600007.
[140] S. Korte, Experimental and Numerical Investigation of the Fracture Behaviour and Fatigue Resistance of Self-Compacting Concrete, Ghent University, Belgium, 2014. doi:10.1017/CBO9781107415324.004.
[141] P. Ameen, M. Szymanski, Fatigue in Plain Concrete: Phenomenon and Methods of Analysis, ACI J. Proc. (2006) 1–59.
[142] R.C. 36-DRL, Long term random dynamic loading of concrete structures, 1984. doi:10.1007/BF02473567.
[143] H.K. Hilsdorf, C.E. Kesler, Fatigue Strength of Concrete Under Varying Flexural Stresses, ACI J. Proc. 63 (1966) 1059–1076. doi:10.14359/7662.
[144] E. Farhani, J.P. Lloyd, Influence of rest periods on fatigue strength of concrete tested in water, Oklahoma State University, 1992.
[145] K.L. Scrivener, The Use Of Backscattered Electron Microscopy And Image Analysis To Study The Porosity Of Cement Paste, MRS Proc. 137 (1988) 129–140. doi:10.1557/proc-137-129.
[146] J. An, S.S. Kim, B.H. Nam, S.A. Durham, Effect of aggregate mineralogy and concrete microstructure on thermal expansion and strength properties of concrete, Appl. Sci. 7 (2017) 5–7. doi:10.3390/app7121307.
[147] R.F. Feldman, Application of the helium inflow technique for measuring surface area and hydraulic radius of hydrated portland cement, Cem. Concr. Res. 10 (1980) 657–664. doi:10.1016/0008-8846(80)90029-0.
[148] R.A. Cook, K.C. Hover, Mercury porosimetry of cement-based materials and associated correction factors, Constr. Build. Mater. 7 (1993) 231–240. doi:10.1016/0950-0618(93)90007-Y.
[149] Afnor, NF P18-459 Essai pour béton durci : essai de porosité et de masse volumique, 2010.
[150] Z. Tomičevć, F. Hild, S. Roux, Mechanics-aided digital image correlation, J. Strain Anal. Eng. Des. 48 (2013) 330–343. doi:10.1177/0309324713482457.
[151] M. Poncelet, G. Barbier, B. Raka, S. Courtin, R. Desmorat, J.C. Le-Roux, L. Vincent, Biaxial high cycle fatigue of a type 304L stainless steel: Cyclic strains and crack initiation detection by digital image correlation, Eur. J. Mech. A/Solids. 29 (2010) 810–825. doi:10.1016/j.euromechsol.2010.05.002.
[152] R. Hohberg, Zum Ermüdungsverhalten von Beton, Berlin, 2004.
[153] B. Klimkeit, Etude expérimentale et modélisation du comportement en fatigue multiaxiale d'un polymère renforcé pour application automobile, (2010).
[154] X.R. Xiao, Modeling of load frequency effect on fatigue life of thermoplastic composites, J. Compos. Mater. 33 (1999) 1141–1158. doi:10.1177/002199839903301205.

[155] L. Divet, Les réactions sulfatiques internes au béton : contribution à l'étude des mécanismes de la formation différée de l' ettringite, 2001.
[156] V. Baroghel-Bouny, Caractérisation microstructurale et hydrique des pâtes de ciment et des bétons ordinaires et à très hautes performances, Ecole Nationale des Ponts et Chaussées, 1994.
[157] Q. Zhou, F.P. Glasser, Thermal stability and decomposition mechanisms of ettringite at <120°C, Cem. Concr. Res. 31 (2001) 1333–1339. doi:10.1016/S0008-8846(01)00558-0.
[158] A. Noumowé, Effet de hautes températures (20-600°C) sur le béton. Cas particulier du béton à hautes performances, Institut National des Sciences Appliquées de Lyon, 1995.
[159] M. Choinska, Effets de la température, du chargement mécanique et de leurs interactions sur la perméabilité du béton de structure, Ecole Centrale de Nantes, 2006.
[160] M.H.H. Hettema, The thermomechanical behavior of sedimentary: an experimental study, Technische Universiteit Delft, 1996.
[161] J. Saliba, A. Loukili, F. Grondin, J.P. Regoin, Identification of damage mechanisms in concrete under high level creep by the acoustic emission technique, Mater. Struct. Constr. 47 (2014) 1041–1053. doi:10.1617/s11527-013-0113-6.
[162] C. Maggiore, J. Grenfell, G. Airey, A.C. Collop, Evaluation of fatigue life using dissipated energy methods, in: 7th RILEM Int. Conf. Crack. Pavements, 2012: pp. 643–652. doi:10.1007/978-94-007-4566-7_63.
[163] M. Bode, S. Marx, A. Vogel, C. Völker, Dissipationsenergie bei Ermüdungsversuchen an Betonprobekörpern, Beton- Und Stahlbetonbau. (2019) 548–556.
[164] B. Isojeh, M. El-Zeghayar, F.J. Vecchio, Concrete Damage under Fatigue Loading in Uniaxial Compression, ACI Mater. J. 114 (2017) 225–235.
[165] M.P. Luong, Infrared thermography of fatigue in metals, SPIE. 1682 (1992) 222–233. doi:10.1016/s0963-8695(97)87796-1.
[166] Y. Mohammadi, S.K. Kaushik, Flexural fatigue-life distributions of plain and fibrous concrete at various stress levels, J. Mater. Civ. Eng. 17 (2005) 650–658. doi:10.1061/(ASCE)0899-1561(2005)17:6(650).
[167] B.-T. Huang, Q.-H. Li, S.-L. Xu, B.-M. Zhou, Frequency effect on the compressive fatigue behavior of ultrahigh toughness cementitious composites: Experimental study and probabilistic analysis, J. Struct. Eng. (United States). 143 (2017). doi:10.1061/(ASCE)ST.1943-541X.0001799.
[168] H.A. Cornelissen, Fatigue failure of concrete in tension, HERON. 29 (1984).
[169] M. Briffaut, Étude de la fissuration au jeune âge des structures massives en béton : Influence de la vitesse de refroidissement , des reprises de bétonnage et des armatures, Université Paris 6, 2010.
[170] J.G.M. van Mier, Multiaxial strain-softening of concrete - Part I: Load- Fracture,

Mater. Struct. 19 (1986) 179–190. doi:10.1007/BF02472035.

[171] J.G.M. Van Mier, S.P. Shah, M. Arnaud, J.P. Balayssac, A. Bascoul, S. Choi, D. Dasenbrock, G. Ferrara, C. French, M.E. Gobbi, B.L. Karihaloo, G. König, M.D. Kotsovos, J. Labuz, D. Lange-Kornbak, G. Markeset, M.N. Pavlovic, G. Simsch, K.C. Thienel, A. Turatsinze, M. Ulmer, H.J.G.M. Van Geel, M.R.A. Van Vliet, D. Zissopoulos, Strain-softening of concrete in uniaxial compression, Mater. Struct. Constr. 30 (1997) 195–209. doi:10.1007/bf02486177.

[172] Skarżyński, I. Marzec, J. Tejchman, Fracture evolution in concrete compressive fatigue experiments based on X-ray micro-CT images, Int. J. Fatigue. 122 (2019) 256–272. doi:10.1016/j.ijfatigue.2019.02.002.

[173] H. Zhao, D. Darwin, Quantitative Backscattered Electron Analysis of Cement Paste, Cem. Concr. Res. 22 (1992) 695–706.

[174] E.S. Lappa, High Strength Fibre Reinforced Concrete Static and fatigue behaviour in bending door, 2007.

APPENDIX A

A-1 : *Number of cycles to failure at two loading frequencies for the reference high strength grout*

Frequency [Hz]	Stress Level $S_{c,max}$	Number of cycles to failure N_f						Average
10 Hz	0,90	2255	2435	2664	2693	3156	4417	2937
	0,80	9041	10881	13469	13479	19225	19873	14328
	0,75	23098	36572	51918	53577	62609	64915	48782
	0,70	>400000	>400000	>400000	173112	180579	194272	
1 Hz	0,90	194	216	674	928	957	968	656
	0,80	9091	11884	12750	16125	16671	20800	14554
	0,75	29801	36287	57060	84856	97853	194272	83355

A-2 : *Mean number of cycles to failure with minimum and maximum values for each stress level as bar errors*

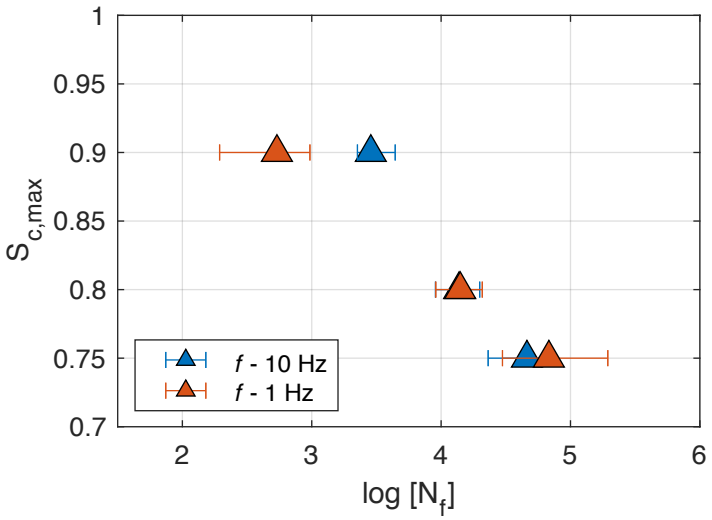

APPENDIX B

B-1 : *Temperature evolution at* $S_{c,max} = 0{,}70$

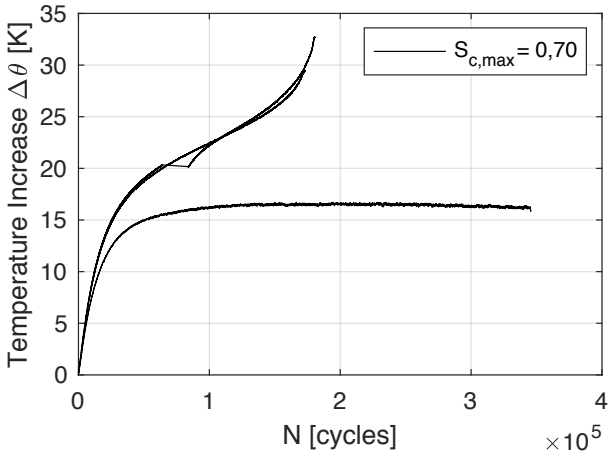

B-2 : *Comparison of temperature evolution at two loading frequencies for* $S_{c,max} = 0{,}75$ *(left) ;* $S_{c,max} = 0{,}90$ *(right)*

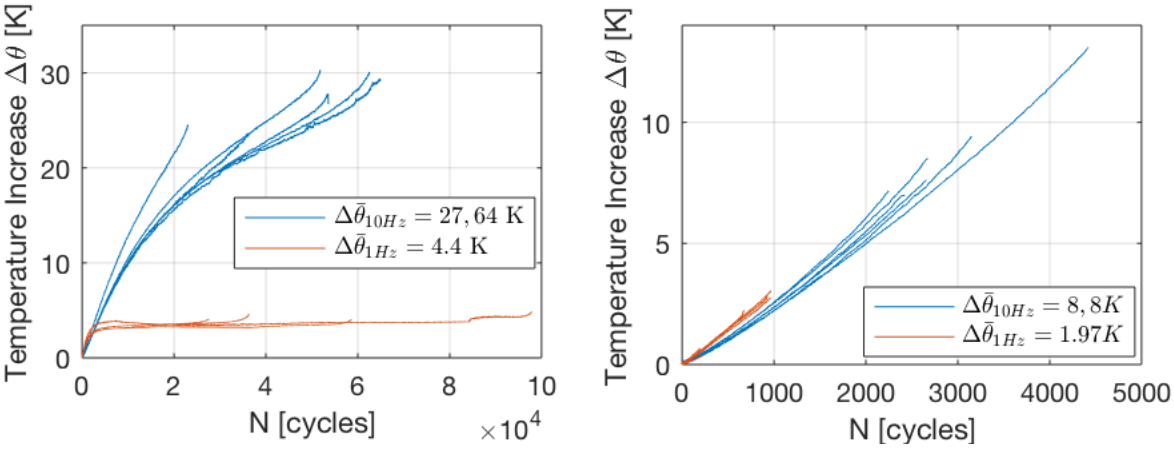

B-3 : *Maximum Strain developments $\varepsilon_{c,max}$ for $S_{c,max}$ = 0,90 at two loading frequencies*
Total strain developments (left) ; Relative Strain (right)

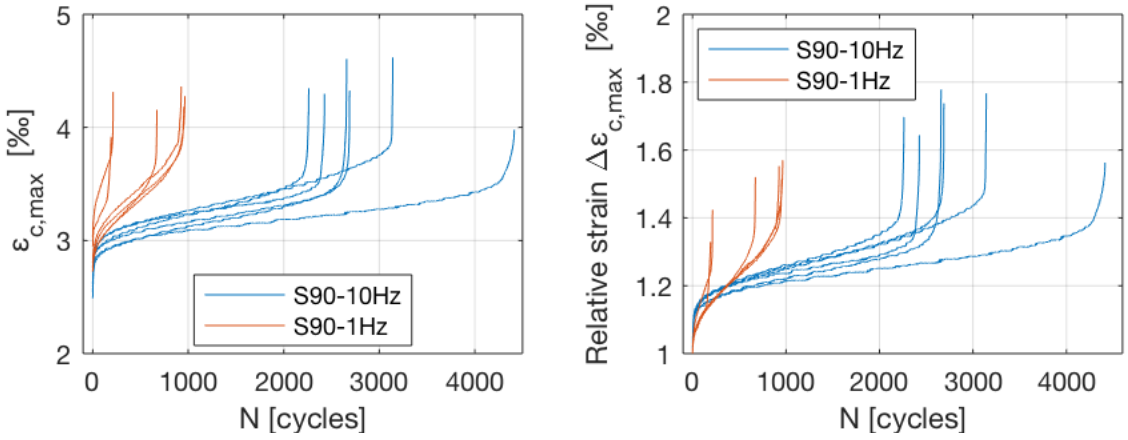

B-4 *Maximum Strain developments $\varepsilon_{c,max}$ for $S_{c,max}$ = 0,75 at two loading frequencies*
Total strain developments (left) ; Relative Strain (right)

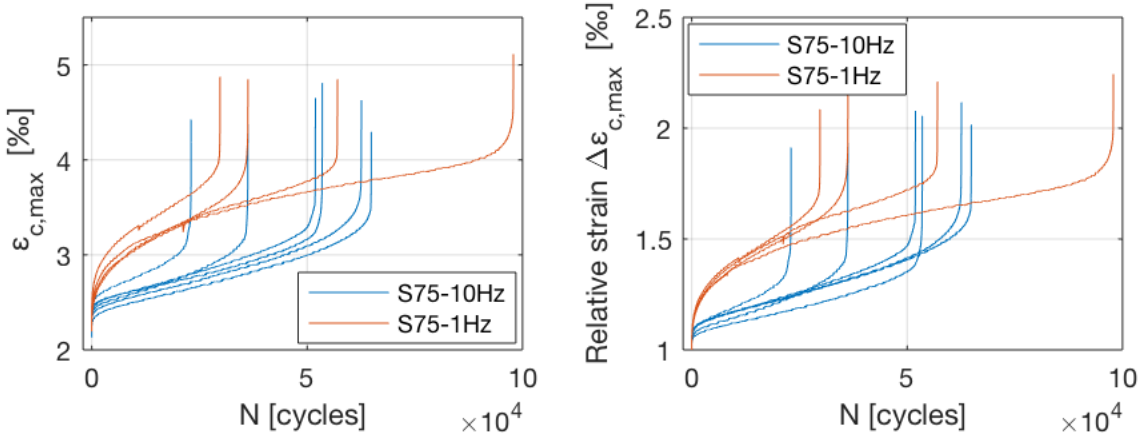

B-5 *Energy Dissipation at different fatigue life ratios for both loading frequencies*

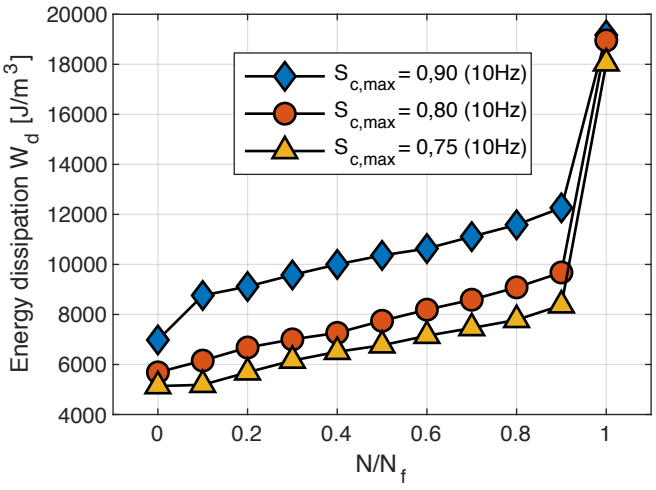

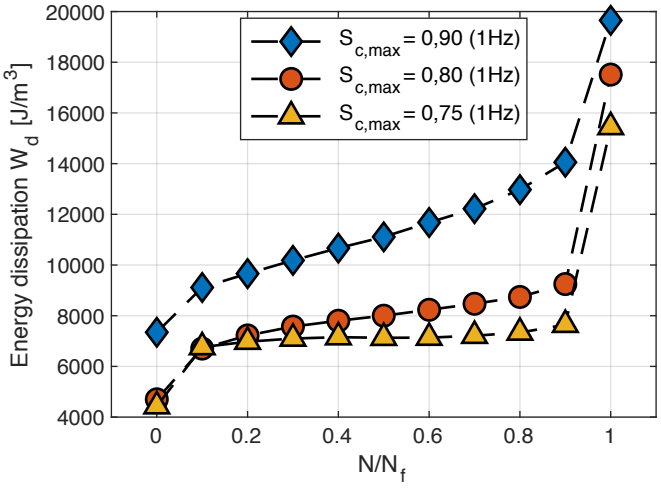

B-6 *Accumulative dissipated energy*

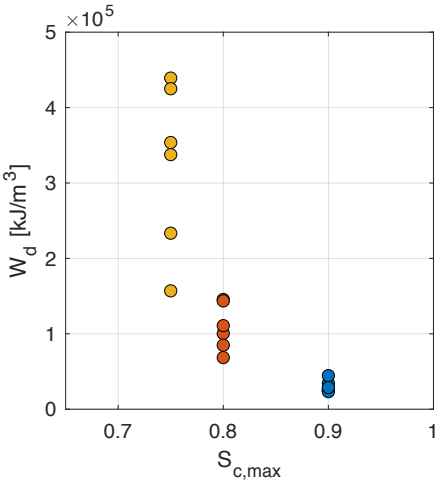

B-7 *Secant modulus evolution for median curves at each stress level between two loading frequencies and comparison with the stiffness E_0 measured in quasi-static tests*

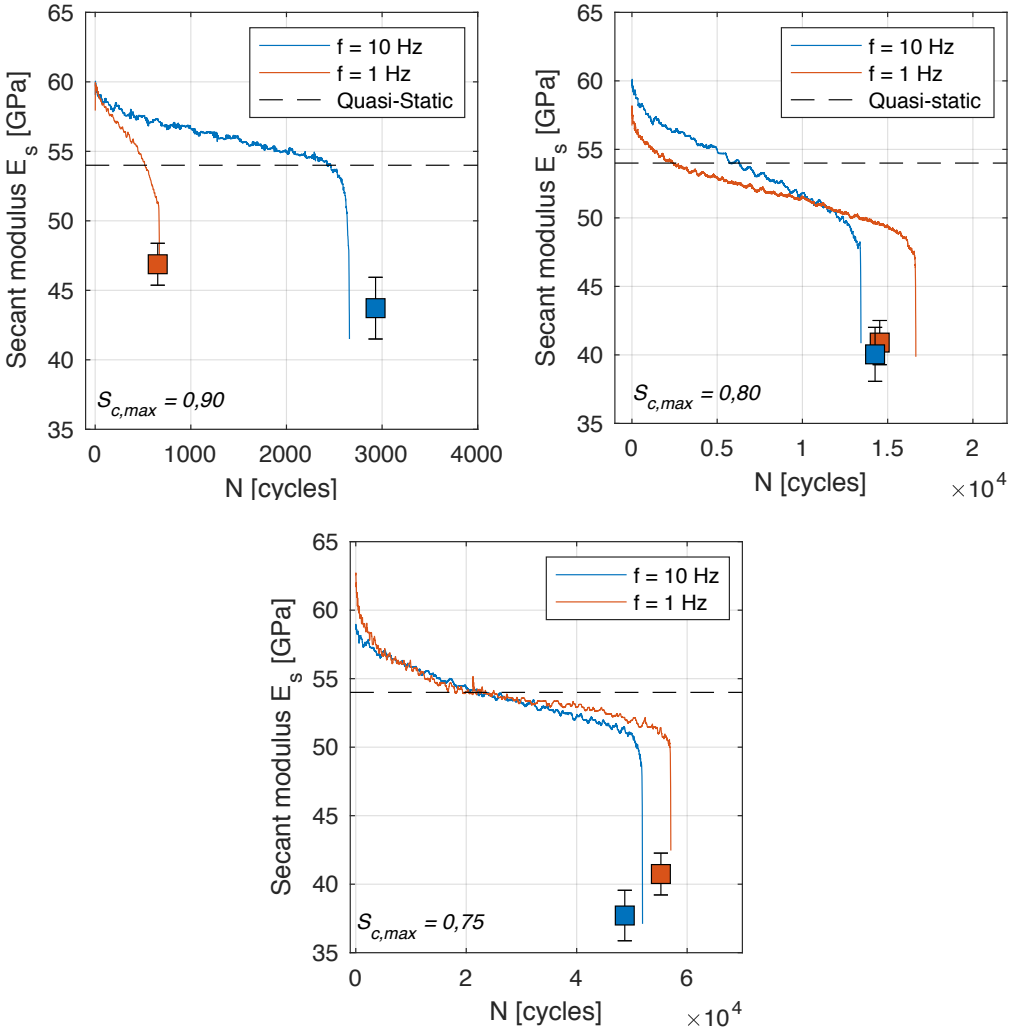

B-8 *Hysteresis evolution for $S_{c,max} = 0{,}70$ which did not fail*

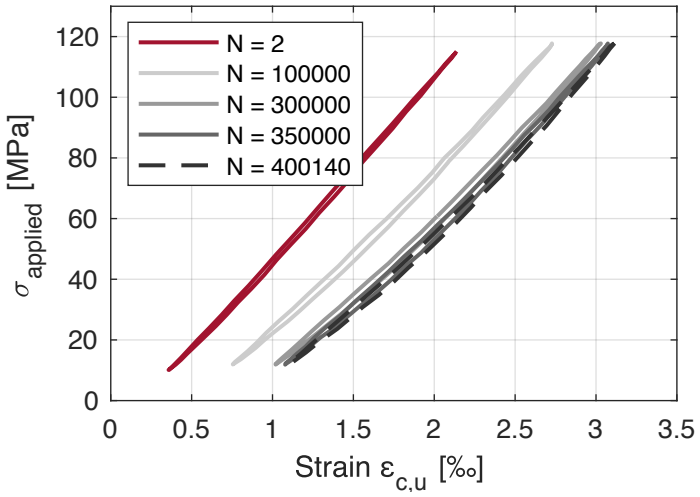

B-9 *Number of cycles to failure for specimens with a length of 180mm at three stress levels and corresponding mean values*

Frequency [Hz]	Stress Level $S_{c,max}$	Number of cycles to failure N_f						Average
	0,90	189	509	926	928	951	1456	827
10Hz	0,80	2387	9344	9415	10146	10942	11063	8883
	0,75	10938	13151	19712	22979	24298	25213	19382

B-10 *Secant modulus evolution for specimen with a length of 180mm at three stress levels and comparison with the stiffness E_0 measured in quasi-static tests for both specimen sizes*

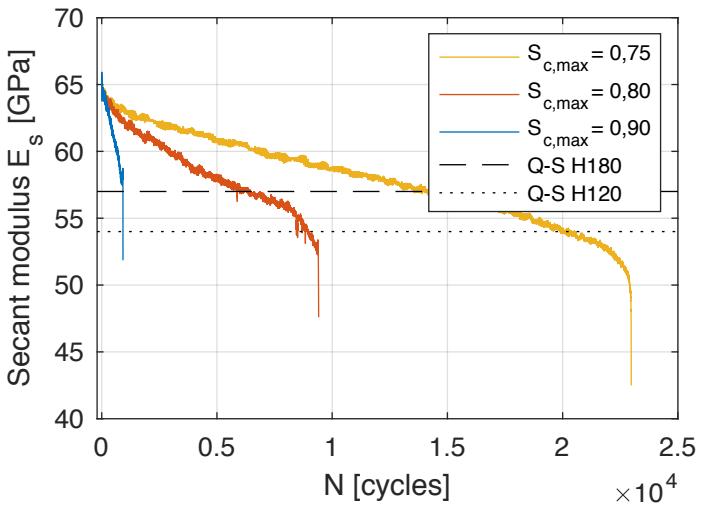

B-11 *Microcrack state evolution for 2 specimens at the minimum stress level* $S_{c,min}$

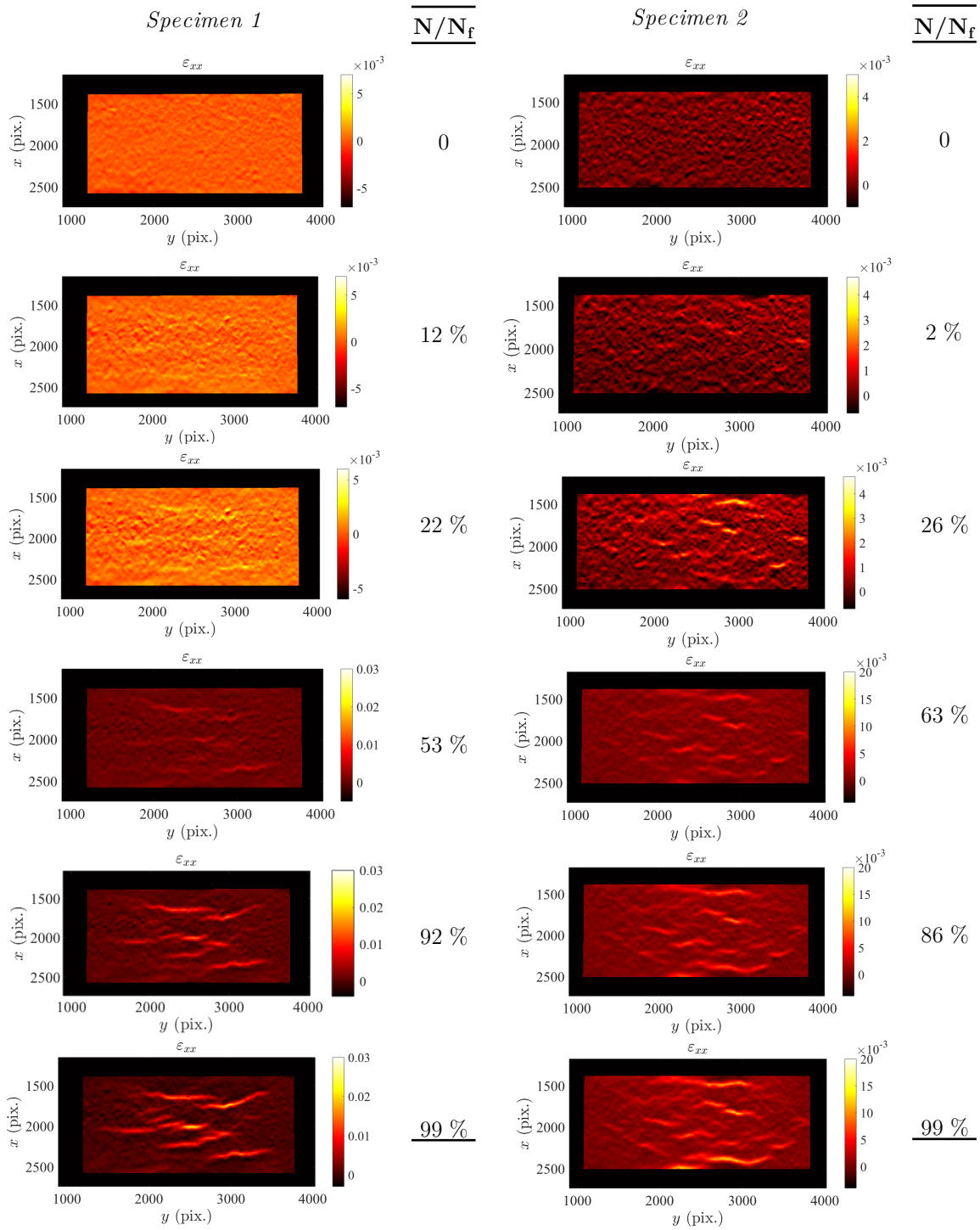

APPENDIX C

C-1 *Mean number of cycles at each stress level for three different mixes with different aggregate types*

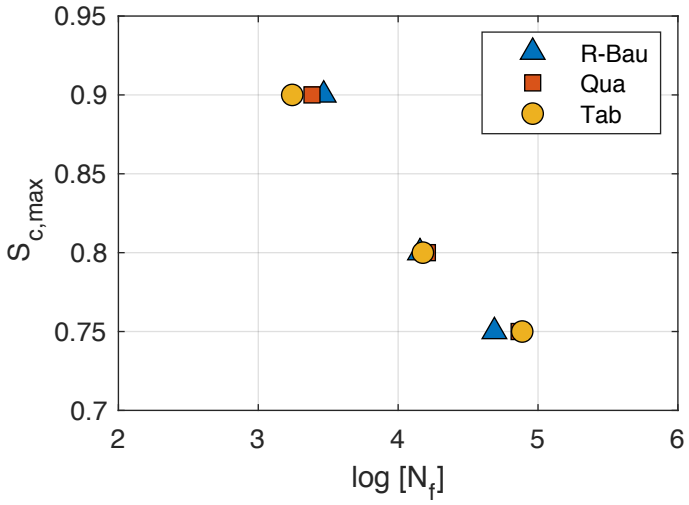

C-2 *Secant modulus for Bau, Qua and Tab mixes in relation to the first cycle for $S_{c,max}$ 0,90 (left) ; Secant modulus evolution as absolute values and comparison with quasi-static tests (right)*

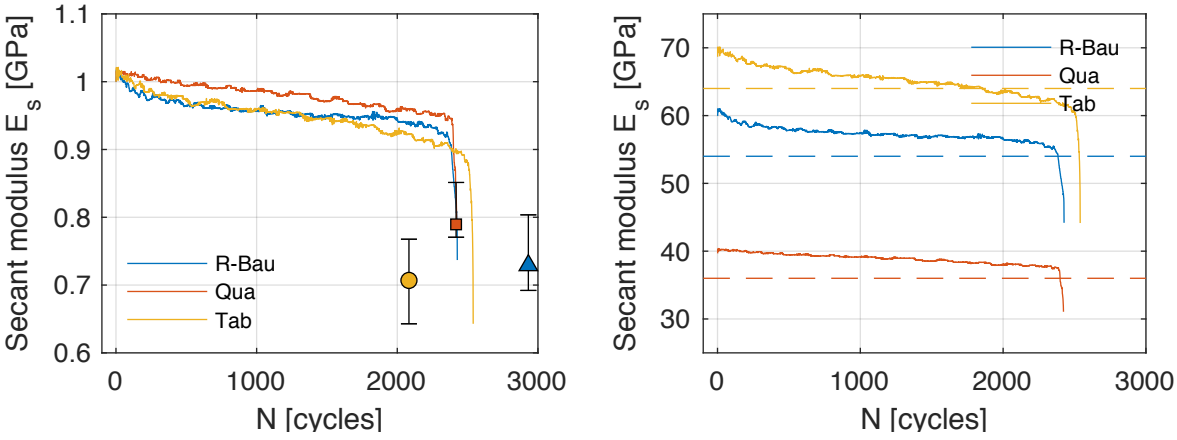

Secant modulus for Bau, Qua and Tab mixes in relation to the first cycle for $S_{c,max}$ 0,75 (left) ; Secant modulus evolution as absolute values and comparison with quasi-static tests (right)

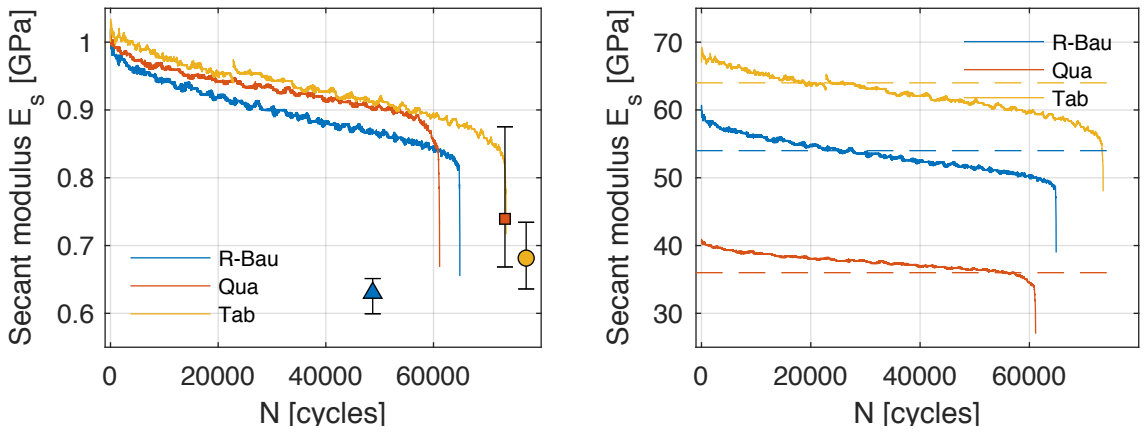

C-3 *Relative maximum strain evolution for specimens of each mix with similar number of cycles to failure at $S_{c,max}$ = 0,75 (left) and 0,85 ; Corresponding minimum and maximum strain evolutions (right)*

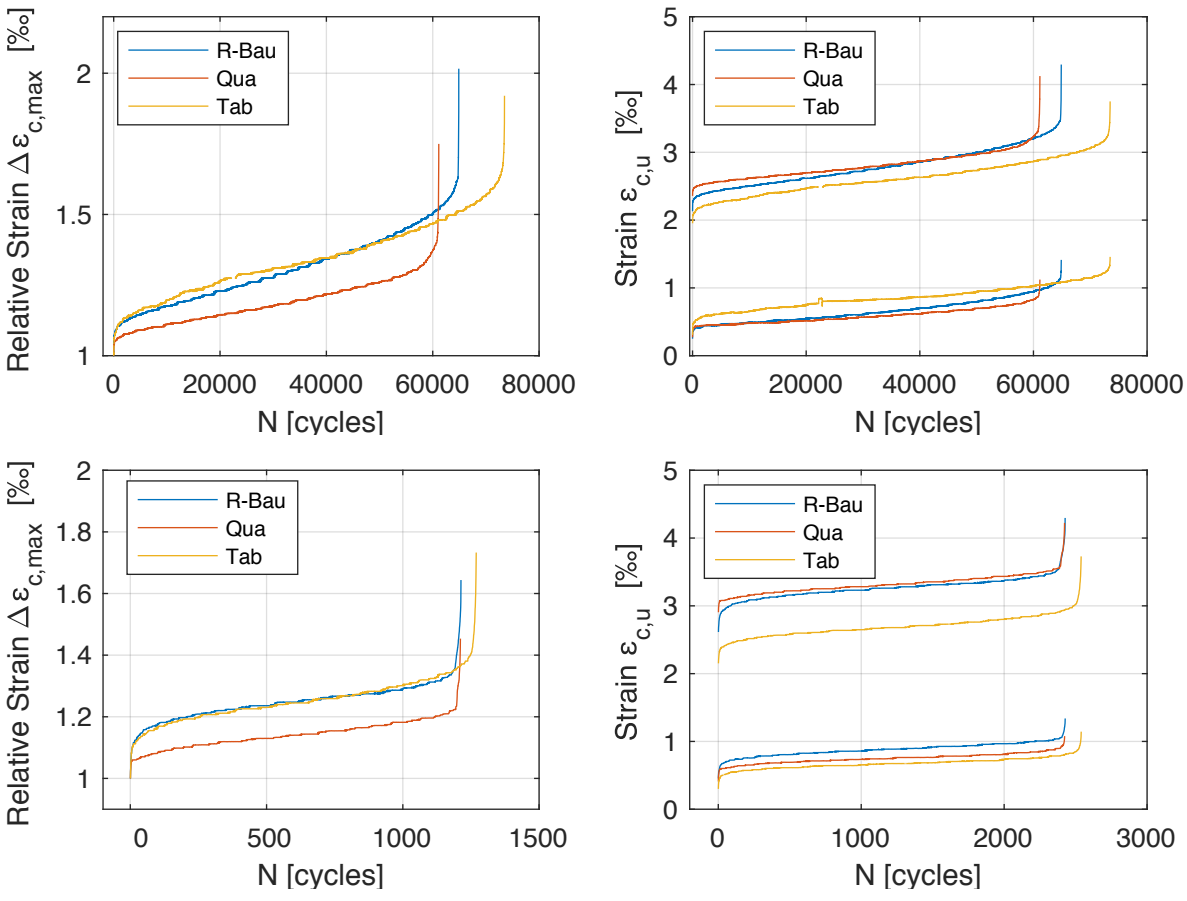

C-4 *Images with overlap of all elements detected during EDS mapping for both* aggregate types

Quartz

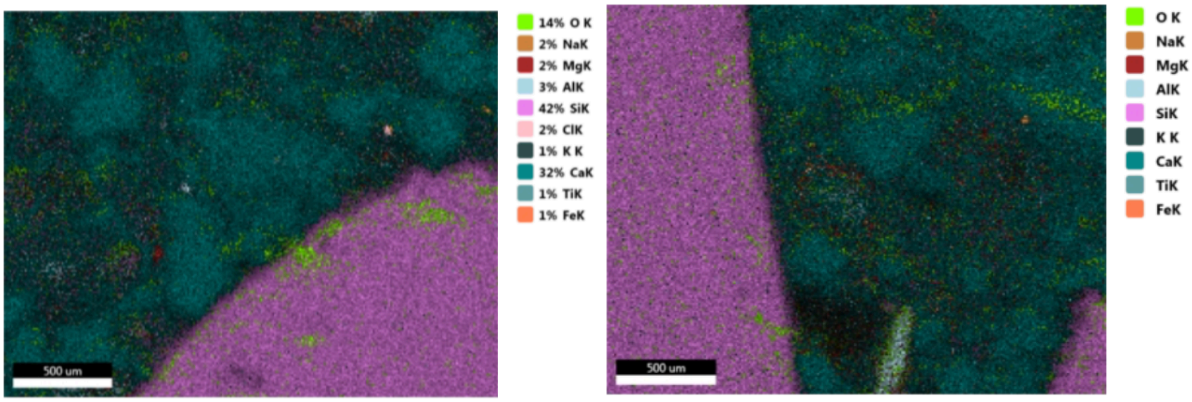

Bauxite

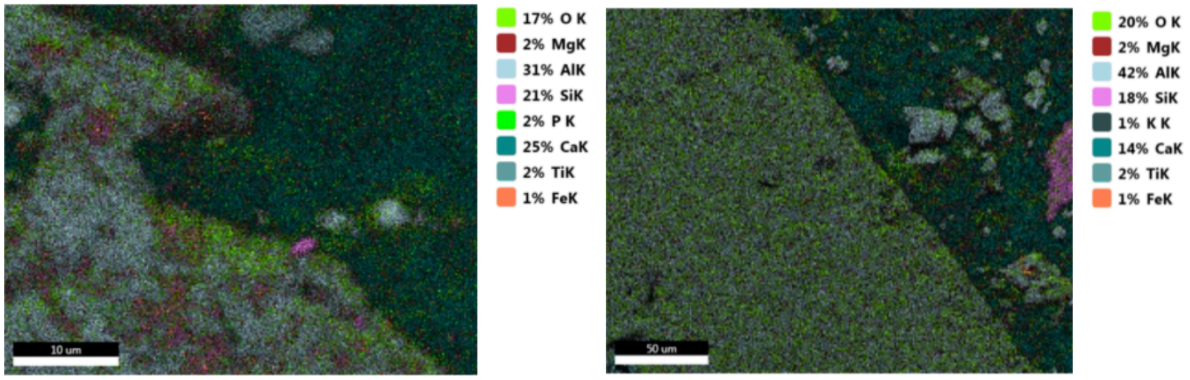

C-5 *Interface observations at different magnifications for a sample with bauxite aggregates*

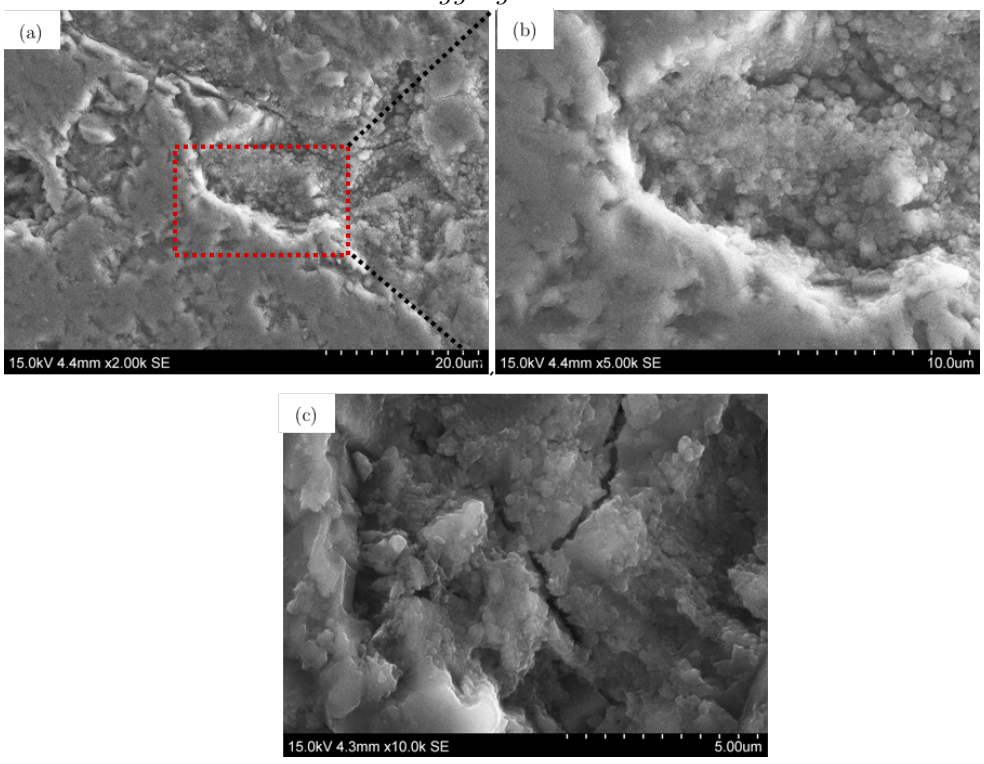

C-6 *Number of cycles to failure at three stress levels and corresponding mean values (f = 10Hz) for mixes composed of bauxite and quartz aggregates and mixes with combined fractions of bauxite and quartz*

Mix	Stress Level $S_{c,max}$	Number of cycles to failure N_f						Average
R-Bau	0,90	2255	2435	2664	2693	3156	4417	2937
	0,80	9041	10881	13469	13479	19225	19873	14328
	0,75	23098	36572	51918	53577	62609	64915	48782
Qua	0,90	1989	2034	2350	2425	2801	2924	2421
	0,80	8724	12324	13188	13888	19185	29756	16775
	0,75	17212	21269	61125	73528	101414	165023	73262
Bau-G	0,90	1009	1546	1874	2212	2424	2961	2004
	0,80	14733	15587	15755	16071	16551	17160	15977
	0,75	48447	55876	60906	64248	73564	86305	64891
Qua-G	0,90	903	1146	1385	1863	4643	5198	2523
	0,80	10423	11181	12054	13553	25242	25916	17263
	0,75	20909	22526	23769	30130	36024	62735	32682

C-7 *Temperature evolution for Qua-G and Bau-G with comparable number of cycles to failure at $S_{c,max} = 0,90$*

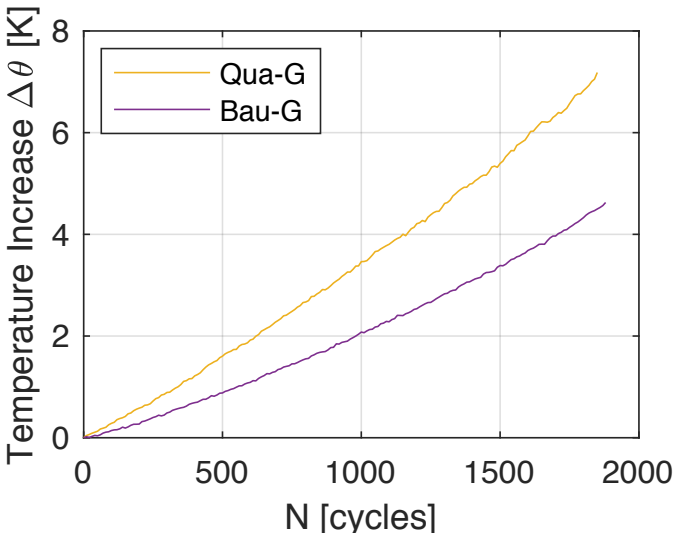

C-8 *Relative maximum strain development for Qua-G and Bau-G (left figures); Corresponding maximum strain development (right figures)*

$S_{c,max} = 0{,}75$

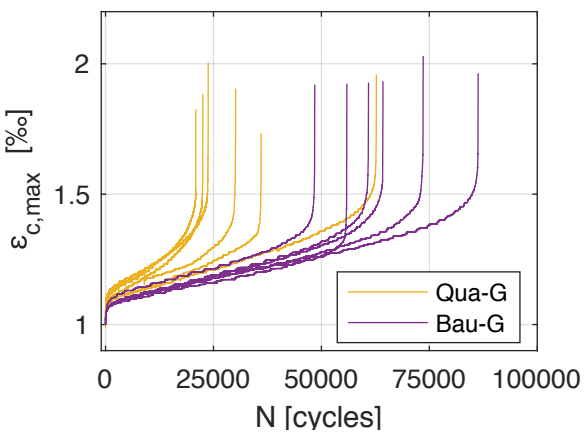

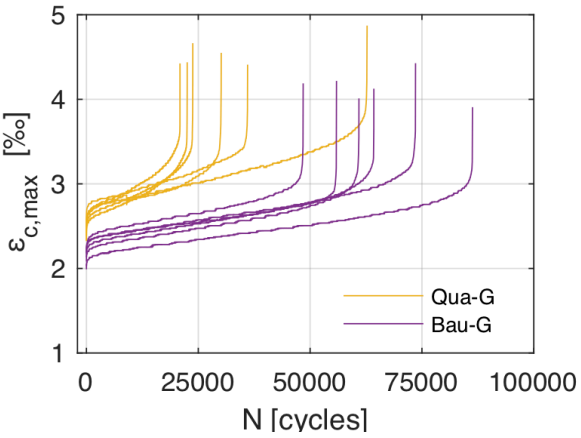

$S_{c,max} = 0{,}80$

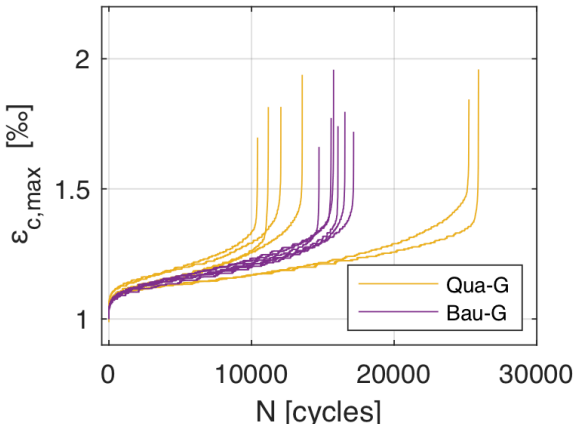

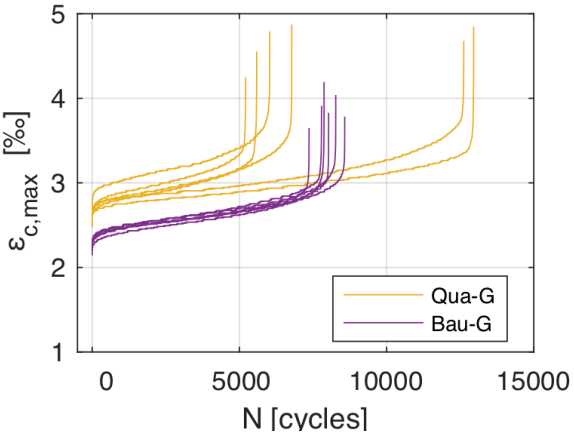

$S_{c,max} = 0{,}90$

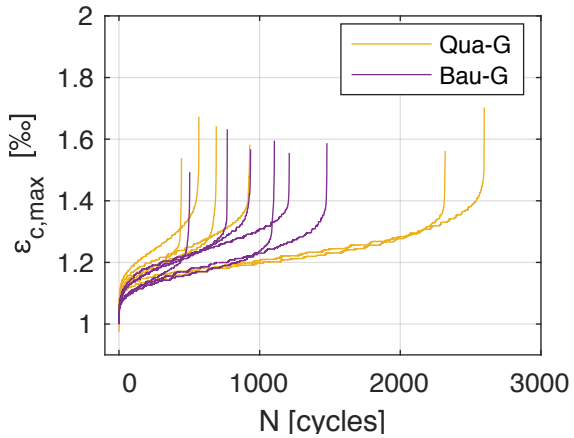

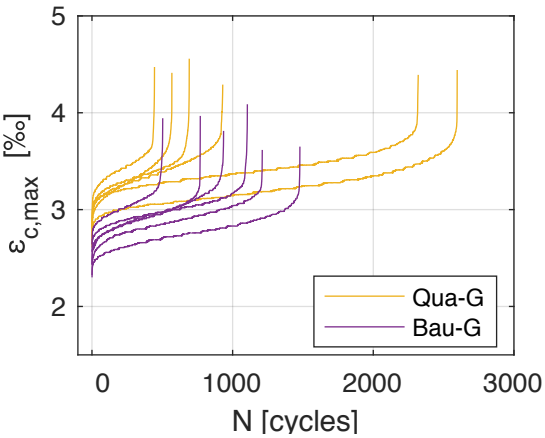

C-9 *Secant modulus evolution for specimens with similar number of cycles to failure at $S_{c,max}$= 0,75 (left) and $S_{c,max}$= 0,90 (right)*

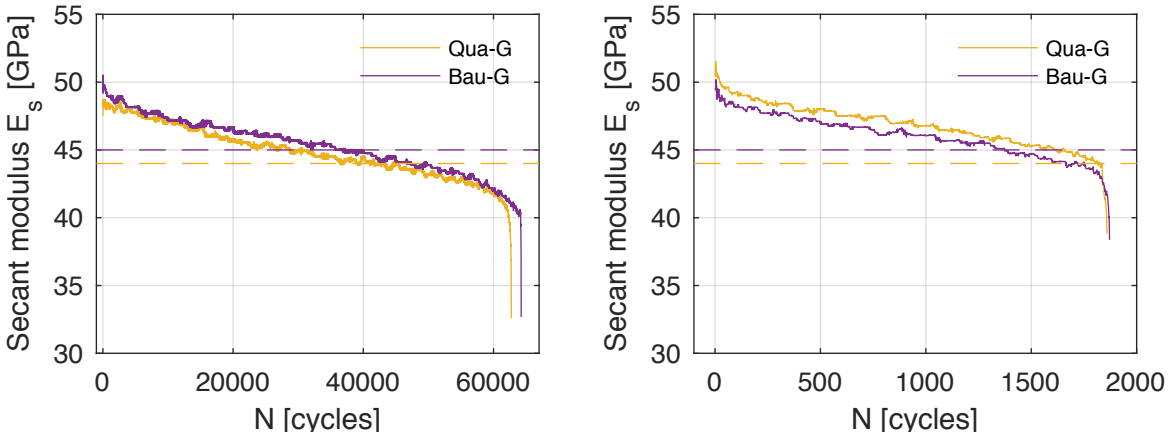

C-10 *Mean fatigue life and regression curves for the reference grout and mixes with increased porosity levels*

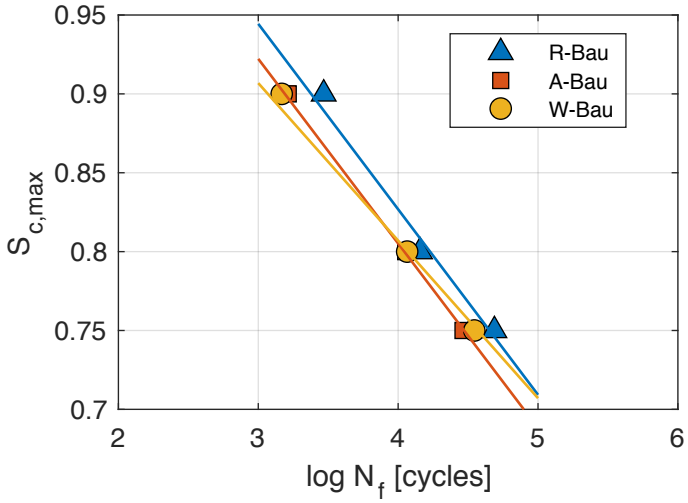

C-11 *Temperature evolution with comparable number of cycles to failure $S_{c,max} = 0{,}80$ (left); $S_{c,max} = 0{,}90$ (right) between the reference mix and mixes with increased porosity*

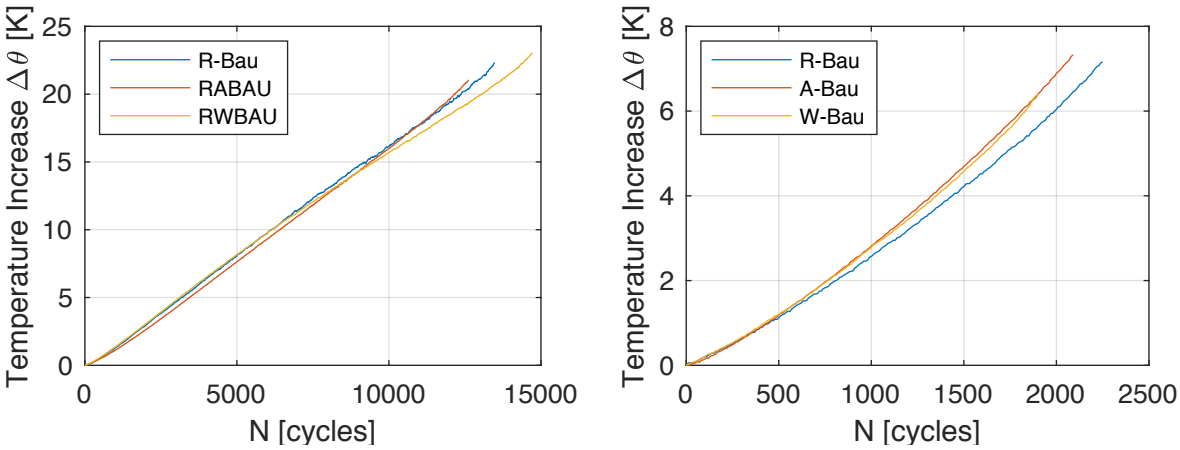

C-12 *Relative maximum strain evolution for specimens of each mix with similar number of cycles to failure at $S_{c,max} = 0{,}80$ (upper left) and $S_{c,max} = 0{,}90$ (lower left) ; Corresponding minimum and maximum strain evolutions and mean values of strain at failure (right)*

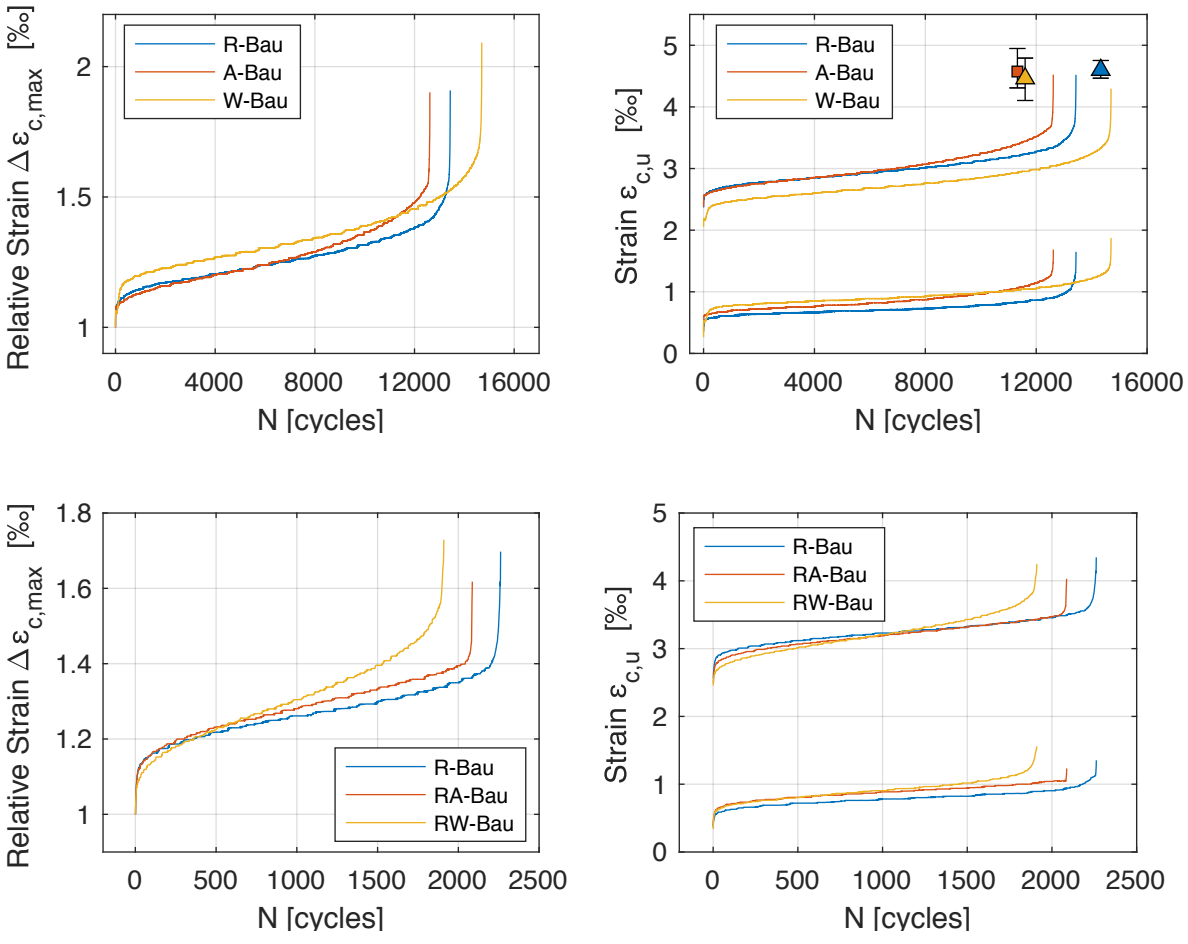

C-13 *Relative secant modulus evolution for specimens of each mix with similar number of cycles to failure at $S_{c,max} = 0{,}80$ (upper left) and $S_{c,max} = 0{,}90$ (lower left) ; Corresponding absolute values of secant modulus and comparison with the elastic modulus (right)*

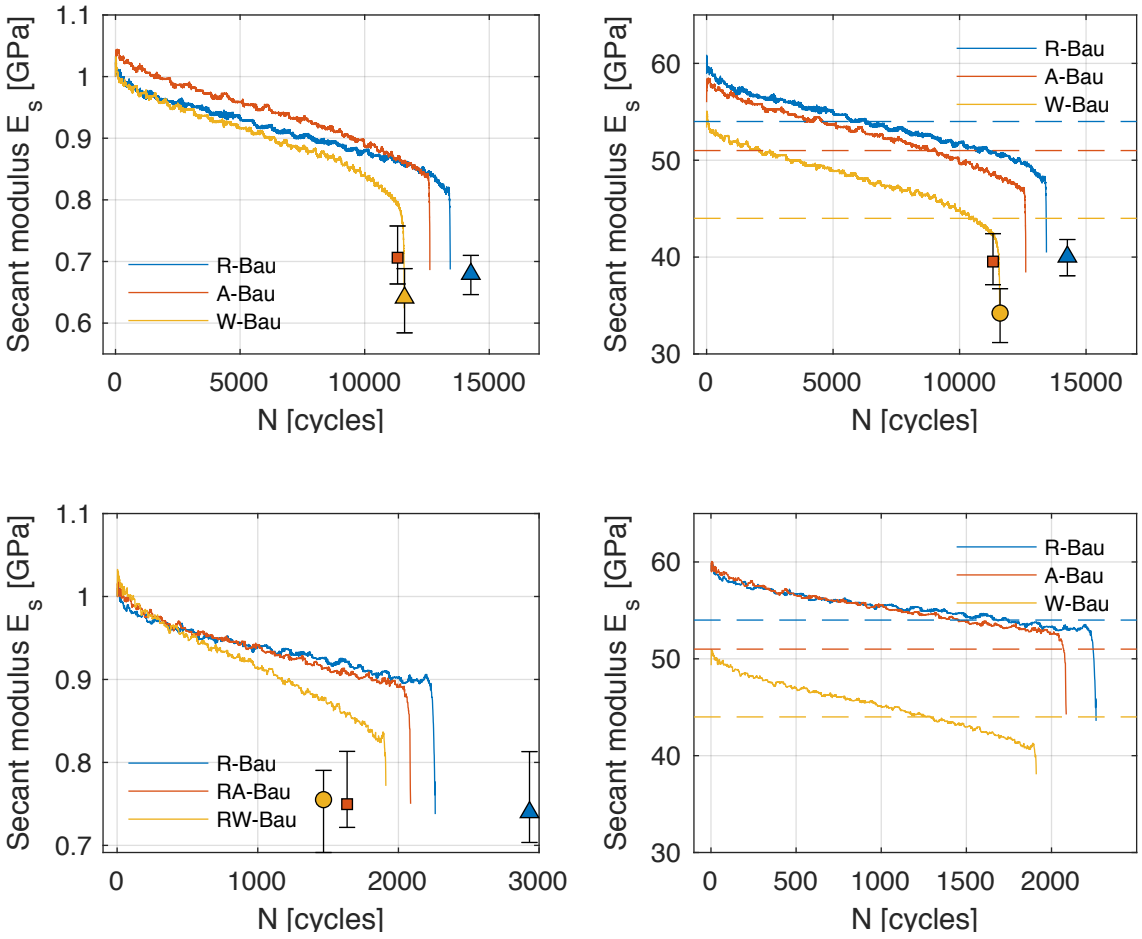

université PARIS-SACLAY

ÉCOLE DOCTORALE
Sciences mécaniques et énergétiques, matériaux et géosciences (SMEMAG)

Titre : Comportement des mortiers haute performance sous sollicitations de fatigue en compression

Mots clés : Mortier ; Haute performance ; Fatigue ; Endommagement ; Compression

Résumé : Le travail de cette thèse concerne la durabilité d'un point de vue mécanique des mortiers haute performance. De nombreuses structures sont soumises à des efforts de fatigue au cours de leur durée de vie comme des structures offshore, joints de chaussée, pistes d'aéroport ou planchers industriels.
Bien que ce phénomène soit assez connu pour les constructions métalliques, pour les ouvrages en béton et les mortiers, les chargements en fatigue sont rarement explicitement pris en compte dans les règles de dimensionnement. De plus, les éléments mentionnés dans la littérature concernant les phénomènes qui influent sur la résistance à la fatigue et qui déterminent la durée de vie des ouvrages, tels que le nombre de cycles, l'amplitude des contraintes avant rupture, niveau de fréquence appliqué sont assez contradictoires probablement en raison de la nature hétérogène du matériau.
Ainsi, l'objectif de cette thèse est d'abord d'étudier l'endommagement par fatigue principalement en compression à l'aide de différentes méthodes expérimentales.

Une partie importante de cette étude consiste à identifier les paramètres qui ont une influence sur la durée de vie et l'évolution de déformations et rigidité durant le chargement. Parmi ces paramètres, les suivants sont principalement étudiés : le niveau de fréquence, la contrainte maximale appliquée, l'élévation de température. Par la suite, des méthodes alternatives pour estimer la limite d'endurance et la durée de vie des mortiers sont proposées.

Un deuxième volet de cette thèse consiste à analyser l'influence de différents paramètres de formulation sur le comportement à la fatigue. Des formulations ont été développés avec des granulats de nature différentes, fractions granulaires et augmentation de porosité par air entrainé et E/C. Ainsi, l'influence de la microstructure est étudiée et complétée par différentes techniques de mesure expérimentales comme MEB-EDS, DRX, corrélation d'images, caméra infrarouge, porosité mercure, porosité à l'eau.

Title : Behavior of high-strength grouts under compressive fatigue loading

Keywords : Grout ; High-strength ; Fatigue ; Damage ; Compression

Abstract : The work in this thesis is related to the durability of high-strength grouts, in a mechanical perspective. Numerous structures are subjected to fatigue loading during their service lifetime such as offshore structures, wind turbines, road joints, airport runways or industrial floors.
Despite the fact that this phenomenon is well known in steel structures, it can be noticed that for concrete structures and grouts, fatigue loading is rarely explicitly considered in the design codes. Furthermore, the information available in the literature concerning the phenomena influencing fatigue resistance and which determine the lifetime of structures, such as the number of cycles, the amplitude of stresses before failure, the frequency level applied are quite contradictory, in part because of the heterogeneous nature of the material.
Thus, the aim of this thesis is firstly to analyze the damage induced by fatigue loading mainly in compression by means of different experimental methods.

An important part of this study consists in identifying the parameters which have an influence on the fatigue life and the strain and stiffness evolution during loading. Among these parameters, the following are predominantly investigated : the loading frequency, the maximum stress applied, the temperature increase. Subsequently, alternative methods are proposed in order to evaluate the endurance limit and the fatigue life of grouts.

A second part of this thesis consists in analyzing the influence of different mix components on the fatigue behavior. Different mixes have been developed with different aggregate types, in different grain fractions and an increased porosity level by entrained air and W/B. Therefore, the influence of the microstructure is examined and completed by different measuring techniques such as SEM-EDS, XRD, digital image correlation, infrared camera, mercury intrusion porosimetry and total water porosity.